The Organisation and Dynamics of *Escherichia coli* Outer Membrane Proteins

Patrick George Inns

Corpus Christi College, University of Oxford

A thesis presented for the degree of

Doctor of Philosophy

September 2021

Supervised by Professor Colin Kleanthous

Co-supervised by Professor Shabaz Mohammed

Abstract

The outer membrane of *E. coli* is a component of the cell envelope with significant physiological importance. This multifunctional membrane allows the influx of nutrients and simultaneously excludes toxic compounds, such as antibiotics, which must cross this membrane to elicit their cytotoxic effect. The composition and general structure of this membrane are well known, an asymmetric lipid bilayer containing LPS in the outer leaflet, phospholipids in the inner leaflet, densely populated by integral β-barrel outer membrane proteins and extensively linked to the underlying peptidoglycan through certain lipoylated inner leaflet outer membrane proteins. Little is known, however, about the lateral organisation and dynamics of the proteins in this membrane. In this thesis I investigate the organisation and dynamics of two highly abundant outer membrane proteins: the general porin, OmpF, and the lipoprotein, Pal.

OmpF distribution—visualised with Colicin N fluorescent fusion proteins—could be sorted into distinct categories related to the cell cycle, and these distributions arose due to the biased insertion of OmpF at mid-cell. This biased mid-cell insertion also caused old OmpF to localise to the cell poles during growth. Superresolution investigations showed that at fine resolutions, OmpF displayed a significant degree of clustering in the outer membrane and was highly restricted in its diffusion (D_{app}: 0.0018 $\mu m^2 s^{-1}$).

Pal, investigated by PALM-SPT, was shown to accumulate at the septum of dividing cells, revealing a key mechanism by which this protein stabilises the outer membrane during division. Pal diffusion was highly restricted (0.0042 $\mu m^2 s^{-1}$) as a result of peptidoglycan

binding, demonstrated by an almost 5 fold increase in diffusion coefficient (0.0205 $\mu m^2 s^{-1}$) upon removal of the PG binding domain.

This work shows that integral β-barrel OMP distribution and dynamics are dictated by the subcellular biased assembly of these proteins into a membrane that does not permit lateral diffusion. In addition, analysis of Pal demonstrates the vastly different diffusive environment of the inner leaflet of the outer membrane and the contribution of underlying cell envelope components on protein diffusion.

Declaration

I confirm that the work presented in this thesis, submitted for the degree of Doctor of Philosophy, is my own original work. Work that is not my own is referenced. This thesis has not been previously submitted at this or any other university.

Patrick Inns - September 2021

Word count (excluding bibliography): 47,000 words.

Acknowledgements

There are many people who I would like to thank for their help and support throughout my DPhil. Firstly, I would like to thank Professor Colin Kleanthous for the opportunity to pursue this exciting project and for his valuable supervision, support and advice. I would like to thank my co-supervisor Professor Shabaz Mohammed. I would like to thank Dr Nicholas Housden for the invaluable training he provided to me in all things Biochemistry related. I would like to thank Dr Patrice Rassam for introducing me to the world of fluorescence microscopy. I would like to thank Dr Renata Kaminska for providing the RKCK16 and RKCK19 *E. coli* strains used in this thesis. I would like to thank our collaborators Professor Bart Hoogenboom and Georgina Benn for providing the IMB317 *E. coli* strain. Many thanks to Dr Stephan Uphoff for providing the pROD85 plasmid encoding PAmCherry.

I would like to thank all members of the Kleanthous group past and present—Cara, Connor, Danny, Gideon, Hannah, Iva, Joanna, Jonathan, Melissa, Nathalie, Nick, Patrice, Renata, Ruth, Sandip and Vivian—for their friendship, help and advice.

Many thanks to all my fellow past and present Corpus Christi College "Corpuscles" for being such wonderful friends. Many thanks to my good friend Tyson Jones for his friendship and his valuable advice: learn to code. I would especially like to thank my partner Alma Chapet--Batlle for her love and support.

Finally, I would like to thank my parents Howard and Linda Inns and my sister Heather Inns for their constant support, I certainly would not have got to this point without them. I would also like to thank Pepper Inns for being such a wonderful and loyal friend.

I am extremely grateful to the Medical Research Council for funding this work.

Contents

List of Tables

List of Figures

List of Abbreviations

AFM Atomic Force Microscopy

ATP Adenosine Triphosphate

AU Arbitrary Units

BAM Beta Barrel Assembly Machinery

CI Confidence Interval

ColB Colicin B

ColE9 Colicin E9

ColIa Colicin Ia

ColN Colicin N

CSR Completely Spatially Random

DAP Diaminopimelate

Dapp Apparent Diffusion Coefficient

FRAP Fluorescence Recovery After Photobleaching

GFP Green Fluorescent Protein

IM Inner Membrane

IMP Inner Membrane Protein

ITC Isothermal Titration Calorimetry

kDa Kilo Dalton

KOH Potassium Hydroxide

LPS Lipopolysaccharide

NA Numerical Aperture

OBS OmpF Binding Sites

OM Outer Membrane

OMP Outer Membrane Protein

PAGE Polyacrylamide Gel Electrophoresis

Pal Peptidoglycan Associated Lipoprotein

PALM Photoactivated Localisation Microscopy

PE Phosphatidylethanolamine

PG Peptidoglycan

PMF Proton Motive Force

PSF Point Spread Function

SE Standard Error

SDS Sodium Dodecyl Sulphate

SMLM Single Molecule Localisation Microscopy

SPT Single Particle Tracking

STD-NMR Saturation Transfer Difference Nuclear Magnetic Resonance

TABS TolA Binding Site

Chapter 1

Introduction

During the course of over a century of intense research, the antiquated view of *E. coli* as a simple organism devoid of any notable subcellular organisation has been steadily disproven. With the advent of advanced optical microscopes—such as Frits Zernike's phase contrast microscope [1]—and powerful electron microscopes in the 1930s, *E. coli* was shown to display subcellular organisation not appreciated previously.

1.1 Early Investigations Into *E. coli* Subcellular Organisation

Where, at one time, it was thought that the genetic material of bacteria was diffuse throughout the cell, multiple investigations throughout the 1940s indicated beyond doubt that the genetic material of *E. coli* and many other bacteria was, in fact, organised into nucleoids that could be clearly visualised in both optical and electron microscopes [2–4]. At this time, however, technical limitations still precluded the investigation of many other physiological components of *E. coli* that we now appreciate are highly organised. No more was this relevant than in studies of the *E. coli* cell envelope. At approximately 40 nm in width, [5] studies of the cell envelope required both high resolution imaging methods and advanced sample

preparation techniques. These came in the form of electron microscopy and cell sectioning [6]. Early investigations revealed the presence of the Gram negative cell envelope [7–9]. Many, however, came to the erroneous conclusion that these bacteria had a single plasma membrane surrounded by a thick cell wall [8–10]. By the late 1960s the true structure of the Gram negative cell envelope had been elucidated, wherein there existed three components, at the time named: the plasma membrane, the dense intermediate layer of the cell wall and the outer membrane of the cell wall (Figure 1.1) [11]. Evidently, work was still required to correct the mistaken conflation of the cell wall and the outer membrane. The nomenclature eventually evolved into the more familiar "inner membrane", "peptidoglycan cell wall" and "outer membrane".

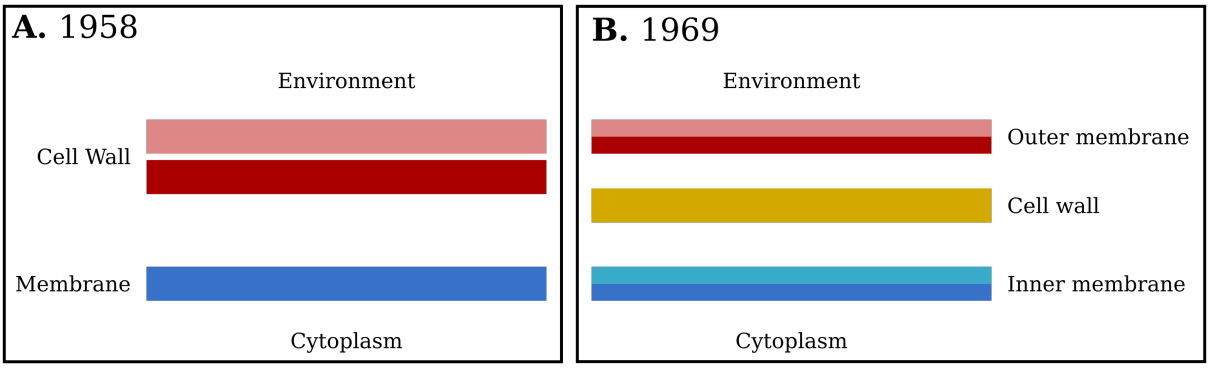

Figure 1.1: Advances in understanding of the *E. coli* cell envelope. A. Schematic outlining the fundamental organisation of the *E. coli* cell envelope, as understood in 1958. It was predicted that the inner membrane was a single layer structure and the "cell wall" was a double layered structure. **B.** Schematic outlining the fundamental organisation of the *E. coli* cell envelope, as understood in 1969. Electron micrographs could identify the two leaflets of both the inner and outer membrane. At the time, the cell wall was referred to as the "dense intermediate layer", reflecting its propensity to stain intensely. Figures adapted from [9, 11].

1.2 The Organisation of the *E. coli* Cell Envelope

Techniques that visualise cells directly are clearly valuable for investigating the organisation of the cell envelope, however, biochemical techniques are equally practical for this purpose. Around the time that electron microscopy of sectioned *E. coli* was providing robust evi-

dence for the presence of a three component cell envelope, ultracentrifugation was being used to separate the inner and outer membrane to allow for the quantification of their respective components [12]. In 1970, Schnaitman analysed radioactively labelled outer and inner membrane fractions by SDS-PAGE where he was able to demonstrate, unambiguously, a significant difference in the protein compositions of these membranes. In the same study, the outer membrane was also shown to be enriched in LPS [13], an observation that would be replicated in another Gram negative bacteria, *Salmonella typhimurium* [14, 15]. In the process of improving the procedures for solubilising the proteins of both membranes and generating membrane vesicles, numerous studies further confirmed the differences between the two membranes [16–19]. The next steps in *E. coli* cell envelope research involved localising specific proteins to these membranes. At the time of the first SDS-PAGE investigations of the inner and outer membrane, some proteins had already been localised, one notable example being Succinate Dehydrogenase, the reductive activity of which was shown to localise to the inner membrane [20]. This was confirmed biochemically by White, *et al.* in 1972 in addition to Coenzyme Q—an essential component of the electron transport chain—which was also shown to localise to the inner membrane [17]. These studies had therefore shown that the inner membrane of *E. coli* housed the energy generating apparatus of the cell. Over the coming years, a number of physiologically important proteins and protein complexes would also be localised to this membrane, such as: ATP synthase [21], SecYEG [22–24], the Tat system [25], and many proteins constituting the inner membrane components of large transmembrane complexes.

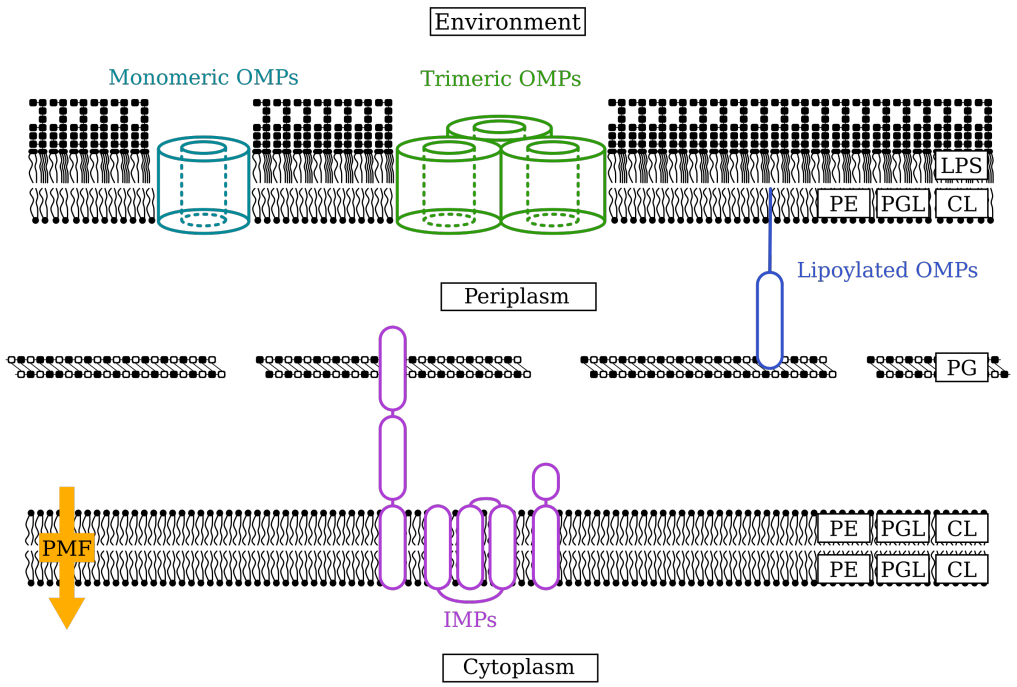

Figure 1.2: The *E. coli* cell envelope. Diagram of the *E. coli* cell envelope. The outer membrane is an asymmetric bilayer, of LPS in the outer leaflet and phosphatidylethanolamine (75%), phosphatidylglycerol (20%), and cardiolipin in the inner leaflet [26]. Monomeric OMPs and Trimeric OMPs are integral β-barrel proteins that span both leaflets. Lipoylated OMPs are embedded into the inner leaflet of the outer membrane by N-terminal acyl groups. A thin peptidoglycan cell wall is found in the periplasm between both membranes. The symmetric inner membrane is energised through the presence of a proton gradient and many energy dependent inner membrane protein systems.

1.3 The *E. coli* Outer Membrane

Concurrently to research on the inner membrane, investigations into the outer membrane would reveal the properties, functions, clinical relevance and unique organisation of this critically important structure.

1.3.1 Lipopolysaccharide

One of the notable early discoveries regarding the outer membrane was the presence of lipopolysaccharide [13, 17]. It was later shown that this lipopolysaccharide was almost exclusively located in the outer leaflet of the outer membrane, with the inner leaflet consisting

of phosphatidylethanolamine (75%), phosphatidylglycerol (20%) and cardiolipin [15, 26–29]. Full length Lipopolysaccharide is made up of three components: Lipid A, the core oligosaccharide and the repeating units of O antigen (Figure 1.3) [27, 30]. There is a significant variety of LPS lengths in *E. coli*, dependent on strain. Generally, wild type strains contain O antigen (termed "smooth"), laboratory strains—such as those derived from *E. coli* K12 and B—generally lack this O antigen [31] (termed "rough") and certain strains exist which lack certain core oligosaccharide elements (termed "deep rough") [27,30]; [32]. The structure of LPS has significant phenotypic effects on these strains. O antigen confers resistance to physiologically relevant toxins such as bile salts [27,33] and can reduce *E. coli*'s sensitivity to certain antibiotics [34, 35], notably protein antibiotics such as colicins [36]. Despite the large variety of LPS mutants, there is an absolute minimum length of LPS required for survival, this is the LPS precursor lipid IVA, which lacks the two Kdo residues normally found in the LPS inner core. These cells are viable but have profound growth defects [37–39].

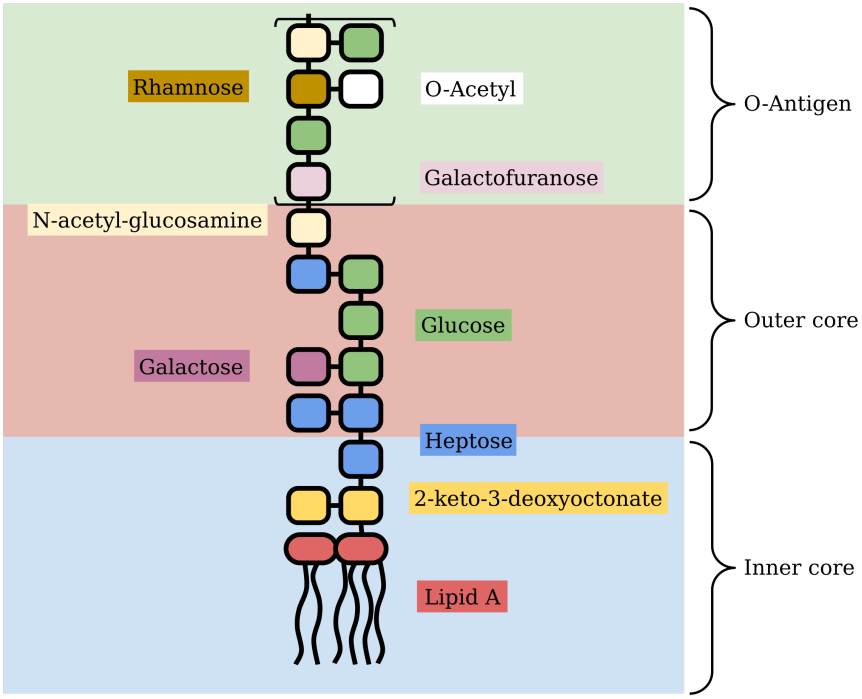

Figure 1.3: The structure of *E. coli* K12/O16 lipopolysaccharide. Diagrammatic representation of *E. coli* K12/O16 lipopolysaccharide. The inner core, outer core and O-antigen are shaded in blue, red and green, respectively. [40, 41]

1.3.2 Proteins

Proteins represent the other major component of the outer membrane. In early investigations two highly abundant proteins were found to be associated with the outer membrane, one a 7,000 Da lipoprotein which accounted for 40% of the total weight of the peptidoglycan cell wall [42] and the other a 44,000 Da protein that accounted for 70% of the protein content of the outer membrane [13].

1.3.3 Integral Outer Membrane Proteins

It was soon discovered that this 44,000 Da protein could actually be separated into four further bands ranging from 36,000 to 40,000 Da [43]. The 7,000 Da protein was Lpp, the most abundant protein in *E. coli* [44]. Research showed that the so-called "major outer membrane proteins" identified in numerous SDS-PAGE analyses were predominantly β structured [45, 46]. In the 1980s, it was decided to name many of the outer membrane proteins after the name of the gene that encoded them, thereby eliminating much confusion caused by different laboratories using their own nomenclature [47]. This confusion is perfectly exemplified by OmpA which by 1978 was known by the following names: TolG protein, Peak 7, B, 3a, II*, 0-10, d and HM 1-2 [47]. Over the proceeding years much research would be conducted on these outer membrane proteins (OMPs) revealing the existence of porins such as OmpF, OmpC and PhoE [48–50], enzymes such as OmpT and OMPLA [51,52], selective channels such as BtuB and LamB [53,54] and biogenesis machinery such as BamA and LptD (Figure 1.4) [55–57]. The porins represent—with bacteriorhodopsin—some of the first membrane proteins studied by X-ray crystallography [58–63]. These investigations into porin structure confirmed many of the previous observations of the major outer membrane proteins consisting predominantly of β strands. They revealed that the porins OmpF and PhoE consisted of 16 antiparallel β strands organised into a barrel structure, known as a β-barrel [61,62]. In the outer membrane, these β-barrel OMPs represent nearly all of the integral membrane proteins, most other proteins associated with this membrane are lipoylated and anchored predominantly to the

inner leaflet [64, 65].

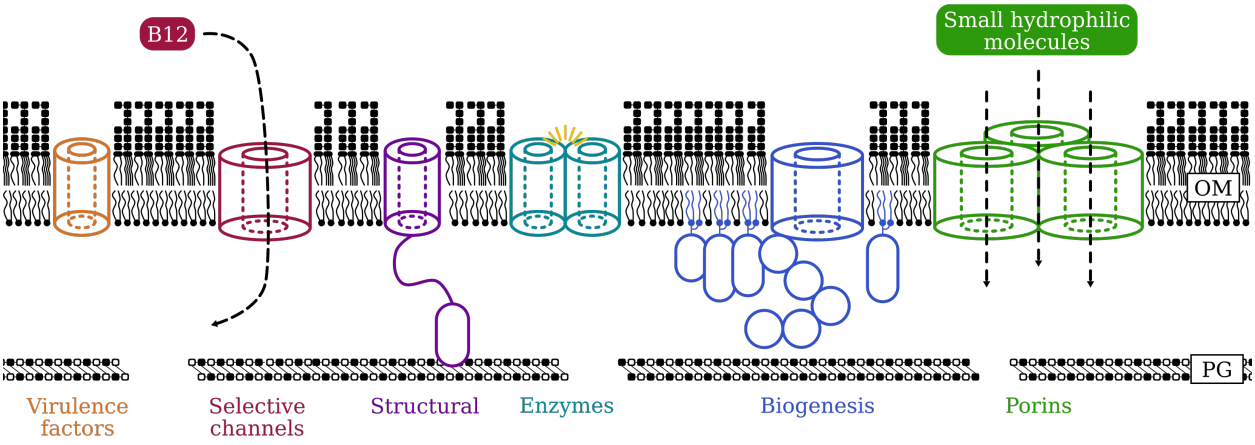

Figure 1.4: *E. coli* integral outer membrane proteins. Diagrammatic representation of the major categories of integral OMPs in *E. coli*. Some OMPs act as virulence factors such as OmpA and OmpT [66, 67]. Selective channels, such as BtuB, allow the diffusion of specific substrates across the OM. OmpA is a structurally important OMP, containing a peptidoglycan binding domain which non-covalently binds to the underlying cell wall. OMP enzymes exist in the form of the protease OmpT and the phospholipase OMPLA, which exists as a dimer in the OM. Two OMPs play an important role in OM biogenesis, BamA and LptD facilitate the assembly of OMPs and LPS into the OM, respectively. Porins, such as OmpF, allow the diffusion of small hydrophilic molecules across the OM.

1.3.4 Lipoylated Outer Membrane Proteins

The first of these lipoproteins to be discovered was the major outer membrane lipoprotein, or simply Lpp [42]. The pioneering investigation that discovered this protein also revealed a wealth of important details: it was approximately 7,000 Da in size, hugely abundant, anchored to the outer membrane, covalently linked to the peptidoglycan by lysine residue, and played a critically important role in cell envelope stability [42]. Almost all of these observations and inferences would be confirmed many times in the following years [68, 69]. Many other lipoproteins would be discovered, none however, at the abundance of Lpp or having the unique feature of covalent attachment to the peptidoglycan [68]. Further lipoproteins would be shown to be involved in a multitude of functions in *E. coli*. Pal, discovered 10 years after Lpp [70] is also involved in cell envelope stability [71] and plays an important role in outer membrane invagination during cell division [72]. BamD, the essential lipoprotein component

of the Bam complex, plays a critical role in outer membrane protein biogenesis [73]. LolB, the essential lipoprotein of the Lol complex, is responsible for lipoprotein assembly into the membrane [74]. LptE, the essential lipoprotein of the Lpt complex, is required for transport and assembly of LPS into the outer membrane [75].

The peptidoglycan cell wall of *E. coli* plays an important role in maintaining the structural integrity of the cell. Furthermore, many structural outer membrane proteins such as the lipoproteins Lpp and Pal, and the integral outer membrane protein OmpA, are critical in transducing this stability to the outer membrane.

The cell wall of *E. coli* consists of long glycan strands: alternating subunits of N-acetylglucosamine and N-acetylmuramic acid linked through β 1-4 glycosidic bonds. These glycan strands are cross linked to one another by short peptides (Figure 1.5) [76].

To each N-acetylmuramic acid residue, a 4 residue peptide is attached, consisting of L-alanine, D-glutamic acid, *meso*-diaminopimelic acid and D-alanine. Cross linking of glycan strands is facilitated by the formation of an amide bond between the *meso*-diaminopimelic acid of one peptide to the D-alanine of another. In *E. coli* the cell wall is relatively thin, ranging from 1 to 3 layers [76, 77] and contains numerous pores 10 nm in diameter [78].

Uncrosslinked *meso*-diaminopimelic acid acts as both the non-covalent binding site for Pal and OmpA and the covalent binding site for Lpp [79–81].

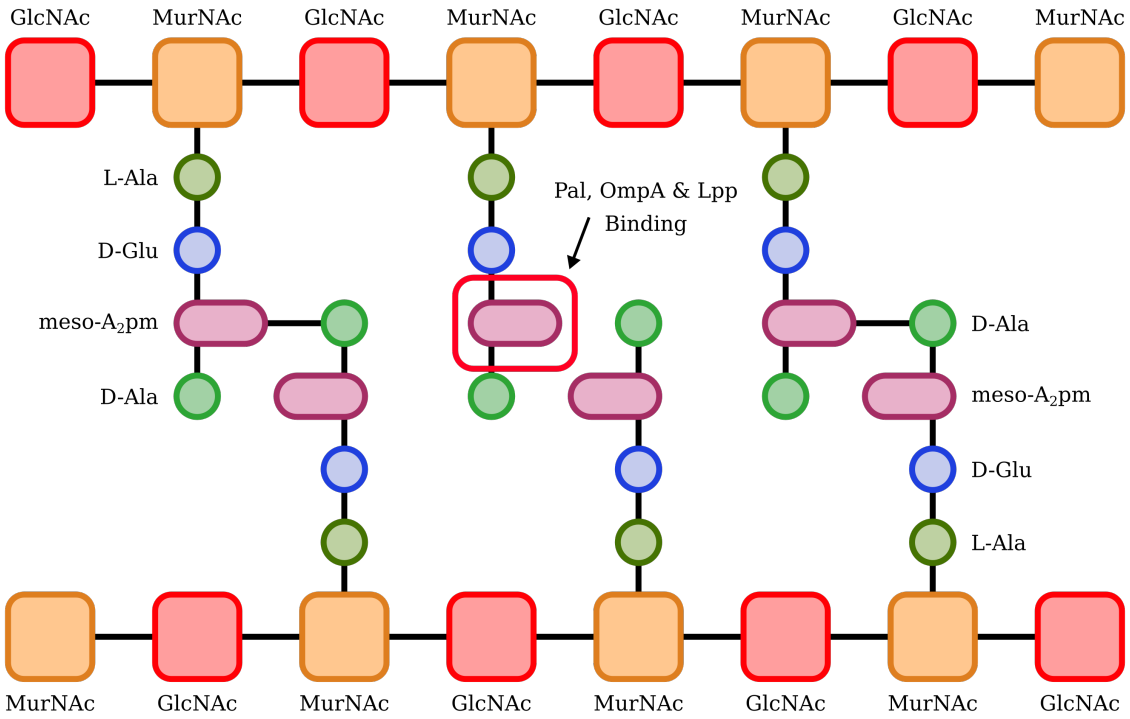

Figure 1.5: The structure of *E. coli* peptidoglycan. Diagrammatic representation of a single layer *E. coli* peptidoglycan. The binding site of Pal, Lpp and OmpA is highlighted by the red box. Figure adapted from [76].

1.3.5 Porins

The outer membrane of *E. coli* is partially permeable, allowing the diffusion of water and small hydrophilic molecules such as amino acids and glucose, hydrophobic and larger molecules are excluded. Even before the discovery of porins, the outer membrane was known to exclude neutral hydrophilic sugars larger than 900 Da, oligosaccharides, hydrophobic antibiotics and hydrophobic dyes [82–84]. Porins are chiefly responsible for this partial permeability. It was discovered that a single protein from *E. coli*, when reconstituted into membrane vesicles containing phospholipids and LPS was sufficient to restore the diffusion of sugars less than 550 Da in size [85]. It was in this study that the name "porins" was first coined. These observations were further confirmed when *E. coli* strains deficient in nutrient import were found to lack the "porin" protein band in SDS-PAGE analyses [86, 87]. Similar observations were made in other Gram negative bacteria such as *S. typhimurium* [84]. Porins,

such as OmpC, were later shown to assemble into trimers in the outer membrane [88, 89]. Shortly after establishing OmpF and OmpC as porins [89, 90], a more enigmatic protein, named "protein e", joined this category. When expressed, protein e could complement, to a degree, the diffusion deficient phenotypes in *E. coli* strains lacking OmpF [90]. At this time, expression of this protein had never been observed in wild type *E. coli* K-12. It was shown, however, that when these cells were grown under phosphate limited conditions, protein e was expressed [90, 91]. This protein was later renamed to PhoE [50].

E. coli tunes the expression of these porins via a number of pathways in response to a variety of environmental conditions. Arguably, the most extensively studied is the expression of OmpF and OmpC. Temperature, osmolarity, pH, nutrient availability, toxic stress and growth phase all affect the expression of these porins [92]. Functionally, OmpF and OmpC differ in one important aspect: the rate of solute diffusion permitted through their pores. OmpF has a pore diameter of 1.2 nm, whereas OmpC has a slightly smaller pore diameter of 1.1 nm. The result of this is that solutes diffuse through the OmpF at a higher rate than OmpC [92]. The observations that OmpF is favoured in low nutrient environments and OmpC favoured in nutrient rich environments are logically consistent with this difference in diffusion rates [92]. The *ompB* locus was shown to be responsible for the balance of expression between OmpF and OmpC [93]. Further genetic analysis revealed that this locus contained two genes: *envZ* and *ompR* [93]. The proteins EnvZ and OmpR constitute a two component regulatory system. EnvZ, an inner membrane sensor protein monitors the environment and through its kinase and phosphatase activity controls the level of phosphorylated OmpR. a transcriptional regulator. Under conditions of low osmolarity the levels of phosphorylated OmpR are low and hence only bind to high affinity sites on the *ompF* promoter, thereby increasing the expression of OmpF. Under conditions of high osmolarity, the levels of phosphorylated OmpR are increased, OmpR thus binds to both high and low affinity sites on the *ompF* and *ompC* promoters, which represses *ompF* transcription by creating a bend in the DNA, facilitated by the integration host factor; *ompC* transcription,

on the other hand, is promoted (Figure 1.6) [92]. It has also been shown that the stationary phase sigma factor negatively regulates the expression of OmpF [92]. A homologous two component regulatory system controls the expression of the other porin, PhoE: this system consists of a PhoR sensor protein and PhoB transcriptional regulator. Under conditions of phosphate starvation, PhoR phosphorylates PhoB which in turn binds to regulatory consensus sequences called pho boxes, enhancing the expression of multiple genes, including *phoE* [94].

The porins OmpF, OmpC and PhoE exist as trimers in the outer membrane. These trimers can consist of any combination of these porins from homotrimers of just one porin to heterotrimers consisting of one of each porin [89, 95, 96]. OmpF and OmpC comprise predominantly β strands, 16 of these strands are organised in an anti-parallel manner, the 1st strand interacts with the 16th to form a complete, hollow barrel structure [97, 98]. All integral OMPs share this β barrel structure.

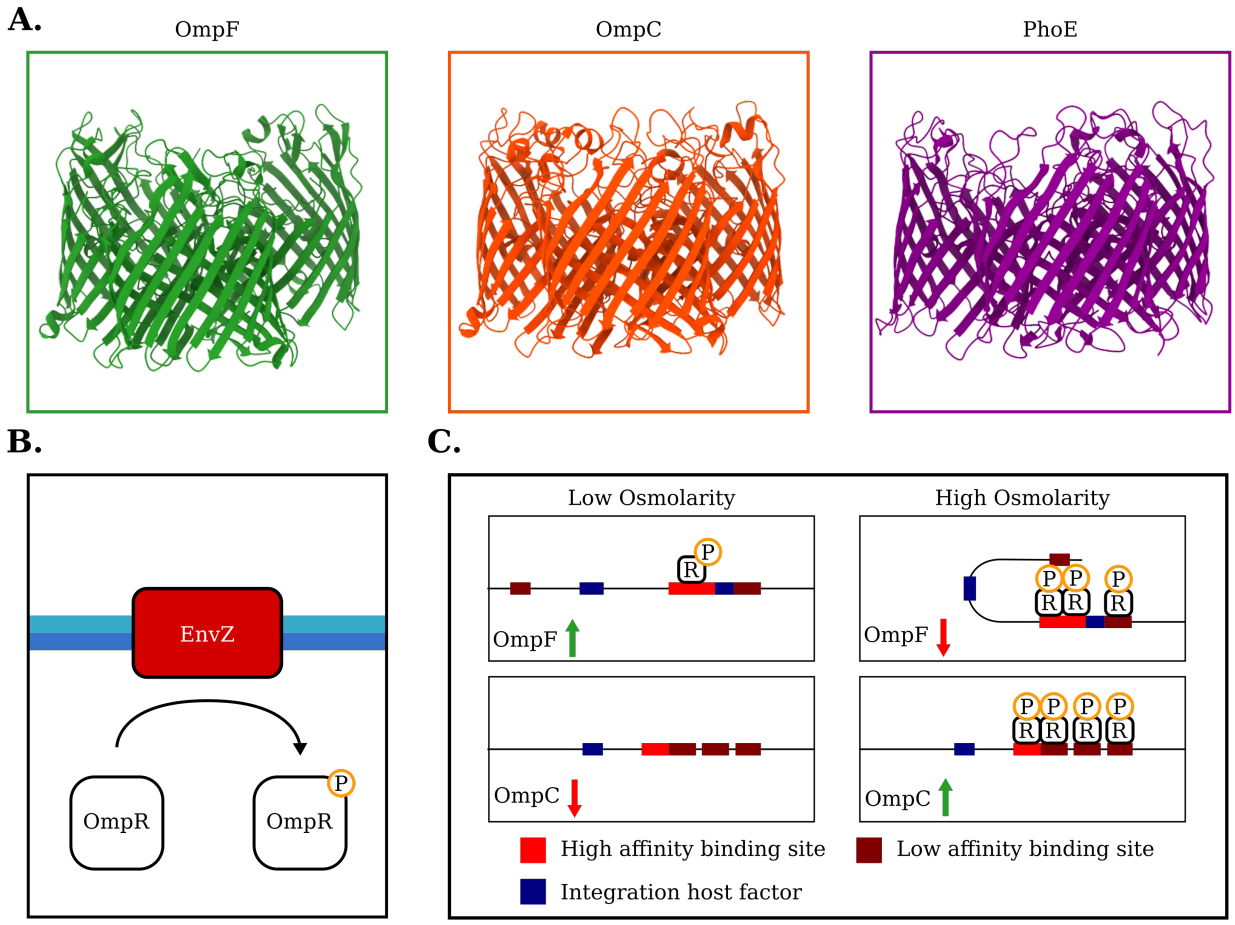

Figure 1.6: *E. coli* general outer membrane porins. **A.** Crystal structures of the trimeric porins: OmpF (green), OmpC (orange) and PhoE (purple). **B.** The inner membrane protein EnvZ phosphorylates OmpR in response to an increase in osmolarity. **C.** Regulation of OmpF and OmpC expression in response to changes in osmolarity, adapted from [92].

Unsurprisingly, both being hugely abundant, LPS and the porins interact extensively. These interactions are physiologically important for *E. coli* in that they affect the biogenesis of porins into the outer membrane. This was first observed in *E. coli* mutants producing defective LPS, wherein the outer membrane showed an appreciable decrease in OmpF and OmpC, however the non-porin OMP, OmpA was unaffected [99]. Further investigations showed interaction between OmpF trimers and LPS by SDS-PAGE [100]. Soon after these suggestions of the importance LPS plays in porin biogenesis, it was also found that LPS is critical for the trimerisation of these porins in the outer membrane [100, 101]. It had been previously identified that prior to the formation of stable trimers in the outer mem-

brane, porins can initially form metastable dimers and trimers, which unlike the mature stable trimers are not heat-stable [102, 103], LPS aids OmpF assembly in the step between metastable trimers to stable trimmers [104]. Recent investigations into these porin LPS interactions has revealed that porins have positively charged LPS binding sites and can form complexes with variable numbers of LPS molecules, stabilised by calcium ions [105].

1.3.6 Enzymes

The outer membrane of *E. coli* houses relatively few enzymes, of those that it does, OmpT and OMPLA represent the most extensively studied. The major source of proteolytic activity in the outer membrane of *E. coli* comes from OmpT. This protein was first discovered when it was observed that *E. coli* strains incapable of degrading extracellular Bacteriophage T7 RNA polymerase lacked the *ompT* gene and that this phenotype could be complemented by plasmid expression of the *ompT* gene [51]. One important use of this protein was demonstrated in its ability to degrade antimicrobial peptides: it was found that the cytoplasmic membrane permeabilising peptide protamine, when added to the growth medium, was degraded in minutes in an OmpT dependent manner [106]. The structure of OmpT was solved in 2001, revealing a vase shaped β-barrel consisting of 10 antiparallel strands [107], this structure revealed the active site of OmpT—which is conserved across all Omptins (outer membrane proteases)—as an aspartyl protease [107].

OMPLA (Outer membrane phospholipase A), first purified in 1971 [108], is a phospholipase encoded by the *pldA* gene in *E. coli* [109, 110]. In its active state, OMPLA is a homodimer of two 12 stranded β-barrels, the catalytic sites of each monomer found at the dimer interface [110]. The activity of OMPLA *in vivo* results in the formation of free acyl chains and lysophospholipids [108]. OMPLA exists in active and inactive states and it has been observed that perturbations in OM integrity—such as EDTA treatment, heat shock and phage induced lysis—cause a shift to the active state [109–112]. Importantly, OMPLA has been implicated in autolysis in *N. gonorrhoeae* [113] and has been found to be essential

in colicin secretion in *E. coli* [110, 114–116].

1.3.7 Biogenesis Machinery

Only two OMPs are essential for the survival of *E. coli*. These are BamA and LptD. BamA represents the integral outer membrane component of the β-barrel assembly machinery, responsible for assembling all of the other integral OMPs into the outer membrane. LptD represents the integral outer membrane component of the large Lpt system that spans the length of the periplasm, in the form of a proteinaceous bridge, responsible for the trafficking of LPS to the outer leaflet of the outer membrane.

1.3.8 BamA and the BAM Complex

BamA was first identified as being involved in OMP biogenesis in investigations of its *N. meningitidis* homologue: Omp85. Omp85 was shown to be essential for *N. meningitidis* survival and it was observed that in cells expressing little Omp85, the trimeric porins PorA and PorB did not form stable trimers in the OM, and instead accumulated as monomers [55]. It was also shown that Omp85 had homologues in a vast number of Gram negative bacteria [117]. After this pioneering work in *N. meningitidis*, the Omp85 homologue in *E. coli*—known then as YaeT, later renamed to BamA—was investigated [118]. Like Omp85, BamA in *E. coli* was essential for survival, BamA was also implicated in the assembly of OmpF, OmpC, TolC and OmpA assembly into the outer membrane [118]. BamA and its homologues all consist of a β-barrel domain and periplasmic POTRA (polypeptide-transport-associated) domains, the number of which depends on the BamA homologue [119]. The POTRA domains were the first element of BamA to have their structure solved by X-Ray crystallography [120], revealing a hook-like structure. The structure of *N. gonorrhoeae* BamA has been solved in its entirety [121], revealing that a lateral gate exists between β strands 1 and 16 of the barrel, which was shown in many subsequent studies to be important for the assembly of β-barrel proteins into the membrane [122, 123]. Investigations into the structure of *E. coli*

BamA with the transmembrane domain and POTRA domain 5 intact, revealed a similar structure to that of *N. gonorrhoeae* and *H. ducreyi* BamA, notably the existence of weakly interacting β strands 1 and 16 [123]. Molecular dynamics simulations of *E. coli* BamA, generated by homology models of *N. gonorrhoeae* and *H. ducreyi* BamA, indicated that over the course of a 500 ns simulation the lateral gate between β strands 1 and 16 opened. It was also shown in this investigation that when these strands were locked in close proximity by the introduction of a disulphide bridge, they lacked full BamA function, further indicating that OMPs are likely inserted through a process that involves the opening of this lateral gate [122]. A recent investigation into the mitochondrial BamA homologue, Tom59, has provided detailed evidence of the manner by which β-barrel OMPs are inserted into the outer membrane through the lateral gate. It was shown that candidate OMPs thread into the lateral gate strand by strand, interacting extensively with Tom50 β strands 1 and 16 and loop 6 [124].

In *E. coli*, BamA does not exist alone, the β-barrel assembly machinery consists of four additional components: BamB, BamC, BamD and BamE, all lipoproteins [125]. Of these lipoproteins, only BamD is essential for survival [73]. BamB and BamD interact directly with BamA through independent binding sites [73]. BamC and BamE bind to BamD in a manner that stabilises the whole Bam complex [73, 126]. Later, the structure of BamA in complex with BamCDE and BamA in complex with BamB were solved, revealing a likely role of BamCDE in the modulation of BamA conformations relating to its function of assembling β-barrel OMPs into the outer membrane [127]. Recently, cryo-EM has been used to determine the structure of the entire *E. coli* BAM complex (Figure 1.7), further supporting the theory that OMPs are assembled into the OM through the BamA lateral gate [128, 129].

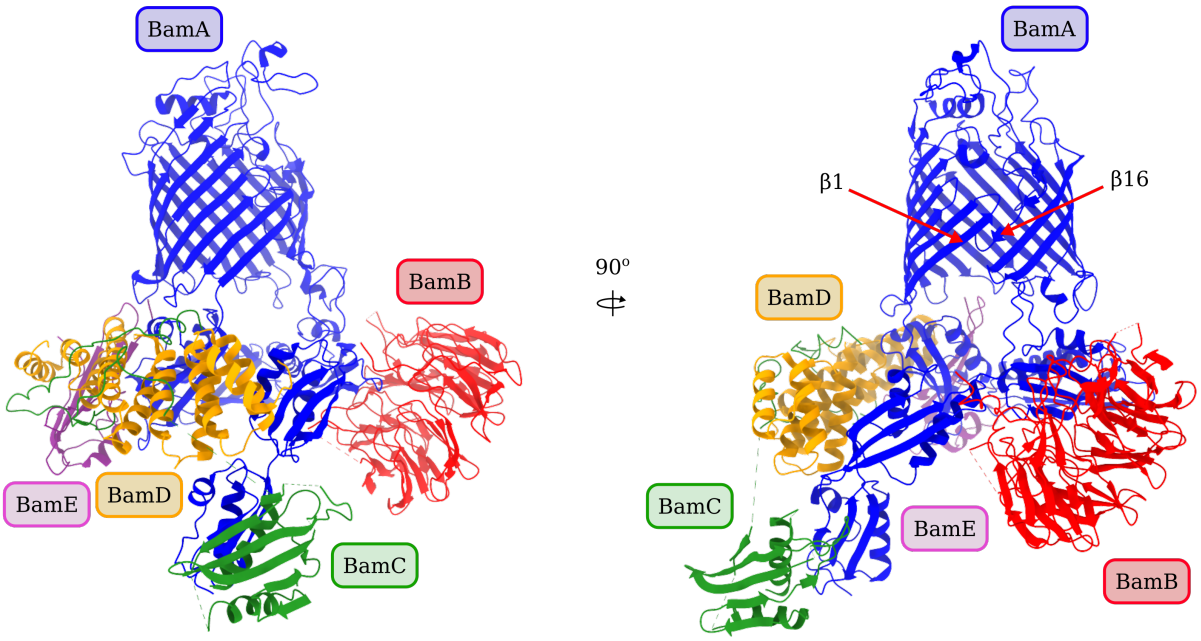

Figure 1.7: Cryo-EM structure of the *E. coli* BAM complex. Left: Cryo-EM structure of the BAM complex. Blue: BamA, Red: BamB, Green: BamC, Yellow: BamD, Purple: BamE. Right: BAM complex rotated 90° the 1^{st} and 16^{th} β strands are highlighted and consist BamA's lateral gate. Structure - PDB: 6LYS [130].

1.3.9 Outer Membrane Protein Trafficking

As with all other *E. coli* proteins, OMPs are synthesised in the cytoplasm of the cell. The nascent polypeptide of an OMP has an N-terminal signal sequence that directs it to the Sec machinery. This nascent polypeptide emerges from the ribosome, at which point peptidyl-prolyl cis-trans isomerase trigger factors bind to the signal sequence. This binding prevents interaction with the signal recognition particle (SRP) and pushes the polypeptide along the SecB dependent secretion pathway [131]. SecB exists as a homotetrameric chaperone that binds to the nascent polypeptide and delivers it to SecYEG via SecA in a post-transcriptional manner [131]. SecA, thought to exist as a dimer, is an ATPase that accepts the nascent polypeptide by the binding of this polypeptide to a preprotein cross linking domain (PPXD) on SecA [131]. During this binding, SecA is, in turn, bound to the heterotrimeric SecYEG complex. ATP molecules bind at the interface between NBF1 and NBF2 causing a conforma-

tional change in SecA, causing the nascent polypeptide to be forced into the SecYEG channel [131]. ATP hydrolysis returns SecA to its original conformation. Multiple rounds of ATP binding and hydrolysis cause the nascent polypeptide to be pushed, in its entirety, through SecYEG. During this process, signal peptidase cleaves of the signal sequence of the nascent polypeptide [131]. Now in the periplasm, the nascent polypeptide must be trafficked to the outer membrane for insertion. This is facilitated by periplasmic chaperones [126, 132, 133]. SurA represents the chaperone of the eponymous SurA pathway. Skp and DegP, likewise, for the Skp/DegP pathway [126]. Generally OMPs prefer the SurA pathway, however, in *surA* deletion mutants, the Skp/DegP pathway can compensate, not, however, without the emergence of a noticeable phenotype [132]. It has been hypothesised that the Skp/DegP pathway functions to save or degrade unfolded OMPs that fall off SurA [126, 133]. SurA or Skp will then deliver the unfolded OMP to the BAM complex. The β signal, found at the C terminus of the unfolded OMP then interacts with the lateral gate of BamA and threads, β strand by β strand into this gate until budding off as a folded OMP into the outer membrane (Figure 1.8) [124, 133].

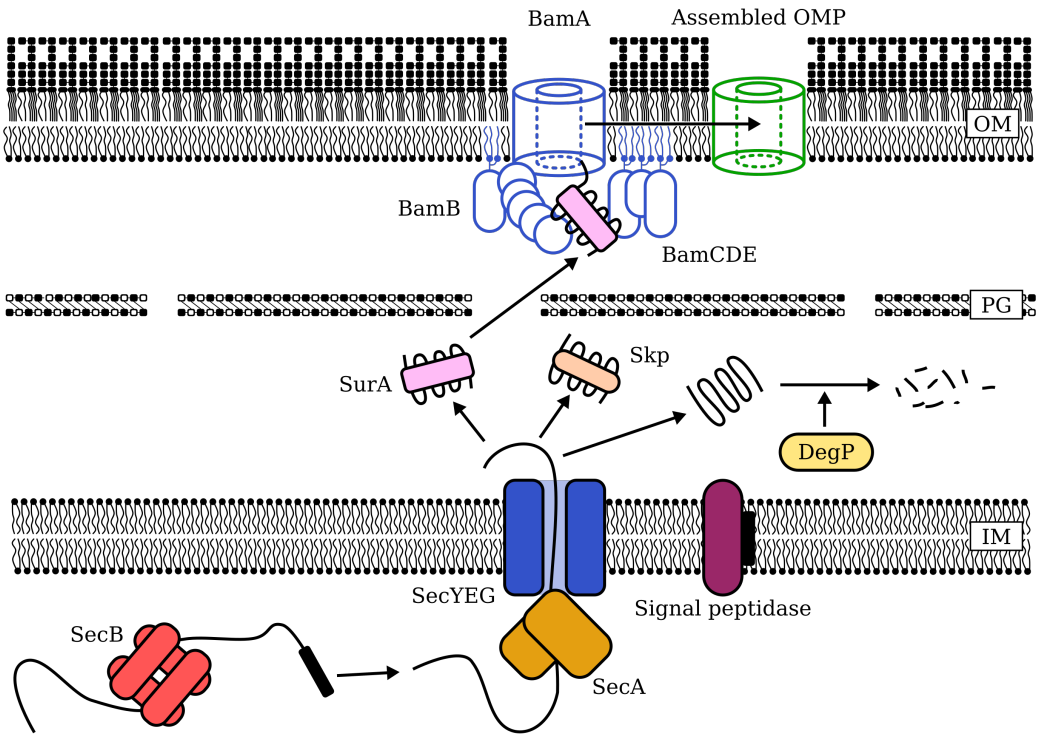

Figure 1.8: *E. coli* outer membrane protein biogenesis. Diagrammatic representation of outer membrane protein trafficking in *E. coli*. The cytoplasmic and inner membrane Sec proteins facilitate the transport of the nascent polypeptide into the periplasm. The periplasmic chaperones SurA and Skp deliver the unfolded OMP to the BAM complex where it is inserted β strand by β strand at the BamA lateral gate.

1.3.10 LptD and the Lpt Complex

LptD was shown to be an outer membrane protein involved in outer membrane biogenesis in the early 2000s. Then known by two names, Imp (increased membrane permeability) and OstA (organic solvent tolerance), LptD was shown to be essential in *E. coli* and from amino acid sequence analysis, likely a β-barrel outer membrane protein [134]. Later it would be shown that LptD, in complex with a lipoylated outer membrane protein called LptE (formerly RlpB), is responsible for assembling LPS into the outer membrane [75]. It was shown that when LptD and LptE were depleted, LPS was not assembled into the outer membrane by analysing the activity of the outer membrane enzyme PagP [75]. The LPS transport system was eventually pieced together in its entirety: MsbA an essential, inner

membrane ABC transporter [135]; LptA and LptB found in the periplasm and cytoplasm, respectively, both essential [136]; LptC an essential inner membrane protein [137]; LptD and LptE, essential and both found in the outer membrane [134] [75]; LptG and LptF, essential inner membrane proteins [138]. A model for transport that relies on all of these proteins was formulated, known as the PEZ model for LPS transport [139].

1.3.11 LPS Transport

LPS, or specifically the Lipid A and core oligosaccharide components, are synthesised on the cytoplasmic leaflet of the inner membrane. This rough LPS is then flipped from the cytoplasmic leaflet to the periplasmic leaflet by the ABC transporter MsbA in an ATP dependent manner [135]. LPS is extracted from the membrane by a complex of multiple Lpt proteins that constitute an ABC transporter. This complex is formed by the inner membrane proteins: LptF, LptG, LptC. The ATPase function of this transporter is carried out by two LptB proteins [139–141]. LptA, originally thought to be a soluble periplasmic membrane protein shuttling LPS from the inner to outer membrane is now known to form a proteinaceous bridge between the LptB2FGC complex and the LptDE complex [139]. LptA, the periplasmic domains of LptD, and the periplasmic domain of LptC all belong to the OstA protein superfamily and as such have a hydrophobic groove that would run the length of the protein bridge. This explains how the hydrophobic Lipid A component of LPS would be shielded from the aqueous environment of the periplasm as it is transported to the LptDE complex [139]. LptD is the second largest monomeric β-barrel known to exist, consisting of 26 antiparallel β strands (The largest: SprA contains 36 β strands [142]), LptE acts as a plug and sits within the LptD barrel [143, 144]. Similar to BamA, a lateral gate exists between the two terminal β strands of the barrel, it is theorised that, after being delivered along the LptA bridge, LPS passes through the pore of LptD and then exits through the lateral gate into the outer leaflet of the outer membrane (Figure 1.9) [139, 143, 144].

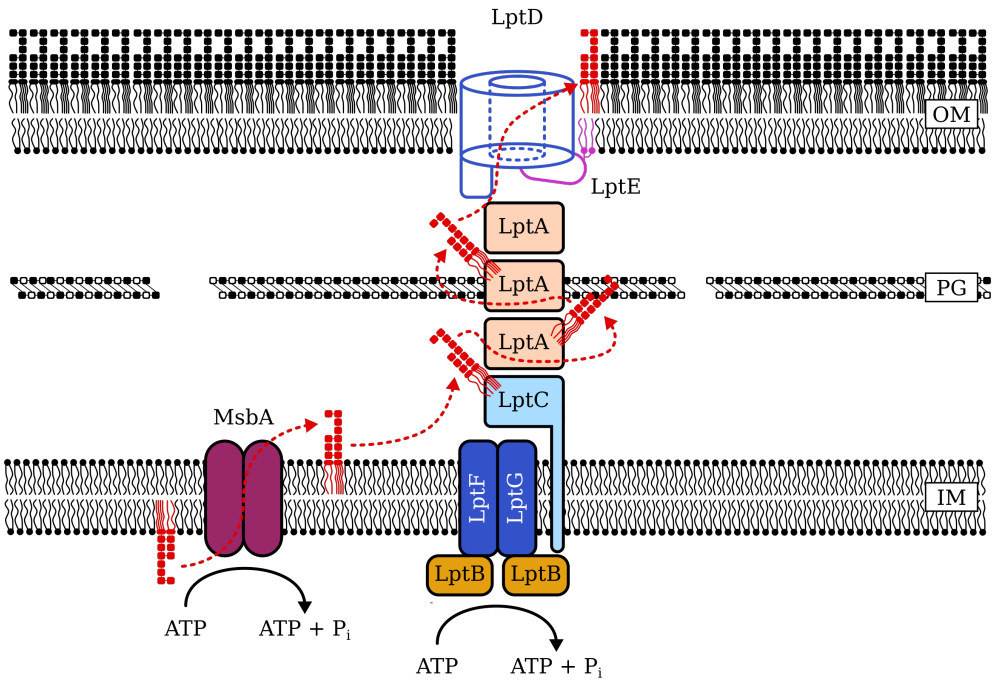

Figure 1.9: Lipopolysaccharide biogenesis in *E. coli*. Diagrammatic representation of lipopolysaccharide trafficking in *E. coli*. LPS is synthesised at the inner leaflet of the inner membrane and flipped into the outer leaflet by MsbA. The components of the Lpt complex form a transmembrane proteinaceous bridge across which LPS is transported, eventually being inserted into the outer leaflet of the outer membrane through the lateral gate of LptD.

1.3.12 Structural Proteins

A number of proteins found localised to the outer membrane play an important role in maintaining the structural integrity of the cell envelope. The three most extensively studied of these being: the β-barrel outer membrane protein, OmpA; the highly abundant lipoprotein, Lpp; and the lipoprotein component of the Tol-Pal system, Pal.

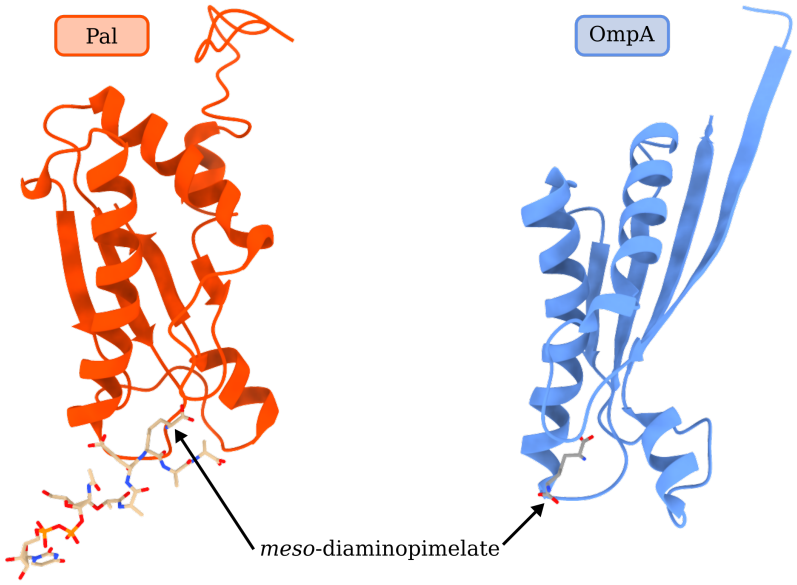

Figure 1.10: Structure of Pal and OmpA peptidoglycan binding domains. Orange: NMR structure of the peptidoglycan binding domain of *Haemophilus influenzae* Pal bound to UDP-MurNac-L-Ala-D-Glu-m-Dap-D-Ala-D-Ala. Blue: Crystal structure of the peptidoglycan binding domain of *Acinetobacter baumannii* OmpA bound to *meso*-diaminopimelate. Pal peptidoglycan binding domain - PDB: 2AIZ [79]. OmpA peptidoglycan binding domain - PDB: 3TD4 [80].

1.3.13 Outer Membrane Protein A

The investigation into OmpA began with rudimentary investigations of the protein content of the outer membrane. In one such investigation the mass of OmpA—known then as protein II*— was determined at between 32 - 34 KDa by SDS-PAGE [145]. The gene for OmpA was first cloned in 1979 [146] and one year later the full nucleotide sequence of the *ompA* gene and the OmpA primary structure were elucidated [147, 148]. The first indications that OmpA played a role in cell envelope integrity by interacting with the peptidoglycan came from experiments showing that strains lacking OmpA adopted spherical morphologies, were more resistant to antibiotics and detergents, displayed extensive blebbing and a dissociation of the peptidoglycan cell wall from the outer membrane [149]. OmpA became a subject of intense study in the proceeding years and many investigations revealed the multifaceted role it plays in *E. coli*. OmpA was found to act as the receptor for bacteriophages TuII*

and K3 [150–152]. As well as acting as a receptor for bacteriophages, OmpA was also found to be a receptor for bacteriocins, specifically the group A colicins K and L [153, 154]. Studies in proteoliposomes into which purified OmpA had been reconstituted revealed another function: that of a gated, unspecific pore [155,156]. Osmotic swelling was observed in these proteoliposomes, the rate of which was similar to that observed previously for the porins OmpF and OmpC [155]. Before the structure of the OmpA transmembrane domain was solved by X-ray crystallography and NMR, it was correctly predicted through bioinformatic methods to be a 8 stranded, anti parallel β-barrel [157]. In 1998, the structure of the OmpA transmembrane domain was solved to 2.5 Å resolution by X-ray crystallography [158]. Three years later the structure of OmpA would also be determined using multidimensional heteronuclear NMR spectroscopy, representing, at that time, one of very few membrane proteins whose structure was determined using this technique [159]. An important feature of OmpA is its interaction with the peptidoglycan cell wall. Before the structure of OmpA was solved, it had been suggested that the C-terminal region of OmpA constituted a conserved peptidoglycan binding domain that was found across many species and within many distinct proteins, such as Pal and MotB [160]. This interaction with peptidoglycan was shown in the crystal structure of the *Acinetobacter baumannii* OmpA C-terminal domain, which was bound to *meso*-diaminopimelate, an amino acid found within the pentapeptide cross linker of peptidoglycan (Figure 1.10) [80]. Molecular dynamics of full length OmpA indicated that both monomers and homodimers of OmpA can interact with peptidoglycan. It was observed that OmpA monomers bring the peptidoglycan up to the outer membrane whereas OmpA homodimers have little effect on the location of peptidoglycan [161].

1.3.14 Braun's Lipoprotein

Braun's lipoprotein or Lpp, was the first lipoprotein discovered. In a pioneering study, investigating the effect of Trypsin on the *E. coli* cell envelope, Braun and Rehn, discovered a protein covalently cross-linked to the peptidoglycan by a lysine residue [42]. In this study,

it was also shown that the protein contained a lipid group. This protein was predicted to occur one every 10 repeating units of peptidoglycan and had a molecular mass of 7 kDa. In the investigation, a prediction of the abundance of Lpp was made in the order of 100,000 proteins per cell [42]. It would be later shown that even this high an abundance was an underprediction, with more recent estimates sitting at 1,000,000 Lpp proteins per cell [44]. Further investigation into Lpp revealed that the covalent linkage to peptidoglycan occurs between the epsilon amino group of the C-terminal lysine and the carboxyl group of the *meso*-diaminopimelate residue of the peptidoglycan peptide cross linker [81, 162]. The nature of Lpp's lipid group was revealed in 1973, it was shown that the N-terminal amino acid glycerylcysteine was the attachment site for two fatty acids and the N-terminal group was an attachment site for an additional fatty acid [163]. It was shown that Lpp had two forms in *E. coli*, that of covalently bound to the peptidoglycan and a free form not covalently linked to the peptidoglycan. Inouye *et al.* discovered that two thirds of Lpp was found in this free form and the covalent link to the peptidoglycan was a reversible one [164]. Furthermore, it was found that free Lpp also binds to peptidoglycan, but in a non-covalent manner [165]. Early studies based on the Lpp amino acid sequence and circular dichroism measurements suggested that the protein was predominantly α-helical [81] [162]. This was confirmed when the crystal structures were solved revealing Lpp to exist as an alpha helical, trimeric coiled coil [166]. Lpp plays an important role in maintaining cell envelope integrity. This is highlighted in *lpp* mutants which show membrane blebbing and sensitivity to a variety of chemical agents: detergents such as SDS, metal chelating agents such as EDTA and antibiotics such as vancomycin [68]. Lpp has also been shown to play a critical role in delineating the width of the periplasm, wherein increasing the length of the Lpp protein, increases the width of the periplasm, proportionally [167, 168].

1.3.15 The Tol-Pal System

Years after the discovery of Braun's lipoprotein, a distinct lipoprotein would be discovered which, like Lpp, associates with the peptidoglycan [70, 169]. This protein was eventually named peptidoglycan associated protein (Pal) [170]. The crystal structure of *Haemophilus influenzae* Pal revealed that the non-covalent interaction between Pal and the peptidoglycan occurs at the *meso*-diaminopimelate amino acid of the peptidoglycan peptide cross-linker (Figure 1.10) [79]. The N-terminus of Pal is homologous to Lpp and is hence associated to the inner leaflet of the outer membrane in the same manner [171]. The structural role Pal plays in the cell is exemplified in *pal* strains which, though viable, display a phenotype associated with a loss in cell envelope integrity. This includes an increased formation of outer membrane vesicles [172] and the leaking of periplasmic proteins into the extracellular medium [173].

Pal, however, does not exist in isolation. It forms a part of the Tol-Pal complex which consists of a core complex of the proteins: TolQ, TolR, TolA, TolB and Pal itself. TolA and TolB interact with Pal directly [174–177]. TolB is a periplasmic protein containing two distinct domains, one responsible for binding to TolA and one that binds to the peptidoglycan binding domain of Pal in such a way as to prevent Pal binding to peptidoglycan. TolA is a component of the TolQRA nanomachine, of which TolQ-TolR represents a stator complex and TolA represents the mobile component. The inner membrane components of the Tol-Pal system have homologous systems for which more structural information is known. Two of these systems are Mot and Ton. The stator complexes of these systems are MotA-MotB and ExbB-ExbD, respectively. The MotA-MotB stator complex is required for driving the rotation of the bacterial flagella and the ExbB-ExbD is required for the TonB mediated uptake of certain nutrients through TonB dependent receptors. The TolQ-TolR stator complex drives the action of TolA which disrupts complexes of Pal-TolB, allowing Pal to bind to the peptidoglycan [72]. It is through the action of TolA that the concentration of Pal in a form bound to the peptidoglycan is increased at the septum of dividing cells to aid in the

invagination of the outer membrane (Figure 1.11) [72].

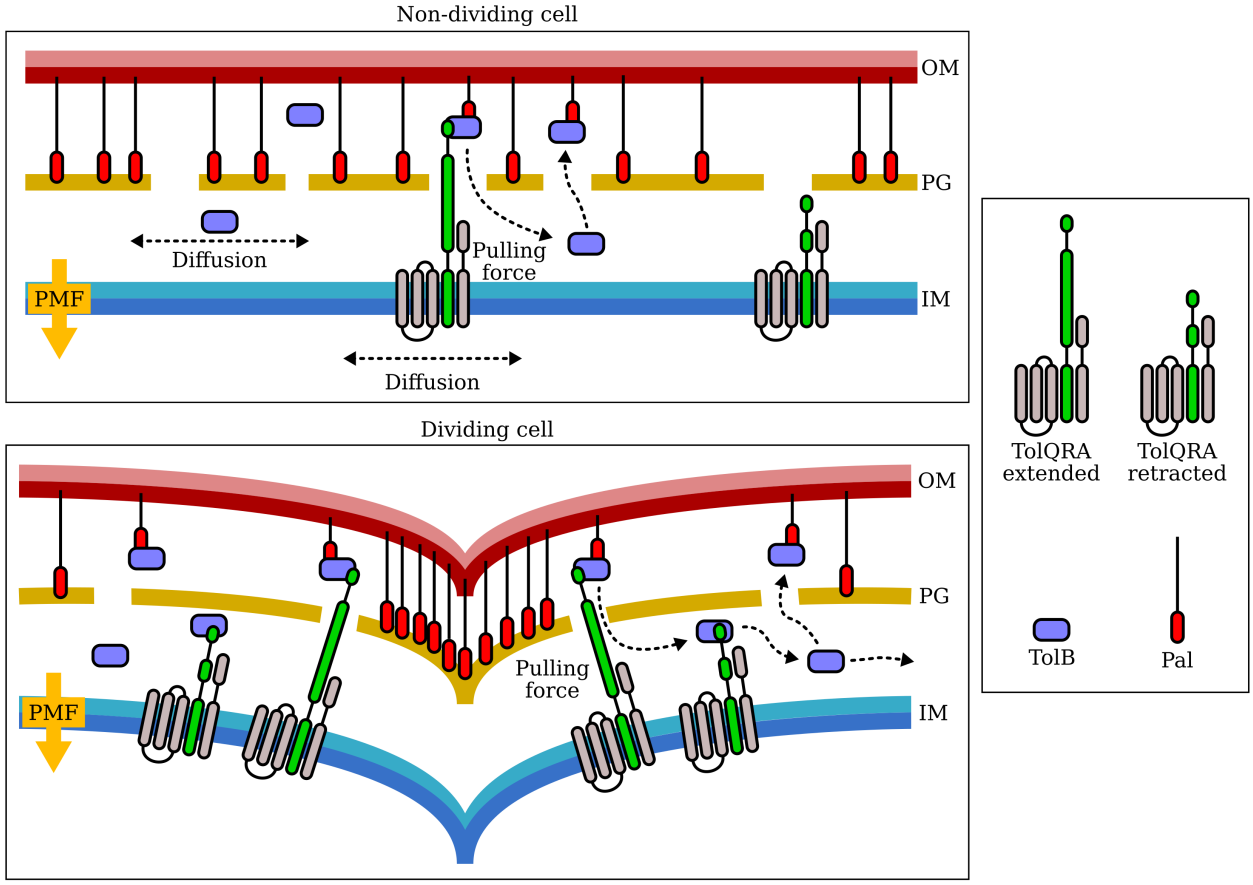

Figure 1.11: Stabilisation of the outer membrane during division by the Tol-Pal system. Diagrammatic representation of the stabilisation of the outer membrane of *E. coli* by the Tol-Pal system. Top: Tol-Pal in non-dividing cells. TolQRA is free to diffuse in the inner membrane, TolA can bind to complexes of Pal-TolB and dislodge TolB and pull it into the inner periplasm, allowing Pal to bind to the peptidoglycan. Bottom: Tol-Pal in dividing cells. TolQRA is recruited to the septum of dividing cells, thereby dislodging more TolB proteins from Pal, this enriches the local concentration of Pal bound to peptidoglycan at the septum, aiding the invagination of the outer membrane.

1.4 Bacteriocins

It is estimated that 0.1% of the gut microbiota is composed of *E. coli* [178]. The large intestine is an environment of significant competition. *E. coli* have developed mechanisms to exploit this crowded niche and eliminate competing strains. These include the type VI secretion system used to deliver toxins through a syringe structure into the cytoplasm of

competing strains [179]; contact dependent inhibition mediated by the proteins CdiA and CdiB [180]; and the secretion of antibacterial proteins called colicins [181].

Colicins encompass a broad group of antibacterial proteins that are secreted by certain *E. coli* strains that target and kill competing *E. coli* strains. Due to the large number and variety of colicins, they are subdivided into categories depending on the inner membrane system they parasitise to energise their import and the method by which they elicit their cytotoxic activity. This first subdivision splits colicins into groups A and B [181].

All known colicins bind to an outer membrane protein as their receptor and then deposit, through either the same OMP or a distinct OMP, an unstructured translocation domain into the periplasm. If this unstructured domain contacts the proteins of the Tol-Pal system to energise the translocation of the whole colicin across the outer membrane, the colicin belongs to group A [154]. If the unstructured domain contacts the proteins of the Ton system to energise import, the colicin belongs to group B [182].

Some colicins can elicit their cytotoxic activity in the periplasm, these colicins will either form pores in the inner membrane, thereby dissipating the PMF [183] or they will affect the synthesis of the peptidoglycan cell wall [184]. All colicins that don't use these methods to kill their target cell translocate across the inner membrane to gain entry to the cytoplasm where they kill the cell by nuclease activity, degrading DNA, rRNA or tRNA, depending on the colicin [181].

Colicin N, like all other colicins, is a plasmid encoded bacteriocin that acts as an intraspecies competition agent in *E. coli*. Expression of Colicin N is under the control of the SOS response, hence the Colicin N operon harbours two LexA binding sites which repress transcription. Upon detection of DNA damage, RecA induces LexA autocleavage permitting the expression of the Colicin N operon. This operon contains the *cna* gene, encoding Colicin N; the *cnl* gene, encoding a lysis protein required for releasing Colicin N into the environment; and the *cni* gene, encoding an immunity protein conferring resistance of Colicin N toxicity to the producing cell [181].

After synthesis and release from cells via lysis effected by the Colicin N lysis protein, Colicin N must bind, translocate into and kill a target cell.

The first stage in Colicin N mediated cell killing is controversial: receptor binding. Historically, it has been the consensus that the central globular receptor binding domain of Colicin N binds to OmpF in the outer membrane as its "primary receptor" [185, 186]. Recent investigations, however, have suggested that LPS acts as Colicin N's primary receptor in the outer membrane [187, 188]. This suggestion is investigated in Chapter 3 of this thesis, where OmpF is shown to be the primary receptor for Colicin N in *E. coli*. After receptor binding, the N-terminal translocation domain of Colicin N threads through the lumen of an OmpF subunit presenting a TolA binding epitope into the periplasm. An N-terminal OmpF binding site binds within the lumen of an OmpF subunit. The contact with TolA energises Colicin N's translocation across the outer membrane. Once in the periplasm, the pore forming domain of Colicin N can insert into the inner membrane, depolarising the membrane and dissipating the PMF thereby killing the target cell (Figure 1.12) [181].

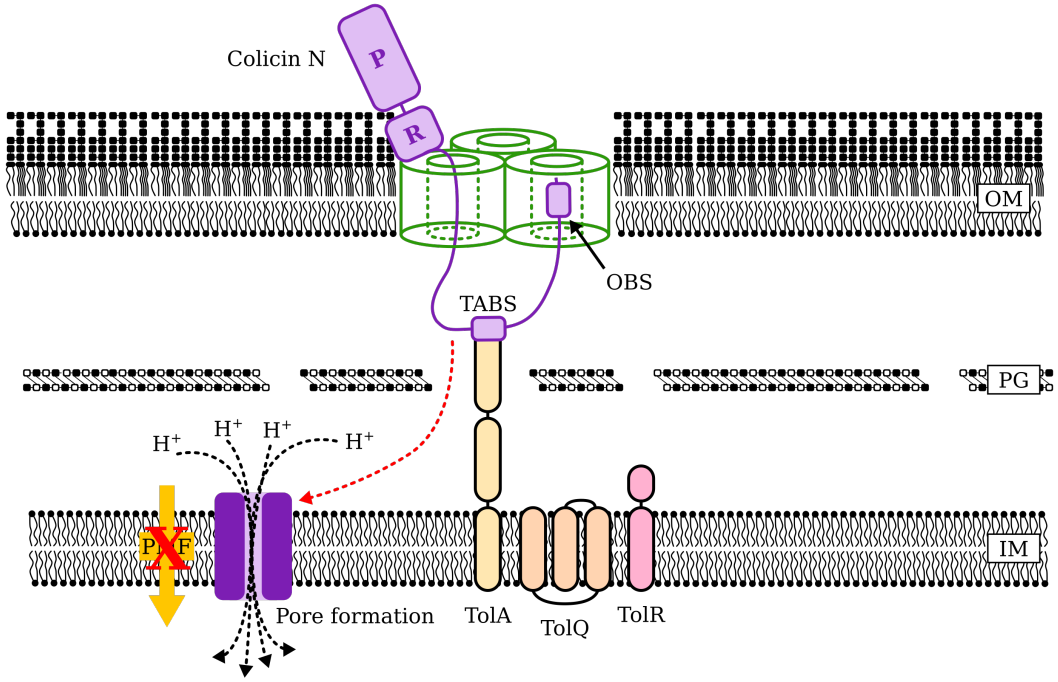

Figure 1.12: Mechanism of action of Colicin N. Diagrammatic representation of the mechanism by which Colicin N translocates across the OM and kills a target cell. The globular receptor binding domain binds to the surface of OmpF and the disordered N-terminal translocation domain translocates through the pore of a single OmpF subunit, a TolA binding epitope (TABS) binds to TolA and an N-terminal OmpF binding site (OBS) binds within the lumen of a single OmpF monomer. TolA provides the force by which Colicin N is pulled into the cell wherein the pore forming domain can insert into the inner membrane, depolarising it and dissipating the PMF, killing the cell.

An important aspect of all colicins is their ability to bind a specific β-barrel outer membrane protein as their receptor. This aspect is important as it can be exploited to design colicin based fluorescent labels for specific OMPs. Colicin E9 and Colicin Ia to which organic fluorophores were conjugated, for example, have been used successfully to investigate the organisation and dynamics of their receptors: BtuB and Cir [189]. Hence it stands to reason that Colicin N could also be developed into a specific fluorescent label for OmpF in *E. coli*.

1.5 Outer Membrane Protein Organisation and Dynamics

As shown in this chapter, the biochemistry of many *E. coli* outer membrane proteins, both lipoylated and integral, have been characterised extensively. Structures of many physiologically important OMPs have been solved and their interactions with elements of the cell envelope established. Despite this, little is known about the lateral organisation and dynamics of these OMPs in the outer membrane. To date, the organisation and dynamics of only a handful of OMPs have been investigated. Of the β-barrel OMPs only LamB, BtuB, Cir, TolC and the BAM complex have been investigated [189–194]. Even less is known about the organisation of lipoylated inner leaflet outer membrane proteins, notably the lateral dynamics have never been measured for any of these proteins.

LamB represents one of the first outer membrane proteins to have its organisation and dynamics investigated extensively. Non-uniform distribution of LamB was observed on the surface of *E. coli* when labelled with fluorescent lambda phage tails [190]. More recent investigations of covalently labelled LamB revealed a punctate distribution that resulted from short bursts of assembly into the outer membrane [191]. The dynamics of LamB have been investigated using single particle tracking, revealing highly restricted diffusion confined to an area of radius 25 nm [192].

The most comprehensive investigation into OMP organisation and dynamics focussed on the low copy number monomeric β-barrels: BtuB and Cir [189]. When these proteins were labelled with fluorescent Colicin E9 and Colicin Ia constructs, puncta were identified on the surface of the cell. These puncta represented protein rich "islands" which were driven in their formation by extensive protein-protein interactions [189]. Notably, such puncta have also been observed when imaging the organisation of BAM complex components [194]. Single particle tracking of labelled BtuB revealed slow, highly restricted diffusion in the outer membrane. Lastly, it was observed that over generations, old BtuB migrated to the poles of

cells in a process termed "binary partitioning". The force for this process was hypothesised to come from the biased biogenesis of new OMPs into the outer membrane at mid-cell [189]. However the underlying process that causes such biased insertion has not been determined.

1.6 Aims of this Thesis

In this thesis I detail the development and characterisation of Colicin N based fluorescent fusion proteins for the *in vivo* labelling of OmpF. The development of such labels allowed for investigation into the mechanism of action of Colicin N.

Little is known about the lateral organisation and dynamics of OmpF in the OM of *E. coli*. Hence, the development of Colicin N based fluorescent fusion proteins enabled fluorescence microscopy investigations into OmpF organisation and dynamics. A number of techniques were used for this investigation into OmpF. OMP distribution simulation, high throughput widefield microscopy, photobleaching analysis, and PALM were used to assess both snapshots of OmpF organisation and how this organisation changed over the *E. coli* cell cycle. Colicin based fluorescent labels also enabled the use of FRAP, PALM-SPT and pulse chase labelling experiments to track OmpF dynamics over multiple distinct timescales. These experiments enabled comprehensive analysis of the organisation and dynamics of a high copy number outer membrane protein (OmpF: approximately 90,000 copies per cell), expressed at an order of magnitude greater than the extensively studied BtuB (564 - 2295 copies per cell) [44]. By comparing these two proteins, universal properties of outer membrane protein organisation and dynamics could be determined, such as highly restricted diffusion and polar localisation of old OMPs driven by the biased insertion of new OMPs at mid-cell.

Finally, the organisation and dynamics of the outer membrane lipoprotein, Pal were measured using a distinct labelling method but analogous microscopy techniques to investigate the distinct properties of outer membrane proteins anchored within the inner leaflet of the outer membrane.

Chapter 2

Materials and Methods

2.1 Media

Table 2.1: Media used in this thesis.

Abbreviation	Description
LB (HS)	Lysogeny broth (Luria Bertani: 10 g/L tryptone, 5 g/L yeast extract, 10 g/L NaCl)
LB (LS)	Lysogeny broth (Lennox: 10 g/L tryptone, 5 g/L yeast extract, 5 g/L NaCl)
M9	Minimal media (2 mM $MgSO_4$, 0.1 mM $CaCl_2$)
M9G	Minimal media (2 mM $MgSO_4$, 0.1 mM $CaCl_2$, 0.4% (w/v) D-glucose)
M9GC	Minimal media (2 mM $MgSO_4$, 0.1 mM $CaCl_2$, 0.4% (w/v) D-glucose, 0.05 % (w/v) Casamino acids)
PBS	Phosphate buffered saline (CSH protocol: 137 mM NaCl, 2.7 mM KCl, 10 mM Na_2HPO_4, 1.8 mM KH_2PO_4)

2.2 Strains

Table 2.2: Strains used in this thesis.

Strain	Description	Source
BL21 (DE3)	*fhuA2 [lon] ompT gal (λ DE3) [dcm] ΔhsdS λ DE3 = λ sBamHIo ΔEcoRI-B int::(lacI::PlacUV5::T7 gene1) i21 Δnin5*	NEB
NEB-5α	*fhuA2 Δ(argF-lacZ)U169 phoA glnV44 Φ80 Δ(lacZ)M15 gyrA96 recA1 relA1 endA1 thi-1 hsdR17*	NEB
BW25113	*Δ(araD-araB)567 ΔlacZ4787(::rrnB-3) λ- rph-1 Δ(rhaD-rhaB)568 hsdR514*	[195]
JW0912-1	*Δ(araD-araB)567 ΔlacZ4787(::rrnB-3) λ- rph-1 ΔompF756::kan Δ(rhaD-rhaB)568 hsdR514*	Keio Collection
JW2203-1	*Δ(araD-araB)567 ΔlacZ4787(::rrnB-3) λ- rph-1 ΔompC768::kan Δ(rhaD-rhaB)568 hsdR514*	Keio Collection
MG1655	*λ rph-1*	[196]
IMB317	*λ rph-1, ΔompA*	Georgina Benn, UCL
BE3000	*ΔompC*	[197]
BZB1107	*ΔompF ΔompC ΔlamB*	[198]
RKCK16	BW25113 *pal::pal-GGGGS-PAmCherry*	[72]
RKCK19	BW25113 *pal::pal(1-59)-PAmCherry*	[72]

2.3 Plasmids and Primers

Table 2.3: Plasmids used in this thesis.

Plasmid	**Description**	**Source**
pKBJ51	Colicin N^{1-185}mCherry	Katarina Jansen
pPGI1	Colicin N^{1-185}GFP	Patrick Inns
pPGI2	Colicin N(Y62A)$^{1-185}$mCherry	Patrick Inns
pPGI3	Colicin N^{1-185}PAmCherry	Patrick Inns
pPGI4	Colicin N^{1-185}mCherryHis6-Cys	Patrick Inns
pNP4	TolA-GFP	Patrice Rassam
pNGH71	pBAD-HismycB OmpF	Nicholas Housden
pNGH312	pET21a OmpF	Nicholas Housden
pROD85	PAmCherry	Stephan Uphoff

Table 2.4: Primers used in this thesis.

Primer	**Description**
5'-TTCCCCTCTAGATTTAAGAAGGA GAGGATCCTATGAGTAAAGGAGAAG AACTTTTCACTGGAGTTGTCCCA-3'	Amplify GFP from pNP4 and introduce 5' BamHI site for pPGI1 (forward)
5'-GGATCCGCGACCCATTTGCTGTC CACCAGTCATCTCGAGTTTGTATAG TTCATCCATGCCATGTGTAATC-3'	Amplify GFP from pNP4 and introduce 3' XhoI site for pPGI1 (reverse)
5'-CCACAGCGATGGTAGCGCGCACA TCACCTTTCACGGTG-3'	Introduce Y62A mutation into pKBJ51 to generate pPGI2 (forward)
5'-CACCGTGAAAGGTGATGTGCGCG CTACCATCGCTGTGG-3'	Introduce Y62A mutation into pKBJ51 to generate pPGI2 (reverse)
5'-CCGCTGCTGGTTCTGGGGATCCC GTGAGCAAGGGCGGCGAGG-3'	Amplify PAmCherry from pROD85 for pPGI3 (forward)
5'-CGAAGCAGCTCCAGCCTACACCC CTCGAGCTTGTACAGCTCGTCCATG CC-3'	Amplify PAmCherry from pROD85 for pPGI3 (reverse)
5'-GGGCTTTGTTAGCAGCCGGATCT CAGCAGTGGTGGTGGTGGTGGTGCT CGAGC-3'	Introduce C-terminal cysteine into pKBJ51 to generate pPGI4 (forward)
5'-GCTCGAGCACCACCACCACCACC ACTGCTGAGATCCGGCTGCTAACAA AGCCC-3'	Introduce C-terminal cysteine into pKBJ51 to generate pPGI4 (reverse)

2.4 Molecular Biology Techniques

2.4.1 Polymerase Chain Reaction

Whole plasmid PCR was performed to generate pPGI2 (Colicin N(Y62A)$^{1-185}$mCherry) and pPGI4 (Colicin N$^{1-185}$PAmCherryHis6-Cys) from the pKBJ51 plasmid, encoding Colicin N$^{1-185}$mCherry. Table 2-5 details the components used in whole plasmid PCR.

Table 2.5: Whole plasmid PCR components.

Component	**Stock Concentration**	**Volume (µl)**	**Final concentration**
pKBJ51	50 ng/µl	2.5	2.5 ng/µl
Forward primer	10 µM	1.25 - 2.5	0.25 - 0.5 µM
Reverse primer	10 µM	1.25 - 2.5	0.25 - 0.5 µM
dNTPs	10 mM	1.25	0.25 mM
DMSO	100%	6	12%
HF buffer	5X	10	1X
Phusion polymerase	N/A	0.625	1 unit
MiliQ water	N/A	Up to 50 µl	N/A

Whole plasmid PCR was conducted in three steps to generate pPGI2 (Table 2-6) and two steps to generate pPGI4 (Table 2-7).

Table 2.6: Three step whole plasmid PCR thermocycling conditions.

Step	**Temperature (°C)**	**Time**
Initial denaturation	98	3 min
Cycle step 1 (30X)	98	70 s
Cycle step 2 (30X)	50	30 s
Cycle step 3 (30X)	68	5 min
Final extension	72	10 min
Hold	4	∞

Table 2.7: Two step whole plasmid PCR thermocycling conditions.

Step	**Temperature (°C)**	**Time**
Initial denaturation	98	3 min
Cycle step 1 (30X)	98	10 s
Cycle step 2 (30X)	72	5 min
Final extension	72	10 min
Hold	4	∞

PCR was used to amplify small gene fragments in order to generate novel Colicin N fusion proteins: pPGI1 (Colicin N^{1-185}GFP) and pPGI3 (Colicin N^{1-185}PAmCherry). Table 2-8 details the components used in this PCR.

Table 2.8: Gene fragment amplification PCR components.

Component	Stock Concentration	Volume (µl)	Final concentration
Plasmid	1 ng/µl	10	0.2 ng/µl
Forward primer	5 - 10 µM	2.5 - 5	0.5 µM
Reverse primer	5 - 10 µM	2.5 - 5	0.5 µM
dNTPs	10 mM	1	0.2 mM
DMSO	100%	1.5	3%
HF buffer	5X	10	1X
Phusion polymerase	N/A	0.5	1 unit
MiliQ water	N/A	Up to 50 µl	N/A

PCR was conducted in three steps to amplify the gene fragments (Table 2-9).

Table 2.9: Three step PCR thermocycling conditions for gene fragment amplifications.

Step	Temperature (°C)	Time
Initial denaturation	98	30 s
Cycle step 1 (30X)	98	10 s
Cycle step 2 (30X)	50-59	30 s
Cycle step 3 (30X)	68-72	30 s
Final extension	72	10 min
Hold	4	∞

2.4.2 Agarose Gel Electrophoresis

Agarose gels were made at an agarose concentration between 1 and 1.3%. 50 ml of agarose was poured into a gel holder with 5 µl of Syber Safe dye. All gels were run for 1 hour at 80V.

2.4.3 Restriction Enzyme Digest

For the digestion of gene fragments and their vectors, double restriction enzyme digests were performed with single units of BamHI and XhoI in NEB CutSmart buffer. These reactions were conducted at 37°C for 60 minutes. For whole plasmid PCR mutagenesis, DpnI digest was performed in NEB CutSmart buffer at 37°C for 60 - 120 minutes followed by heat inactivation at 80°C for 20 minutes.

2.4.4 DNA Ligation

DNA ligation was performed using NEB T4 ligase, the ratio of vector to insert was varied to maximise the likelihood of success.

2.4.5 Generating Chemically Competent Cells

The strain to be made chemically competent was streaked out onto LB (HS)-agar plate from a glycerol stock and grown overnight at 37 °C. The following day 10 ml of LB (HS) was inoculated with a single colony of the strain and grown overnight at 37°C, shaking. Autoclaved solutions of 100 mM $CaCl_2$, 100 mM $MgCl_2$ and 85 mM $CaCl_2$, 15% (v/v) glycerol were cooled to 4°C overnight. The following day 50 ml LB (HS) was inoculated with 0.5 ml overnight culture and grown at 37°C, shaking. At an OD_{600} of 0.3 - 0.4 cells were placed in ice for 20 minutes. Cells were pelleted by centrifugation (3000 g, 15 min, 4°C). The supernatant was discarded and the pellet resuspended in 20 ml, 4°C, 100 mM $MgCl_2$. Resuspended cells were pelleted by centrifugation (2000 g, 15 min, 4°C). The supernatant was discarded and the pellet resuspended and incubated in 10 ml, 4°C, 100 mM $CaCl_2$ for 30 min. Resuspended cells were pelleted by centrifugation (2000 g, 15 min, 4°C). The supernatant was discarded and the pellet resuspended in 2 ml, 4°C, 85 mM $CaCl_2$, 15 % (v/v) glycerol. 100 µl aliquots were stored at -80°C.

2.4.6 Transforming Chemically Competent Cells

A 20 µl aliquot of chemically competent cells were placed on ice. 1 - 2.5 µl of plasmid DNA was added and mixed. The sample was incubated on ice for 30 min. A 42°C heat shock was conducted for 30 - 60 s and the sample was returned to ice for 10 min. 200 µl SOC outgrowth media was added to the sample which was incubated at 37°C, shaking for 40 - 50 minutes. 20 and 150 µl aliquots of incubated sample were spread on LB (HS)-agar plates, supplemented with the appropriate antibiotic. Plates were incubated overnight at 37°C. A negative control was always conducted in parallel.

2.4.7 Plasmid Purification and Sequencing

Plasmid purification was conducted using a Promega midiprep kit. Sequencing was conducted by GeneWiz using T7 promoter and terminator primers.

2.5 Expression and Purification of Colicin N fluorescent fusion proteins

2.5.1 Expression

All genes were expressed using BL21 (DE3) strain. BL21 (DE3) cells were transformed (2.4.6) with the desired plasmid. A day prior to expression, two 50 ml aliquots of LB (HS) were inoculated with individual transformed BL21 (DE3) colonies and grown overnight at 37°C, shaking. The following day, 10 ml aliquots of overnight culture were used to inoculate 6 aliquots of 830 ml LB (HS) (5 L total) pre-warmed to 37°C. Cells were grown to an optical density of 0.5 - 0.7, expression was then induced with 1 mM IPTG for 3 - 4 hr. Cells were then pelleted by centrifugation at 5000 g for 12 minutes at room temperature. The supernatant was discarded and the pellet resuspended in a solution of 5 mM imidazole, 500 mM NaCl, 20 mM Tris-HCl pH 7.5. If necessary, resuspended cells were stored at -20°C.

To release the expressed protein, resuspended cells were lysed by sonication. Prior to this sonication, cells were treated with 1 mM PMSF to inhibit degradation by proteases. Sonication was conducted in two steps to allow for mixing in between. Each step was conducted as detailed in Table 2-9.

Table 2.10: Sonication settings used for cell lysis.

Total time	1 min 30 s
Amplitude	70
On time	3 s
Off time	7 s

Cell debris was pelleted by centrifugation (12,500 RPM, 4°C, 30 min). The supernatant was collected and passed through a 220 nm filter to remove any remaining debris.

2.5.2 Purification

All Colicin N based fluorescent labels harboured a C-terminal His6 tag. The first step in the purification was Ni affinity chromatography.

Two GE HisTrap columns were connected in parallel. Filtered protein sample was loaded onto the column by either direct syringe injection or by superloop. 5 mM imidazole, 500 mM NaCl, 20 mM Tris-HCl pH 7.5 was flowed through the columns to elute unbound protein. An increasing gradient of 750 mM imidazole, 500 mM NaCl, 20 mM Tris-HCl pH 7.5 was used to elute the target protein. Fractions were collected and analysed by SDS-PAGE (2.7.1) to determine what fractions should be pooled together. After pooling, the sample was treated with 5 mM EDTA. Pooled, EDTA treated sample was concentrated to < 20 ml. Concentrated sample was dialysed in 4 L, 25 mM Tris, 150 mM NaCl, pH 7.5 at 4°C, overnight (dialysis membrane: 12,000-14,000 MWCO).

Dialysed sample was passed through a 220 nm filter. Size exclusion chromatography was conducted with a Superdex S200 26/60 column with a running buffer of 25 mM Tris,

150 mM NaCl, pH 7.5. Fractions collected were analysed by SDS-PAGE (2.5.3) and pooled accordingly. The concentration of protein was determined as described in 2.8.1. Protein samples were stored at -20°C.

2.6 Maleimide Labelling of Colicins

2.6.1 AF647 Maleimide Labelling

1 ml of 50 µM protein to be labelled was incubated with 10 mM DTT on a rotary shaker for 2 hours at room temperature. Immediately prior to labelling DTT was removed by desalting using a 5 ml column. The desalting chromatogram was used to determine which fractions to pool. After pooling and mixing, the sample was incubated with 150 µM AF647 for 1 hour at room temperature on a rotary shaker in the absence of light. The conjugation reaction was quenched with a 10 minute incubation with 5 mM DTT. DTT and unconjugated AF647 were removed by desalting using a 5 ml column. From the desalting chromatogram and subsequent analysis by SDS-PAGE (2.7.1) fractions were pooled.

Labelling efficiency was determined by analysis of the absorbance spectrum of the sample. The relative concentrations of protein and AF647 was established through absorbance at 280 and 640 nm, respectively. Using the Beer-Lambert law:

$$c = \frac{A}{\epsilon l}$$

Where c equals concentration, A equals absorption, ϵ equals extinction coefficient and l equals path length.

2.7 Protein Characterisation

2.7.1 SDS-PAGE

All SDS-PAGE experiments conducted were done so with gels made up of two components: a 12% bis-acrylamide running gel and a small 5% bis-acrylamide stacking gel into which the wells of the gel were formed. Prior to loading, protein samples were heated to 98°C for 5 - 10 min in the presence of reductant (β-mercaptoethanol). All SDS-PAGE gels were run at a constant current of 30 mAmps per gel, for approximately 30 minutes.

2.7.2 Peptide Mass Fingerprinting

All mass spectrometry was conducted by the Oxford Advanced Proteomics facility.

2.7.3 N-Terminal Sequencing

The sample to be sequenced was run on a 12% Bis-acrylamide, SDS-PAGE gel. Proteins were transferred to a PVDF membrane via a wet (tank) transfer, in a 10 mM CAPSO, 10% Methanol, pH 11 buffer. Transfer was conducted overnight at 4°C (30 V, 90 mAmps). The blotted PVDF membrane was stained with Ponceau S. Bands of interest were excised and sent to Alta Bioscience, Birmingham for N-terminal sequencing.

2.7.4 Protein Cytotoxicity Assays

A day prior to the assay, a single BE3000 colony was used to inoculate 10 ml of LB (HS) and grown overnight at 37°C, shaking. The following day, 200 µl of overnight culture was used to inoculate 10 ml of fresh LB (HS) and grown at 37°C, shaking to an OD_{600} of approximately 0.5. 5 ml soft LB (HS)-agar was melted and cooled to 45°C, to this 200 µl of the mid-log *E. coli* BE3000 was added, mixed by inversion, immediately poured on pre-set LB (HS)-agar plates and allowed to set. 3 fold serial dilutions of the protein of interest were prepared (10

µM to 57 pM). 2.5 µl of each concentration was spotted onto the plate and allowed to dry. Plates were then inverted and incubated overnight at 37°C. Killing was observed as a clear area in the bacterial lawn.

2.8 Biophysical Techniques

2.8.1 UV/Vis Spectrophotometry

The absorbance of protein samples at 280 nm was measured in a cuvette with a 1 cm path length. Protein concentration was then calculated using the Beer-Lambert law:

$$A = \epsilon c l$$

Where A is absorbance, ϵ is the protein extinction coefficient at 280 nm, c is the protein concentration and l is the path length of the cuvette.

2.8.2 Fluorescence Spectroscopy

All fluorescence spectroscopy was conducted on a Horiba Fluoromax 4 instrument. The excitation and emission wavelengths used were dependent on the experiment that was conducted, however, for all experiments slit widths of 1 nm were used.

2.9 Microscopy Sample Preparation

2.9.1 Detergent Coverslip and Slide Cleaning

#1.5 high precision coverslips were sonicated at 44 kHz, 50°C for 15 minutes in a solution of 2% neutracon. Coverslips were then rinsed with 2 L of MiliQ filtered water and dried at a temperature of 60°C.

2.9.2 KOH Coverslip Cleaning

#1.5 high precision coverslips were sonicated at 44 kHz, 50°C for 15 minutes in a solution of 1 M KOH. Coverslips were then transferred into a pure MiliQ filtered water and sonicated at 44 kHz, 50°C for 15 minutes, this was repeated three times. After the third sonication in MiliQ filtered water, coverslips were transferred to 70% ethanol for storage.

2.9.3 Cell Immobilisation

In all microscopy experiments, an agarose pad of between 60 - 200 µl was formed by injecting the respective volumes of 1% agarose pad (diluent dependent on the experiment being performed) into a geneframe placed on a (dimensions) slide. The surface of the agarose was flattened using a cleaned coverslip. The flattening coverslip was removed before 3 - 7.2 µl of resuspended cells was spotted onto the surface of the agarose, a clean coverslip was used to press down on the cells and immobilise them between the glass surface and the agarose.

2.9.4 Growth Conditions

For all strains, a day prior to microscopy a single colony of the target strain was grown in 10 ml LB (HS or LS, dependent on strain) at 37°C, shaking. 500 µl of culture was pelleted and cells were resuspended in M9G or M9GC to grow overnight at 37°C, shaking. On the following day 50 - 500 µl of culture was pelleted and cells were resuspended in 4 ml M9G or M9GC and grown to the required OD_{600}.

2.9.5 Fluorescent Labelling of Cells

Unless otherwise stated, an equivalent of 500 µl OD_{600} 0.6 culture was pelleted by centrifugation for 1 min at 7000 g and resuspended in 200 µl M9GC or M9G supplemented with 0.2 - 2 µM Colicin N fluorescent label. Cells were placed in the dark on a rotary shaker at room temperature for 5 - 10 minutes. For live cell imaging cells were pelleted by centrifugation

for 1 min at 7000 g and washed a minimum of three times. Washing was conducted by a series of pelleting and resuspension steps in 500 µl of selected media. The volume of the final resuspension prior to imaging was determined by visual analysis of the size of the final pellet.

2.9.6 Formaldehyde Fixing

Unless otherwise stated, fixation was conducted immediately after fluorescent labelling. Labelled cells were pelleted by centrifugation for 1 min at 7000 g and immediately resuspended in 4°C, 4% formaldehyde (diluent: PBS). Fixation was conducted for 30 minutes in the dark. Fixed cells were pelleted by centrifugation for 1 min at 7000 g and washed a minimum of two times. Washing was conducted by a series of pelleting and resuspension steps in 500 µl of PBS. The volume of the final resuspension prior to imaging was determined by visual analysis of the size of the final pellet.

2.9.7 Cell Loading onto Agarose Pads

For real time tracking of cell growth, 3 µl of resuspended cells were spotted onto a 60 µl 1% agarose pad. For all other experiments 7.2 µl of resuspended cells were spotted onto a 200 µl 1% agarose pad. A coverslip was placed onto the geneframe to secure cells between the agarose pad surface and the coverslip.

2.10 Microscopy

2.10.1 Confocal Microscopy

All confocal microscopy was conducted on the Zeiss LSM 780 with a 100x 1.4 NA oil immersion objective lens.

mCherry labelled proteins were visualised with a 2% 561 nm laser line at a digital gain

of between 800 and 900. A 512 × 512 area was imaged at a zoom value of 10 with a pixel dwell time of 1.58 µs. A pinhole diameter of 90 µm was used, light was collected between 578 - 696 nm. Transmitted light was collected to generate a DIC image of the cell, digital gain: 333.

GFP labelled proteins were visualised with a 2% 488 nm laser line at a digital gain of 703. A 512 × 512 area was imaged at a zoom value of 10 with a pixel dwell time of 1.58 µs. A pinhole diameter of 90 µm was used, light was collected between 493 - 598 nm. Transmitted light was collected to generate a DIC image of the cell, digital gain: 344.

2.10.2 Fluorescence Recovery After Photobleaching

All FRAP experiments were conducted on the Zeiss LSM 780. mCherry and GFP labelled proteins were visualised as described in 2.10.1. Bleaching was conducted by scanning over a 30 × 70 px region at the pole of the cell at 100% laser power (561 nm for mCherry, 488 nm for GFP) for 15 iterations. A single pre-bleach image was collected, bleaching was conducted, after which an image was collected every 4 s for up to a total of 120 s. Transmitted light was collected to generate a DIC image of the cell for each frame.

Analysis of FRAP data was conducted using FIJI and custom written python scripts. 2 channel image stacks were opened in FIJI. Image stacks that displayed no significant drift in X, Y and Z were moved to the next analysis step. Image stacks that display a significant amount of Z drift were discarded, Image stacks that displayed no significant Z drift but significant XY drift were corrected using the FIJI registration plugin: correct 3D drift, referencing the DIC channel. Multi time scale computation, sub pixel drift correction and image edge enhancement were used for drift correction.

For each FRAP image sequence three 50 × 50 px areas were defined: target area (tA), background area (bA) and reference area (rA). The target area was defined as the area of the cell that was bleached, the background area was defined as a random background area of the image, the reference area was defined as the pole of the cell that was not bleached and

so could be used to correct for small amounts of Z drift and whole cell bleaching throughout the course of the experiment.

The relative fluorescence recovery was calculated with the following equation:

$$(tA_n - bA_n) \times \left(\frac{rA_0 - bA_0}{rA_n - bA_n} \right)$$

Where n represents the frame currently being analysed and 0 represents the single frame acquired prior to bleaching. The FRAP curve was then normalised so that the pre-bleach relative fluorescence intensity was 100%.

2.10.3 Widefield Fluorescence Microscopy

All widefield fluorescence microscopy was conducted on an Oxford Nanoimaging Nanoimager-S with a 100× 1.49 NA oil immersion objective. For GFP and AF488 labelled proteins, excitation was conducted using a 473 nm laser line and light was collected between 500 - 550 nm. The excitation laser power used was dependent on the sample being imaged. Unless stated otherwise, an exposure time of 100 ms was used. For mCherry labelled proteins, excitation was conducted using a 561 nm laser line and light was collected between 575 - 616.5 nm and 665.8 - 693.4 nm. An excitation laser power of 20 mW was used for both 473 nm and 561 nm laser lines. Unless stated otherwise, an exposure time of 100 ms was used.

2.10.4 High-Throughput Widefield Fluorescence Microscopy

All high-throughput widefield fluorescence microscopy was conducted on an Oxford Nanoimaging Nanoimager-S with a 100× 1.49 NA oil immersion objective. The imaging conditions described in 2.10.3 were used. The inbuilt nanoimager autofocus feature was used to ensure cells were kept in focus throughout the multiple acquisitions. A grid of 20 × 10 field of views (FOVs) were collected, 100 frames at 100 ms exposure for each FOV. Each FOV was separated by a distance of 10 µm in X and Y to avoid any overlap.

2.10.5 Photoactivated Localisation Microscopy

All PALM experiments were conducted on an Oxford Nanoimaging Nanoimager-S with a 100× 1.49 NA oil immersion objective, cells imaged in PALM were always formaldehyde fixed and imaged in PBS. PALM images were collected using two distinct methods that differed in the modulation of the 405 nm activation laser. In the first method, the 561 nm excitation laser was on constantly throughout the experiment at between 20 - 40 mW, the 405 nm activation laser was also kept on throughout the experiment at low levels (beginning at less than 0.1 mW) and was steadily increased over the course of the experiment to account for the photobleaching of fluorophores. The second method involved using constant illumination from the 561 nm excitation laser at between 20 - 40 mW. However, the 405 nm activation laser was manually pulsed at between 0.1 - 1 mW to sparsely activate fluorophores. Exposure times used varied between 50 - 100 ms and a maximum of 20,000 frames were collected.

2.10.6 Total Internal Reflection Fluorescence Photoactivated Localisation Microscopy

All TIRF-PALM experiments were conducted on an Oxford Nanoimaging Nanoimager-S with a 100× 1.49 NA oil immersion objective. TIRF-PALM experiments were conducted in the same manner as described in 2.10.5, with the only exception being an illumination angle of 54.5°.

2.10.7 Photoactivated Localisation Single Particle Tracking

All PALM-SPT experiments were conducted on an Oxford Nanoimaging Nanoimager-S with a 100× 1.49 NA oil immersion objective. Unless for a negative control for diffusion, cells used for single particle tracking were live. Cells were constantly illuminated with a 561 nm excitation laser at between 20 - 40 mW. A 405 nm activation laser was manually pulsed at between 0.1 - 1 mW to sparsely activate fluorophores. For all SPT experiments an exposure

time of 50 ms was used and a maximum of 20,000 frames were collected.

2.10.8 Basic Microscopy Analysis

The following basic microscopy analyses were conducted in FIJI:

1. Image cropping.
2. Superimposing scale bars.
3. Generating timelapses.
4. Image file conversions.
5. Image datatype conversions.
6. Applying lookup tables to images.
7. Z-projection to average individual FOVs.
8. Binarisation of images.
9. Drift correction for diffraction limited and superresolution datasets.
10. Single molecule localisation (ThunderSTORM).
11. Determining tracks between localisations (TrackMate & TrackMate CSV importer).

2.11 Advanced Analysis and Simulations

2.11.1 Cell Segmentation

Binary image generation was conducted in either FIJI or with custom written Python Scripts using a simple user defined threshold intensity. In all cases, binary image clean-up to remove erroneously segmented noise and cell clumps was conducted in Python. Noise and cell clumps

were eliminated by interrogating 3 variables for each segmented object: solidity, eccentricity and size.

Table 2.11: Cell segmentation system requirements

Python 3.9.1 64-bit
matplotlib 3.3.3
scikit-image 0.18.1
numpy 1.19.5
PIL 8.1.0

2.11.2 Average Fluorescence Intensity Calculation

Average cell fluorescence intensity calculations were conducted using custom written Python scripts. These scripts took as inputs fluorescence images and their cognate binary images. The pixel intensities of making up each cell were measured by referencing the binary image in which all the cells had been identified. Plotting of the final data was conducted using matplotlib.

Table 2.12: CSR surface distribution simulator

Python 3.9.1 64-bit
matplotlib 3.3.3
scikit-image 0.18.1
numpy 1.19.5
PIL 8.1.0

2.11.3 Completely Spatially Random Surface Protein Distribution Simulator

Detailed explanation of the CSR surface protein simulator is provided in section 4.2.1. The simulator was written in Python. A range is instantiated between -1 and 1 for φ and 0 and 2 π for θ both with 1,000,000 intervals. For each simulated protein molecule a random number between 0 and 1,000,000 is generated and used to index the phi and theta ranges (a distinct random number is used to sample each range). The xyz coordinates of each randomly distributed molecule is saved and can then be used to generate simulated diffraction limited images (section 4.2.1) or simulated PALM datasets (section 4.2.5).

Table 2.13: Average fluorescence intensity analysis system requirements

Python 3.9.1 64-bit
matplotlib 3.3.3
scipy 1.6.0
numpy 1.19.5
PIL 8.1.0

2.11.4 2D Fluorescence Intensity Heatmaps

Detailed explanation of the 2D fluorescence intensity heatmap program is provided in Figure 4.15. Cell segmentation, bounding box identification, cropping and normalisation was performed with custom written python scripts. Individual normalised cells were opened in FIJI and categorised manually. Average 2D fluorescence intensity distributions were generated through FIJI average Z projection.

Table 2.14: 2D fluorescence intensity heatmap program system requirements

Python 3.9.1 64-bit
matplotlib 3.3.3
scikit-image 0.18.1
numpy 1.19.5
PIL 8.1.0

2.11.5 Kymograph Generator

Upon generation of normalised cells for 2D fluorescence intensity heatmaps, the major axis length for each cell was recorded. Kymographs were generated by taking the average cell intensity profile along the length of the normalised cell and representing this profile as a single column of pixels, these were then sorted by major axis length from the shortest cell on the left to the longest cell on the right.

Table 2.15: Kymograph generator system requirements

Python 3.9.1 64-bit
matplotlib 3.3.3
scikit-image 0.18.1
numpy 1.19.5
PIL 8.1.0

2.11.6 PALM Spatial Statistics Pipeline

The removal of compounded localisations and general PALM-TIRF preprocessing program detailed in Figure 4.26 and Figure 4.27 was written in Python.

Table 2.16: PALM spatial statistics preprocessing program system requirements

Python 3.9.1 64-bit
matplotlib 3.3.3
numpy 1.19.5
scikit-learn 0.24.2
shapely 1.7.1
more-itertools 8.8.0

Ripley's K, L and H functions, Poisson point processes and 2D CSR simulations were performed using the spatstat (2.1-0) package in R (4.1.0). Data was exported and plotted in Python (3.9.1 64-bit) matplotlib (3.3.3).

2.11.7 FRAP Analysis

The equation detailed in section 2.10.2 and normalisation of recovery curves with respect to the first post-bleach frame were implemented in Python.

Table 2.17: FRAP analysis system requirements

Python 3.9.1 64-bit
matplotlib 3.3.3
numpy 1.19.5
scipy 1.6.0

2.11.8 PALM-SPT Analysis Pipeline

The PALM-SPT pipeline utilised a number of different programs (see Figure 5.5). The FIJI plugin ThunderSTORM was used to localise particles. Custom written Python scripts edited ThunderSTORM output files to be compatible with import into the FIJI plugin TrackMate,

which was used to link particles thereby generating single particle tracks. TrackMate output files were analysed using custom written Python scripts.

Table 2.18: PALM-SPT Pipeline Python scripts system requirements

Python 3.9.1 64-bit
matplotlib 3.3.3
numpy 1.19.5
scipy 1.6.0
scikit-image 0.18.1

2.11.9 1D Fluorescence Intensity Profiles

The "plot profile" function was used in FIJI to record the raw fluorescence profiles of all cells. Processing, including defining the start and end of the cell profile, normalisation along the long axis, fluorescence intensity normalisation and profile flipping to ensure the maximum intensity region always appeared on the left hand side of the profile was conducted in Python.

Table 2.19: 1D fluorescence intensity profile program system requirements

Python 3.9.1 64-bit
matplotlib 3.3.3
numpy 1.19.5

2.12 Statistics

Details of what statistical tests were performed are included in individual figure legends.

2.12.1 Student's t-test

In all cases where a Student's t-test was performed, it was performed as a two-tailed t-test assuming unequal variances in Python (3.9.1 64-bit) with the scipy (1.6.0) function:

stats.ttest_ind.

2.12.2 Bootstrapping

In all cases where Bootstrapping was conducted, it was done so using custom written Python scripts. In each case, data was resampled 100,000 times. The percentile method was used to determine the 95, 99 and 99.9% confidence intervals.

Table 2.20: Bootstrapping program system requirements

Python 3.9.1 64-bit
numpy 1.19.5

Chapter 3

Colicin N Fluorescent Fusion Protein Characterisation

3.1 Introduction

Colicin N consists of three distinct domains. An intrinsically disordered translocation domain (residues: 1 - 89) at the N terminus, a central, globular receptor binding domain (residues: 90 - 185) and a cytotoxic pore forming domain at the C terminus (residues: 186 - 387) (Figure 3.1.A) [199].

These three domains enable Colicin N to bind, translocate and ultimately kill a target cell.

The first step in Colicin N mediated killing is receptor binding. All colicins bind to an outer membrane protein as their "primary receptor", in the case of Colicin N this primary receptor is the highly abundant trimeric porin: OmpF. The globular receptor binding domain (Figure 3.1.A. Turquoise) enriched in β strands is responsible for binding to OmpF and together with the N-terminal OBS binds to OmpF with a Kd of 119 nM [199].

Translocation is the second step in Colicin N mediated killing. In order for the cytotoxic domain of a colicin to reach its subcellular target, it must be transported across the outer

membrane. Colicins achieve this by translocating through an outer membrane protein, this translocation protein is distinct from the colicin's primary receptor, with the exception of Colicin N and Colicin B. Colicin N's primary receptor and translocator protein are the same: OmpF. The intrinsically disordered translocation domain (Figure 3.1.A. Purple) threads through the lumen of OmpF, presenting a TolA binding site (TABS) in the periplasm, this binds to TolA of the TolQRA inner membrane complex [200]. TolA uses the PMF to stabilise the outer membrane and aid in outer membrane invagination during cell division [72], hence by binding to TolA, Colicin N energises its translocation across the outer membrane. At the N terminus, Colicin N contains an OmpF binding site (OBS), this binds to the lumen of a single subunit of the OmpF trimer (Figure 1.12) [199].

After translocation, the final step in Colicin N mediated killing is pore formation in the inner membrane. The C terminal pore forming domain (Figure 3.1.A. Orange) inserts into the inner membrane, dissipating the PMF, killing the target cell [201, 202].

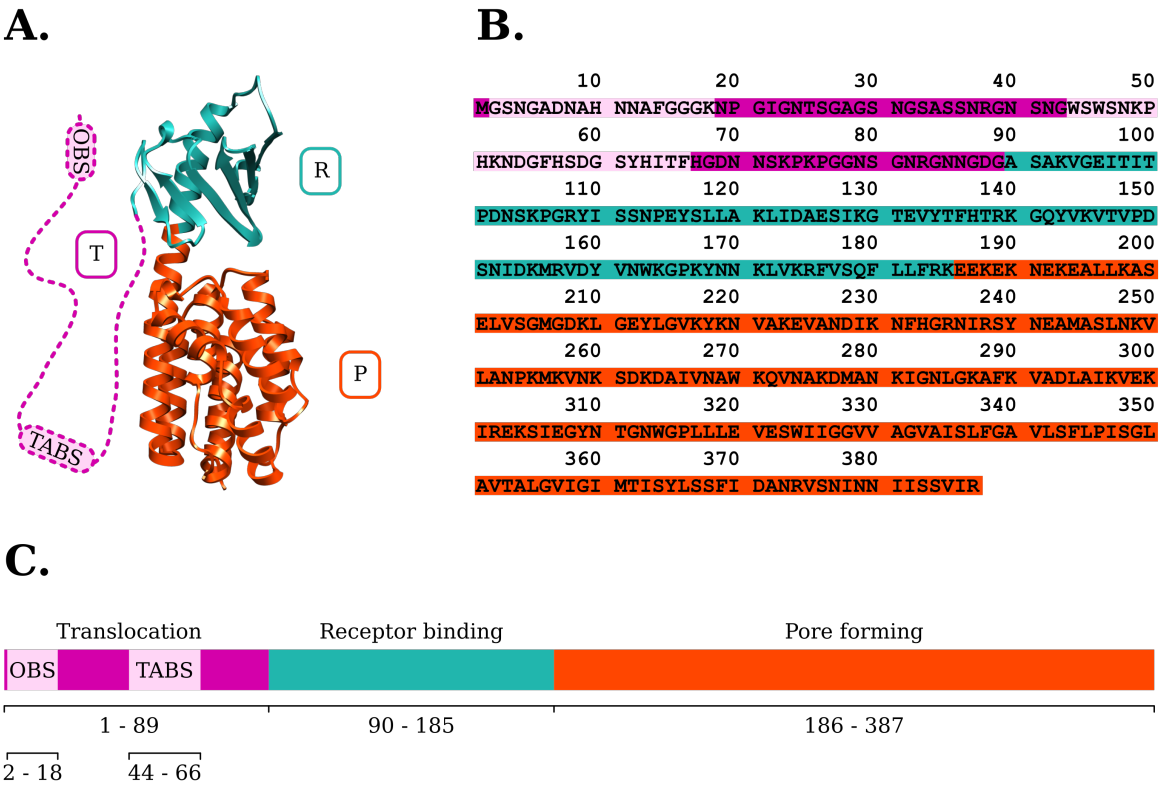

Figure 3.1: Colicin N structure, sequence and domains. A. Structure of Colicin N (PDB:1A87) Purple: translocation domain (T) with OBS and TABS highlighted. The OBS is found at the N-terminus and binds within the lumen of an OmpF subunit. The TABS is a TolA binding epitope that binds to TolA, thereby energising colicin N's import into cells. Represented by a dashed line as the domain is intrinsically disordered and hence does not appear in the Colicin N crystal structure. Turquoise: receptor binding domain (R). Orange: pore forming domain (P). **B.** Colicin N amino acid sequence, colour coded according to domain. **C.** Linear graphical representation of Colicin N domains.

A number of recent investigations have highlighted the importance of LPS in the first step of Colicin N mediated cell killing, receptor binding. Genome wide screening of colicin toxicity revealed that genes encoding enzymes involved in LPS biosynthesis were essential for Colicin N toxicity. Additionally, mutations in genes resulting in a deep rough phenotype also conferred resistance to Colicin N [187]. Complementing this investigation, studies using STD-NMR have showed that the receptor binding domain of Colicin N interacts extensively with LPS [188].

In light of these investigations, it has been recently accepted in the literature that LPS acts as the primary receptor of Colicin N, not OmpF [203]. This would make Colicin N unique in being the only known colicin to lack an outer membrane protein receptor.

In this chapter, I detail the development and characterisation of Colicin N fluorescent fusion proteins—focussing on Colicin N^{1-185}mCherry—as high affinity fluorescent labels that bind exclusively to OmpF in the outer membrane, despite contrary suggestions in the literature.

3.2 Results and Discussion

3.2.1 Colicin N^{1-185}mCherry Design and Purification

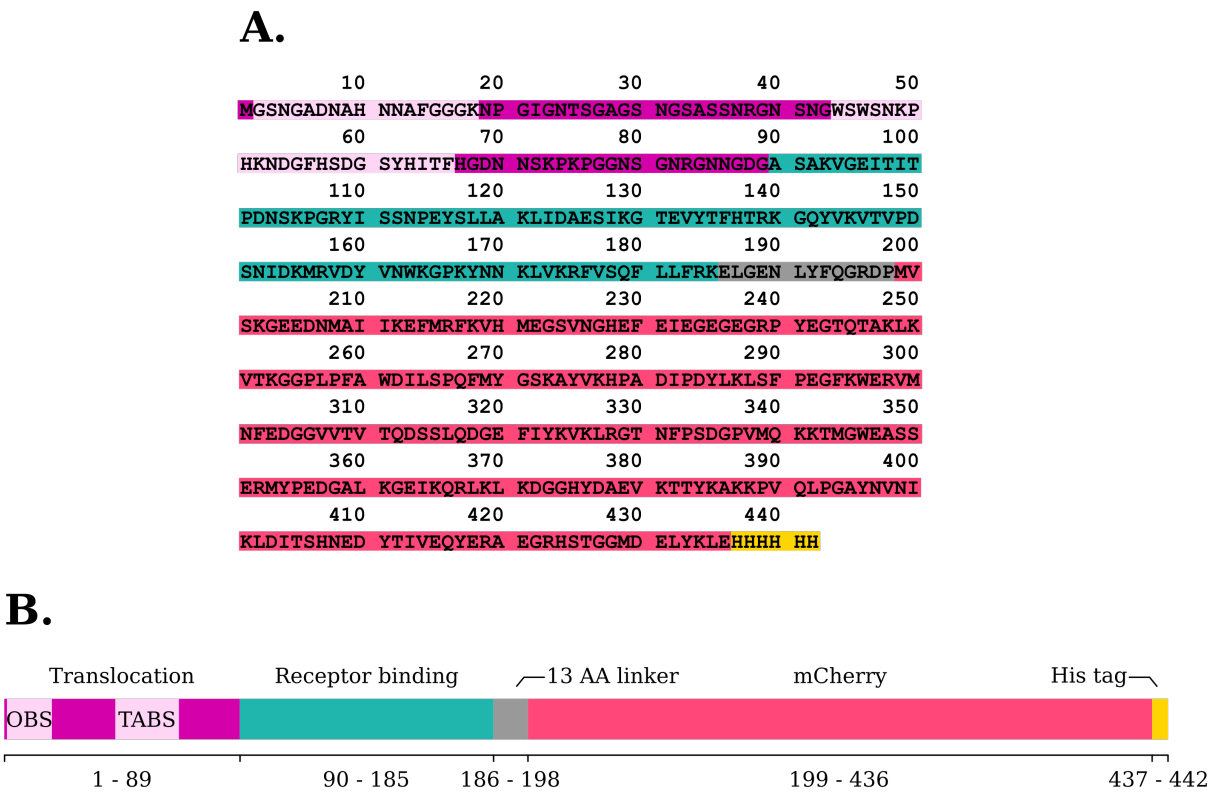

Figure 3.2: Colicin N^{1-185}mCherry sequence and domains. **A.** Colicin N^{1-185}mCherry amino acid sequence, colour coded according to domain. Purple: translocation domain. Light purple: OBS and TABS. Turquoise: receptor binding domain. Grey: 13 amino acid linker. Pink: mCherry. Yellow: His tag. **B.** Linear graphical representation of Colicin N^{1-185}mCherry domains.

The ability of Colicin N to bind to OmpF with nanomolar affinity makes it an appropriate candidate for an OmpF specific label. However, in order to develop Colicin N into a fluorescent label two of its defining properties must be attenuated: its ability to translocate across the outer membrane and its ability to kill *E. coli*. By replacing the pore forming domain with mCherry, the first Colicin N based label was developed: Colicin N^{1-185}mCherry (Figure 3.2). Theoretically, replacing the pore forming domain of Colicin N with mCherry

should eliminate both cytotoxicity and importantly translocation as the mCherry will act as an stable plug [204], preventing transport across the outer membrane. Colicin based labels for OMP labelling are useful as canonical protein labelling methods are not effective for β-barrel OMPs. OMP fluorescent fusion proteins would be an ideal method for imaging OMP organisation but the addition of a fluorescent protein inhibits OMP maturation into the OM [189]. Colicins also represent a more appropriate label than antibodies which are generally larger (average: 150 kDa) and bind with a reduced affinity in comparison to colicins.

The construct described in Figure 3.2 was expressed in *E. coli* BL21(DE3). Cells were lysed by sonication, debris were pelleted by centrifugation and the supernatant was passed through a 220 nm filter. Ni affinity chromatography was carried out on this filtered supernatant (Figure 3.3.A.). Elution occurred in two peaks. SDS-PAGE analysis revealed that Colicin N^{1-185}mCherry was eluted at greater concentrations and purity in the second larger peak compared to the first smaller peak (Figure 3.3.B.).

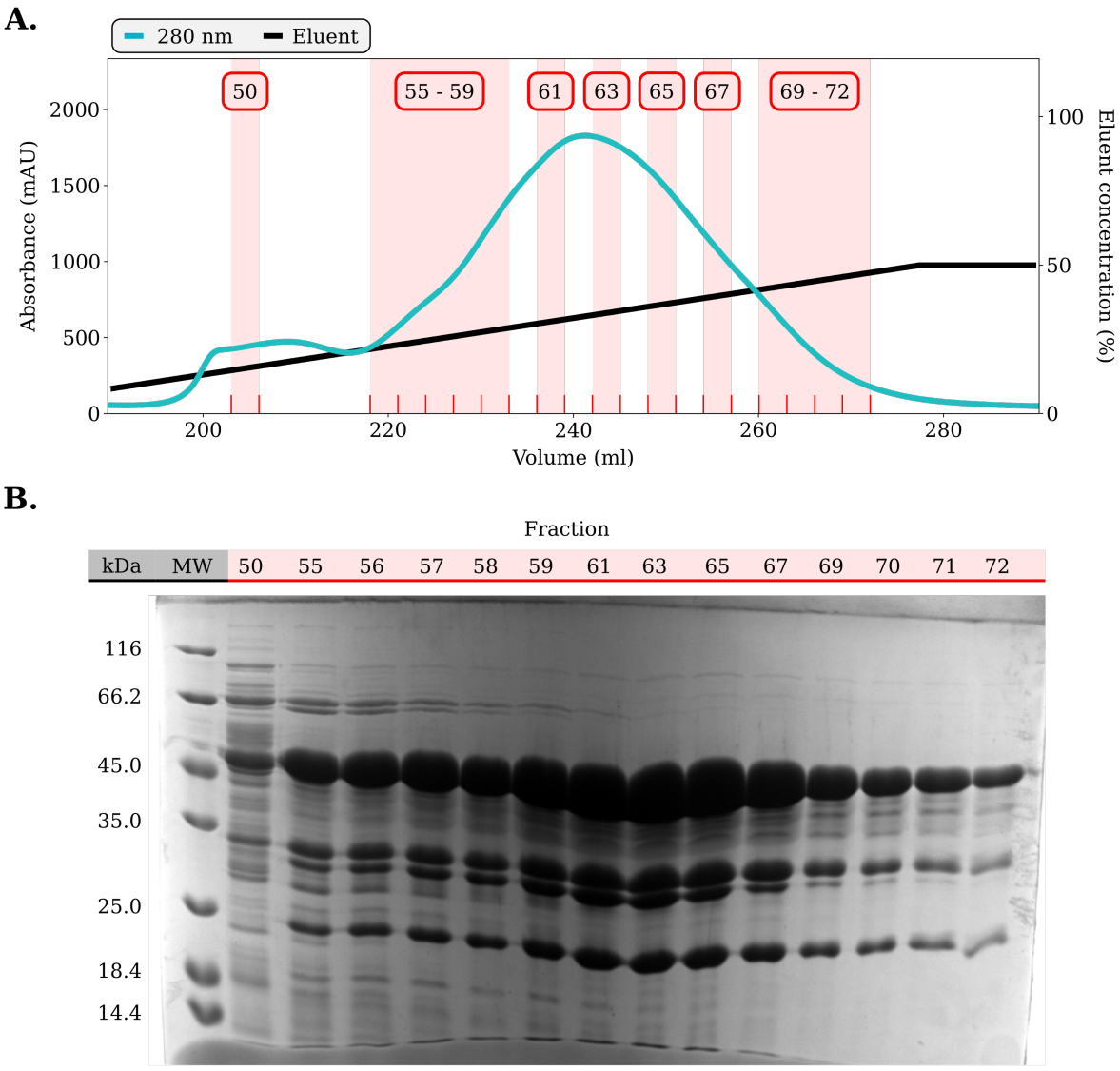

Figure 3.3: Colicin N^{1-185}mCherry purification: Ni affinity chromatography. A. Ni affinity chromatogram of filtered cell extract. Elution of protein was monitored at an absorbance of 280 nm (blue). Eluent (750 mM imidazole, 500 mM NaCl, 20 mM Tris-HCl pH 7.5) concentration was increased at a gradient to 50% (black). Fractions analysed by SDS-PAGE are highlighted. **B.** SDS-PAGE (12% polyacrylamide) analysis of Ni affinity chromatography fractions.

Ni affinity chromatography was not sufficient to purify Colicin N^{1-185}mCherry. Hence, an additional purification step was performed. Ni affinity chromatography fractions 55 - 72 were pooled, treated with EDTA and dialysed. Size exclusion chromatography was carried out on the dialysed protein sample (Figure 3.4.A.). Three distinct elution peaks were observed: a small initial peak (visible in Figure 3.4.A. Inset), a large central peak containing a shoulder

and a final small peak. Fractions were collected from all peaks and analysed by SDS-PAGE (Figure 3.4.B.). This revealed that all fractions from the central peak (D4 - E3) contained pure Colicin N^{1-185}mCherry.

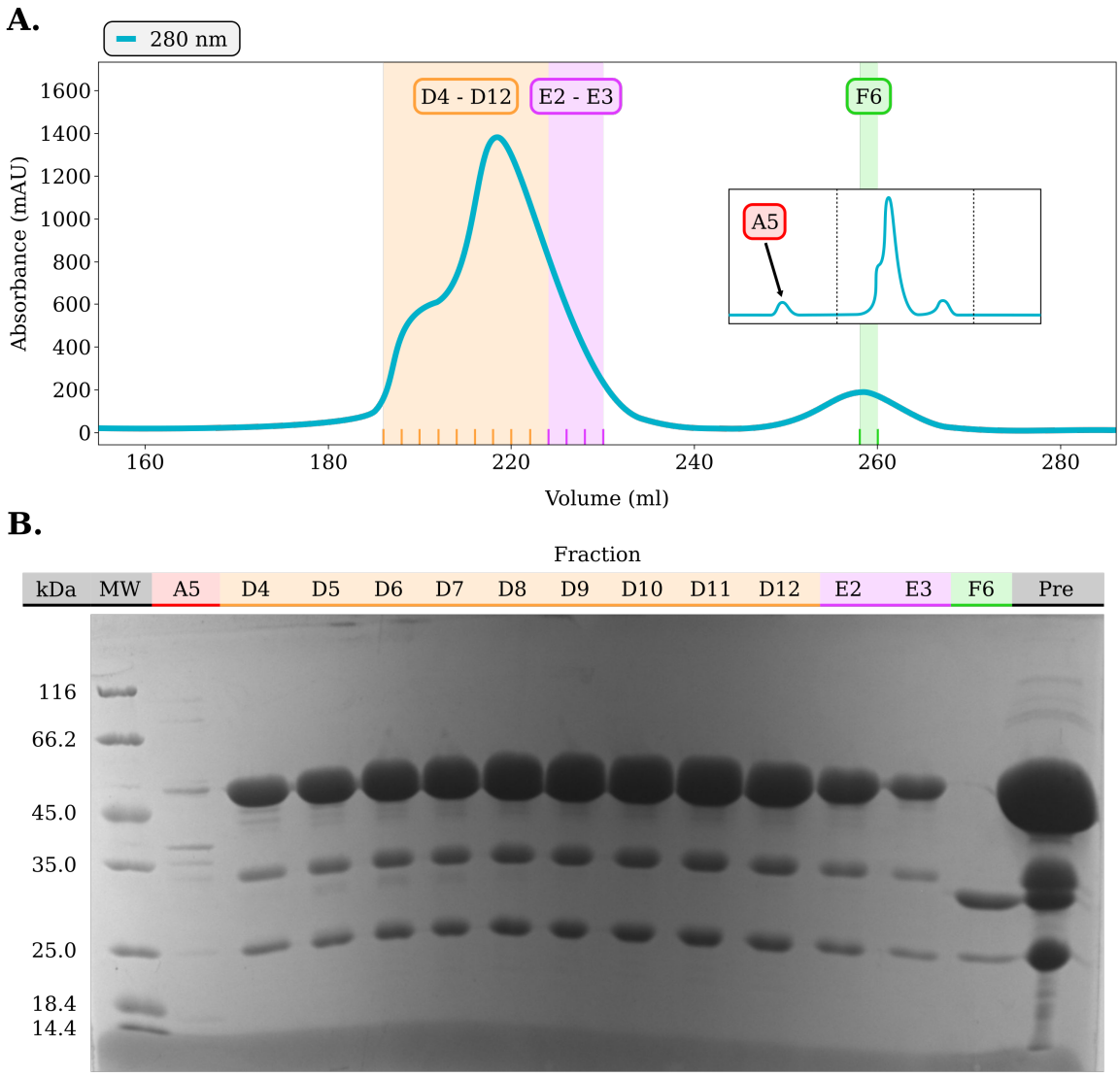

Figure 3.4: Colicin N^{1-185}mCherry purification: size exclusion chromatography. **A.** Size exclusion chromatogram of pooled, dialysed Ni affinity chromatography fractions. Elution of protein was monitored at an absorbance of 280 nm (blue). A 25 mM Tris, 150 mM NaCl, pH 7.5 running buffer was used. Fractions analysed by SDS-PAGE are highlighted. Inset: Full SEC chromatogram with fraction A5 highlighted. **B.** SDS-PAGE (12% polyacrylamide) analysis of size exclusion chromatography fractions.

Size exclusion chromatography was performed in two independent runs. The first run is presented in Figure 3.4. For both runs, fractions taken from the large central peak were

pooled. The final yield of purified Colicin N^{1-185}mCherry was 21.1 mg per litre of culture.

3.2.2 dsRed Derived Fluorescent Colicin N Fusion Proteins Display a Degree of Hydrolysis

Upon expression and purification of Colicin N^{1-185}mCherry, analysis by SDS-PAGE revealed the presence of three bands of molecular weights: 47, 33 and 23 kDa (Figure 3.5.A). It was hypothesised that the highest molecular weight band of 47 kDa represented full length Colicin N^{1-185}mCherry, which has an expected molecular weight of 49 kDa.

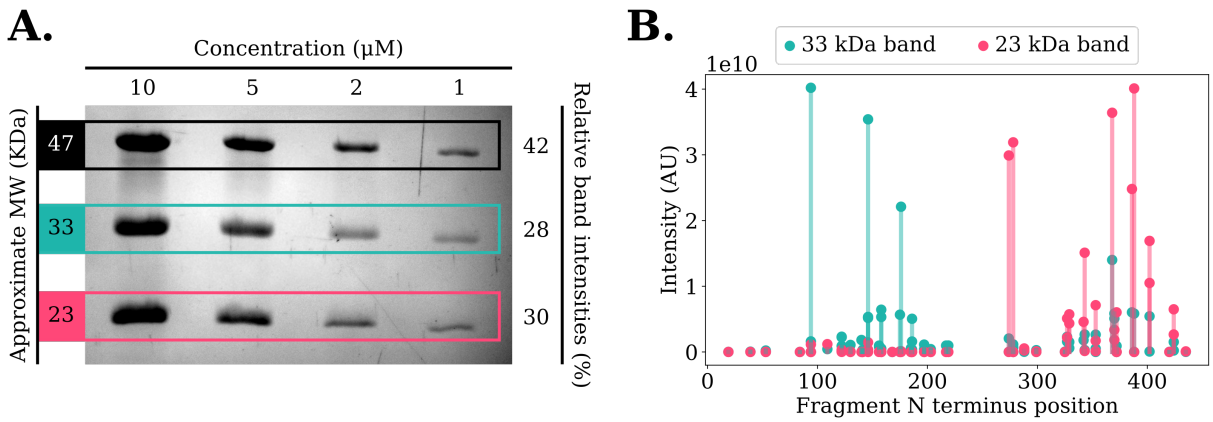

Figure 3.5: Colicin N^{1-185}mCherry SDS-PAGE banding and peptide mass fingerprinting. A. SDS-PAGE (12% polyacrylamide) of Colicin N^{1-185}mCherry dilution series stained with Coomassie blue, displaying the presence of three bands. The integral of intensity of each band was determined to calculate relative band intensities. **B.** Peptide intensities of the 33 and 23 kDa bands, mapped to the position of their N-termini within the full length Colicin N^{1-185}mCherry sequence. 33 kDa band: turquoise. 23 kDa band: pink.

It was hypothesised that the two lower molecular weight bands at 33 and 23 kDa were cleavage products of full length Colicin N^{1-185}mCherry. These bands were therefore extracted and analysed by peptide mass fingerprinting following trypsin treatment. In both bands, peptides were identified that shared sequences with Colicin N^{1-185}mCherry. Peptides from each band were mapped to full length Colicin N^{1-185}mCherry (Figure 3.5.B). From the 33 kDa band, the intensities of peptides detected were greatest within the first half of the Colicin

N^{1-185}mCherry sequence. From the 23 kDa band, the inverse was true, peptide intensities were greatest in the second half of the Colicin N^{1-185}mCherry sequence. Hence the two bands observed are cleavage products of Colicin N^{1-185}mCherry, the 33 kDa band containing the N-terminus and the 23 kDa band containing the C-terminus.

Previous investigations into the monomeric red fluorescent protein: DsRed also reveal a similar banding pattern, consisting of a high molecular intact band and two lower molecular weight cleavage products [205].

mCherry is a derivative of the monomeric red fluorescent protein, DsRed. The chromophore of DsRed consists of the amino acids glutamine, tyrosine and glycine post translationally modified to form an imidazolinone group. Crucially, this chromophore contains an acylimine bond that has been shown to hydrolyse upon boiling prior to SDS-PAGE. The chromophore of mCherry is similar, consisting of methionine, tyrosine and glycine that also form an imidazolinone group after post translational modification. The mCherry chromophore, like DsRed, also contains an acylimine bond [206] (Figure 3.6).

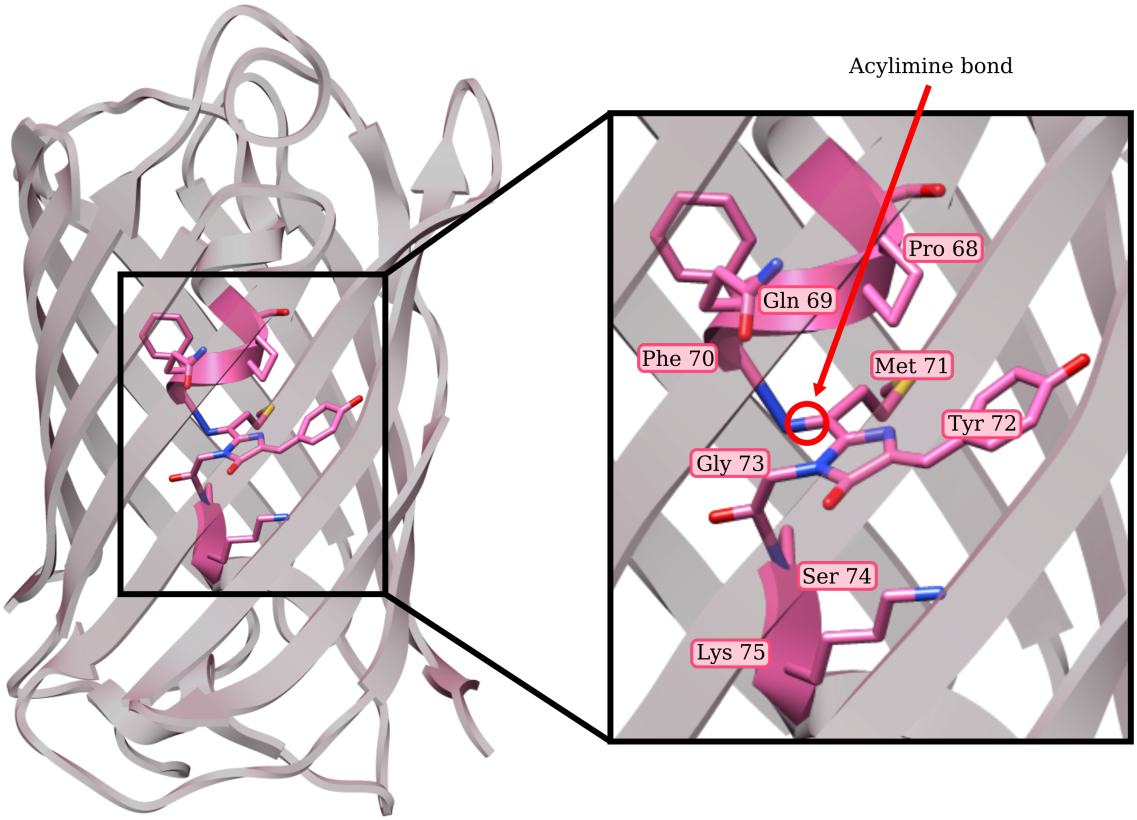

Figure 3.6: mCherry chromophore structure. The structure of mCherry (PDB: 2H5Q) with the amino acids found around the chromophore highlighted in pink. Inset: close up view of the amino acids surrounding and consisting the mCherry fluorophore. Met 71, Tyr 72 and Gly 73 make up the mCherry chromophore. The acylimine bond shown to hydrolyse in DsRed is highlighted.

To investigate whether the SDS-PAGE banding pattern observed for Colicin N^{1-185}mCherry was due to acylimine bond hydrolysis an experiment was conducted to isolate the Colicin N^{1-185}mCherry cleavage products.

A 1 ml sample of 45 µM Colicin N^{1-185}mCherry was heated to 95°C for 90 minutes to hydrolyse the acylimine bond before being diluted 1/10 in 6 M guanidinium hydrochloride (GdnHCl) and run on a Ni affinity chromatography column. Elution was carried out with an increasing concentration of 750 mM Imidazole, 0.5 M NaCl, 20 mM Tris-HCl pH 7.5.

Elution was monitored by absorbance at 280 nm and 587 nm. A single 587 nm absorbance peak (Figure 3.7.A. Pink) and three 280 nm absorbance peaks (Figure 3.7.A. Turquoise) were observed.

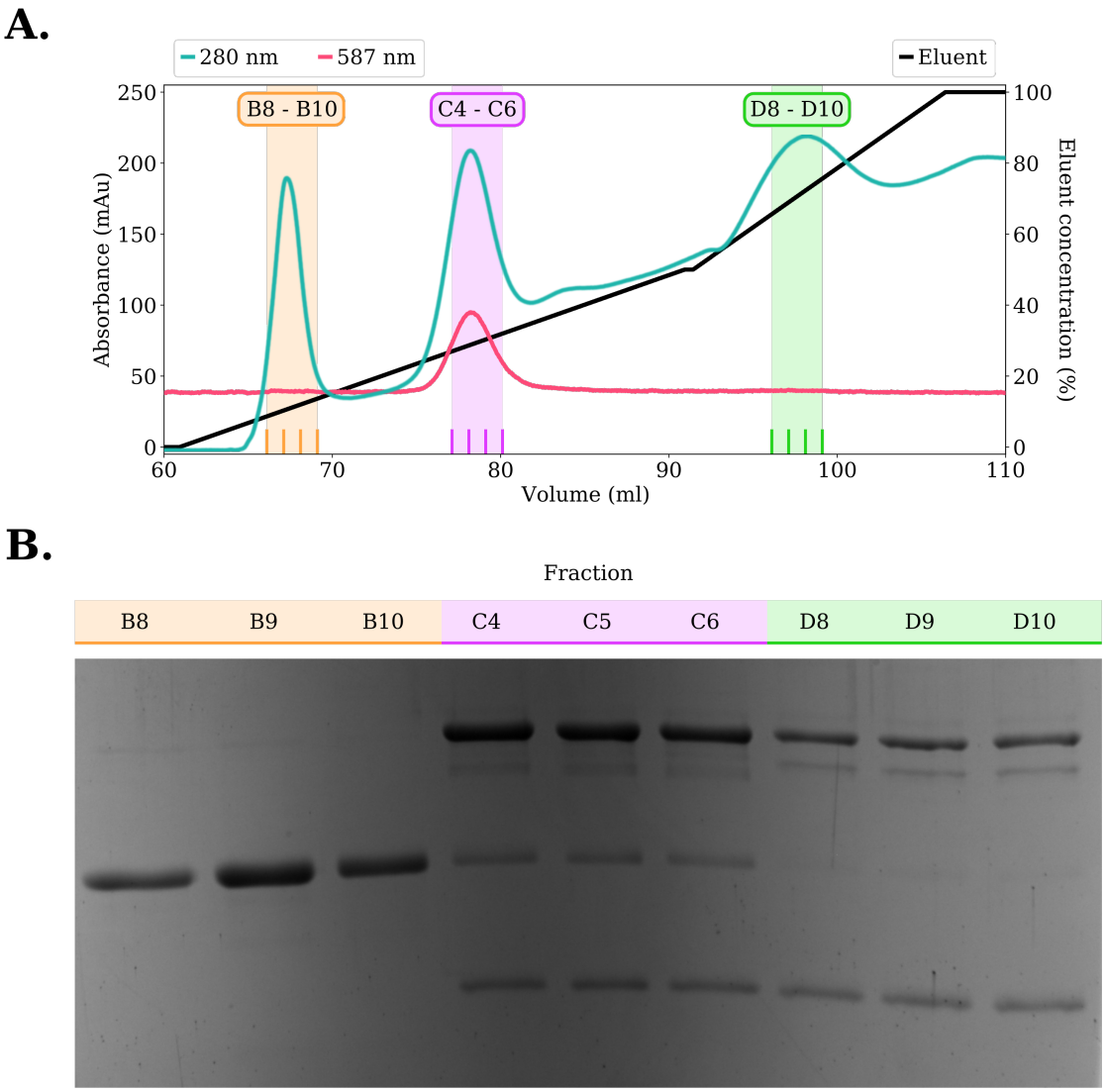

Figure 3.7: Ni affinity chromatogram and SDS-PAGE analysis of denatured Colicin N^{1-185}mCherry. A. Chromatogram from Ni affinity chromatography of denatured Colicin N^{1-185}mCherry in GdnHCl. 587 nm absorbance (pink), 280 nm absorbance (turquoise), eluent concentration (black). Fractions analysed by SDS-PAGE highlighted in orange, purple and green. **B.** SDS-PAGE (12% polyacrylamide) analysis of the three peaks from denatured Colicin N^{1-185}mCherry from Ni affinity chromatography.

The contents of the three 280 nm absorbance peaks from the Ni affinity chromatogram were analysed by SDS-PAGE (Figure 3.7.B). The first peak yielded the single 33 kDa band, identified previously by peptide mass fingerprinting to be the N-terminal cleavage product. The second 280 nm absorbance peak, which also coincided with a 587 nm absorbance peak, yielded the triple banding pattern observed after Colicin N^{1-185}mCherry purification. The

presence of the 587 nm absorbance peak indicates that a significant proportion of mCherry in this peak is still active. Within the final 280 nm absorbance peak the 23 kDa band is enriched, identified by peptide mass fingerprinting to be the C-terminal cleavage product.

These results support the hypothesis that hydrolysis of the acylimine bond is the cause of the triple banding pattern observed by SDS-PAGE. The elution of the 33 kDa band first and the 23 kDa band last is consistent with the former lacking a His Tag and the latter containing a His Tag and therefore remaining bound to the Ni charged beads within the column until higher eluent concentrations. Further, these two bands fail to register 587 nm absorbance peaks on the chromatogram, indicating inactive mCherry to be expected after denaturation via acylimine bond hydrolysis.

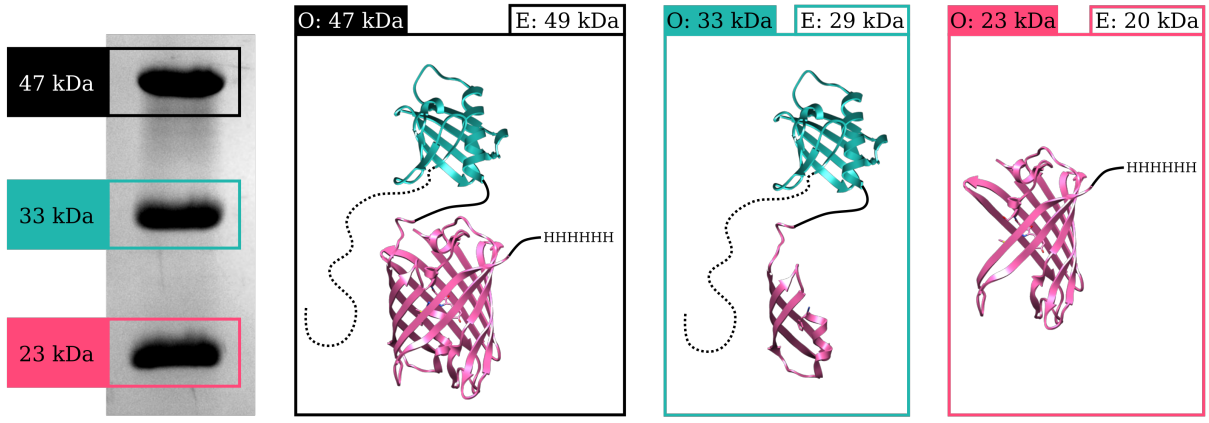

Figure 3.8: Colicin N^{1-185}mCherry protein fragments consisting each band observed by SDS-PAGE. Left: SDS-PAGE (12% polyacrylamide) analysis of Colicin N^{1-185}mCherry with observed molecular weights highlighted. Right: representations of each protein fragment represented by SDS-PAGE bands resulting from acylimine bond hydrolysis. "O": observed mass, "E": expected mass. Black: full length Colicin N^{1-185}mCherry, turquoise: N-terminal protein fragment, pink: C-terminal protein fragment.

Upon acylimine bond hydrolysis the N-terminal and C-terminal fragments would have expected masses of 29 and 20 kDa, respectively. This is in agreement with masses for these fragments observed by SDS-PAGE analysis: 33 kDa and 23 kDa, respectively (Figure 3.5.A and Figure 3.8). It can hence be concluded that acylimine bond hydrolysis is occurring in Colicin N^{1-185}mCherry leading to the formation of two cleavage products (Figure 3.8).

In total, four Colicin N fluorescent fusion proteins were designed, expressed and pu-

rified for use in fluorescence microscopy. These include Colicin N^{1-185}mCherry; Colicin N(Y62A)$^{1-185}$mCherry, the Y62A mutation occurring in the TABS thereby eliminating TolA binding; Colicin N^{1-185}PAmCherry for use in PALM and PALM-SPT experiments and Colicin N^{1-185}GFP for use in two colour OmpF labelling experiments.

Upon analysis of these proteins by SDS-PAGE (Figure 3.9) the triple banding pattern can be observed in all constructs containing a DsRed derived fluorescent protein. A single band is observed for Colicin N^{1-185}GFP, consistent with the theory that acylimine bond hydrolysis is the cause of banding as GFP lacks the acylimine bond within its chromophore [207].

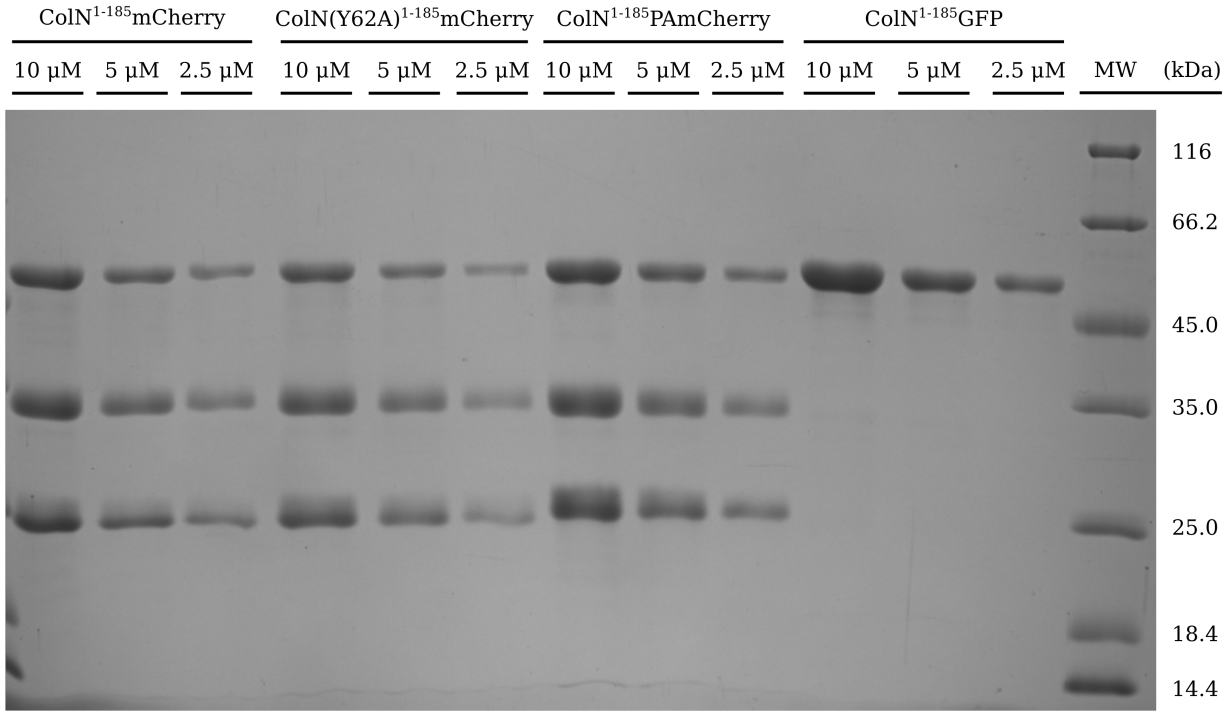

Figure 3.9: SDS-PAGE analysis of all Colicin N fluorescent fusion proteins used for fluorescence microscopy in this investigation. Serial dilutions from 10 - 2.5 µM of each Colicin N fluorescent fusion protein were run on a 12% polyacrylamide gel. Each lane was loaded with 5 µl of sample.

3.2.3 Hydrolysis of dsRed Derived Fluorescent Colicin N Fusion Proteins do not Affect Activity Under Microscopy Conditions

The hydrolysis of the acylimine bond raises questions about the suitability of Colicin N^{1-185}mCherry as a fluorescent label. From Ni affinity chromatography of denatured Colicin N^{1-185}mCherry, the N-terminal fragment and C-terminal fragment when independently purified lacked absorbance at 587 nm. This is concerning when it is considered that only 42% of pure Colicin N^{1-185}mCherry exists in its intact form (Figure 3.5.A) when analysed by SDS-PAGE. Hence if acylimine bond hydrolysis both occurs under the conditions used in microscopy and results in an elimination of mCherry activity, it may preclude the use of Colicin N^{1-185}mCherry in fluorescence microscopy experiments.

To assess the activity of mCherry in Colicin N^{1-185}mCherry, its absorbance spectrum was measured (Figure 3.10).

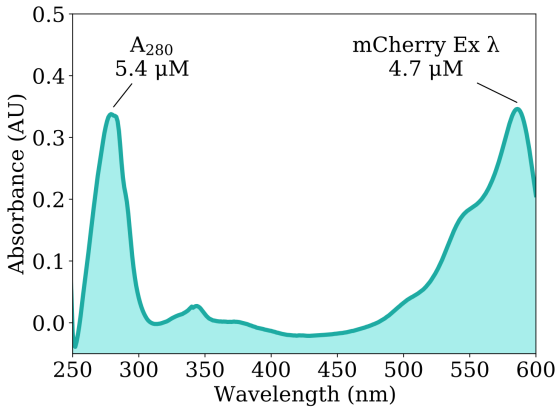

Figure 3.10: Colicin N^{1-185}mCherry absorbance spectrum. The absorbance spectrum of 5.4 µM Colicin N^{1-185}mCherry in 150 mM NaCl, 25 mM Tris-HCl, pH 7.5. Colicin N^{1-185}mCherry concentration determined from absorbance at 280 nm. mCherry concentration determined from absorbcance at 587 nm.

The concentration of Colicin N^{1-185}mCherry ($\varepsilon_{280\ nm}$: 62800) determined from an absorbance of 0.337 at 280 nm was 5.4 µM. The relative concentration of mCherry ($\varepsilon_{587\ nm}$: 72000) determined from an absorbance of 0.345 was 4.7 µM. Therefore the percentage of

active mCherry within Colicin N^{1-185}mCherry is 87%.

If mCherry acylimine bond hydrolysis was occurring and inactivating mCherry under the conditions used to collect the absorbance spectrum, it would be expected that the relative concentration of mCherry would be 42% that of Colicin N^{1-185}mCherry. A relative mCherry concentration of 87% indicates that under these conditions Colicin N^{1-185}mCherry can be used appropriately as a fluorescent label and it is likely that acylimine hydrolysis only occurs under denaturing conditions such as those used in SDS-PAGE sample preparation, a conclusion that is supported in the literature [205].

3.2.4 Colicin N Fluorescent Fusion Proteins are not Cytotoxic

The pore forming domain, removed in all Colcin N fluorescent fusion protein constructs, is responsible for Colicin N's cytotoxicity. It has been shown, however, that truncations of Colicin N lacking the pore forming domain still display cytotoxicity [208]. For use in live cell fluorescence microscopy, the Colicin N fluorescent fusion proteins must lack cytotoxicity. To assess the cytotoxicity of all of the Colicin N fluorescent fusion constructs, killing assays were conducted on *E. coli* BE3000 with serial dilutions of each protein, from 10 µM to 57 pM (Figure 3.11).

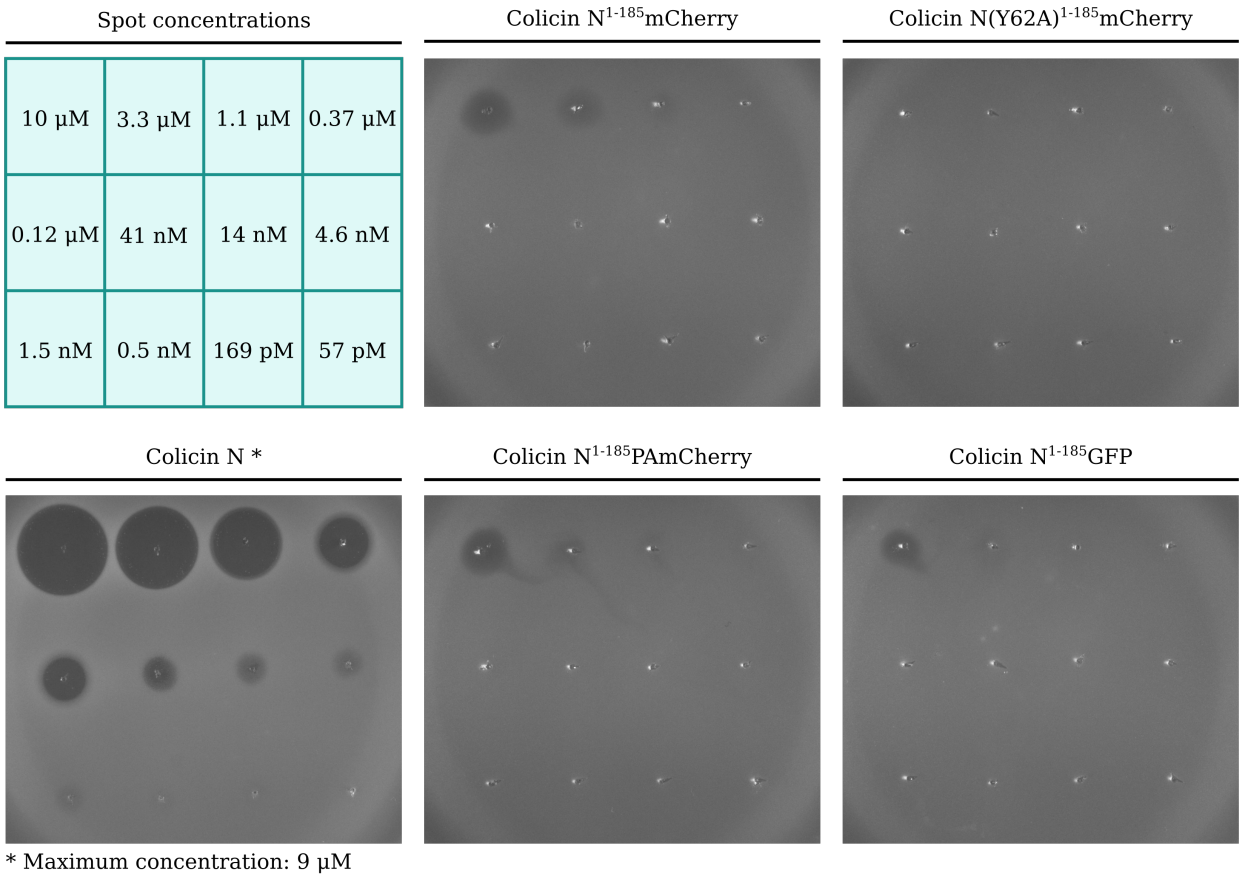

Figure 3.11: Colicin N fluorescent fusion protein spot killing assays. For each protein, 2.5 µl aliquots of each serial dilution were spotted onto plates inoculated with *E. coli* BE3000. The highest concentration of wild type Colicin N used was 9 µM.

Wild type Colicin N displayed killing zones down to a concentration of 1.5 nM. By contrast, the cytotoxicity of all of the Colicin N fluorescent fusion proteins was attenuated significantly. Hazy and poorly defined killing zones could be observed down to a concentration of 1.1 µM for Colicin N^{1-185}mCherry, Colicin N^{1-185}PAmCherry and Colicin N^{1-185}GFP. Notably, Colicin $N(Y62A)^{1-185}$mCherry, with the TABS knocked out displayed no killing zones. Killing was not observed for any of the fusion proteins at concentrations used during microscopy (200 nM).

It is likely that the cause of the hazy effect seen at high concentrations for three of the fluorescent fusion proteins is related to TolA binding. As elimination of the TolA binding site eliminates all killing (Colicin $N(Y62A)^{1-185}$mCherry). It has been shown that Colicin

E9 can sequester TolA away from the division site when used as a BtuB label in *E. coli*, leading to morphological changes in the cell [209]. Therefore, to investigate whether Colicin N fluorescent fusion proteins induced changes in cell morphology, *E. coli* BE3000 cells were incubated overnight in LB supplemented with either 3.3 µM Colicin N^{1-185}mCherry or Colicin N(Y62A)$^{1-185}$mCherry and their morphology analysed by microscopy (Figure 3.12).

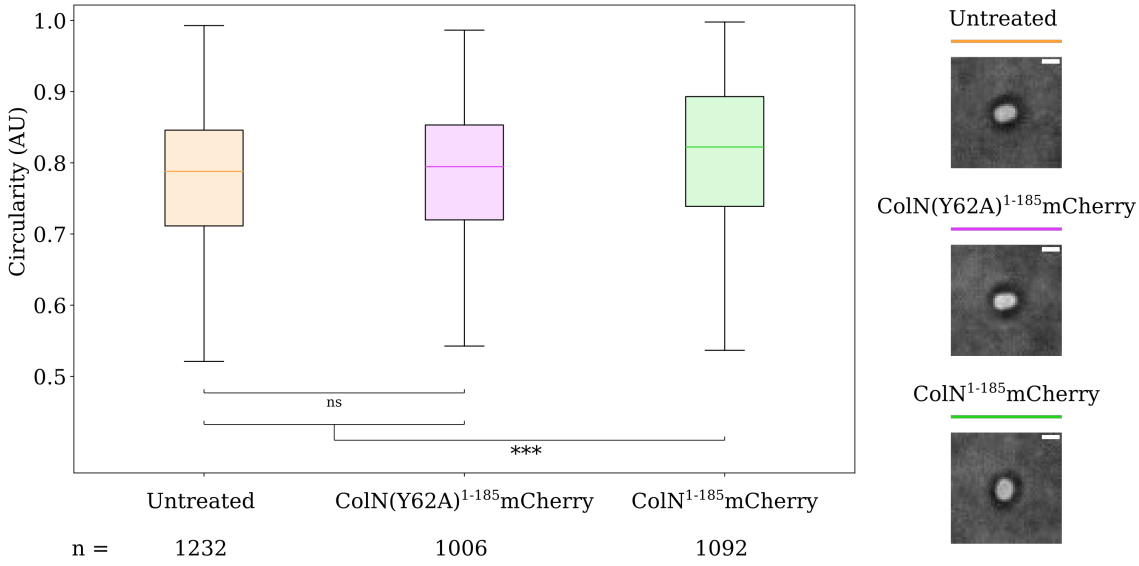

Figure 3.12: Colicin N fluorescent fusion protein effect on *E. coli* cell morphology. Left: Box plots of cell circularity after no treatment, treatment with 3.3 µM Colicin N(Y62A)$^{1-185}$mCherry or treatment with 3.3 µM Colicin N^{1-185}mCherry. Median circularity is represented by the coloured line, the upper and lower quartiles are represented by the bounds of each box, the largest and smallest data points within 1.5 times the interquartile range from either the upper quartile or lower quartile are represented by the whiskers. Circularity was determined from the ratio of the minor axis length to the major axis length of each cell. Right: representative trans illumination cell images for each treatment. Scale bars represent a distance of 1 µm. Statistical significance was determined from bootstrapping, the data was resampled 100,000 times and the 95, 99 and 99.9% confidence intervals were determined. ns: no significant difference. * $p < 0.05$. ** $p < 0.01$. *** $p < 0.001$.

Circularity was used to quantify the morphology of cells. An ellipse was fitted to each cell and circularity calculated by dividing the major axis length of the ellipse by the minor axis length. Therefore a value of 1 represents a perfect circle. As expected for cells in stationary phase, the untreated sample had a high circularity value of 0.78. Colicin N(Y62A)$^{1-185}$mCherry treated cells displayed no significant difference in circularity whereas

Colicin N^{1-185}mCherry, still able to bind to TolA, displayed a marginally greater circularity value of 0.81. Though statistically significant, this difference in morphology is minor. This experiment, combined with the fact that labelling concentrations in the following experiments will be conducted at significantly reduced concentrations, shows that Colicin N^{1-185}mCherry and its derivatives can be used for further microscopy experiments and will not induce notable morphological changes in the cells.

3.2.5 Colicin N Fluorescent Fusion Proteins do not Translocate Across the Outer Membrane

In addition to attenuating cytotoxicity, the replacement of the Colicin N pore forming domain with a fluorescent protein was hypothesised to prevent translocation across the outer membrane. Due to their β-barrel structure, fluorescent proteins such as mCherry are extremely stable, hence the translocation process should be halted when it reaches the mCherry of the fusion protein which will act as a plug preventing further translocation.

If this were the case, the mCherry portion of the Colicin N^{1-185}mCherry label will be surface exposed. To determine if mCherry is working effectively as a plug and arresting translocation, *E. coli* BE3000 cells were labelled with 200 nM Colicin N^{1-185}mCherry followed by treatment of increasing concentrations of trypsin, cells were imaged and their average fluorescence intensity quantified (Figure 3.13).

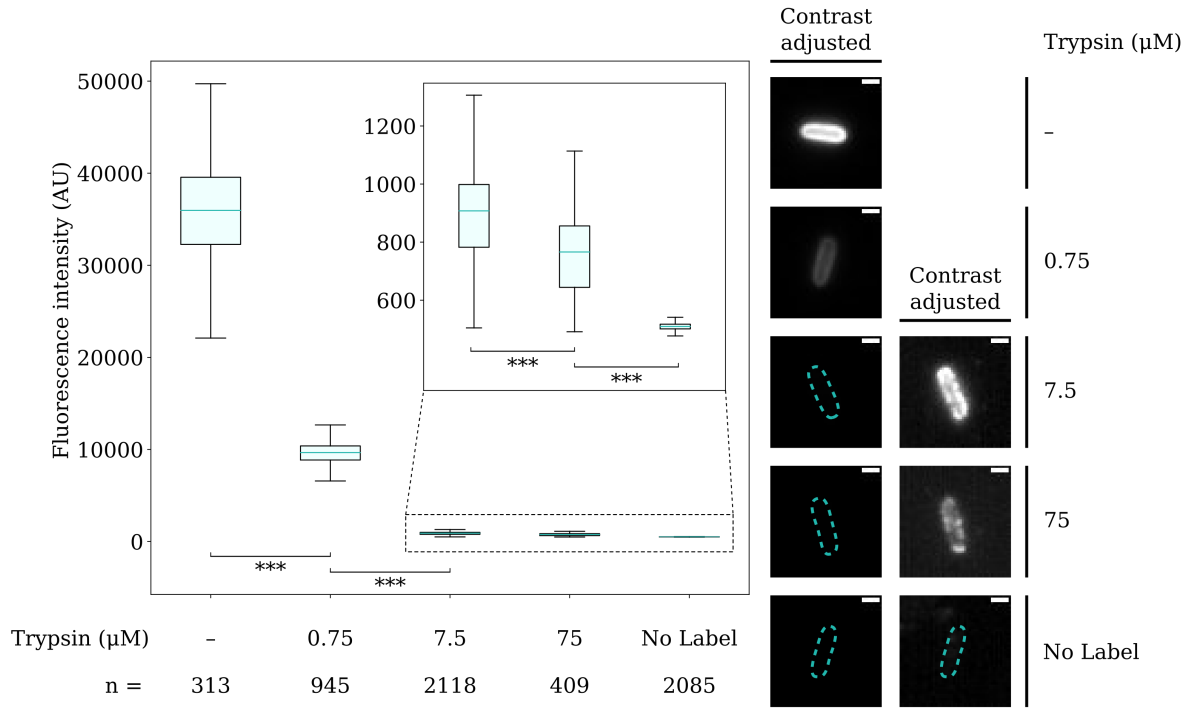

Figure 3.13: Colicin N^{1-185}mCherry labelling of *E. coli* BE3000 following trypsin treatment. Left: Box plots of average cell fluorescence after labelling with 200 nM Colicin N^{1-185}mCherry followed by: no treatment, 0.75 µM trypsin for 60 minutes, 7.5 µM trypsin for 60 minutes, 75 µM trypsin for 60 minutes and a no label control. Inset: Expanded view of the 7.5 µM trypsin treatment, 75 µM trypsin treatment and no label control. Median fluorescence intensity is represented by the blue line, the upper and lower quartiles are represented by the bounds of each box, the largest and smallest data points within 1.5 times the interquartile range from either the upper quartile or lower quartile are represented by the whiskers. Right: representative epifluorescence cell images for each condition. Each column represents images contrast adjusted to the same degree. Scale bars represent a distance of 1 µm. Statistical significance was determined from bootstrapping, the data was resampled 100,000 times and the 95, 99 and 99.9% confidence intervals were determined. ns: no significant difference. * $p < 0.05$. ** $p < 0.01$. *** $p < 0.001$.

In the absence of trypsin treatment, *E. coli* BE3000 cells display high intensity fluorescence signal, which is reduced significantly upon treatment with 0.75 µM trypsin. Higher concentrations of trypsin reduce average cell fluorescence intensity to levels only marginally greater than an unlabelled control (Figure 3.13). These results indicate that the mCherry portion of Colicin N^{1-185}mCherry is surface exposed as it is accessible to trypsin. It should be noted that residual fluorescence signal is detected in samples treated with 7.5 and 75 µM trypsin that is significantly greater than the unlabelled control. This is likely due to incom-

plete trypsin digestion of a small proportion of Colicin N^{1-185}mCherry molecules inaccessible to trypsin. Distribution of fluorescence signal at these trypsin concentrations indicates that residual, undigested Colicin N^{1-185}mCherry remains untranslocated as the fluorescence signal is both distributed peripherally and consists of immobile puncta. If translocation into the periplasm had occurred, puncta would not be observed as Colicin N^{1-185}mCherry would be diffusing freely diffusing.

3.2.6 Colicin N Fluorescent Fusion Proteins Label OmpF Exclusively *in vivo*

In order to be an effective fluorescent label for OmpF, Colicin N^{1-185}mCherry must bind it specifically. Colicin N binding to the inner core of LPS has been reported [188] and as a result recent reviews of Colicin biology suggest that Colicin N binds to LPS as its primary receptor in the outer membrane of *E. coli* [203]. Furthermore, OmpF expression is balanced with its homologue, OmpC in the outer membrane. It has been shown *in vitro* that Colicin N can bind to OmpC with similar affinities as to OmpF [210].

In order to establish that Colicin N^{1-185}mCherry binds to OmpF exclusively *in vivo*, multiple *E. coli* strains that differed in porin expression were labelled with Colicin N^{1-185}mCherry. The strains used were as follows: BW25113 (OmpF+, OmpC+), JW2203-1 (OmpF+, OmpC-), JW0912-1 (OmpF-, OmpC+) and BZB1107 (OmpF-, OmpC-). Crucially, all of these strains expressed the same length of rough LPS.

Fluorescence intensity quantification after labelling (Figure 3.14) shows that appreciable fluorescence signal is only present in cells expressing OmpF. Cells expressing solely OmpC and cells expressing neither OmpC nor OmpF display little fluorescence signal against the unlabelled control. This indicates that *in vivo* Colicin N^{1-185}mCherry is not binding to OmpC nor LPS and is exclusively labelling OmpF in the *E. coli* outer membrane.

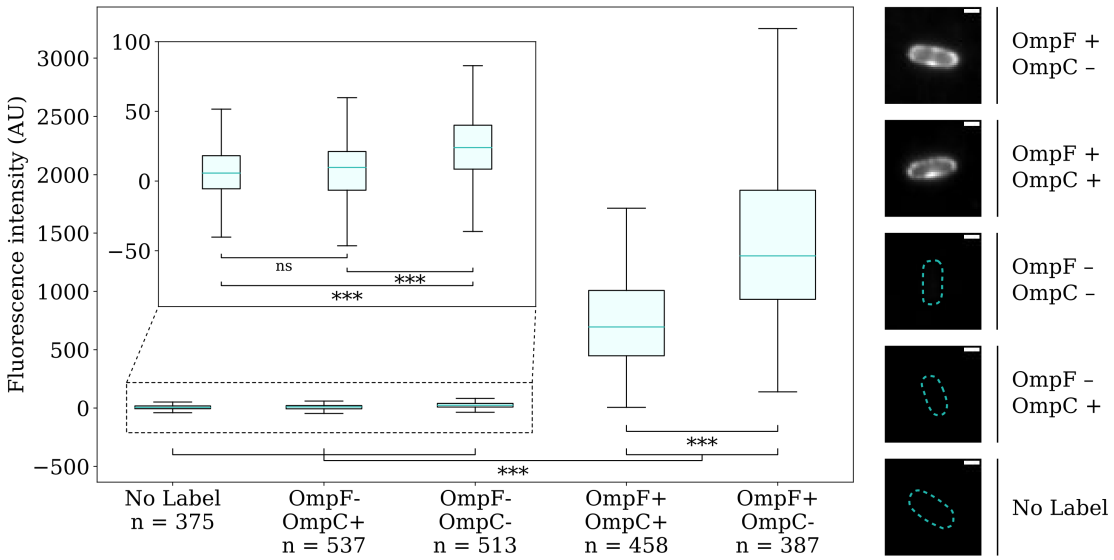

Figure 3.14: Colicin N^{1-185}mCherry labelling of *E. coli* strains. Left: Box plots of average cell fluorescence after labelling the following strains with 200 nM Colicin N^{1-185}mCherry: No Label, BW25113 untreated; OmpF- OmpC+, JW0912-1; OmpF- OmpC-, BZB1107; OmpF+ OmpC+, BW25113; and OmpF+ OmpC-, JW2203-1. Median fluorescence intensity is represented by the blue line, the upper and lower quartiles are represented by the bounds of each box, the largest and smallest data points within 1.5 times the interquartile range from either the upper quartile or lower quartile are represented by the whiskers. Right: representative epifluorescence cell images for each strain. Images were contrast adjusted to the same degree. Scale bars represent a distance of 1 µm. Statistical significance was determined from bootstrapping, the data was resampled 100,000 times and the 95, 99 and 99.9% confidence intervals were determined. ns: no significant difference. * $p < 0.05$. ** $p < 0.01$. *** $p < 0.001$.

3.3 Conclusions

Four Colicin N fluorescent fusion proteins were expressed and purified. Three of these fusion proteins: purified Colicin N^{1-185}mCherry, Colicin N(Y62A)$^{1-185}$mCherry and Colicin N^{1-185}PAmCherry displayed banding when analysed by SDS-PAGE. This banding was caused by acylimine bond hydrolysis within the chromophore of mCherry and PAmCherry but likely only occurs upon boiling with SDS prior to SDS-PAGE analysis. Colicin N fusion proteins with intact TABSs displayed mild toxicity at high concentrations in *E. coli* strains with OmpF enriched outer membranes. In the wild type K12 *E. coli* strains MG1655 and

BW25113 no cytotoxicity was observed for any of the fusion proteins. Long term exposure of cells to TABS containing colicin N fusion proteins had little effect on cell morphology. The fusion of Colicin N to fluorescent proteins effectively blocked import into *E. coli* and fluorescence of various *E. coli* strains quantification revealed that Colicin N fluorescent fusion proteins bind to OmpF exclusively *in vivo*.

Through establishing this, Colicin N fluorescent fusion proteins can be used to investigate the organisation and dynamics of OmpF in *E. coli*.

Chapter 4

OmpF Organisation

4.1 Introduction

The composition and structure of the *E. coli* outer membrane has been investigated in great detail over decades. Early investigations revealed that this membrane was asymmetric, containing lipopolysaccharide in the outer leaflet and phospholipids (phosphatidylethanolamine (75%), phosphatidylglycerol (20%) and cardiolipin) in the inner leaflet [26]. Further investigations began to localise various proteins to this membrane, fitting predominantly into two classes: lipoylated proteins and integral OMPs. The lipoylated proteins, such as Pal and Lpp were found anchored to the inner leaflet of the outer membrane, projecting into the periplasm [42, 70]. The integral OMPs were found to be enriched in beta strands which fold into an antiparallel β-barrel structure. A large number of these OMPs were discovered with a vast diversity of functions: biogenesis machinery, porins, selective channels, enzymes and virulence factors [48–57].

Despite this wealth of knowledge on the composition and structure of the outer membrane, little is known about the *lateral* organisation of this membrane. In the case of integral OMPs, the organisation of only a handful of these have been studied.

Arguably the first OMP to have its organisation in the OM investigated was the trimeric

maltoporin, LamB. Labelled with lambda bacteriophage tails covalently modified with Texas Red, LamB was shown by widefield epifluorescence microscopy to form a number of non-uniform distributions in the outer membrane [190]. More recent investigations into LamB distribution indicate a more punctate distribution that results from short bursts of insertion into the outer membrane [191].

The most comprehensive investigation into lateral OMP organisation focussed on the low-copy number monomeric OMPs: BtuB and Cir. Fluorescent constructs of Colicin E9 and Colicin Ia were used to label BtuB and Cir, respectively. Widefield TIRF microscopy revealed that BtuB and Cir displayed a punctate distribution in the outer membrane and that these puncta were in fact protein enriched "islands" formed by BtuB and Cir protein - protein interactions [189].

The abundant, trimeric, general porin OmpF which is expressed at copy numbers on the order of 100,000 proteins per cell has been the subject of intense study. The structure and function of this protein is comprehensively understood, however, very little is known about its lateral organisation in the outer membrane. The organisation of OmpF in lipid reconstituted OmpF crystals has been investigated by AFM which provided high resolution data [211], but as a highly synthetic system has little relevance to the *in vivo* organisation of OmpF wherein OmpF is incorporated into a significantly more complex membrane. *in vivo* AFM investigations into OmpF organisation provided more biologically relevant data but lacked sufficient resolution to unambiguously identify porins and as a label free approach was unable to distinguish OmpF from any of the other protein components of the OM [212].

In this chapter, I detail fluorescence microscopy investigations into OmpF organisation in *E. coli* by labelling cells with various Colicin N^{1-185} fluorescent fusion proteins and compare this distribution to that of previously categorised BtuB and Cir. I detail the development of a simulation program used to generate datasets of completely uniform distributions of surface proteins. Using this program to generate control datasets I investigate how clustering artefacts can be introduced by diffraction limited imaging of low copy number proteins and

how such artefacts relate to the observed distributions of BtuB and FepA in *E. coli*. Using high throughput diffraction limited widefield microscopy I show that OmpF can both form uniform and non-uniform distributions. When the distribution of OmpF is observed as a function of cell cycle these non-uniform distributions can be recapitulated indicating that OmpF distribution is directly affected by cell cycle. Lastly, I use Colicin N^{1-185}PAmCherry to conduct photoactivated localisation microscopy (PALM) and analyse the resultant datasets with spatial statistics to show that on short distance scales, OmpF is highly clustered in the outer membrane.

4.2 Results and Discussion

4.2.1 OmpF Organisation is Distinct From Low Copy Number OMPs

When observing and making assessments of protein distributions in cells, simulation programs represent powerful tools in generating control datasets to which experimental data can be both qualitatively and quantitatively compared.

In order to assess the differences in distribution between OmpF, BtuB and FepA in *E. coli* I have developed a program to simulate completely spatially random (CSR) protein distributions on the surface of a capsule Figure 4.1.

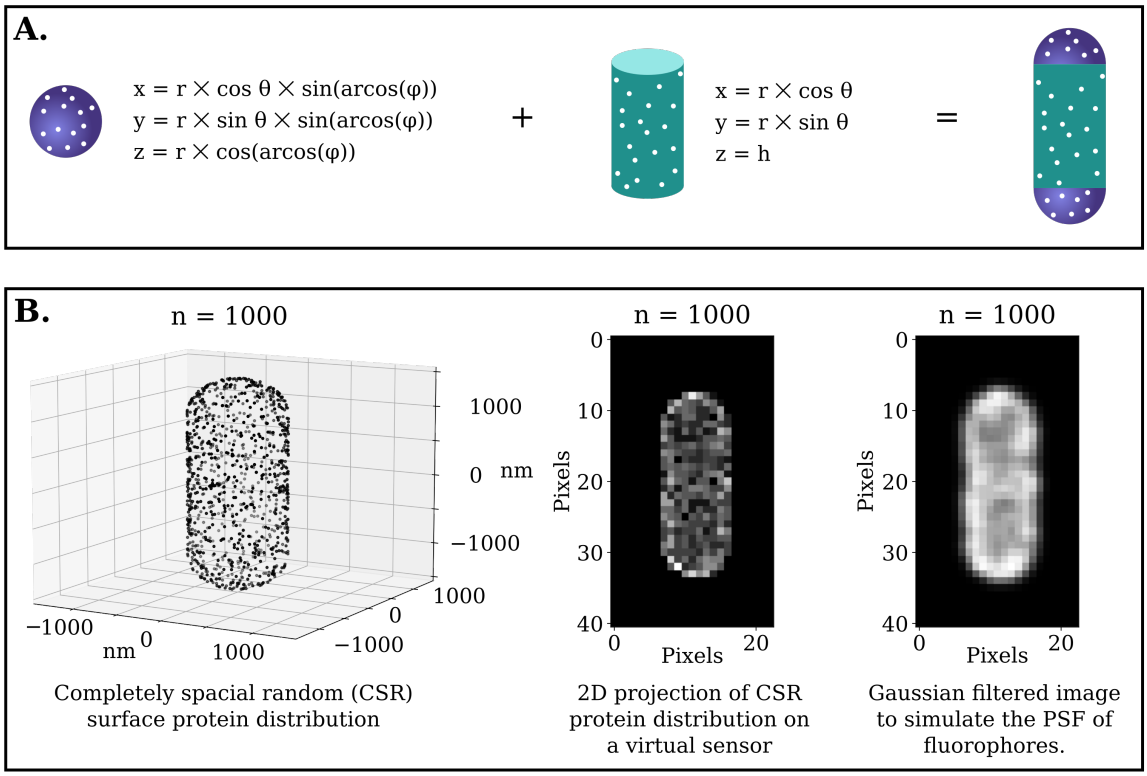

Figure 4.1: CSR surface protein distribution simulation program. A. Diagrammatic representation of the sphere and cylinder geometries combined to approximate the *E. coli* cell shape and associated equations to randomly distribute points on their surface. **B.** Left: 3D output of 1000 surface points distributed in a CSR manner for a cell with a radius of 500 nm and height of 3000 nm. Centre: 2D projection of CSR point data onto a virtual sensor with a pixel size of 117 nm. Right: Simulation of a diffraction limited microscopy image captured from the simulated point distribution.

The capsule shape, approximating the shape of an *E. coli* cell can be decomposed into two simple geometries, a sphere and a cylinder Figure 4.1.A. To simulate CSR protein distributions on the surface of a capsule, spatial coordinates must be generated for random points on both of these geometries. The spatial coordinates of a random point placed on the surface of a sphere can be determined using:

$$\begin{aligned} x &= r\,cos(\theta) \times sin(arcos(\varphi)) \\ y &= r\,sin(\theta) \times sin(arcos(\varphi)) \\ z &= r \times cos(arcos(\varphi)) \end{aligned} \tag{4.1}$$

Where r equals the radius of the sphere, θ equals a real, random number between 0 and 2π and φ equals a real, random number between -1 and 1.

The spatial coordinates of a random point placed on the surface of a cylinder can be determined using:

$$\begin{aligned} x &= r\,cos(\theta) \\ y &= r\,sin(\theta) \\ z &= h \end{aligned} \tag{4.2}$$

Where r equals the radius of the sphere, θ equals a real, random number between 0 and 2π and h equals a real, random number bounded by the height of the cylinder.

The simulated distributions of the sphere are then split into two hemispheres and appended to the top and bottom of the simulated distributions of the cylinder, generating the full capsule shape Figure 4.1.B. Simulated datasets can then be used to, in turn, simulate what widefield fluorescence microscopy images of these protein distributions would look like. This requires two key processing steps:

1. Projection of simulated distributions onto a virtual sensor. For image simulations generated in this chapter, each pixel of this sensor represents a distance of 117 nm to match that of the microscope used to capture the experimental data.

2. Simulation of fluorophore point spread functions by applying a Gaussian filter to the 2D projected data. The standard deviation of this Gaussian filter is estimated by determining the diffraction limit of the simulated system:

$$d = \frac{\lambda}{2NA} \tag{4.3}$$

Where d equals the diffraction limited distance, λ equals the maximum emission wavelength of the fluorophore used and NA equals the numerical aperture of the microscope system to be simulated.

When simulating these distributions it is critical to consider how the random numbers for θ and φ are generated to avoid introducing artefacts. As stated previously, these random numbers are selected between a specific range (θ, selected between 0 and 2π, for example) the number of samples populating this range must be great enough to ensure that the cell surface is not populated in an uneven manner. To achieve this, a large number of samples—1,000,000—is used to populate random number ranges.

A second important consideration is selecting the random numbers between the most relevant range. This is especially evident when distributing points in a CSR manner on the surface of the sphere element (Figure 4.2).

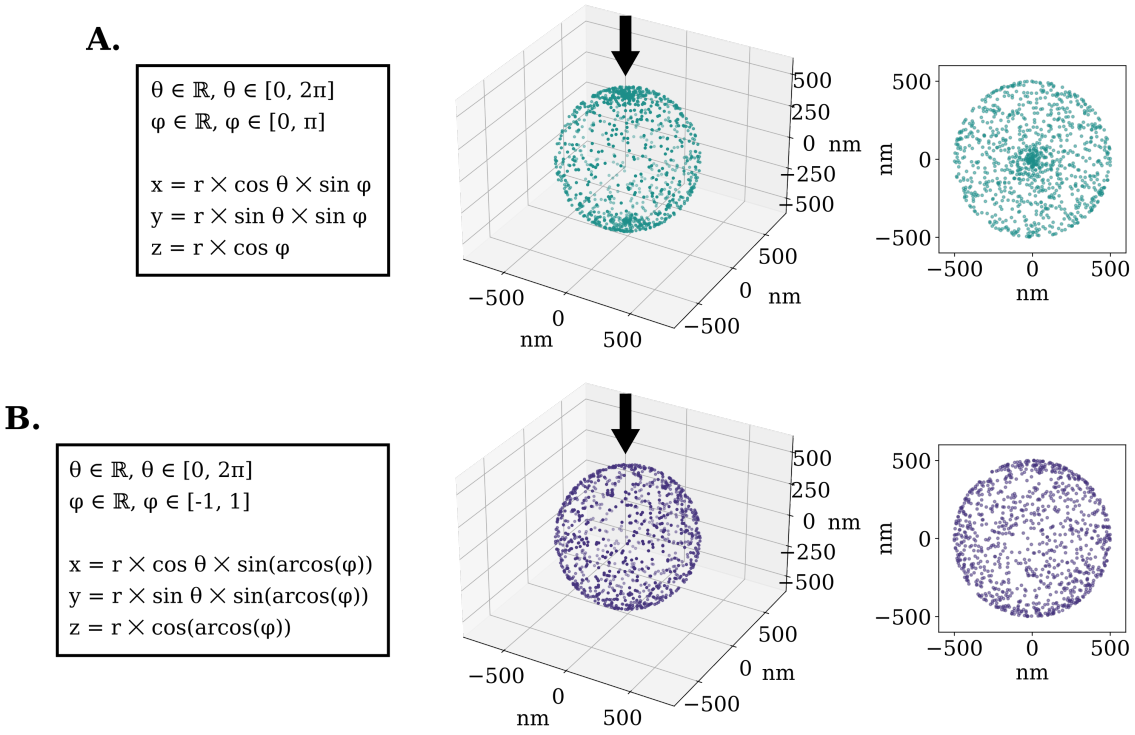

Figure 4.2: Distributing points randomly on the surface of a sphere. A. Surface distribution of 1000 points on a sphere wherein the value for φ is selected randomly between 0 and π. **B.** Surface distribution of 1000 points on a sphere wherein the value for φ is selected randomly between -1 and 1.

Points can be distributed on the surface of a sphere using two methods, one in which the value for φ is selected randomly between 0 and π and the x and y coordinates are determined by taking the sin of this value. This, however leads to artificial clustering at the two poles

of the sphere (Figure 4.2.A) resulting in a distribution of points which is no longer spatially random. This is overcome by randomly selecting the value for φ between -1 and 1 and taking the sin of the arcos of this value to generate the x and y coordinates. In doing so, artificial clustering at the poles is eliminated in the simulation (Figure 4.2.B.).

Completely spatially random surface protein distribution simulations represent a robust negative control for "organised" protein distribution. Previous investigations into low copy number BtuB and Cir showed that these proteins organised into enriched islands in the outer membrane driven by protein-protein interactions. Much of the evidence for this came in the form of widefield diffraction limited microscopy images showing puncta on the cell surface [189].

The CSR simulation program provides a framework wherein the effect of copy number on puncta formation can be interrogated. Simulations of cell images with 100 - 100,000 CSR surface proteins were conducted (Figure 4.3). Each image generated was contrast adjusted such that the most intense pixel was set to 1 and least intense pixel set to 0. This ensured that the distribution of proteins for each copy number could be directly compared. Resultant images were encoded as 8-bit greyscale images. For each cell, maxima points at an arbitrary prominence value of 20 or greater were identified using the find maxima tool in imageJ.

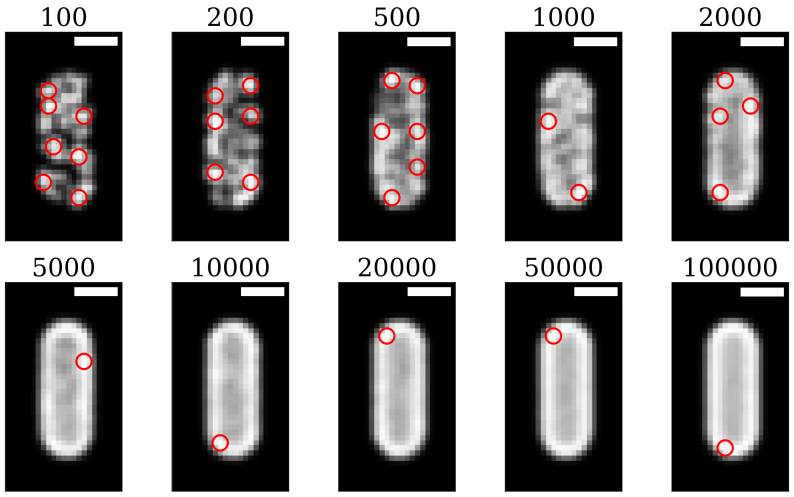

Figure 4.3: Simulated images of CSR surface protein distributions at increasing copy numbers. Simulations of increasing copy numbers of proteins, indicated with the number above each image, were conducting in cells with a radius of 500 nm and a height of 3000 nm. Red circles highlight maxima with a prominence greater than 20.

This revealed that at low copy numbers, a greater number of local maxima were identified and as copy number increased the number of maxima decreased. This dataset exemplifies the effect copy number can have on apparent distribution of proteins on the surface of the cell. In this case it would be erroneous to conclude from the low copy number images that proteins organise into puncta as their distribution is in fact entirely random and no different from the high copy number distributions.

The cause of this copy number effect results from sampling a sparse field of points on a low resolution sensor. At low copy numbers, due to the random nature of the point distributions some areas of the cell will have more points than others. As there are relatively low numbers of proteins overall, the difference between enriched and impoverished regions are more pronounced than that for high copy number proteins. Furthermore, as each pixel represents a relatively large area (117 by 117 nm) particles that in reality may be distant e.g. 100 nm, would be collected by the same pixel on the sensor further promoting the appearance of puncta.

To investigate both the effect of copy number on OMP organisation and to qualitatively compare the outer membrane organisation of different OMPs; BtuB, FepA and OmpF were

labelled with fluorescent Colicin constructs and imaged by widefield microscopy and illuminated in both epifluorescence and TIRF.

Epifluorescence illumination refers to imaging where the excitation laser enters the sample perpendicular to the orientation of the slide (0 °). In doing so the excitation laser penetrates deep into the sample, in the case of *E. coli*, exciting the whole cell. By contrast, TIRF illuminates samples at the "critical angle" to achieve total internal reflection, this causes an evanescent wave to penetrate only approximately 200 nm into the sample. In the case of *E. coli*, this excites only fluorophores on the surface of the cell touching the coverslip surface.

BtuB was labelled in *E. coli* MG1655 using a Colicin E9 construct conjugated to AF488. Widefield epifluorescence microscopy revealed the punctate distribution of BtuB on the cell surface (Figure 4.4.A.). The copy number of BtuB per cell has previously been estimated at a range between 564 to 2295 [44]. Simulations of CSR BtuB distribution were therefore conducted within this range from 600 to 2200 copies per cell. This simulated data, notably at lower copy numbers, also displayed a punctate distribution (Figure 4.4.B.).

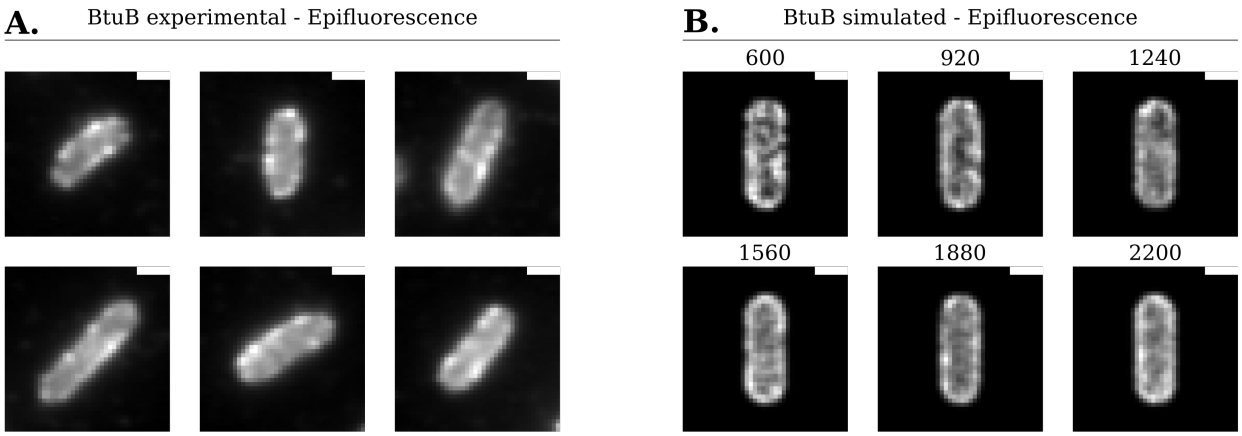

Figure 4.4: BtuB distribution in *E. coli* MG1655 imaged in epifluorescence and CSR BtuB simulated cell images. A. Fixed *E. coli* MG1655 labelled with ColE9-AF488 for 10 minutes, imaged on an ONI Nanoimager S at an illumination angle of 0° with a 473 nm laser line (20 mW) for each cell image, 50 consecutive frames collected at an exposure time of 100 ms were averaged. The fluorescence intensity of each individual cell image was normalised between 0 and 1. **B.** Simulated cell images of CSR BtuB distribution. Each simulated cell was 3000 nm in height and had a radius of 500 nm. 600 to 2200 points were simulated on the surface of the cell. The standard deviation of the Gaussian blur applied to the simulated images was determined using the parameters defined by the experimental data: a numerical apertures of 1.49 and a maximum emission wavelength of 525 nm. Scale bars represent a distance of 1 µm.

When illuminated in TIRF, thereby imaging approximately 200 nm into the sample, puncta on the surface of the cell could be visualised with greater clarity (Figure 4.5.A.). In simulations of CSR TIRF data, wherein a surface slice of 200 nm in depth was projected onto the virtual sensor, puncta were also clearly visible and shared visually similar distributions with experimental data (Figure 4.5.B.).

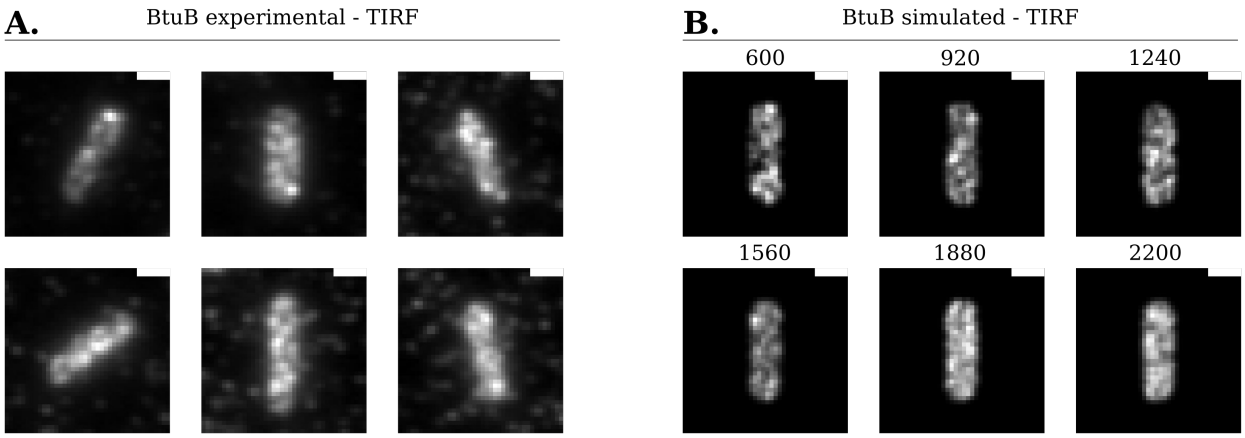

Figure 4.5: BtuB distribution in *E. coli* MG1655 imaged in TIRF and TIRF CSR BtuB simulated cell images. A. Fixed *E. coli* MG1655 labelled with ColE9-AF488 for 10 minutes, imaged on an ONI Nanoimager S at an illumination angle of 54°, to achieve total internal reflection fluorescence, with a 473 nm laser line (20 mW) for each cell image, 50 consecutive frames collected at an exposure time of 100 ms were averaged. The fluorescence intensity of each individual cell image was normalised between 0 and 1. **B.** Simulated cell images of TIRF CSR BtuB distribution. Each simulated cell was 3000 nm in height and had a radius of 500 nm. 600 to 2200 points were simulated on the surface of the cell. A 200 nm slice of the surface of the cell was projected onto the virtual sensor to simulate TIRF illumination. The standard deviation of the Gaussian blur applied to the simulated images was determined using the parameters defined by the experimental data: a numerical aperture of 1.49 and a maximum emission wavelength of 525 nm. Scale bars represent a distance of 1 µm.

FepA, like BtuB is a monomeric OMP, but under iron limitation conditions is expressed at greater copy numbers in the cell. Experiments quantifying the copy number of the Ton system components and FepA found that under iron limitation conditions—simulated by growing cells in iron chloride containing media with the metal chelator: diethylenetriamine-pentaacetic acid (DPTA)—FepA was expressed at copy numbers 4108 and proteins per cell [213]. Simulations of CSR FepA distribution were therefore conducted at 4000 copies per cell.

FepA distribution is notably less punctate than that of BtuB, however around the periphery of the cell a number of puncta are still present (Figure 4.6.A.). Epifluorescence simulations follow the same trend as the experimental data, having a distinctly less punctate distribution compared to BtuB simulations (Figure 4.6.B.).

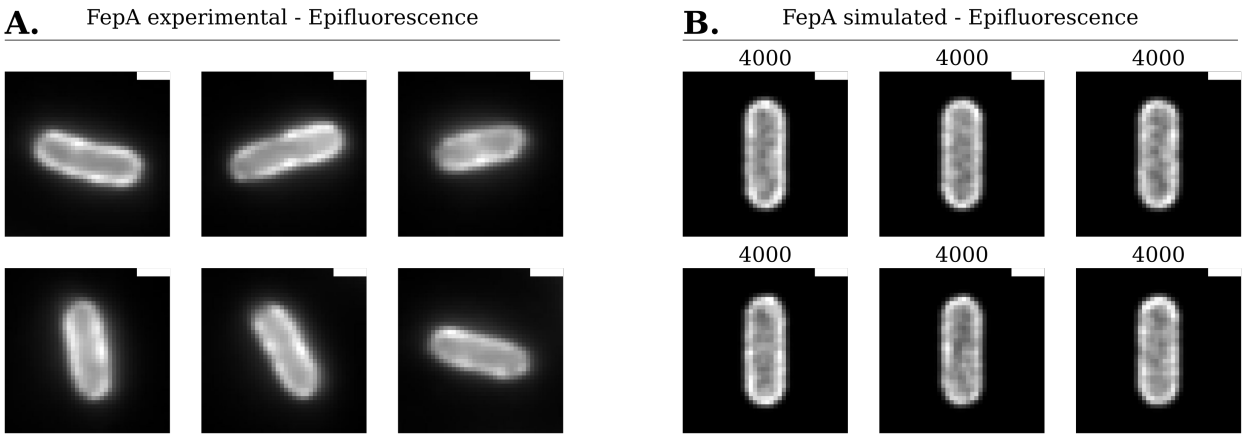

Figure 4.6: FepA distribution in *E. coli* MG1655 imaged in epifluorescence and CSR FepA simulated cell images. A. Fixed *E. coli* MG1655 labelled with ColB-GFP for 10 minutes, imaged on an ONI Nanoimager S at an illumination angle of 0° with a 473 nm laser line (20 mW) for each cell image, 50 consecutive frames collected at an exposure time of 100 ms were averaged. The fluorescence intensity of each individual cell image was normalised between 0 and 1. **B.** Simulated cell images of CSR FepA distribution. Each simulated cell was 3000 nm in height and had a radius of 500 nm. 4000 points were simulated on the surface of the cell. The standard deviation of the Gaussian blur applied to the simulated images was determined using the parameters defined by the experimental data: a numerical aperture of 1.49 and a maximum emission wavelength of 510 nm. Scale bars represent a distance of 1 µm.

Whereas TIRF imaging of BtuB distribution increased the visibility of puncta, no such effect could be observed when imaging FepA. Fluorescence intensity was not uniform across the surface of the cell, however notable puncta could not be observed (Figure 4.7.A.). Simulated images reflected a similar distribution to experimental results (Figure 4.4.B.).

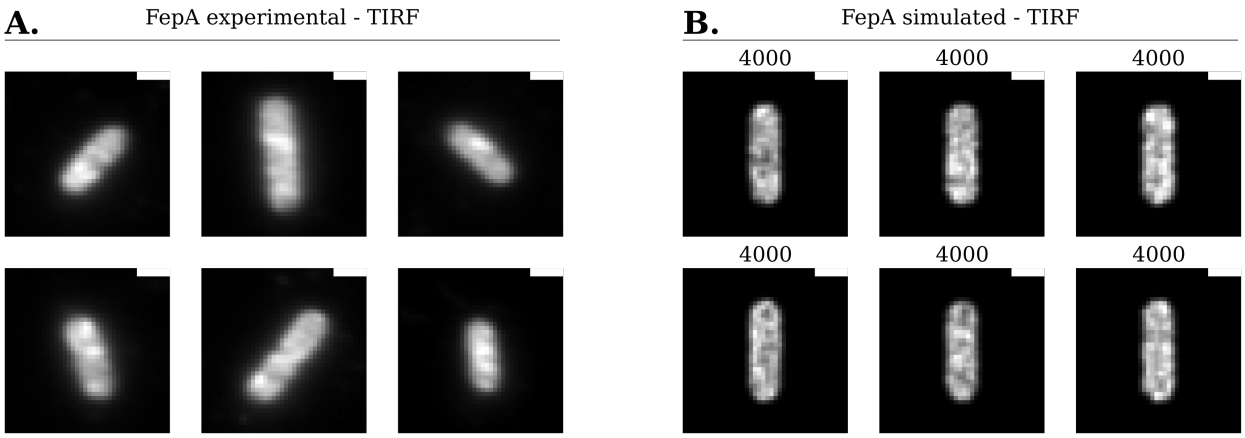

Figure 4.7: FepA distribution in *E. coli* MG1655 imaged in TIRF and CSR FepA simulated cell images. A. Fixed *E. coli* MG1655 labelled with ColB-GFP for 10 minutes, imaged on an ONI Nanoimager S at an illumination angle of 54°, to achieve total internal reflection fluorescence, with a 473 nm laser line (20 mW) for each cell image, 50 consecutive frames collected at an exposure time of 100 ms were averaged. The fluorescence intensity of each individual cell image was normalised between 0 and 1. **B.** Simulated cell images of TIRF CSR FepA distribution. Each simulated cell was 3000 nm in height and had a radius of 500 nm. 4000 points were simulated on the surface of the cell. A 200 nm slice of the surface of the cell was projected onto the virtual sensor to simulate TIRF illumination. The standard deviation of the Gaussian blur applied to the simulated images was determined using the parameters defined by the experimental data: a numerical aperture of 1.49 and a maximum emission wavelength of 510 nm. Scale bars represent a distance of 1 µm.

Compared to BtuB and FepA, OmpF is expressed in *E. coli* at significantly higher levels, estimated to be between 63,340 and 88,988 copies per cell [44]. Labelling with Colicin N^{1-185}mCherry, OmpF appeared to be distributed throughout the cell in an apparently uniform manner (Figure 4.8.A.). Simulated epifluorescence images were in good agreement with experimental data, displaying near identical distributions (Figure 4.8.B.).

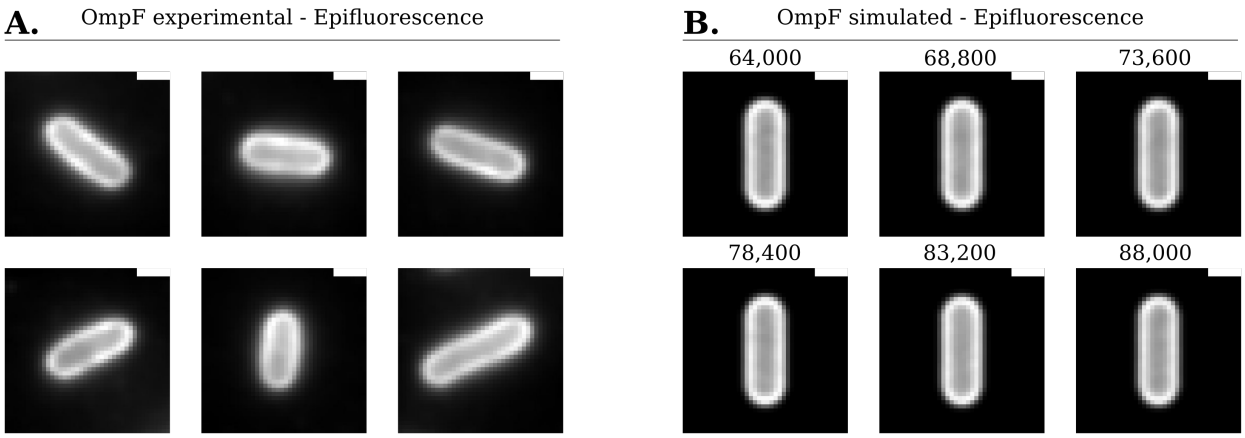

Figure 4.8: OmpF distribution in *E. coli* MG1655 imaged in epifluorescence and CSR OmpF simulated cell images. **A.** Fixed *E. coli* MG1655 labelled with Colicin N^{1-185}mCherry for 10 minutes, imaged on an ONI Nanoimager S at an illumination angle of 0° with a 561 nm laser line (20 mW) for each cell image, 50 consecutive frames collected at an exposure time of 100 ms were averaged. The fluorescence intensity of each individual cell image was normalised between 0 and 1. **B.** Simulated cell images of CSR OmpF distribution. Each simulated cell was 3000 nm in height and had a radius of 500 nm. 64,000 to 88,000 points were simulated on the surface of the cell. The standard deviation of the Gaussian blur applied to the simulated images was determined using the parameters defined by the experimental data: a numerical aperture of 1.49 and a maximum emission wavelength of 610 nm. Scale bars represent a distance of 1 µm.

TIRF imaging of the surface of cells again showed the apparent uniform distribution of OmpF across the surface of the cell (Figure 4.9.A.). TIRF simulations, like their epifluorescence counterparts matched closely with OmpF experimental data (Figure 4.9.B.).

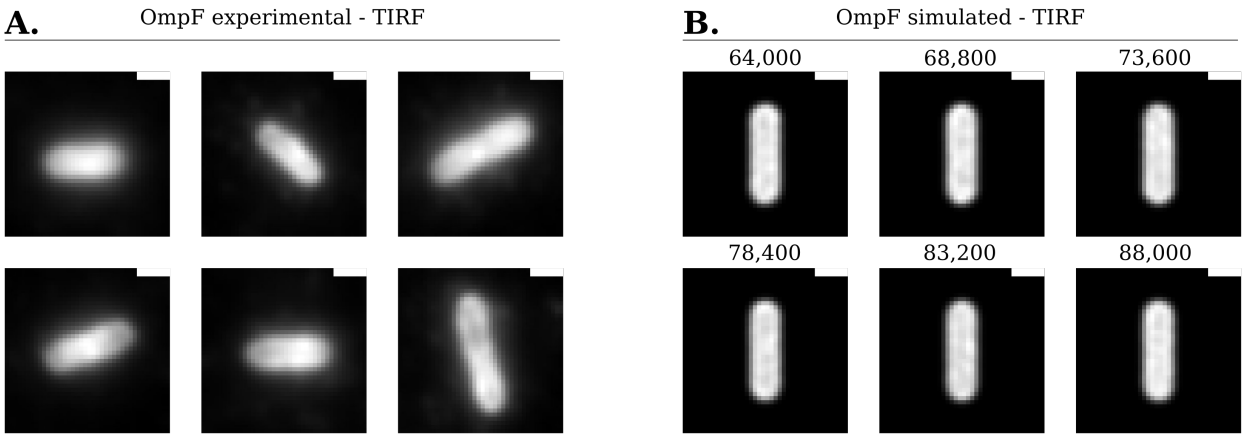

Figure 4.9: OmpF distribution in *E. coli* MG1655 imaged in TIRF and CSR OmpF simulated cell images. A. Fixed *E. coli* MG1655 labelled with Colicin N^{1-185}mCherry for 10 minutes, imaged on an ONI Nanoimager S at an illumination angle of 54°, to achieve total internal reflection fluorescence, with a 561 nm laser line (20 mW) for each cell image, 50 consecutive frames collected at an exposure time of 100 ms were averaged. The fluorescence intensity of each individual cell image was normalised between 0 and 1. **B.** Simulated cell images of TIRF CSR OmpF distribution. Each simulated cell was 3000 nm in height and had a radius of 500 nm. 64,000 to 88,000 points were simulated on the surface of the cell. A 200 nm slice of the surface of the cell was projected onto the virtual sensor to simulate TIRF illumination. The standard deviation of the Gaussian blur applied to the simulated images was determined using the parameters defined by the experimental data: a numerical aperture of 1.49 and a maximum emission wavelength of 610 nm. Scale bars represent a distance of 1 µm.

In order to determine if OmpF organisation distinct from that of the low copy number monomeric OMPs, BtuB and FepA; *E. coli* MG1655 cells were co-labelled, with either Colicin N^{1-185}mCherry (OmpF) and Colicin E9-AF488 (BtuB) or Colicin N^{1-185}mCherry (OmpF) and Colicin B-GFP (FepA). For each co-labelled cell, the fluorescence intensity of the cell was normalised between 0 and 1 in order to be able to directly compare differences in OMP distribution in a fluorescence intensity independent manner. For each co-labelling dataset, local maxima were identified for each cell using the imageJ find maxima tool set to the same arbitrary prominence value. The local maxima per cell were then counted for all cells collected.

When OmpF and BtuB were co-labelled and imaged in epifluorescence and TIRF (Figure 4.10), under both imaging conditions OmpF displayed significantly fewer local maxima

per cell ($p < 0.001$). Indicating that OmpF distribution is significantly less punctate from low copy number BtuB.

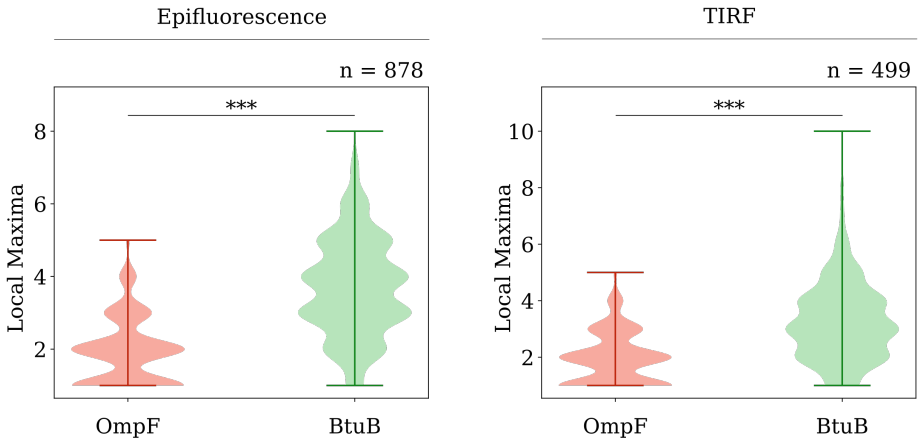

Figure 4.10: OmpF and BtuB local maxima analysis in *E. coli* MG1655. OmpF and BtuB were co-labelled with Colicin N^{1-185}mCherry and Colicin E9-AF488, respectively. Epifluorescence images were collected at an illumination angle of 0° and TIRF images at an illumination angle of 54°. The fluorescence intensity of each cell image was normalised between 0 and 1 and the find maxima tool in imageJ was used to identify local maxima. Statistical significance was determined from bootstrapping, the data was resampled 100,000 times and the 95, 99 and 99.9% confidence intervals were determined. ns: no significant difference. * $p < 0.05$. ** $p < 0.01$. *** $p < 0.001$.

When OmpF and FepA were co-labelled, a similar trend as OmpF BtuB co-labelling was observed (Figure 4.11). OmpF displayed significantly fewer local maxima per cell than FepA ($p < 0.001$). However, consistent with the qualitative data of its distribution (Figure 4.6 & Figure 4.7), FepA, though more punctate than OmpF, does not display as great a difference in maxima per cell compared to the difference observed for OmpF and BtuB. Notably, the number of maxima per cell identified from the TIRF images were lower than expected for both OmpF and FepA. This is likely due to the relatively low sample size of 83 cells collected.

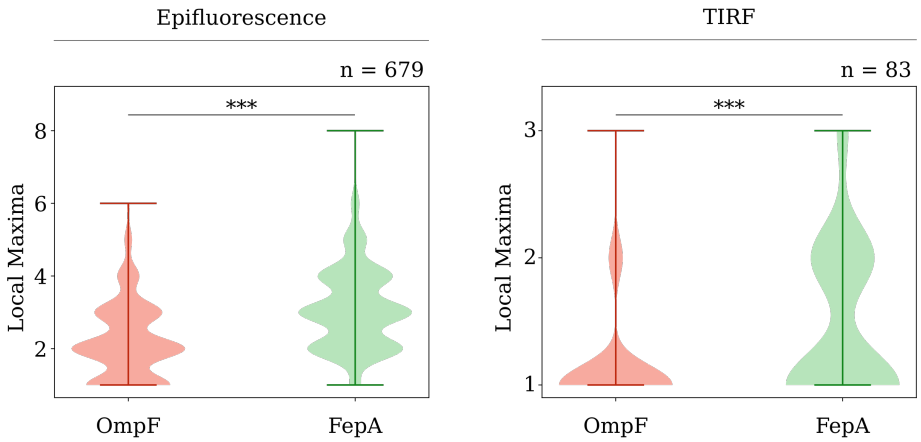

Figure 4.11: OmpF and FepA local maxima analysis in *E. coli* MG1655. OmpF and FepA were co-labelled with Colicin N^{1-185}mCherry and Colicin B-GFP, respectively. Epifluorescence images were collected at an illumination angle of 0° and TIRF images at an illumination angle of 54°. The fluorescence intensity of each cell image was normalised between 0 and 1 and the find maxima tool in imageJ was used to identify local maxima. Statistical significance was determined from bootstrapping, the data was resampled 100,000 times and the 95, 99 and 99.9% confidence intervals were determined. ns: no significant difference. * $p < 0.05$. ** $p < 0.01$. *** $p < 0.001$.

Due to their punctate distribution, BtuB and FepA organisation can be investigated further by determining the number of individual proteins that constitute these puncta. BtuB and FepA were labelled as described previously and field of views (FOVs) were acquired for an extended period of time to allow for complete photobleaching to occur. After complete photobleaching a sparse set of fluorophores entered a blinking state.

Blinking fluorophores were manually selected and the intensity of their on and off states were recorded (Figure 4.12.A. & Figure 4.12.B.) The average value of a single fluorophore could then be calculated for each labelled OMPs. Using this value and the fluorescence intensity of each puncta of BtuB and FepA, the number of single molecules constituting each puncta could be calculated (Figure 4.12).

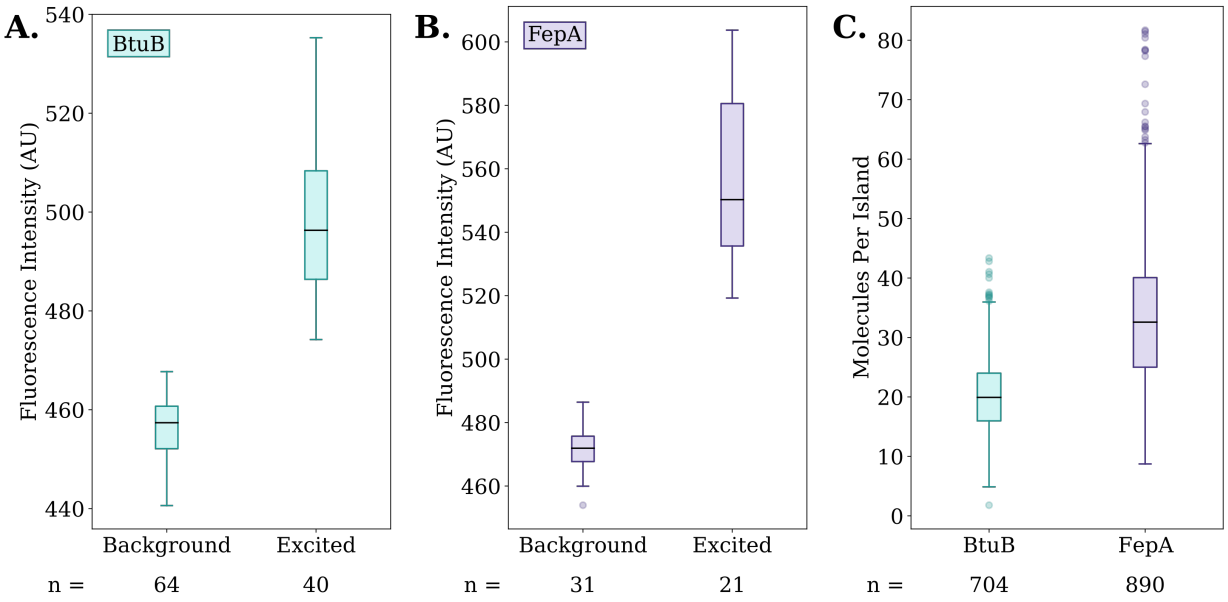

Figure 4.12: Estimation of BtuB and FepA molecules per island. A. Background and excited fluorescence intensities for Colicin E9-AF488 labelled BtuB after entering a blinking state. Mean background fluorescence intensity: 456.5 AU, mean excited fluorescence intensity: 497.8 AU. **B.** Background and excited fluorescence intensities for Colicin B-GFP labelled FepA after entering a blinking state. Mean background fluorescence intensity: 471.7 AU, mean excited fluorescence intensity: 556.3 AU. **C.** Molecules per Island for BtuB and FepA. For each cell the fluorescence intensity of each puncta was measured and using the values for background fluorescence intensity and the value for a single fluorophore was used to estimate the number of molecules constituting a single island. Mean number of BtuB molecules per island: 20.4 [19.8, 21.0] (99.9% CI), mean number of FepA molecules per island: 33.5 [32.4, 34.5] (99.9% CI). The 99.9% CI was determined from bootstrapping, the data was resampled 100,000 times and 99.9% confidence interval was determined using the percentile method.

To estimate the number of molecules per island, the simple following equation is used:

$$Molecules\,per\,island = \frac{i_{fi} - b_{fi}}{e_{fi} - b_{fi}} \tag{4.4}$$

Where i_{fi} equals the fluorescence intensity of an OMP island, b_{fi} equals the background fluorescence intensity of a single blinking fluorophore and e_{fi} equals the excited fluorescence intensity of a single blinking fluorophore.

BtuB puncta were estimated to contain an average of 20.4 [19.8, 21.0] (99.9% CI) individual BtuB proteins and FepA islands were estimated to contain an average of 33.5 [32.4,

34.5] (99.9% CI) FepA proteins.

It should be noted, however, that there are a number of significant limitations with this experiment. Intensity based counting relies on accurate measurement of the single fluorophore standard and hence relies on uniform illumination in each field of view. The Nanoimager S system used to collect the photobleaching data does not have homogenous FOV illumination and hence the intensity of the single fluorophore standard are likely to be inaccurate. Furthermore, techniques such as intensity based counting significantly decrease in accuracy at fluorophore numbers greater than 10 [214].

As identified through simulations, CSR surface protein distributions can yield images that appear punctate (Figure 4.3). Therefore, the proteins per island of BtuB and FepA must be compared to CSR controls before a conclusion that these puncta represent active enrichment of proteins can be made. Consequently, simulated images of CSR surface protein distribution at low copy numbers were generated, puncta identified using the same method as for the experimental data and the number of proteins constituting a puncta measured (Figure 4.13).

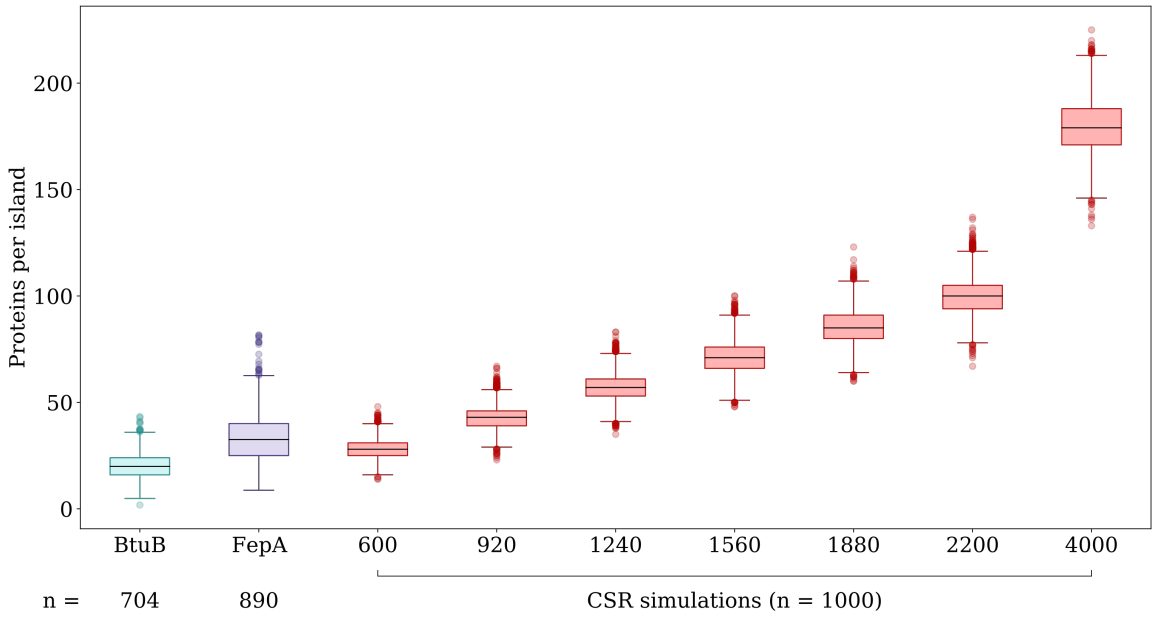

Figure 4.13: Proteins per island observed for BtuB and FepA compared against CSR simulated data. BtuB and FepA proteins per island were determined as previously described. Copy numbers of CSR simulated proteins are displayed. For each copy number 1000 images were simulated, had puncta identified and the number of proteins within each puncta was measured. Statistical significance was determined from bootstrapping, the data was resampled 100,000 times and the 95, 99 and 99.9% confidence intervals were determined, revealing that all of the data was significantly different from one another ($p < 0.001$).

Simulated CSR data revealed that at copy numbers of 600, puncta contained on average 28.3 proteins, this increased to 179.4 per island at copy numbers of 4000. Therefore, for all CSR simulations analysed the average number of proteins per island was greater than that determined for BtuB. Only the CSR simulations at copy numbers of 600 displayed fewer proteins per island compared to FepA.

Taken together, the observations that low copy number CSR distributions of proteins yield clearly defined puncta in cells and that the number of proteins that constitute these puncta are greater than that of BtuB and FepA indicates that BtuB and FepA could be randomly distributed in the outer membrane and that their organisation into islands may be an artefact of diffraction limited imaging of low copy number proteins. It is critical to note, however, that the theory of protein enriched islands cannot be discounted entirely as the experimental data predicting the number of BtuB and FepA molecules making up their

respective islands, that the CSR simulated data was compared to, is likely to be inaccurate.

4.2.2 OmpF Organisation can be Sorted into Six Distinct Categories

OmpF distribution often appears uniform throughout the cell (Figure 4.8 & Figure 4.9), however OmpF can appear distributed in a manner that is both non-punctate and non-uniform (Figure 4.14). These non-uniform OmpF distributions diverge significantly from CSR simulated data and therefore represent local organisation of OmpF proteins. Further to the existence of non-uniform distributions, OmpF can in fact be sorted into six distinct categories of distribution that can be reliably observed when OmpF is labelled with Colicin N^{1-185}mCherry and imaged in epifluorescence (Figure 4.14).

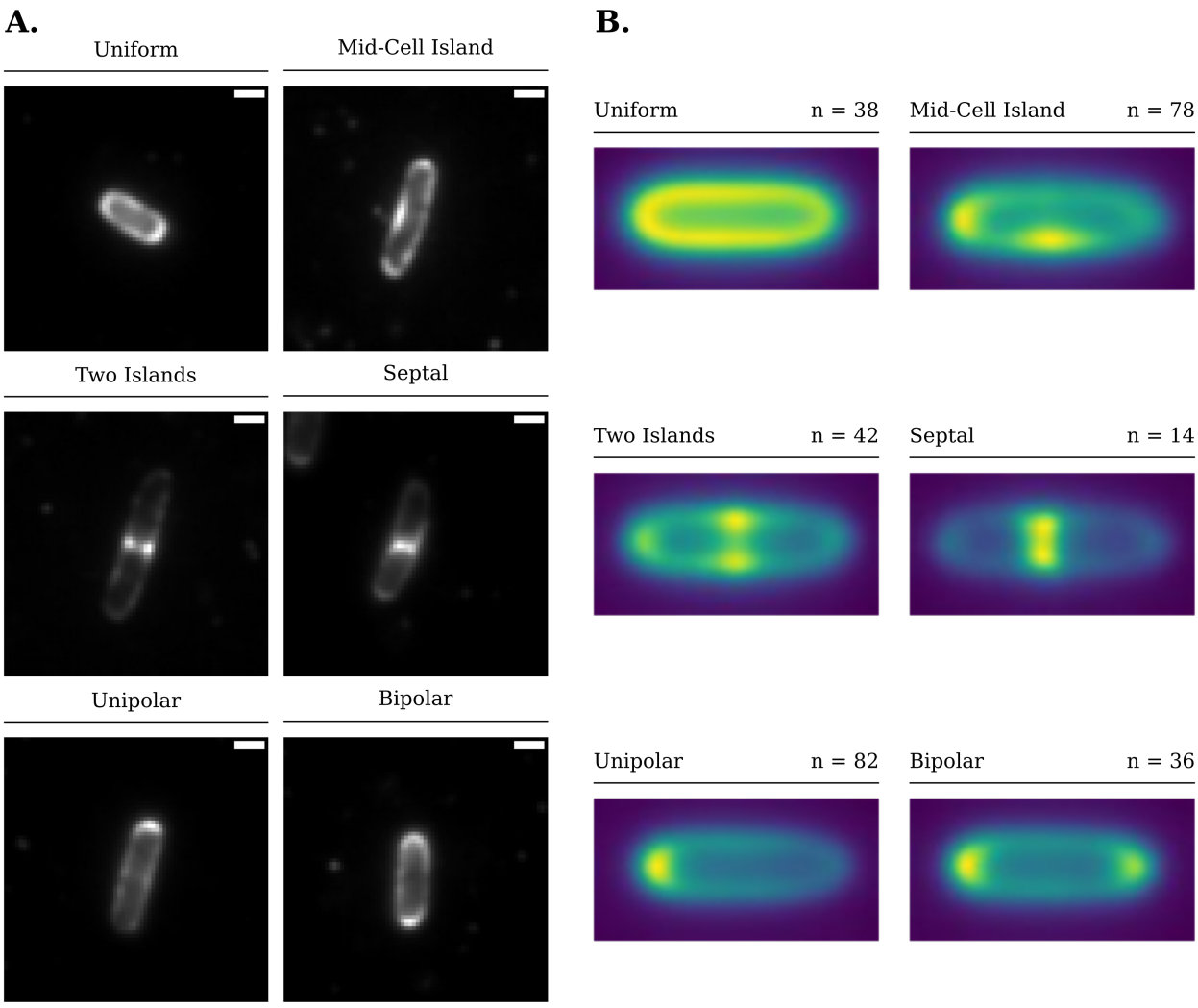

Figure 4.14: Heatmaps of the six categories of observed OmpF distribution in *E. coli* MG1655. *E. coli* MG1655 was labelled with Colicin N^{1-185}mCherry. **A.** Representative images of cells displaying each category of OmpF distribution. **B.** Heatmaps were generated by normalising each cell's rotation, fluorescence intensity and long and short axes lengths. Cells sharing the same distribution pattern were grouped together and the average 2D fluorescence distribution of each category of distribution was plotted.

The following distributions were consistently observed when imaging OmpF organisation:

1. Uniform - Fluorescence intensity observed throughout the cell.

2. Mid-Cell Island - An increase in fluorescence intensity is observed at mid-cell but only on one side of the cell.

3. Two Islands - An increase in fluorescence intensity is observed at mid-cell on both sides

of the cell.

4. Septal - An increase in fluorescence intensity is observed at the septum of dividing cells.

5. Unipolar - An increase of fluorescence intensity is observed at a single pole of the cell.

6. Bipolar - An increase of fluorescence intensity is observed at both poles of the cell.

In order to generate heatmaps of OmpF organisation, image data required a significant amount of preprocessing (Figure 4.15). The first stage of this processing was cell identification. Crude thresholding was conducted to generate an initial binary image of segmented cells. These binary images contain a significant amount of noise and clumps of cells are erroneously segmented as single cells. Filtering is applied to eliminate noise and large cell clumps (Figure 4.15.A.). Using the segmented cell image, bounding boxes are fitted to the cells and used to crop out the identified cells from the fluorescence image (Figure 4.15.B.). The long and short axes are normalised to 100 and 50 pixels, respectively. The fluorescence intensity of the cells are then normalised between 0 and 1 to ensure that fluorescence distribution is directly comparable. Finally, normalised cell images are flipped along the horizontal and vertical axis to ensure that the most intense quadrant of the normalised cell image is the same for each cell (set to the top left corner). After normalisation, heatmaps of fluorescence distribution can be generated (Figure 4.15.C.).

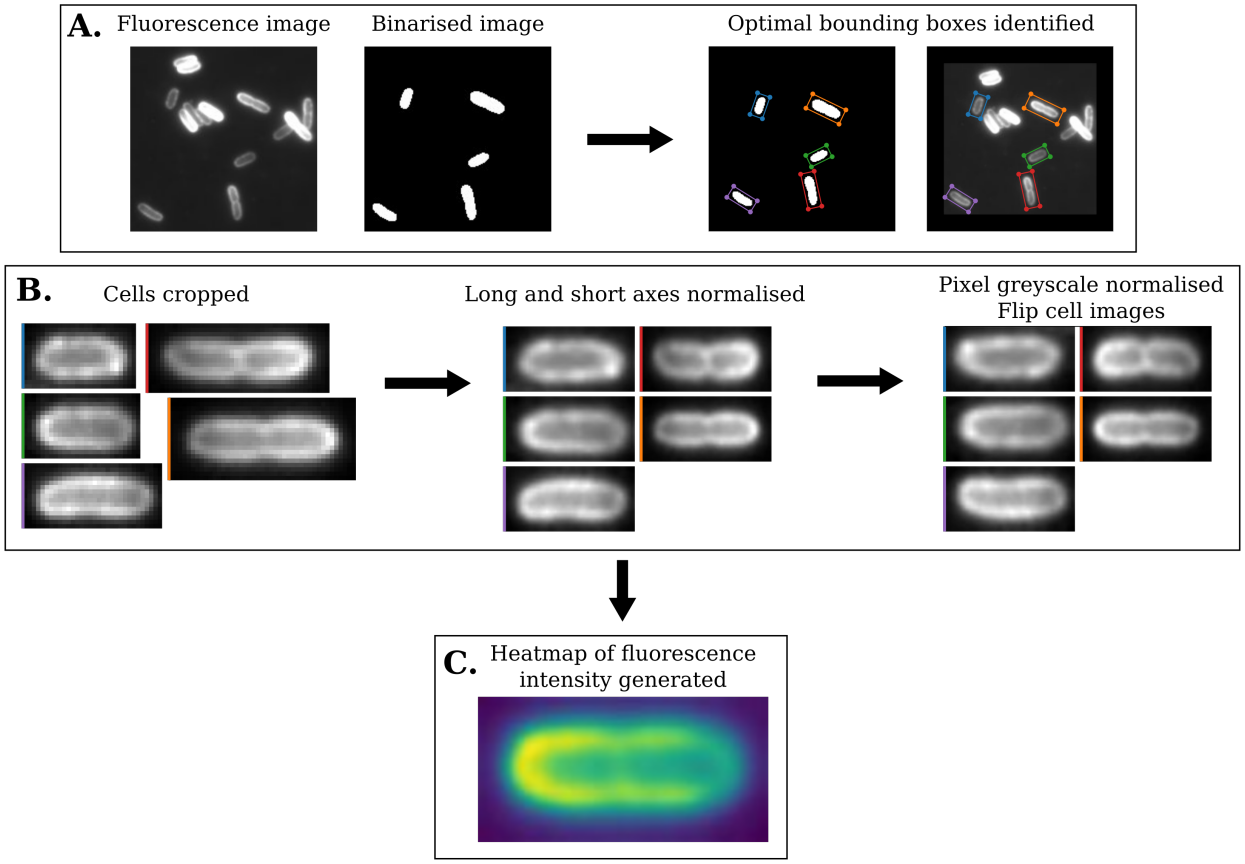

Figure 4.15: Schematic of the data processing required to generate fluorescence intensity heatmaps. **A.** Cell segmentation and bounding box fitting to segmented and fluorescence images. **B.** Cell cropping, axes normalisation, intensity normalisation and cell flipping. **C.** Fluorescence intensity heatmap generation.

4.2.3 Apparent OmpF Distributions are not Artefacts

In order to make robust conclusions based on the six categories of OmpF organisation observed, potential labelling artefacts must be investigated. In the case of Colicin N^{1-185}mCherry labelling of OmpF, two potential artefacts must be investigated.

1. TolA binding - Upon division, TolA is recruited to the divisome and hence TolA accumulates at the septum of dividing cells (Figure 4.16.A.). Colicin N^{1-185}mCherry contains an intact N-terminal translocation domain which contains a TolA binding site (residues: 44 - 66) (Figure 4.16.B.). There is a possibility that the accumulation of TolA at subcellular locations could therefore affect the apparent distribution of OmpF

in the OM.

2. Cell growth - The labelling protocol for OmpF involves incubating cells with 200 nM Colicin N^{1-185}mCherry for 10 minutes followed by a centrifugation step to remove excess label and then fixation in 4% formaldehyde at 4°C for 30 minutes. In the short time period between labelling and fixation of cells, new unlabelled OMPs can be inserted into the membrane, potentially upsetting the true organisation of OmpF (Figure 4.16.C.).

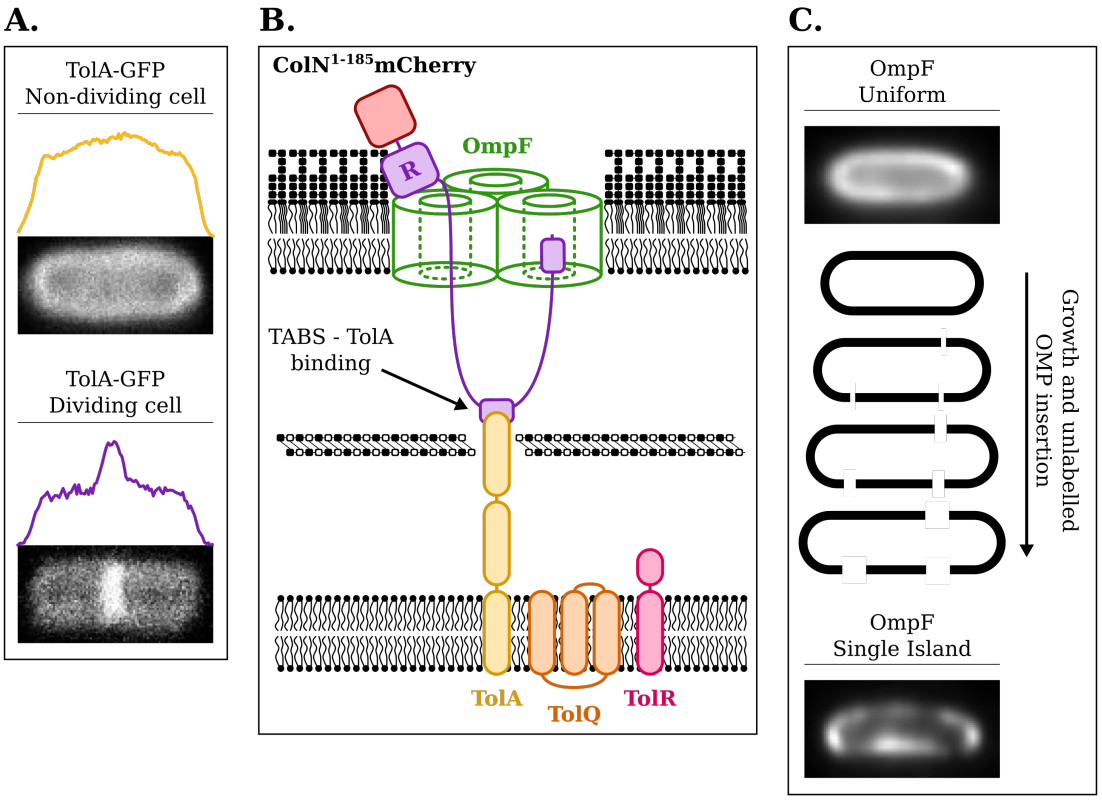

Figure 4.16: Potential artefacts of OmpF organisation imaging. A. Confocal microscopy images of TolA-GFP organisation in *E. coli* BL21(DE3). Fluorescence intensity profiles were measured over the long axis of a non-dividing and a dividing cell. **B.** Schematic of Colicin N^{1-185}mCherry binding to OmpF. The receptor binding domain binds to surface exposed OmpF. The translocation domain threads through the lumen of the OmpF barrel, presenting the TABS epitope which binds to TolA. The N terminal OBS binds within the lumen of an OmpF monomer. **C.** Schematic representing the possible growth artefact on OmpF organisation. Two Colicin N^{1-185}mCherry labelled *E. coli* MG1655 cells categorised as "Uniform" and "Mid-Cell Island" are shown to demonstrate the potential formation of OmpF non-uniform distribution categories through the insertion of unlabelled OMPs forming areas of reduced fluorescence intensity in the OM.

To investigate the effect of cell growth on apparent OmpF organisation, *E. coli* MG1655 cells were fixed in 4% formaldehyde at 4°C for 30 minutes *prior* to labelling with Colicin N^{1-185}mCherry. This ensured that cells could not grow post-labelling and thereby the fluorescence distribution observed was an accurate representation of OMP organisation in the OM at the time of fixation. In these cells, the six categories of OmpF organisation observed under normal labelling protocols (Figure 4.14) could be recapitulated (Figure 4.17).

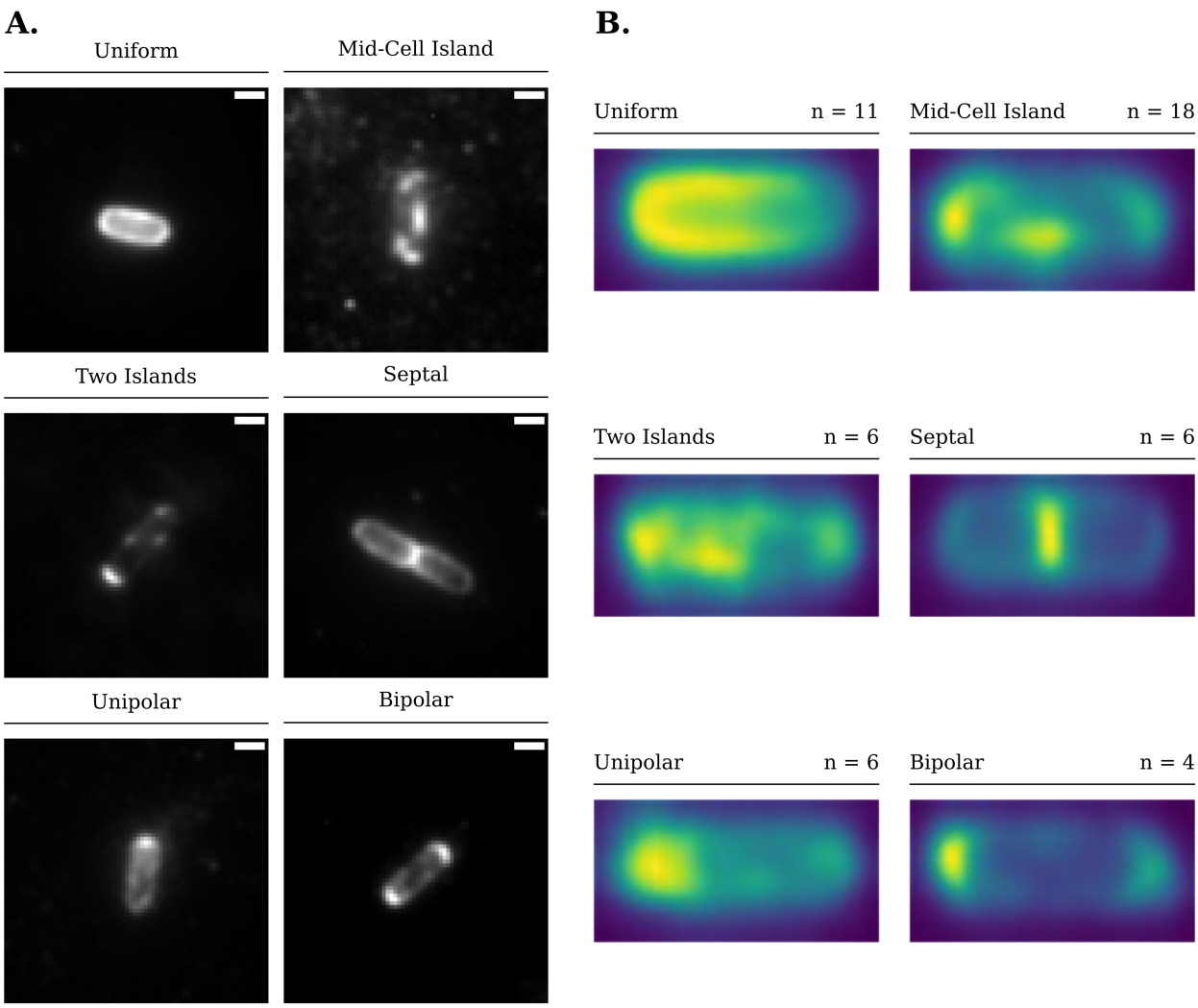

Figure 4.17: Heatmaps of OmpF distribution in *E. coli* MG1655 fixed prior to labelling. *E. coli* MG1655 was fixed with 4% formaldehyde and then labelled with Colicin N^{1-185}mCherry. **A.** Representative images of cells displaying each category of OmpF distribution. **B.** Heatmaps were generated as described in Figure 4.15. OmpF distributions were sorted into their respective categories manually.

The ability to recapitulate the six categories of OmpF distribution in pre-fixed cells strongly suggests that these six categories of distribution are not the result of short-term insertion of unlabelled OMPs into the OM of cells.

To investigate the effect of Colicin N^{1-185}mCherry interaction with TolA on apparent OmpF organisation, three labelling experiments were conducted.

E. coli BW25113, the Keio collection parent strain, was labelled and imaged in an iden-

tical manner to MG1655 (Figure 4.14). As expected, OmpF distributions could be sorted into the six categories of distribution (Figure 4.18)

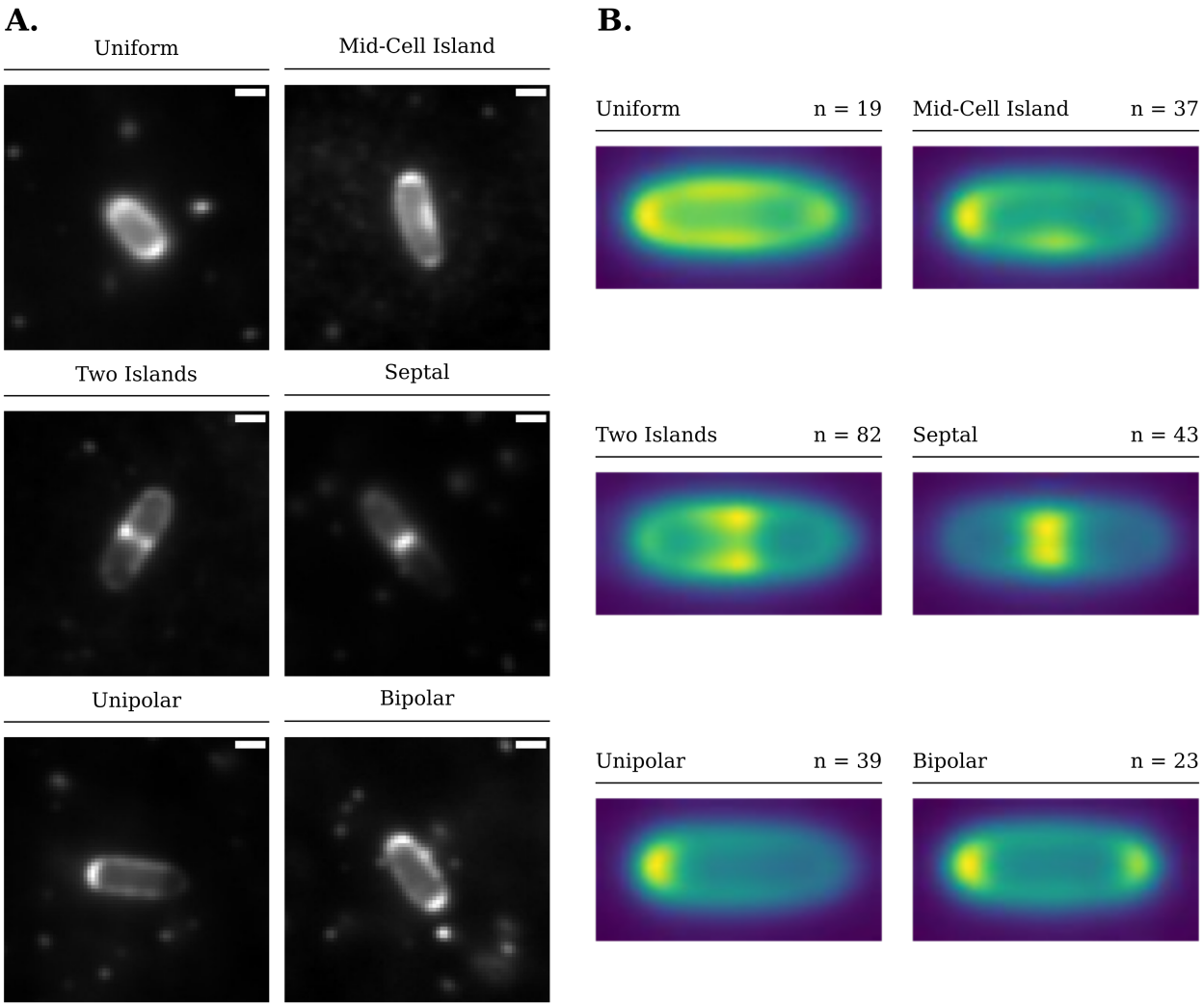

Figure 4.18: Heatmaps of OmpF distribution in *E. coli* BW25113. *E. coli* BW25113 was labelled with Colicin N^{1-185}mCherry. **A.** Representative images of cells displaying each category of OmpF distribution. **B.** Heatmaps were generated as described in Figure 4.15. OmpF distributions were sorted into their respective categories manually.

Investigations into Colicin N TolA interactions revealed that a mutation of tyrosine 62 within the translocation domain to alanine completely abolishes Colicin N binding to TolA [200]. A Colicin $N(Y62A)^{1-185}$mCherry construct was therefore designed, expressed and purified (Chapter 3). *E. coli* BW25113 cells labelled with this construct still displayed the same six categories of OmpF distribution (Figure 4.19) observed for Colicin N^{1-185}mCherry

labelled cells (Figure 4.18).

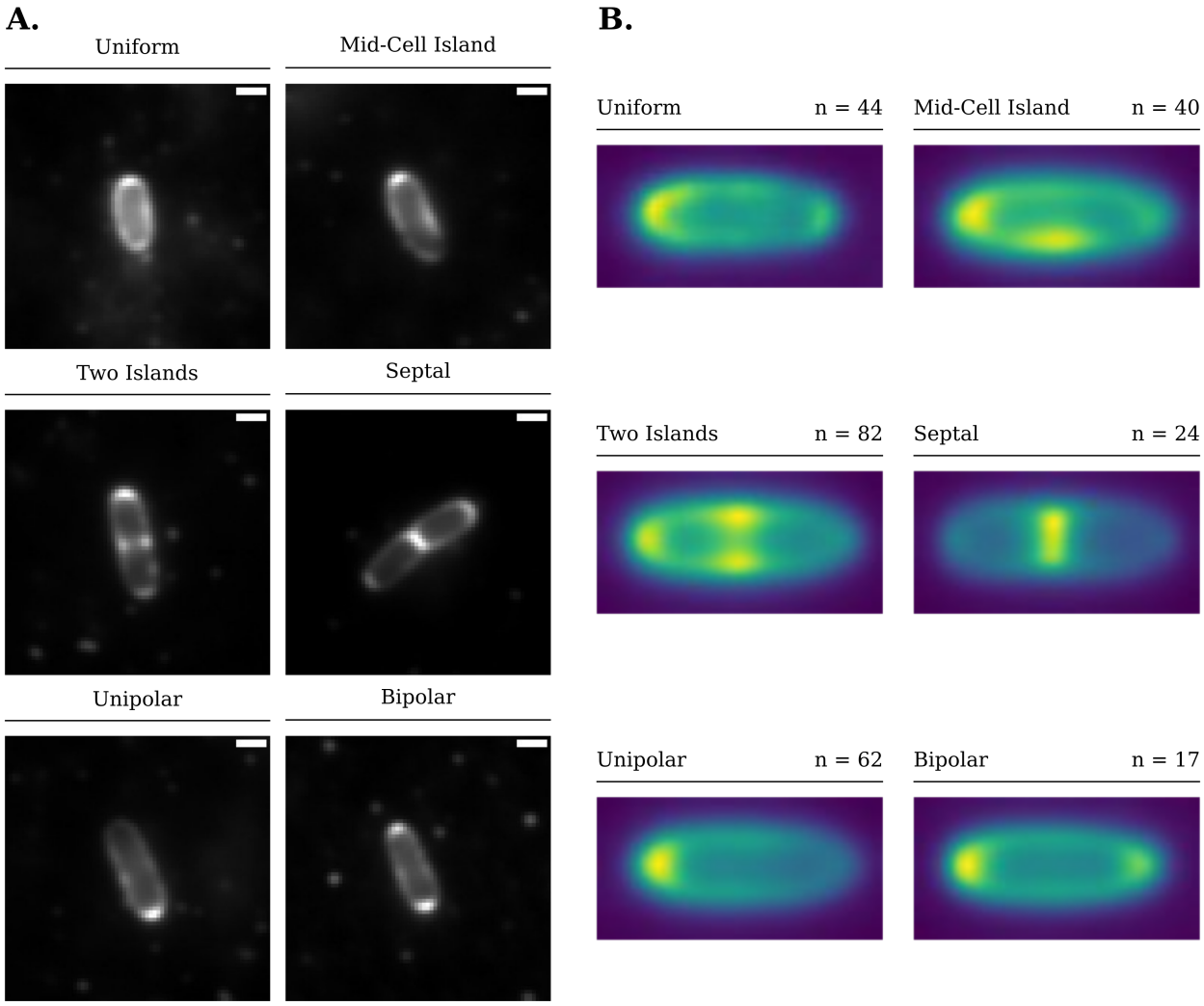

Figure 4.19: Heatmaps of OmpF distribution in *E. coli* BW25113 labelled with Colicin N(Y62A)$^{1-185}$mCherry. *E. coli* BW25113 was labelled with Colicin N(Y62A)$^{1-185}$mCherry. **A.** Representative images of cells displaying each category of OmpF distribution. **B.** Heatmaps were generated as described in Figure 4.15. OmpF distributions were sorted into their respective categories manually.

To further reinforce this observation, the Keio collection TolA knockout strain (JW0729-3) was labelled with Colicin N$^{1-185}$mCherry. Again, upon eliminating TolA binding, the six categories of OmpF distribution were still observed (Figure 4.20).

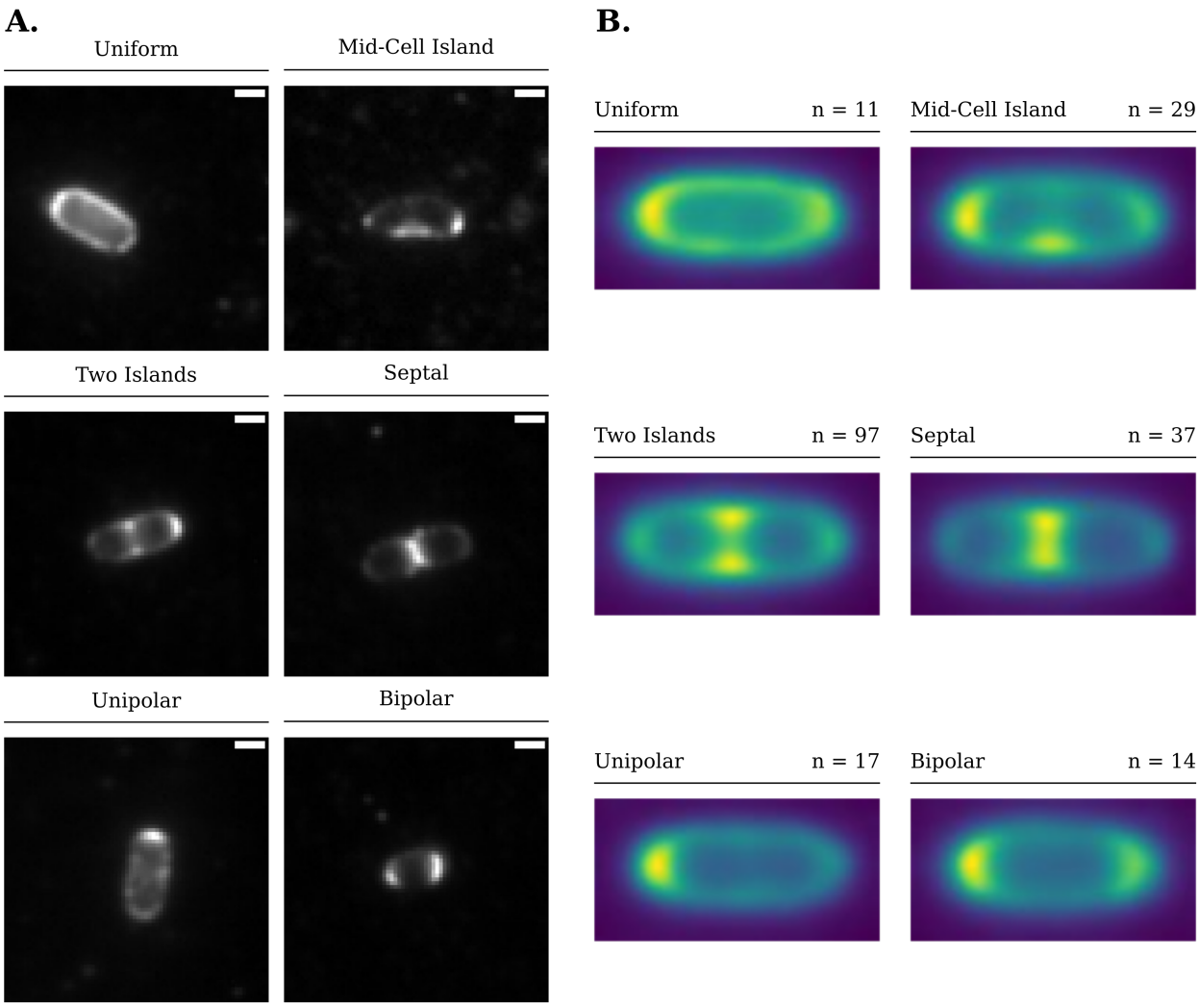

Figure 4.20: Heatmaps of OmpF distribution in *E. coli* JW0729-3 labelled with Colicin N^{1-185}mCherry. *E. coli* JW0729-3 ($\Delta tolA$) was labelled with Colicin N^{1-185}mCherry. **A.** Representative images of cells displaying each category of OmpF distribution. **B.** Heatmaps were generated as described in Figure 4.15. OmpF distributions were sorted into their respective categories manually.

It can therefore be concluded that time between labelling and fixing is not great enough to introduce OmpF distribution artefacts and that Colicin N - TolA interactions do not affect apparent OmpF distribution. The distribution of OmpF observed both in *E. coli* MG1655 and BW25113 is therefore an accurate representation of OmpF distribution in the cell.

4.2.4 OmpF Organisation is Linked to The Cell Cycle

Of the six categories of OmpF organisation, the septal distribution indicated that OmpF organisation could be linked to the *E. coli* cell cycle. When the other distributions are viewed in this context, the link to cell cycle becomes more evident: The "Mid-Cell Island" distribution could represent asymmetric invagination of the membrane during cell division, the "Two Islands" distribution could represent symmetric invagination of the outer membrane and the "Unipolar" distribution could represent daughter cells immediately after septation.

To investigate the link between cell cycle and OmpF organisation a kymograph program was written which can process high-throughput widefield microscopy datasets. This program identifies cells and can measure the fluorescence intensity profile along the long axis of these cells. By recording the long axis length of each cell, fluorescence intensity profiles can be sorted according to cell length. By doing so, the change in fluorescence distribution can be measured as a function of stage in cell cycle. With newly formed cells being shortest and septating cells being longest.

A kymograph of OmpF distribution in *E. coli* MG1655 was generated (Figure 4.21). Cells ranged from a length of 1.64 to 5.14 µm. Shorter cells displayed strong fluorescence intensity at a single pole. As cell length increased the emergence of mid-cell fluorescence intensity could be observed. At the end of the length scales, mid-cell fluorescence intensity increased dramatically and unipolar fluorescence intensity diminished (Figure 4.21).

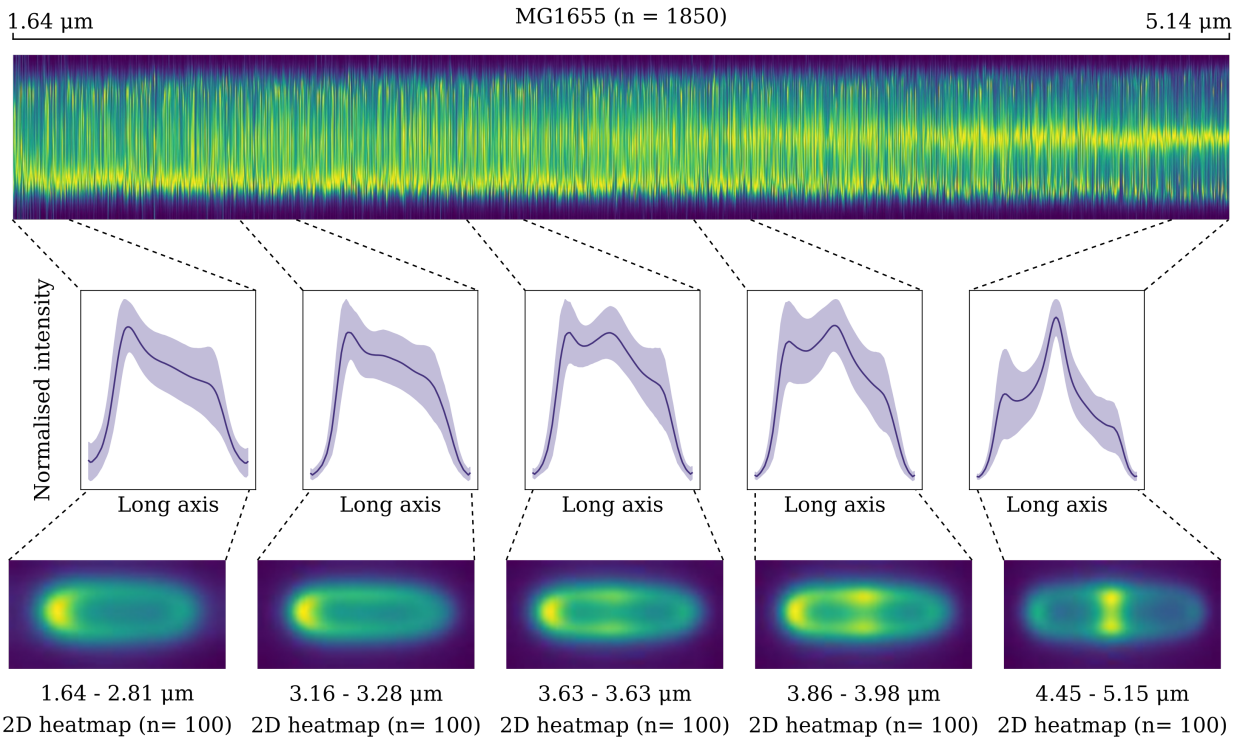

Figure 4.21: Kymograph of OmpF distribution in *E. coli* MG1655 as a function of cell length. Top: Kymograph wherein each vertical line of pixels represents the fluorescence intensity profile along the long axis of a single cell. Cells are sorted by long axis length. 1850 cells were used to construct the kymograph from lengths ranging between 1.64 to 5.14 µm. Centre: Average 1D long axes fluorescence intensity profiles along from 100 cell kymograph slices. Dark purple line: mean intensity profile, light purple envelope: ± standard deviation. Bottom: Average 2D fluorescence profiles from 100 cell kymograph slices, with length ranges denoted.

When 2D fluorescence intensity profiles are extracted from the regions of the kymograph, many of the six categories of OmpF distribution can be recapitulated. Shorter cells fit into the unipolar distribution category. As cells elongate and the septum begins to form the "Two Island" distribution can be observed, notably of these two islands one is of greater intensity than the other likely due to some of the individual cells making up these 2D profiles only containing one mid-cell island. 2D average intensity profiles of the longest cells recapitulate the septal distribution category.

The presence of unipolar distribution in short cells is logically consistent with the kymograph data. A dividing cell forms a septum in which OmpF appears to be enriched resulting

in increased septal fluorescence intensity. Upon division this septum will form the new poles of the two daughter cells, which will therefore be enriched in OmpF resulting in short cells with fluorescence intensity concentrated at a single pole.

When OmpF distribution in the *E. coli* strain BE3000 ($\Delta ompC$) is measured, the inconsistent nature of OmpF distribution can be observed. In this strain OmpF organisation is notably more uniform (Figure 4.22) than that observed for *E. coli* MG1655 (Figure 4.21). However, despite the more uniform nature, septal accumulation of OmpF is clearly visible as cells elongate and septate (Figure 4.22).

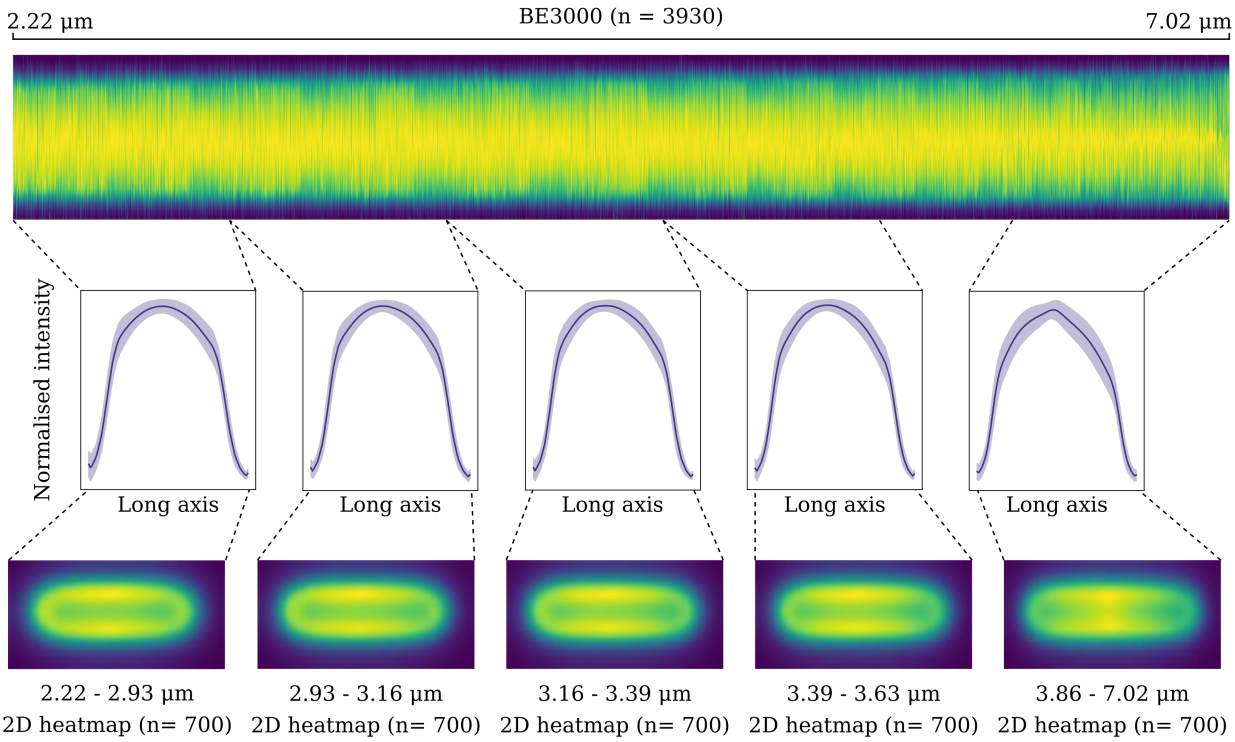

Figure 4.22: Kymograph of OmpF distribution in *E. coli* BE3000 as a function of cell length. Top: Kymograph wherein each vertical line of pixels represents the fluorescence intensity profile along the long axis of a single cell. Cells are sorted by long axis length. 1850 cells were used to construct the kymograph from lengths ranging between 1.64 to 5.14 µm. Centre: Average 1D long axes fluorescence intensity profiles along from 100 cell kymograph slices. Dark purple line: mean intensity profile, light purple envelope: ± standard deviation. Bottom: Average 2D fluorescence profiles from 100 cell kymograph slices, with length ranges denoted.

Widefield microscopy investigations into OmpF organisation have provided a means to

conduct high throughput imaging to gather statistically robust data and has been used to reveal how patterns of OmpF distribution of a large number of cells changes over the cell cycle.

The use of kymographs represents a more robust method of analysis of OmpF distribution compared to the categorisation of OmpF distributions used in section 4.2.3. The OmpF categorisation method relied on the manual sorting of OmpF distributions into arbitrary but repeatedly observed categories. As such, an element of human error was introduced at the sorting stage as there is a level of subjectivity as to what category a particular distribution can be sorted into. If the categorisation method is to be used in future experiments, an algorithm to sort protein distributions should be developed. Machine learning in particular might be appropriate for such an image classification task. The kymograph program used in this section is a more appropriate method to look at the change in OmpF distribution and clearly shows that rather than OmpF distribution falling into a small number of discrete categories, is more likely to change in a continuous manner as a function of the progression through the cell cycle.

It is clear through the generation of kymographs that the 6 categories of OmpF distribution observed are in fact a reflection of the change of OmpF distribution as a function of the cell cycle. Hence, this implies that there are not in fact 6 distributions but a continuous

However, the most significant limitation of these widefield microscopy investigations are revealed in the images of the cells captured. That is, their low resolution. The microscope used to capture the images of OmpF organisation presented in the chapter has a 100x objective with a numerical aperture of 1.49 and the maximum emission wavelength of mCherry used to visualise OmpF organisation, is 610 nm. Using the diffraction limit equation (Equation 4.3), a maximum resolution of 204.7 nm can be determined. Meaning that if two fluorophores come within 204.7 nm of one another they cannot be resolved.

As many of the features of an *E. coli* cell exist on length scales far bellow this diffraction limit, alternative imaging techniques that can overcome the diffraction limit must be used.

As Colicin N^{1-185}mCherry proved to be an effective OmpF label, photoactivated localisation microscopy (PALM) was selected as an appropriate superresolution technique as mCherry in this construct could be replaced by photoactivatable mCherry (PAmCherry).

Therefore, to investigate OmpF distribution at greater resolution, a Colicin N^{1-185}PAmCherry construct was designed, expressed and purified (Chapter 3). *E. coli* BE3000 cells were labelled with Colicin N^{1-185}PAmCherry and fixed to prevent growth over the timecourse of PALM acquisition. Coverslips were cleaned with KOH to reduce noise to a level appropriate for PALM imaging. To capture PALM datasets, cells were imaged over the course of between 10,000 and 20,000 frames at an exposure time of 50 ms. For each frame a sparse set of non-overlapping fluorophores were activated using a 405 nm laser line at 0.1 mW, which was manually pulsed on and off throughout the course of the experiment. Activated fluorophores were imaged and subsequently bleached with a 561 nm laser line at 20 mW which was on throughout the course of the experiment. To fluorophores within each frame 2D Gaussian functions were fitted thereby localising the position of each fluorophore with high precision.

Due to the relatively high density of the data collected, cross correlation drift correction (10x magnification and 20 bins) could be applied to correct for lateral drift.

Superresolution and diffraction limited reconstructions of OmpF distributions were generated from PALM datasets (Figure 4.23). In these PALM datasets, like the widefield microscopy datasets, distributions of OmpF could be sorted into the six categories of distribution. With the improved resolution provided by PALM imaging, features of the cells which could not be observed previously were revealed. Notably, outer membrane invagination is clearly observed both in the "Two Island" and Septal distributions, further confirming their link to the cell cycle.

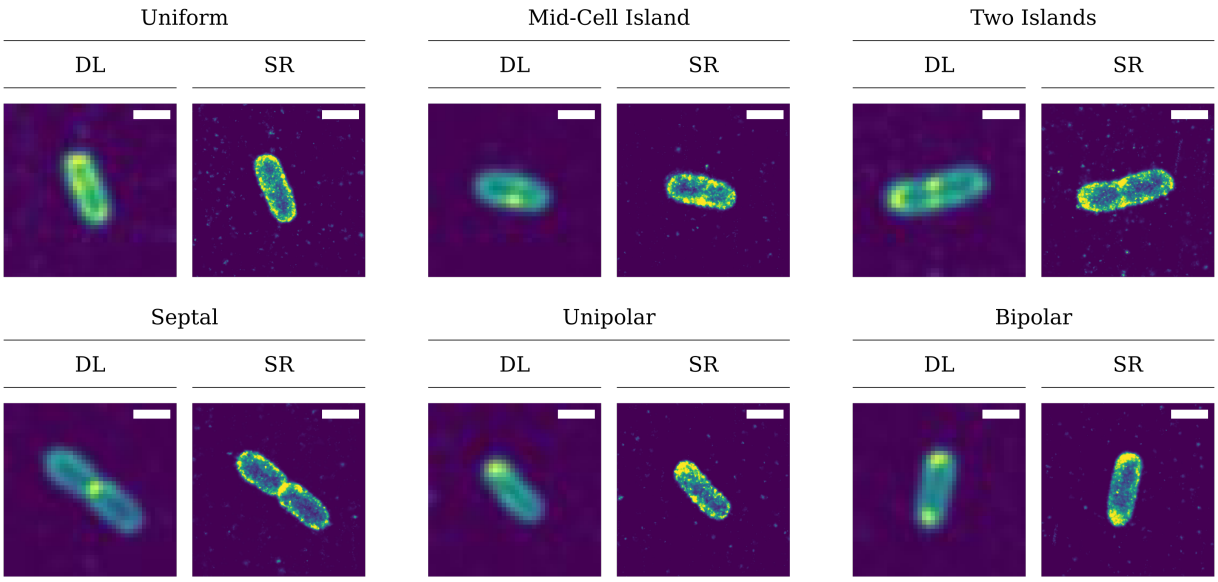

Figure 4.23: The six categories of OmpF distributions in *E. coli* BE3000 imaged by epifluorescence PALM. PALM datasets were processed with the imageJ plugin ThunderSTORM, to localise fluorophores by 2D Gaussian fitting. Superresolution reconstructions (SR) are represented at a resolution 40 times that of the native sensor resolution. Diffraction limited reconstructions (DL) are represented at the native sensor resolution with a Gaussian filter ($\sigma = 1$ pixel) applied. Scale bars represent a distance of 1 µm.

4.2.5 Uniform OmpF Distributions Display Clustering on Short Distance Scales.

When the six categories of OmpF distribution are observed, all but one diverge significantly from simulated CSR OmpF data. Experimental images of "uniform" OmpF distributions are in good agreement with simulated CSR data. Therefore, a qualitative assessment of the data would suggest that OmpF is distributed in a completely spatially random manner in these cells. Qualitative analysis of uniform OmpF organisation after imaging in PALM also supports this conclusion (Figure 4.24).

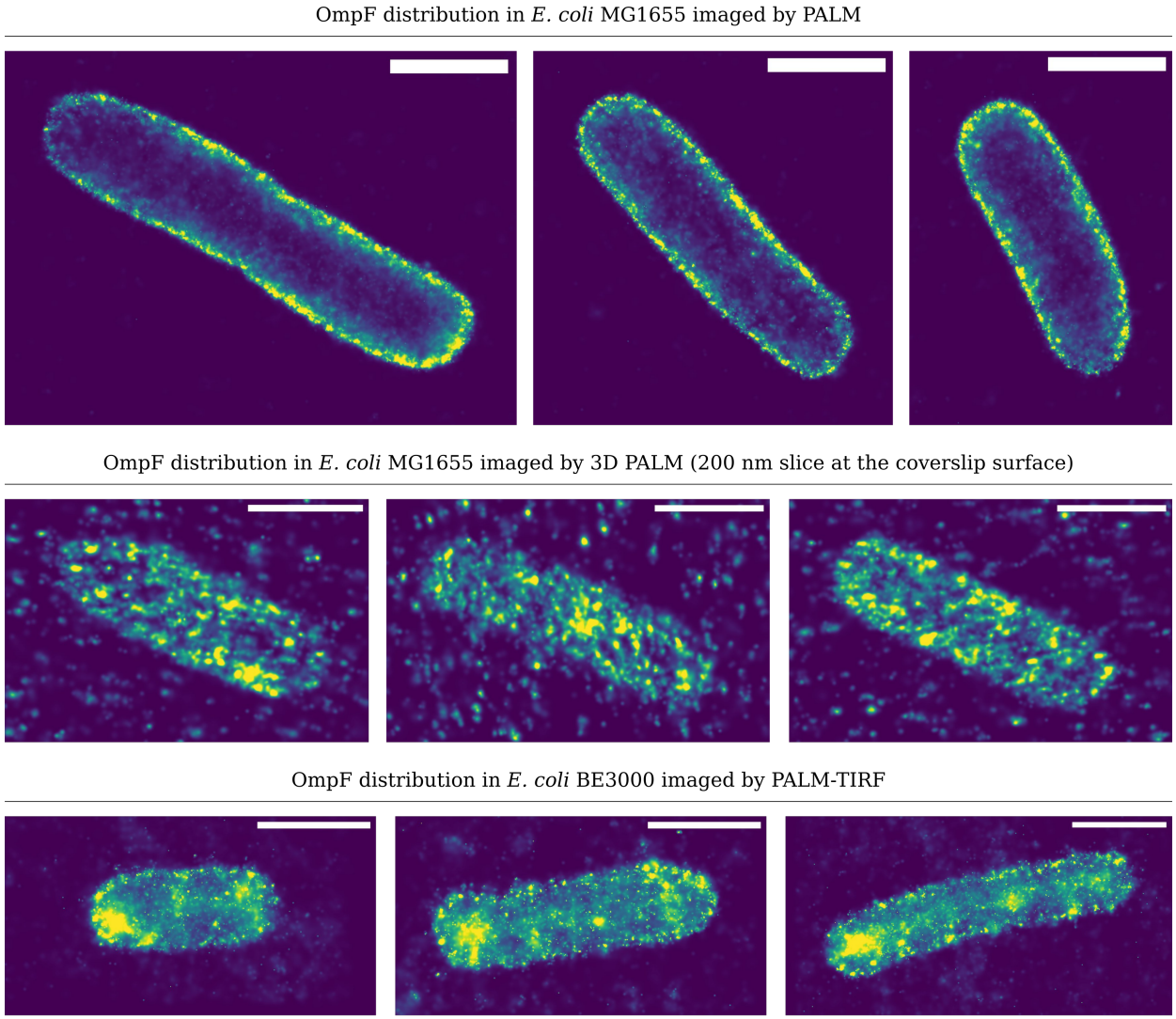

Figure 4.24: OmpF organisation in *E. coli* imaged by various PALM techniques. Superresolution reconstructions were generated from PALM datasets 30,000 frames in length and are represented at a resolution 40 times that of the native sensor resolution. Samples were loaded onto slides containing a sparse field of fluorescent beads which were used as fiducial markers for drift correction. **Top:** OmpF organisation in *E. coli* MG1655 imaged by epifluorescence PALM. **Middle:** OmpF organisation in *E. coli* MG1655 imaged by 3D PALM (using an astigmatic lens element). 200 nm slices of localisations at the coverslip surface are presented. The clustering of this data is quantified in Figure 4.29. **Bottom:** OmpF organisation in *E. coli* BE3000 imaged by PALM-TIRF. The clustering of this data is quantified in Figure 4.28. Scale bars represent a distance of 1 µm.

However, it should be noted that diffraction limited observations into BtuB and FepA organisation in combination with simulations revealed that qualitative analysis without sufficient controls cannot accurately assess the distribution of proteins in the outer membrane.

For this reason, the organisation of OmpF proteins in the "Uniform" category was investigated quantitatively.

Spatial summary statistics represent a family of methods that can be used to quantitatively interrogate the organisation of points in 2D space. PALM datasets are amenable to assessment by such summary statistics as, at their most fundamental, are simply a series of points represented by xy coordinates.

Ripley's K function is a spatial summary statistic that can determine if point data is clustered, spatially random or regularly spaced (Figure 4.25.A.). For a field of xy coordinates, the number of points within a radius expanding from a single point are counted (Figure 4.25.B.). This is conducted for each point in the dataset. The Ripley's K function of the dataset is then compared to a Poisson process representing CSR distribution to determine the spatial pattern of the data at multiple distance scales. Ripley's K function is defined by:

$$K(r) = \frac{1}{n} \sum_{i=1}^{n} N_{p_i}(r)/\lambda \tag{4.5}$$

Where n equals the number of points, $N_{p_i}(r)$ is the number of points within the ith point within radius r. λ is used to normalise by density [215].

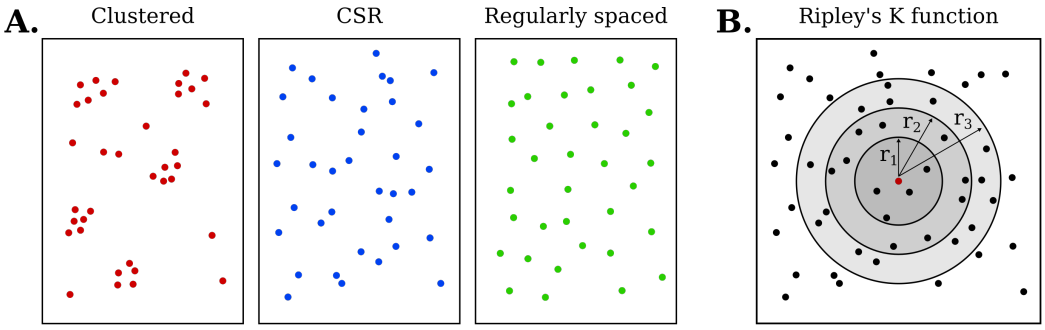

Figure 4.25: Schematic representation of spatial point patterns and Ripley's K function. A. Clustered (red), CSR: completely spatially random (blue) and regularly spaced (green) spatial point patterns. **B.** Diagrammatic representation of Ripley's K function. The number of neighbouring points from a single point are counted within areas of increasing radii, repeated for each point in the data.

Before spatial statistics can be conducted on OmpF PALM data (PALM was conducted as described in 2.10.5), a number of pre-processing steps must be conducted. The most critical of which is the removal of compounded molecule localisations. If a theoretically ideal PALM dataset could be collected a sparse set of single molecules would be activated, imaged and bleached in a single frame before the next frame was collected. In reality, single molecules will often remain in a fluorescing state for multiple frames after activation. Therefore, each PALM localisation cannot be assumed to represent a single OmpF protein in the OM. Assuming a 1 to 1 relation between localisations and OmpF protein locations could lead to artificial clustering of the data. As PALM imaging is conducted in fixed cells, OmpF will be immobile in the OM, if a single labelled OmpF fluoresces for multiple frames, these consecutive localisations will display little appreciable lateral movement, if each localisation were counted as an OmpF location a false cluster of OmpF would be generated.

To remove compounded localisations from OmpF PALM datasets a rudimentary single particle tracking program was developed (Figure 4.26). A square window of dimensions 50 x 50 nm is scanned over the localisations in the order in which they were collected (Figure 4.26.B.). If only one localisation is present in the 50 x 50 nm region, the window moves to the next localisation. If the window encounters a region in which multiple localisations are present (Figure 4.26.C.), the frame number in which each localisation within the window appears is extracted (Figure 4.26.D.i.). Frame numbers are checked to identify localisations that appear in consecutive frames. These consecutive localisations are grouped together as representing a single OmpF protein (Figure 4.26.D.ii.). Consecutive localisations are then treated as single particle tracks and the centroid of these tracks is taken as the position of the OmpF protein they represent (Figure 4.26.E.). This process is repeated for all localisations in the dataset, the resultant xy coordinates therefore represent locations of OmpF proteins in the OM.

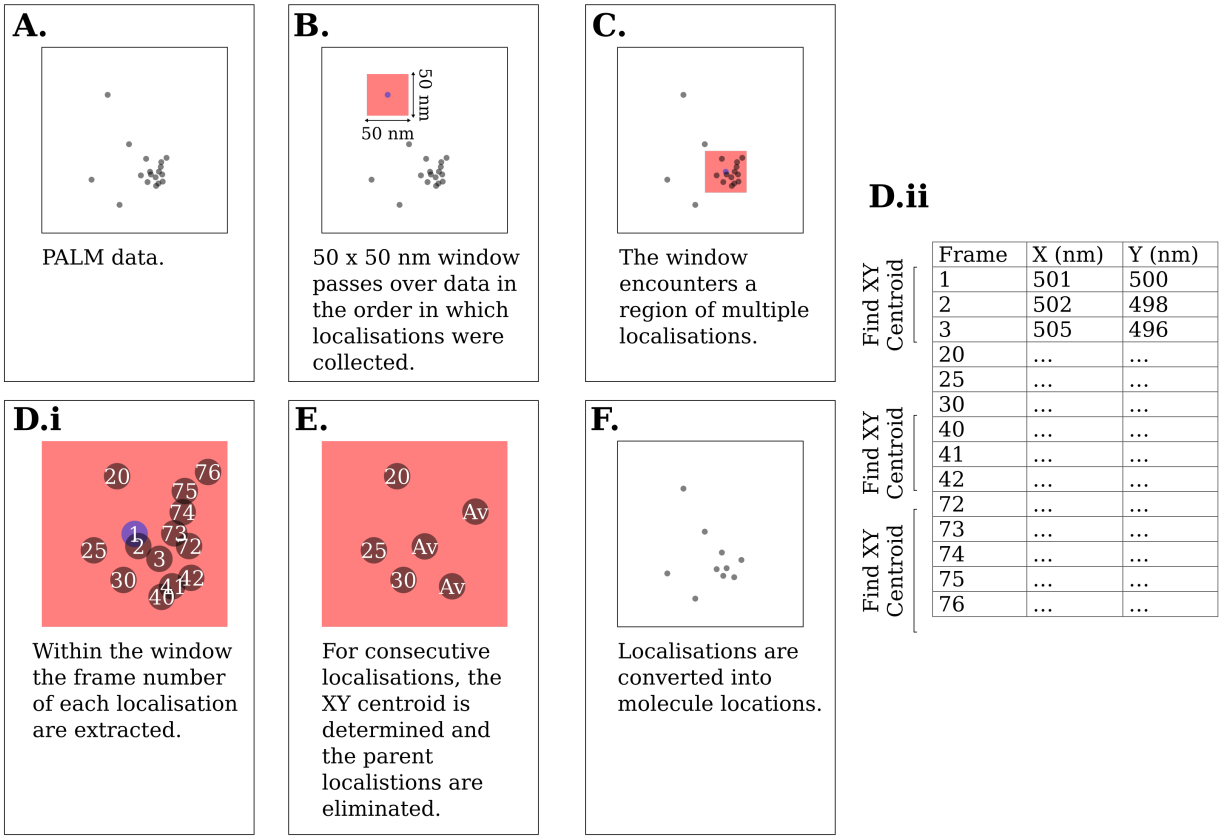

Figure 4.26: Schematic representing the removal of OmpF compounded localisations. Points in this example dataset are fabricated and not to scale.

In addition to the removal of compounded localisations during data post-processing, the selection of certain PALM acquisition parameters can reduce the possibility of artefacts being introduced. By manually pulsing the 405 nm activation laser on and off whilst monitoring the number of localisations in real-time, care was taken to ensure that a sparse non-overlapping field of fluorophores were being captured at any one moment. This hence reduces the number of single particle tracking errors that would otherwise be introduced when imaging a dense field of fluorophores.

A number of further processing steps must be conducted before spatial statistics can be carried out on the data (Figure 4.27). After removing compounded localisations (Figure 4.27.A. to Figure 4.27.B.) The cell is extracted from background noise with the use of DBSCAN in which the parameters for EPS and the minimum number of samples is manually

selected to achieve the best cell segmentation (Figure 4.27.C.). The background localisations are discarded and a convex hull is drawn around the OmpF localisations of the cell through the use of the Graham scan algorithm (Figure 4.27.D.). The OmpF localisations are transformed such that the centroid of the convex hull lays at the origin ([0,0]). The major axis length and rotation of the convex hull polygon is determined (Figure 4.27.E). The rotation of the localisations are then normalised (Figure 4.27.F). Spatial statistics can then be conducted. A rectangle is manually drawn within the bounds of the cell and the point pattern is analysed by Ripley's K function. It is important to note that all of the pre-processing steps preserve the distances between OmpF molecules and do not introduce distortions.

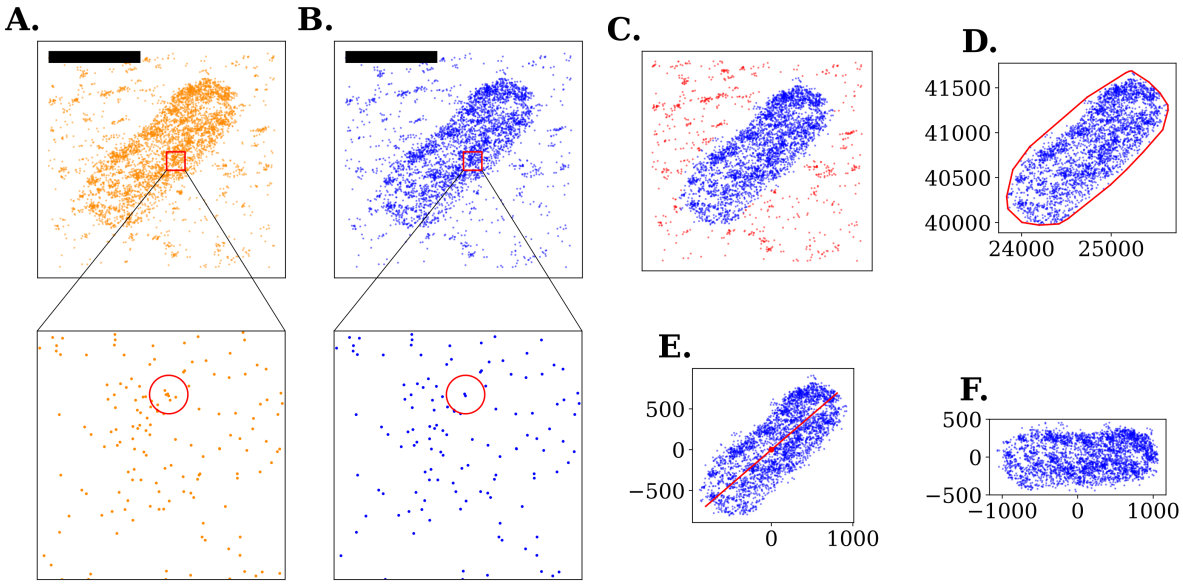

Figure 4.27: Preprocessing steps conducted before analysis by spatial statistics. Dataset presented from PALM imaging of OmpF in *E. coli* MG1655. **A.** Raw localisation data is imported. **B.** Compounded localisations are removed using rudimentary single particle tracking program. **C.** DBSCAN is used to extract OmpF localisations from background. **D.** Graham scan is conducted to generate a convex hull. **E.** OmpF localisations are normalised to 0 and the major axis length and rotation of the convex hull polygon is determined. **F.** localisations rotated.

Three spatial summary statistics were carried out on processed data: Ripley's K function

(Equation 4.5), Ripley's L function: a form of the Ripley's K function linearised using:

$$L(r) = \sqrt{\frac{K(r)}{\pi}} \tag{4.6}$$

and Ripley's H function, a form of the Ripley's K function, in which the a Poisson distribution of points is normalised to 0 using:

$$H(r) = \sqrt{\frac{K(r)}{\pi - r}} \tag{4.7}$$

For each spatial summary statistic conducted on the experimental datasets, 9,999 simulations of 2D CSR data were conducted.

PALM-TIRF data of OmpF organisation in *E. coli* BE3000 was collected and analysed using Ripley's K, L and H functions (Figure 4.28). TIRF illumination was used in order to collect PALM data from a single surface of the cell, thereby approximating a flat 2D surface.

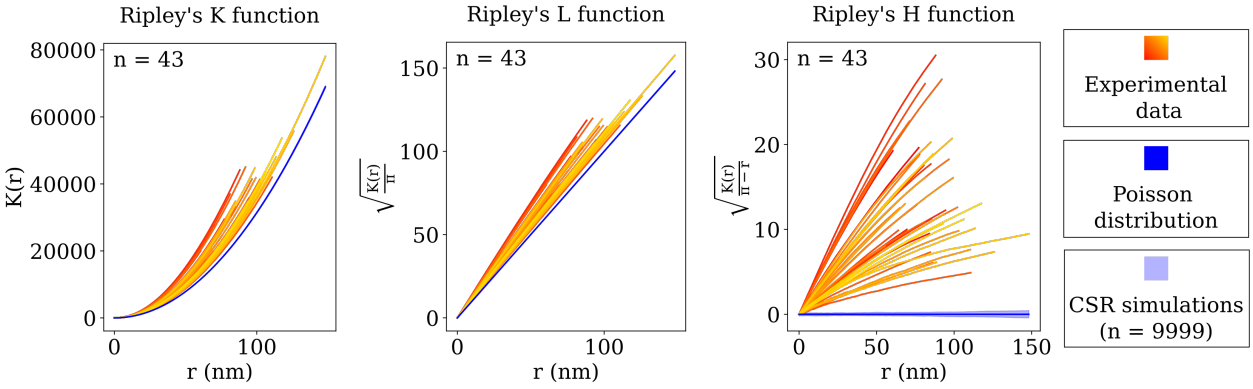

Figure 4.28: Spatial summary statistics of OmpF point patterns in *E. coli* BE3000. PALM-TIRF imaging was conducted for over 20,000 frames at an exposure time of 100 ms with a 0.1 mW 405 nm activation laser and a 20 mW 561 nm excitation laser, illuminating at an angle of 54°. Ripley's K, L and H functions were applied to processed experimental data (orange traces). A Poisson process representing 2D complete spatial randomness was plotted (solid blue line). Simulations of 9,999 2D CSR datasets defined the upper and lower bounds of the CSR envelope (light blue). Escape of experimental data traces from the CSR envelope in a positive direction indicate statistically significant clustering and escape in a negative direction indicates statistically significant regular spacing.

Experimental data curves diverge significantly, in a positive direction, from the Poisson

process for a 2D CSR point pattern. Notably, all experimental data curves escape the envelope defined by simulations of 9,999 2D CSR datasets in a positive direction. This indicates that OmpF in the OM of *E. coli* BE3000 is highly clustered and this clustering is seen over a large range of distances.

PALM data of OmpF in *E. coli* MG1655 was collected in order to investigate the point patterns of OmpF distribution at both lower densities and in a strain that also expresses the OmpF homologue: OmpC. For this dataset, PALM was conducted with an astigmatic lens element thereby allowing the z position of localisations to be encoded.

Fluorophores imaged with a standard spherical lens element will yield circular PSFs on the sensor, even if these fluorophores move out of the plane of focus, their PSF will remain circular. If imaged with an astigmatic lens element, fluorophores in the plane of focus will yield circular PSFs, however if moving out of the plane of focus will form elliptical PSFs. The shape of which can encode the Z position of the fluorophore.

In addition to the 3D PALM data collected for OmpF in *E. coli* MG1655, a calibration dataset of fluorescent beads at multiple known z positions was collected to allow for accurate calibration of the experimental data.

Localisations within a 200 nm slice of the surface of each cell were processed and analysed (Figure 4.29).

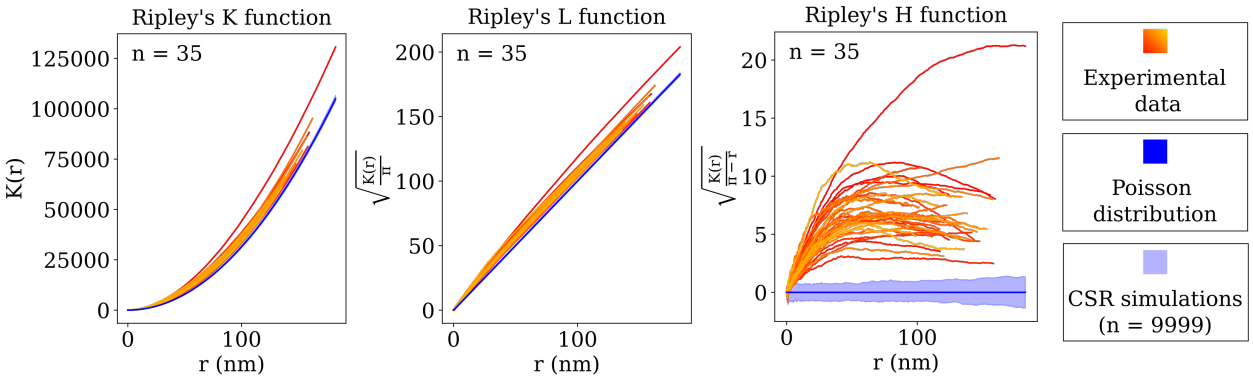

Figure 4.29: Spatial summary statistics of OmpF point patterns in *E. coli* MG1655. 3D PALM imaging was conducted for over 20,000 frames at an exposure time of 100 ms with a 0.1 mW 405 nm activation laser and a 20 mW 561 nm excitation laser. Ripley's K, L and H functions were applied to 200 nm surface slices of processed experimental data (orange traces). A Poisson process representing 2D complete spatial randomness was plotted (solid blue line). Simulations of 9,999 2D CSR datasets defined the upper and lower bounds of the CSR envelope (light blue). Escape of experimental data traces from the CSR envelope in a positive direction indicate statistically significant clustering and escape in a negative direction indicates statistically significant regular spacing.

All experimental traces escaped envelopes of 2D CSR simulations in a positive direction. This revealed that at lower densities, significant clustering is observed for all cells over a large range of distances.

Spatial summary statistics, such as Ripley's K, L and H functions were designed for use on 2D datasets. By imaging in TIRF-PALM and taking 200 nm surface slices in 3D PALM, a 2D surface is approximated. Being only an approximation, in actuality this surface has a significant degree of curvature. This can be visualised using the CSR surface protein distribution simulation program (Figure 4.30), side views of the cell reveal curvature in 200 nm surface slices. As, in the case of PALM experiments, this 3D curved surface is projected onto a 2D sensor there is a possibility of introducing artificial clustering artefacts. Localisation towards the edge of the point pattern will be bunched closer together compared to those in the centre of the point pattern.

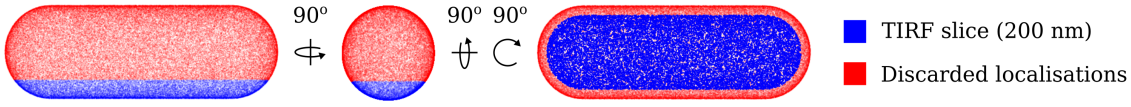

Figure 4.30: Simulation of CSR TIRF PALM datasets. Side view: left, top view: centre, and bottom view: right of 80,000 simulated CSR points on the surface of a bacterium. Blue: points lying within a 200 nm surface slice. Red: points lying outside the 200 nm surface slice which are discarded before analysis by spatial summary statistics. Escape of experimental data traces from the CSR envelope in a positive direction indicate statistically significant clustering and escape in a negative direction indicates statistically significant regular spacing.

To investigate the effect of membrane curvature on clustering, 50 CSR TIRF-PALM datasets were simulated at OmpF copy numbers (80,000 per cell) and analysed by Ripley's K, L and H function (Figure 4.31).

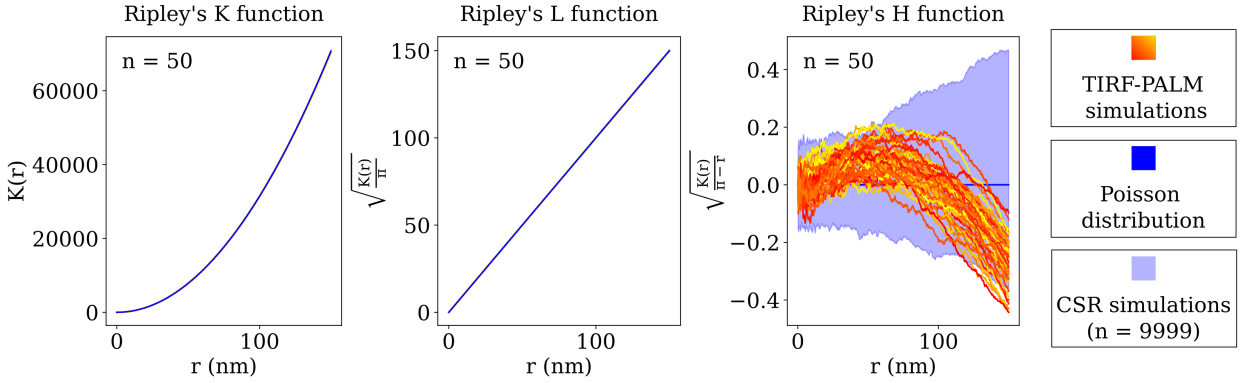

Figure 4.31: Spatial summary statistics of simulated PALM-TIRF CSR point patterns. CSR PALM datasets were simulated at total copy numbers of 80,000 per cell and 200 nm slices of localisations on the surface of 50 cells were analysed. The spatial summary statistics Ripley's K, L and H functions were used. A Poisson process representing 2D complete spatial randomness was plotted (solid blue line). Simulations of 9,999 2D CSR datasets defined the upper and lower bounds of the CSR envelope (light blue).

Simulated TIRF-PALM traces diverge from the Poisson process for CSR distribution, initially rising above an $H(r)$ of zero and then falling below an $H(r)$ of 0 at greater distances of r. This indicates, as expected, that curvature of the membrane is inducing a change in the CSR point pattern. However, only two traces escape the 2D CSR envelope in a positive direction and do so at a relatively small $H(r)$ of 0.2. This indicates that, though membrane curvature contributes to a subtly different point pattern, it is not the cause of

OmpF clustering observed in BE3000 and MG1655. Therefore, we can be confident that OmpF clustering in these two strains is not a result of artefacts induced by membrane curvature.

It is worth noting that phenomena other than membrane curvature could be a significant cause of artificial clustering. Fluorescent proteins such as PAmCherry are known to undergo blinking events that could lead to over-counting [216]. Importantly, the program developed to remove compounded localisations described in Figure 4.26 does not perform gap-fitting. Hence if a PAmCherry molecule fluoresces for multiple frames, blinks into an "off" state and then returns to a fluorescing state, this single PAmCherry molecule would be counted as two. As blinking is a physical property of PAmCherry, in future experiments this blinking must be mitigated using computational methods. A number of methods have been developed to account for blinking, including scanning PALM datasets for "temporal clusters" [217], or by modelling the blinking fluorophore blinking as a continuous time Markov process, successfully implemented on dSTORM datasets [218].

4.3 Conclusions

OmpF, unlike low copy number OMPs, did not display punctate distributions in the outer membrane and was quantitatively more uniform than both BtuB and FepA. Notably, the distribution of low copy number OMPs: BtuB and FepA were in good qualitative agreement with simulations of CSR surface protein distribution at equivalent copy numbers. On average, 20 BtuB's and 34 FepA's constituted their respective puncta in the outer membrane. However, by comparing this to CSR simulations, the number of proteins making up these puncta were likely underestimated. Nevertheless, comparisons with CSR simulation data showed that the observation of puncta in experimental diffraction limited imaging of surface protein distributions is not sufficient, in itself, to conclude that such proteins were clustered into islands.

A further diffraction limited microscopy experiment could definitively answer whether BtuB and FepA puncta formation is an imaging artefact. If BtuB and FepA were co-labelled and imaged, co-localisation of these two proteins would support the hypothesis that these proteins are organised into protein rich islands, however lack of co-localisation would support the hypothesis that the puncta observed for these proteins is an artefact of diffraction limited imaging.

In addition to the uniform OmpF distribution often seen in cells, five other distinct distributions were reliably observed. These distributions were not the result of either cell growth or TolA binding by Colicin N^{1-185}mCherry. High throughput imaging enabled the generation of *E. coli* kymographs sorted by cell length, this revealed that the six distributions of OmpF were associated with stages in the *E. coli* cell cycle. Qualitative analysis of PALM images supported this cell cycle linkage.

Finally, spatial summary statistics of apparently uniform OmpF surface distribution indicated strong clustering at high and low OmpF densities which were not the result of membrane curvature artefacts, but are likely to be artificially inflated due to PAmCherry blinking.

In the following chapter on OmpF dynamics, I investigate both the movement of OmpF on multiple timescales and the nature of OmpF's assembly into the outer membrane. In doing so, the underlying cause for non-uniform OmpF distributions is show to be the result of biased assembly of new OmpF into the outer membrane.

Chapter 5

OmpF Dynamics

5.1 Introduction

The lateral dynamics of the *E. coli* outer membrane have been investigated in multiple studies, using a number of different techniques. Early investigations relied on labelling OM components indiscriminately with Texas Red-X succinimidyl ester. Live cells labelled in this way displayed patterning in the outer membrane, specifically fluorescence intensity at cell poles [219]. This suggested the components labelled with Texas Red lacked long range diffusion in the OM. An analogous indiscriminate labelling method was used to investigate OMP mobility by fluorescence recovery after photobleaching (FRAP). After photobleaching, both OMPs and LPS displayed limited recovery, further indicating that the major components of the OM are immobile [220].

The major downside of these early experiments was the lack of specificity in the labelling protocol. The dynamics of only a small selection of OMPs have been investigated with a specific label. LamB dynamics were investigated through the introduction of a colloidal gold binding epitope. Single particle tracking revealed the apparent existence of slow and fast moving populations of LamB [190]. This investigation was in turn contradicted by single particle tracking of LamB enabled through the introduction of biotin which was labelled

with a streptavidin coated bead. This revealed highly restricted LamB diffusion within an area of radius 25 nm [192].

The dynamics of the highly abundant outer membrane protein OmpA, which contains a peptidoglycan binding site, was investigated through FRAP of an OmpA-mCherry fusion protein. In these experiments OmpA lacked the long range diffusion necessary for fluorescence recovery and importantly, the removal of the OmpA peptidoglycan binding domain had no effect on mobility [221].

Further investigations have built a picture of the outer membrane as a laterally immobile structure wherein OMPs and LPS are inserted and do not significantly diffuse from these locations. The immobile nature of this membrane has subsequently been relied upon to investigate pyocin translocation into cells. To confirm that pyocin S2 outer membrane translocation is PMF dependent, FRAP of pyocin $S2^{NTD}$-AF488 labelled cells treated with CCCP to eliminate the PMF was conducted. The absence of fluorescence recovery observed indicated that pyocin S2 remained bound to the surface of the cell and immobile [204].

Single particle tracking and FRAP investigations are conducted in the range of milliseconds to minutes. The dynamics of outer membrane proteins can, however, be investigated on longer time scales, on the order of hours. By conducting pulse chase labelling of the TolC-AcrAB complex in a microfluidic device called a mother machine which sequesters mother cells at the bottom of narrow channels, the movement of TolC-AcrAB could be tracked on generational timescales. In these experiments TolC-AcrAB accumulated at the pole of the mother cells [193]. Therefore, despite the immobile nature of the OM, some movement is permitted on longer timescales.

Rassam *et al.* [189], in their investigation of BtuB and Cir combined specific OMP labelling protocols, SPT in supported lipid bilayers, FRAP and pulse chase labelling experiments on generational timescales to build a comprehensive picture of BtuB dynamics in the OM. SPT and FRAP of BtuB labelled with Colicin E9 conjugated to organic dyes revealed slow diffusion 0.013 $\mu m^2 s^{-1}$ confined to a region of radius 250 nm. Pulse chase experiments

over generational timescales revealed that BtuB undergoes "binary partitioning" wherein daughter cells will inherit one pole enriched in old BtuB proteins and a "new" pole containing newly inserted OMPs [189].

In this chapter, I investigate the dynamics of OmpF in the outer membrane of *E. coli* on three different timescales. On intermediate timescales on the order of minutes, FRAP shows OmpF lacks long range diffusion in the OM. Furthermore, when the most abundant OMP in the outer membrane, OmpA, is knocked out to ameliorate outer membrane crowding, no significant change in OmpF FRAP is observed. On short timescales on the order of milliseconds, SPT revealed OmpF diffuses in a highly restricted manner in the OM at 0.0018 $\mu m^2 s^{-1}$. When compared to a fixed control it can be concluded that OmpF is essentially immobile in the outer membrane. Pulse chase labelling experiments revealed that old OmpF accumulates at the poles of cells but in a much more gradual manner than the binary partitioning observed for BtuB. Finally, pulsed expression of OmpF reveals that there is a subcellular bias for insertion of new OmpF proteins into the outer membrane. This subcellular bias matches the organisation of constitutively expressed OmpF, indicating that the driving force behind the non-uniform organisation observed in Chapter 4 is biased insertion of OmpF.

5.2 Results and Discussion

5.2.1 OmpF Lacks Long Range Diffusion in the Outer Membrane

To investigate the long range diffusion of OmpF, *E. coli* BL21(DE3) was labelled with Colicin N^{1-185}mCherry and fluorescence recovery after photobleaching was conducted within a region of 30 x 70 pixels at the pole of cells. Full acquisition parameters are described in sections 2.10.1 and 2.10.2. As a control for positive fluorescence recovery, FRAP was repeated on BL21(DE3) expressing TolA-GFP, a freely diffusible inner membrane protein. TolA-GFP underwent significant fluorescence recovery from 8.8 ± 3.3 (SD) % to 43.3 ± 17.7 (SD) %

in 116 s (Figure 5.1.A. Green). OmpF fluorescence did not recover significantly, from a relative fluorescence intensity of 3.3 ± 1.8 (SD) % immediately after bleaching to 6.7 ± 3.6 (SD) % after 116 s (Figure 5.1.A. Red). Representative cell images show that TolA-GFP rapidly diffuses into the bleached area, whereas OmpF shows no significant diffusion into the bleached region (Figure 5.1.B.)

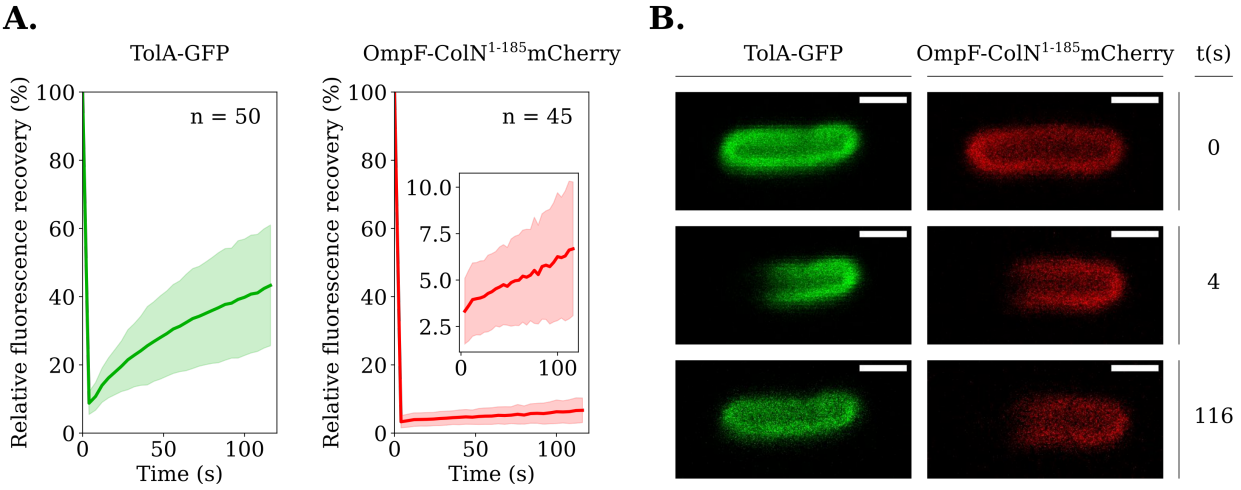

Figure 5.1: OmpF and TolA fluorescence recovery after photobleaching in *E. coli* BL21(DE3). A. Fluorescence recovery curves for TolA-GFP (green) and OmpF-Colicin N^{1-185}mCherry (red). Solid line: average, shaded region: ± standard deviation. Inset: OmpF FRAP curve from 4 to 116 s. **B.** Representative images from a single TolA-GFP (green) and OmpF (red) FRAP experiment. Images presented at timepoints of 0 s (pre bleach frame), 4 s (first post bleach frame) and 116 s (final frame). Scale bars represent a distance of 1 µm. Images captured on a Zeiss LSM780.

Statistical tests between FRAP curves could not be conducted without a degree of processing. As TolA-GFP and OmpF were bleached to different degrees (8.8% of overall fluorescence intensity for TolA, 3.3% of overall fluorescence intensity of OmpF.), recovery curves had to be "zeroed". For each recovery curve this was achieved by measuring the relative fluorescence percentage at the post-bleach frame and subtracting this value from all points on the recovery curve. The zeroed fluorescence recovery at each time-point for OmpF and TolA-GFP was plotted and at each time point a two-tailed students t-test assuming unequal variances was conducted (Figure 5.2). For each time-point OmpF and TolA-GFP recovery differed significantly ($p < 0.00005$).

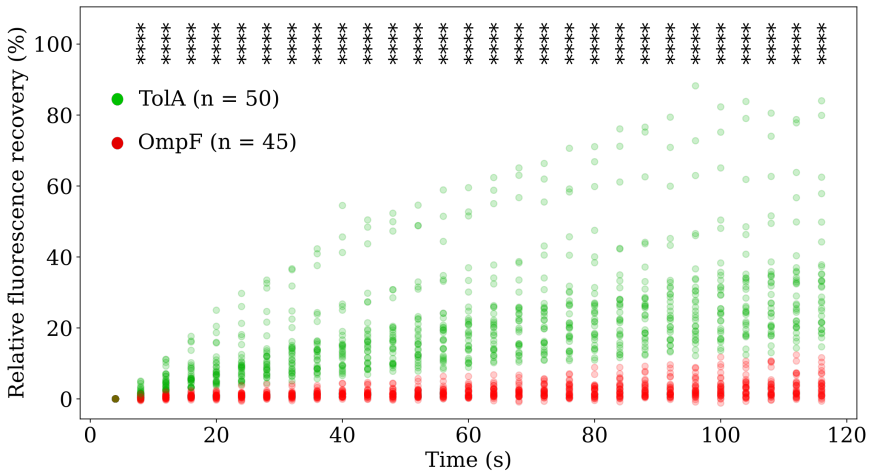

Figure 5.2: OmpF and TolA zeroed fluorescence recovery curve statistical analysis. Fluorescence recovery curves were zeroed from the first post-bleach frame. Each point represents the relative zeroed fluorescence recovery. Green: TolA, 50 repeats; Red: OmpF, 45 repeats. ns: no significant difference. * $p < 0.05$. ** $p < 0.005$. *** $p < 0.0005$. **** $p < 0.00005$. Statistical significance was determined using a two tailed Student's t-test assuming unequal variance.

As explained in Chapter 4, OmpF is one of the most abundant OMPs in the outer membrane. However, work using ribosome profiling to measure the absolute rates of protein synthesis showed that OmpA can be expressed at copy numbers over two fold greater than OmpF (OmpA: 69,396 - 207,618; OmpF: 63,340 - 88,988) [44]. In addition to this it has been observed in preliminary AFM imaging experiments that subpopulations of OmpF exist that diffuse faster than others in OmpA knockout strains [Georgina Benn, UCL, unpublished observations].

One hypothesis that can be proposed based on the high OmpA copy numbers and the preliminary observations of faster OmpF diffusion in OmpA knockout strains is that protein crowding in the outer membrane contributes to the slow diffusion observed for most OMPs. To test this hypothesis, FRAP was performed on OmpF in MG1655 and an OmpA knockout strain in an MG1655 background.

For both of these strains, OmpF was labelled with Colicin N^{1-185}mCherry. Bleaching was conducted within a region of 30 x 70 pixels at the pole of cells. Full acquisition parameters are described in sections 2.10.1 and 2.10.2. OmpF in *E. coli* MG1655 displayed no significant

recovery, bleaching to a relative fluorescence of 1.4 ± 1.2 (SD) % and recovering to 2.7 ± 1.6 (SD) % (Figure 5.3.A. Blue). OmpF in *E. coli* MG1655 Δ*ompA* also displayed no significant recovery, bleaching to a relative fluorescence of 2.8 ± 3.3 (SD) % and recovering to 4.9 ± 2.6 (SD) % (Figure 5.3.A. Orange). The lack of recovery of OmpF into the bleached regions of the cells was clearly visible in the representative cell images (Figure 5.3.B.).

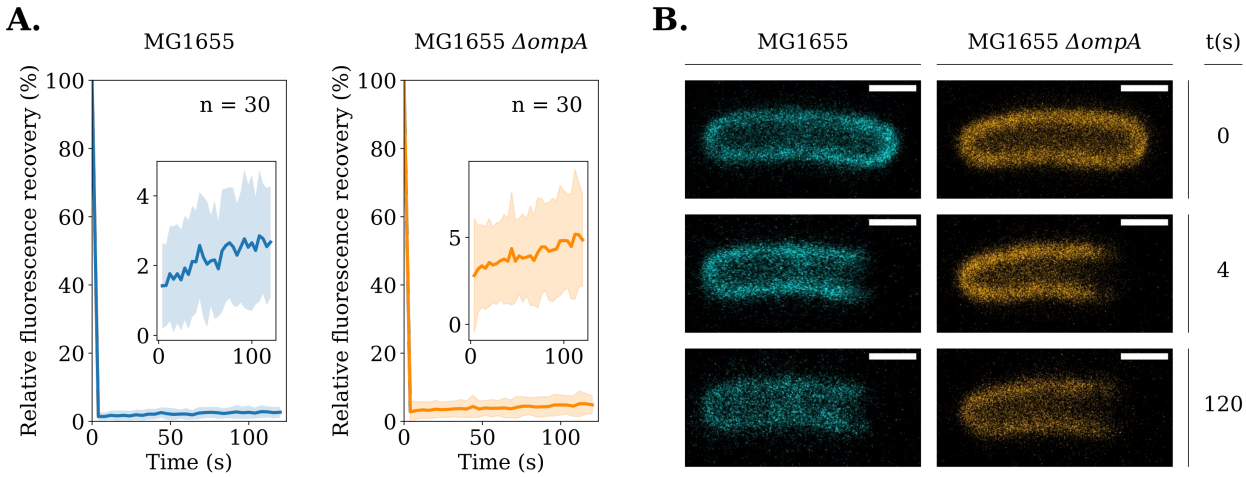

Figure 5.3: OmpF fluorescence recovery after photobleaching in *E. coli* MG1655 and MG1655 Δ*ompA*. A. Fluorescence recovery curves for OmpF in *E. coli* MG1655 (blue) and OmpF in *E. coli* MG1655 Δ*ompA* (orange). Solid line: average, shaded region: ± standard deviation. Insets: OmpF FRAP curves from 4 to 120 s. **B.** Representative images from a single TolA-GFP (green) and OmpF (red) FRAP experiment. Images presented at timepoints of 0 s (pre bleach frame), 4 s (first post bleach frame) and 120 s (final frame). Scale bars represent a distance of 1 µm. Images captured on a Zeiss LSM780.

Statistical analysis was conducted on the zeroed FRAP curves in an identical manner to the OmpF and TolA-GFP FRAP data. Two tailed students t-tests assuming unequal variances revealed no significant difference in recovery between the strains at any timepoint (Figure 5.4). OmpF fluorescence recovery at each time point in *E. coli* MG1655 displayed a notably more constrained range compared to OmpF recovery in *E. coli* MG1655 Δ*ompA* (Figure 5.4).

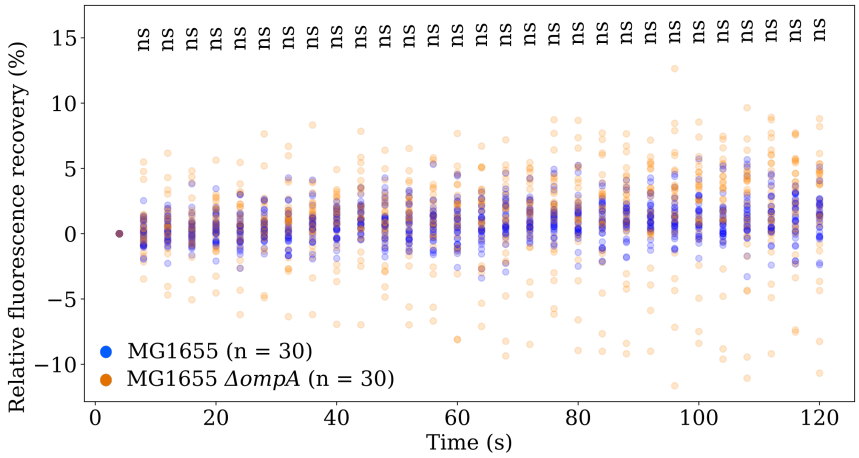

Figure 5.4: *E. coli* MG1655 and MG1655 Δ*ompA* OmpF zeroed fluorescence recovery curve statistical analysis. Fluorescence recovery curves were zeroed from the first post-bleach frame. Each point represents the relative zeroed fluorescence recovery. Blue: OmpF in *E. coli* MG1655, 30 repeats; Orange: OmpF in *E. coli* MG1655 Δ*ompA*, 30 repeats. ns: no significant difference. * $p < 0.05$. ** $p < 0.005$. *** $p < 0.0005$. **** $p < 0.00005$. Statistical significance was determined using a two tailed Student's t-test assuming unequal variance.

These FRAP experiments show that OmpF lacks long range diffusion in the outer membrane. Furthermore, removal of a major proteinaceous component of the OM in the form of OmpA to reduce protein crowding in the outer membrane, results in no significant difference in long range OmpF diffusion.

5.2.2 OmpF Displays Highly Restricted Diffusion in the Outer Membrane

FRAP experiments are ideal for measuring the long range diffusion of proteins across distances of hundreds to thousands of nanometres. However, in the case of OmpF diffusion, little information can be extracted from these FRAP experiments other than showing that OmpF must be restricted in its diffusion. To investigate the nature of OmpF diffusion in greater detail and to obtain quantitative measures of diffusion, such as apparent diffusion coefficients and confinement radii, single particle tracking was performed.

Previous investigations into the diffusion of BtuB and Cir, using colicin E9 and colicin

Ia based fluorescent labels relied on the use of constitutively fluorescing organic dyes. BtuB and Cir were labelled with their respective colicins and photobleaching was conducted until single molecules could be observed. Necessarily, this resulted in a limited number of tracks being analysed (on the order of tens of tracks), as once bleaching had occurred to a sufficient level only a very limited number of non-overlapping molecules could be tracked.

For this reason, using the Colicin N^{1-185}PAmCherry label, photoactivated localisation microscopy single particle tracking (PALM-SPT) of OmpF was conducted and a SPT analysis pipeline to process PALM-SPT data was designed (Figure 5.5).

Each PALM-SPT dataset collected consisted of 10,000 to 30,000 frames collected at an exposure time of 50 ms (Figure 5.5.A.). The imageJ plugin ThunderSTORM was used to fit 2D Elliptical Gaussians to the diffraction limited spots in each frame to estimate the xy coordinates of the fluorophores (Figure 5.5.B.). As tracking was conducted over millisecond timescales, drift correction was not applied to the data as it was negligible over these short timescales. The ThunderSTORM localisation output file was processed to ensure compatibility with the imageJ plugin: TrackMate. TrackMate was used to determine the tracks between localisations, a simple LAP tracker was used with a maximum linking distance of 250 nm (Figure 5.5.C.). Tracking data was exported to be processed, analysed and presented with custom made Python scripts (Figure 5.5.D.). Tracks under 5 frames in length cannot be satisfactorily analysed and hence were eliminated (Figure 5.5.E.). For each PALM-SPT dataset, a segmented cell image was generated, referencing this binary image, tracks not occurring within the bounds of cells (e.g. unbound Colicin N^{1-185}PAmCherry molecules) were eliminated (Figure 5.5.F.). After these processing steps, the diffusion coefficient of tracks were determined. For each track mean squared displacements were calculated at the first 4 lag times: 50, 100, 150 and 200 ms. The regression line for these four points was computed and the gradient used to determine in the instantaneous apparent diffusion coefficient (Figure 5.5.G.). For each track the radius of the smallest circle that encapsulates all the track localisations was calculated (Figure 5.5.H.i.). For an individual track the centroid coordi-

nates were determined (Figure 5.5.H.ii.), from this centroid the distance to each localisation in the track was measured (Figure 5.5.H.iii.). The distance to the furthest localisation from the centroid was saved Figure 5.5.(H.iv.). This distance represents the radius of the smallest circle that encapsulates all localisations of the single particle track (Figure 5.5.H.v.).

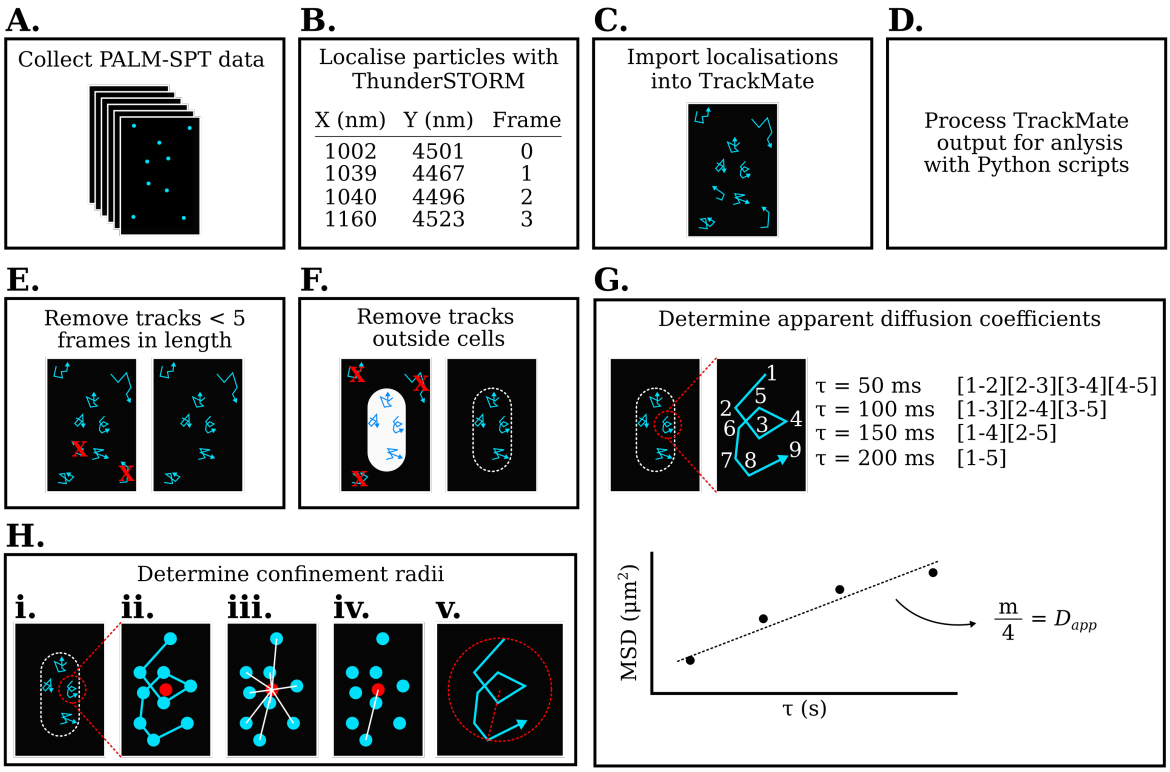

Figure 5.5: Schematic of the PALM-SPT Single particle tracking analysis pipeline.

To investigate the diffusion of OmpF at the high resolution that PALM-SPT enables, *E. coli* MG1655 was labelled with Colicin N^{1-185}PAmCherry. PALM-SPT was conducted, between 10,000 and 30,000 frames were collected at an exposure time of 50 ms. For the duration of PALM-SPT experiments a 561 nm excitation laser was used at approximately 20 mW. To activate a sparse set of non-overlapping fluorophores a 405 nm activation laser was used at approximately 0.1 mW, however, the power of this laser was modulated over the course of the experiment to maintain a relatively constant number of photoactivated fluorophores per frame. PALM-SPT data was processed using the PALM-SPT analysis

pipeline.

The vast majority of OmpF diffusion coefficients in *E. coli* MG1655 were representative of very slow diffusion (Figure 5.6.). From 21,336 individual OmpF single particle trajectories a median diffusion coefficient of 0.0018 [0.00176, 0.00193] $\mu m^2 s^{-1}$ (99.9% CI) was determined. OmpF single particle trajectories from multiple cells were normalised with respect to the cell they appeared in and plotted (Figure 5.6. Inset). Tracks within a narrow window around the median diffusion coefficient (0.0018 - 0.0019 $\mu m^2 s^{-1}$) showed highly restricted diffusion with little lateral movement in the outer membrane.

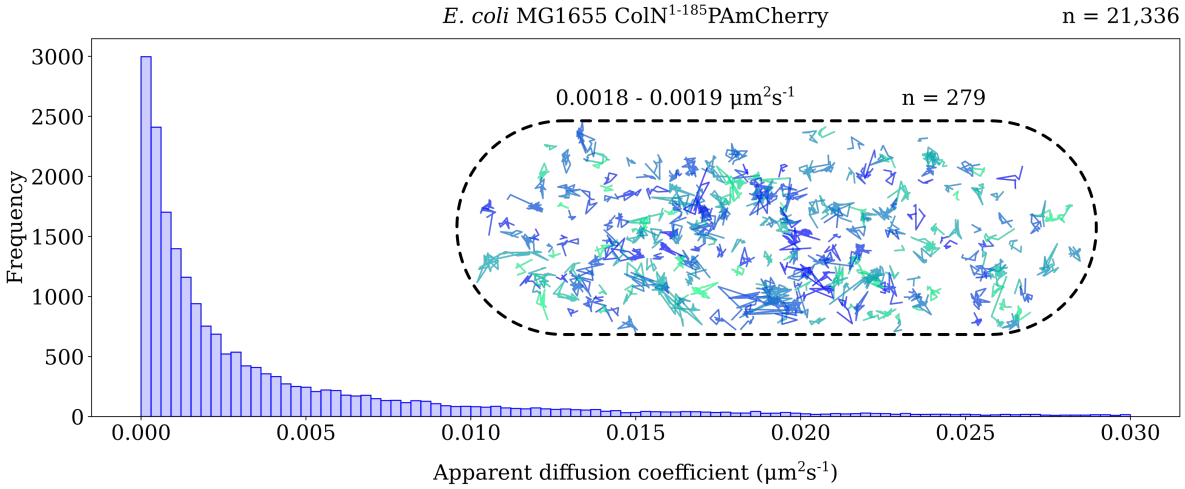

Figure 5.6: OmpF diffusion coefficients and representative single particle tracks in *E. coli* MG1655. Main: diffusion coefficient histogram of OmpF single particle trajectories, the entire range of diffusion coefficients is not shown, only diffusion coefficients from 0 to 0.03 $\mu m^2 s^{-1}$ are displayed. From a total of 21,336 OmpF trajectories a median diffusion coefficient of 0.0018 [0.00176, 0.00193] $\mu m^2 s^{-1}$ (99.9% CI) was calculated. The upper and lower bounds of the median diffusion coefficient were determined from bootstrapping, the data was resampled 100,000 times and the 0.05 and 99.95 percentiles of the resampled medians defined the 99.9% confidence interval. Inset: OmpF representative tracks extracted from a narrow range around the median diffusion coefficient: 0.0018 - 0.0019 $\mu m^2 s^{-1}$. A total of 279 tracks are displayed. Tracks are normalised with respect to the cell they were collected from. Track colouring is for illustrative purposes only.

To investigate the restriction of OmpF diffusion in the outer membrane, the confinement radii for each OmpF single particle trajectory was determined and plotted (Figure 5.7). From the 21,336 tracks a median confinement radius of 72 [71.4, 73.7] nm (99.9% CI) was determined (Figure 5.7.A.) The probability density of all of the confinement radii, in which

the entire range of data can be seen, showed the strong trend towards highly restricted diffusion of OmpF (Figure 5.7.B.).

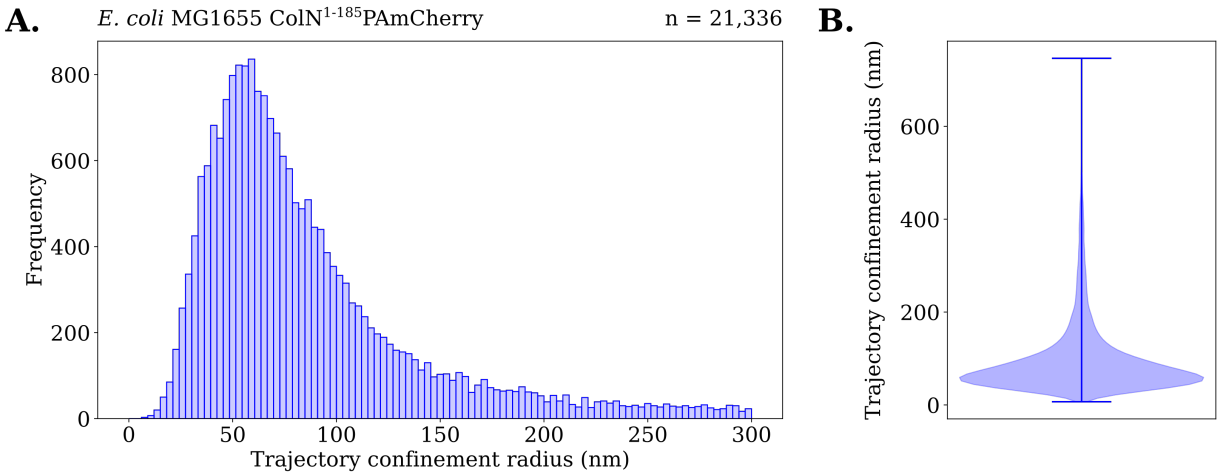

Figure 5.7: OmpF confinement radii in *E. coli* MG1655. A. Confinement radii histogram of OmpF single particle trajectories, the entire range of confinement radii is not shown, only confinement radii from 0 to 300 nm are displayed. From a total of 21,336 OmpF trajectories a median confinement radius of 72 [71.4, 73.7] nm (99.9% CI) was calculated. The upper and lower bounds of the median confinement radii were determined from bootstrapping, the data was resampled 100,000 times and the 0.05 and 99.95 percentiles of the resampled medians defined the 99.9% confidence interval. **B.** Violin plot of OmpF confinement radii displaying the probability density for the entire range of confinement radii observed.

FRAP experiments indicated that there was no significant difference in long range diffusion of OmpF when outer membrane protein crowding was reduced through the elimination of highly abundant OmpA. To investigate the effect of outer membrane protein crowing at the higher resolutions afforded by single particle tracking, PALM-SPT was repeated on OmpF in *E. coli* MG1655 Δ*ompA* (Figure 5.8.). A similar distribution of diffusion coefficients were observed with a significant trend towards very slow diffusion coefficients. From 8224 individual single particle trajectories a median diffusion coefficient of 0.0020 [0.00185, 0.00220] $\mu m^2 s^{-1}$ (99.9% CI) was determined. Not significantly faster than the 0.0018 [0.00176, 0.00193] $\mu m^2 s^{-1}$ (99.9% CI) observed in *E. coli* MG1655. Representative single particle trajectories showed similarly restricted diffusion, diffusing within a small area and not following a Brownian motion pattern (Figure 5.8. Inset).

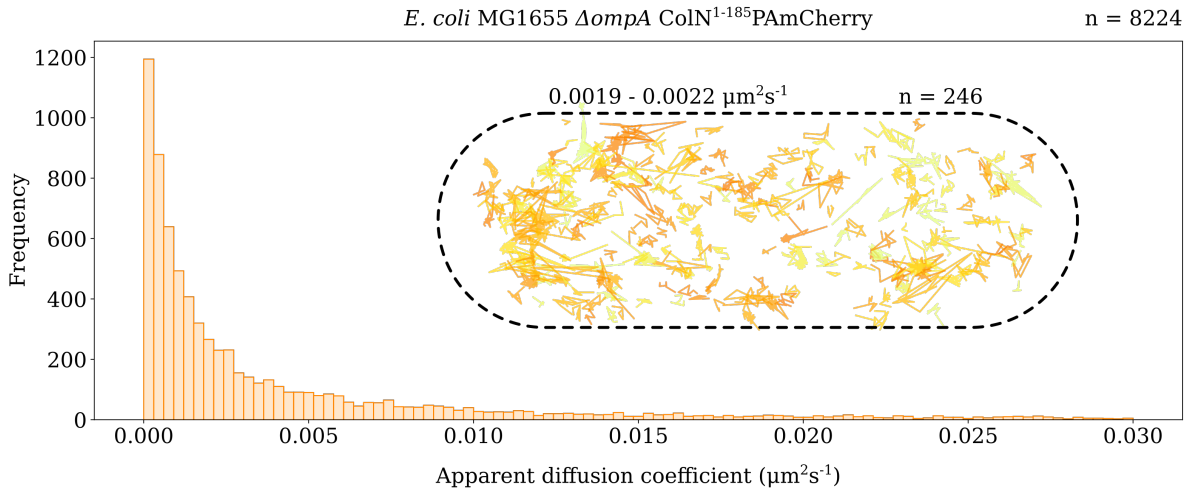

Figure 5.8: OmpF diffusion coefficients and representative single particle tracks in *E. coli* MG1655 Δ*ompA*. Main: diffusion coefficient histogram of OmpF single particle trajectories, the entire range of diffusion coefficients is not shown, only diffusion coefficients from 0 to 0.03 $\mu m^2 s^{-1}$ are displayed. From a total of 8224 OmpF trajectories a median diffusion coefficient of 0.0020 [0.00185, 0.00220] $\mu m^2 s^{-1}$ (99.9% CI) was calculated. The upper and lower bounds of the median diffusion coefficient were determined from bootstrapping, the data was resampled 100,000 times and the 0.05 and 99.95 percentiles of the resampled medians defined the 99.9% confidence interval. Inset: OmpF representative tracks extracted from a narrow range around the median diffusion coefficient: 0.0019 - 0.0022 $\mu m^2 s^{-1}$. A total of 246 tracks are displayed. Tracks are normalised with respect to the cell they were collected from. Track colouring is for illustrative purposes only.

Confinement radii of OmpF in *E. coli* MG1655 Δ*ompA* were consistent with the diffusion coefficient data, with tracks being confined to areas with a very small radius (Figure 5.9.A.). From the 8224 single particle trajectories a median confinement radius of 80 [77.4, 82.2] nm (99.9% CI) was determined, marginally but significantly greater than that of OmpF in *E. coli* MG1655. When the probability density of all of the confinement radii were visualised the strong tendency for particles to be confined in small areas was evident (Figure 5.9.B.).

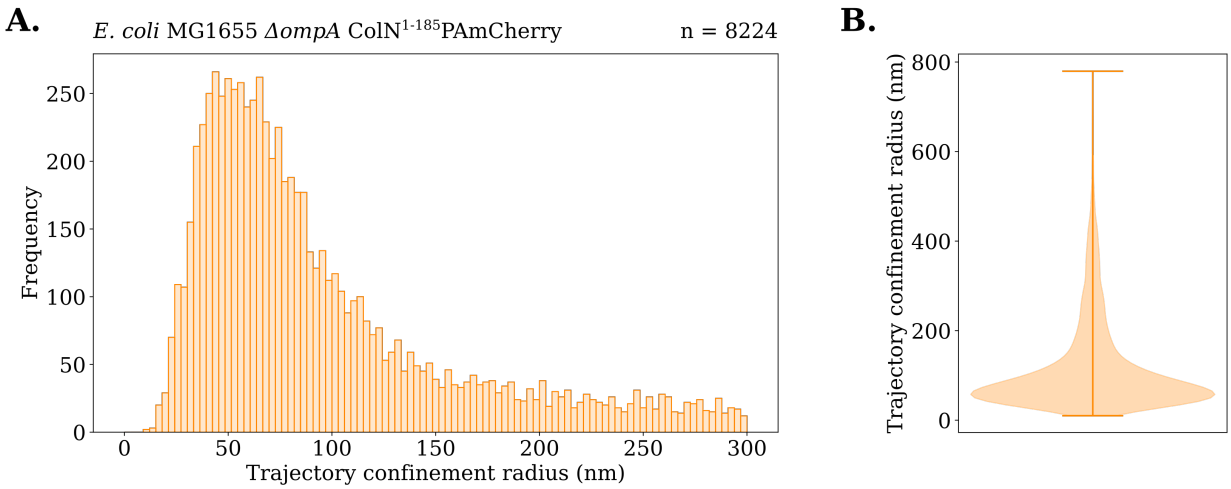

Figure 5.9: OmpF confinement radii in *E. coli* MG1655 Δ*ompA*. A. Confinement radii histogram of OmpF single particle trajectories, the entire range of confinement radii is not shown, only confinement radii from 0 to 300 nm are displayed. From a total of 8224 OmpF trajectories a median confinement radius of 80 [77.4, 82.2] nm (99.9% CI) was calculated. The upper and lower bounds of the median confinement radii were determined from bootstrapping, the data was resampled 100,000 times and the 0.05 and 99.95 percentiles of the resampled medians defined the 99.9% confidence interval. **B.** Violin plot of OmpF confinement radii displaying the probability density for the entire range of confinement radii observed.

It is clear that in both *E. coli* MG1655 and MG1655 Δ*ompA* OmpF diffuses very slowly in the outer membrane. From the observation that single particle tracks completely lacked visible Brownian motion, it was hypothesised that OmpF is effectively immobile in the outer membrane and the diffusion coefficients observed were effectively at the limit of the resolution of the PALM-SPT technique.

To test this hypothesis, OmpF PALM-SPT was repeated in *E. coli* MG1655 where cells were fixed for 30 minutes with 4% formaldehyde prior to imaging to completely immobilise OmpF in the outer membrane. Diffusion coefficients of OmpF fixed cells were slow, but nevertheless marginally faster than both live cell experiments, with a median diffusion coefficient of 0.0029 [0.00260, 0.00321] $\mu m^2 s^{-1}$ (99.9% CI) from 5956 single particle trajectories (Figure 5.10.). Representative tracks also showed highly confined tracks that lacked Brownian motion (Figure 5.10. Inset.).

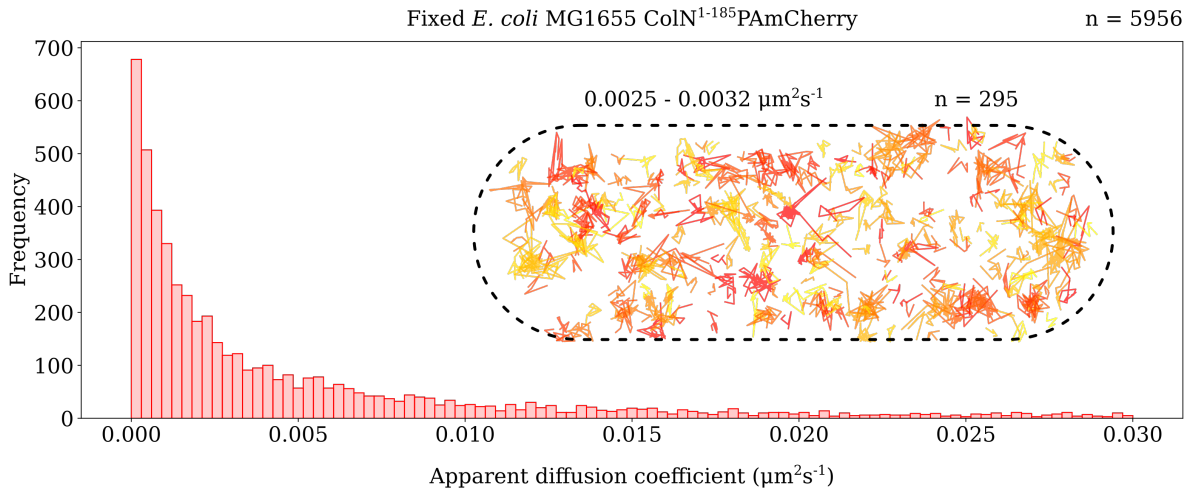

Figure 5.10: OmpF diffusion coefficients and representative single particle tracks in fixed *E. coli* MG1655. Main: diffusion coefficient histogram of OmpF single particle trajectories, the entire range of diffusion coefficients is not shown, only diffusion coefficients from 0 to 0.03 µm^{2}s^{-1} are displayed. From a total of 5956 OmpF trajectories a median diffusion coefficient of 0.0029 [0.00260, 0.00321] µm^{2}s^{-1} (99.9% CI) was calculated. The upper and lower bounds of the median diffusion coefficient were determined from bootstrapping, the data was resampled 100,000 times and the 0.05 and 99.95 percentiles of the resampled medians defined the 99.9% confidence interval. Inset: OmpF representative tracks extracted from a narrow range around the median diffusion coefficient: 0.0025 - 0.0032 µm^{2}s^{-1}. A total of 295 tracks are displayed. Tracks are normalised with respect to the cell they were collected from. Track colouring is for illustrative purposes only.

Confinement radii of OmpF in fixed cells were small at an average of 90 [86.2, 92.9] nm (99.9% CI) from 5956 single particle trajectories (Figure 5.11.A.). Notably however, this was larger than the confinement radii for both live cell PALM-SPT datasets. The probability density of confinement radii also indicated a less potent trend towards very small confinement radii in comparison to both live cell experiments (Figure 5.11.B.).

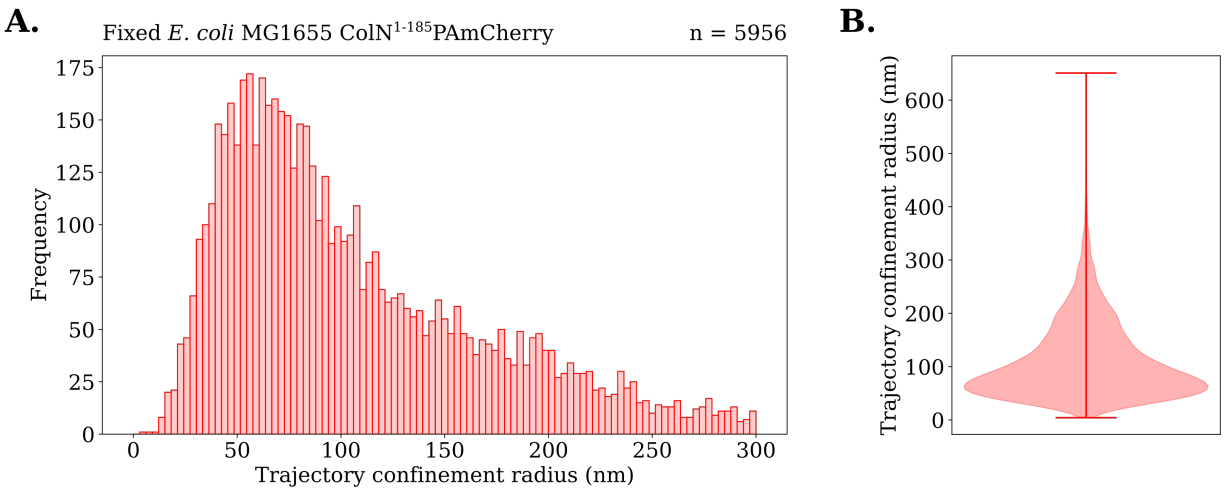

Figure 5.11: OmpF confinement radii in fixed *E. coli* MG1665. A. Confinement radii histogram of OmpF single particle trajectories, the entire range of confinement radii is not shown, only confinement radii from 0 to 300 nm are displayed. From a total of 5956 OmpF trajectories a median confinement radius of 90 [86.2, 92.9] nm was calculated. The upper and lower bounds of the median confinement radii were determined from bootstrapping, the data was resampled 100,000 times and the 0.05 and 99.95 percentiles of the resampled medians defined the 99.9% confidence interval. **B.** Violin plot of OmpF confinement radii displaying the probability density for the entire range of confinement radii observed.

The observation that both the median diffusion coefficient and median confinement radius for OmpF in fixed cells is greater than that of both live cell experiments (Figure 5.12.A. and B.) provides strong evidence that the actual diffusion coefficient for OmpF is likely lower than what can be resolvable with PALM-SPT. It can hence be concluded that on the timescale over which SPT was conducted, OmpF is effectively immobile in the outer membrane.

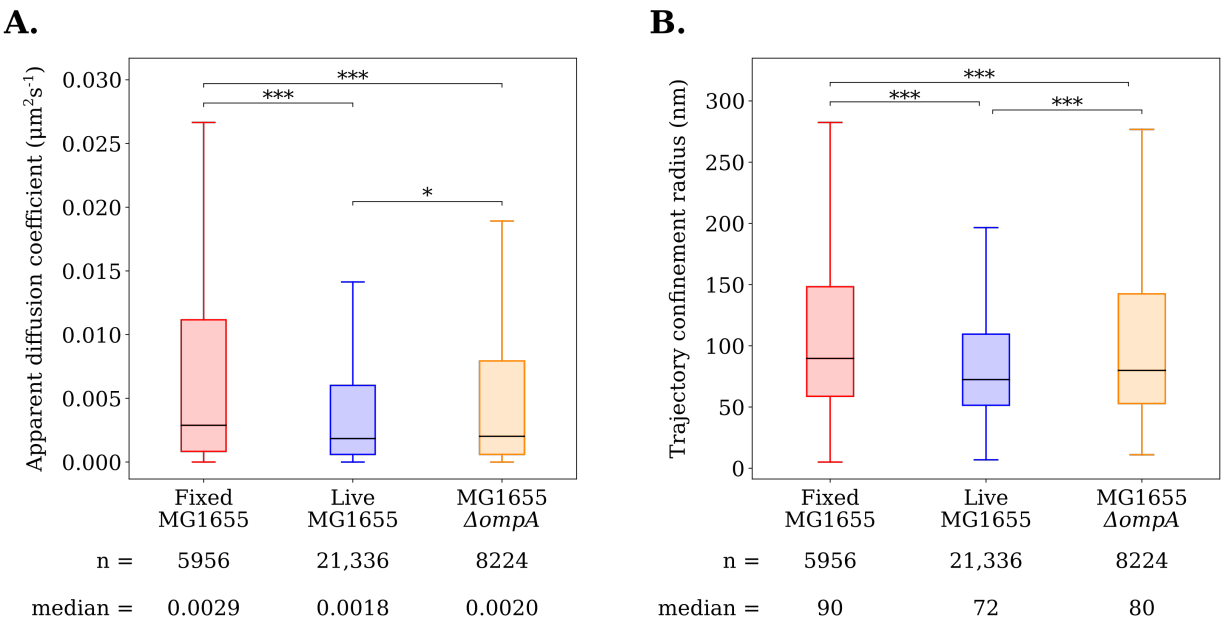

Figure 5.12: Comparison of diffusion coefficients and confinement radii for all PALM-SPT experiments. A. Box plots of OmpF diffusion coefficients in Fixed MG1655 (red), Live MG1655 (Blue) and Live MG1655 Δ*ompA E. coli* cells. **B.** Box plots of OmpF confinement radii in Fixed MG1655 (red), Live MG1655 (Blue) and Live MG1655 Δ*ompA E. coli* cells. Statistical significance was determined from bootstrapping, the data was resampled 100,000 times and the 95, 99 and 99.9% confidence intervals were determined. ns: no significant difference. * $p < 0.05$. ** $p < 0.01$. *** $p < 0.001$.

5.2.3 Over Generational Timescales OmpF is Sequestered to the Cell Poles

Despite the fact that OmpF is essentially immobile in the outer membrane on the millisecond to minute timescales as shown by PALM-SPT and FRAP it is still possible that over generational timescales, OmpF can move in the outer membrane, as observed for the monomeric OMPs BtuB and Cir [189].

To investigate the movement of OmpF on timescales of up to 90 minutes a pulse chase labelling experiment was conducted. *E. coli* BE3000 cells were grown to mid-log phase and labelled with 200 nM Colicin N^{1-185}mCherry for 10 minutes. Excess unbound label was washed off and cells were allowed to grow for 4 time periods at 37°C: 0, 30, 60 and 90 minutes. At each timepoint cells were fixed with 4% formaldehyde and imaged. Cells at the

0 minute timepoint were fixed immediately after labelling.

The change in fluorescence distribution of each cell was determined by measuring the fluorescence intensity profile along the long axis of each cell. These fluorescence intensity profiles were normalised for length and intensity in order that the distribution of OmpF on all cells could be directly compared.

When cells were labelled and immediately fixed without permitting any growth, fluorescence intensity could be observed across the entire length of the cell. Viewed in bulk, the fluorescence intensity traces of all cells analysed displayed significant variability (Figure 5.13.A.), attributable to the non-uniform distribution detailed in Chapter 4. When the average fluorescence profile was calculated (Figure 5.13.B.) fluorescence intensity could be seen along the entire length of the cell with minor bumps at either pole representing the edges of the cells, a central bump was also visible likely contributed to by cells in the process of septating. Representative cell images (Figure 5.13.C.) further confirmed that at this timepoint OmpF is distributed across the entire length of the cell with relative uniformity.

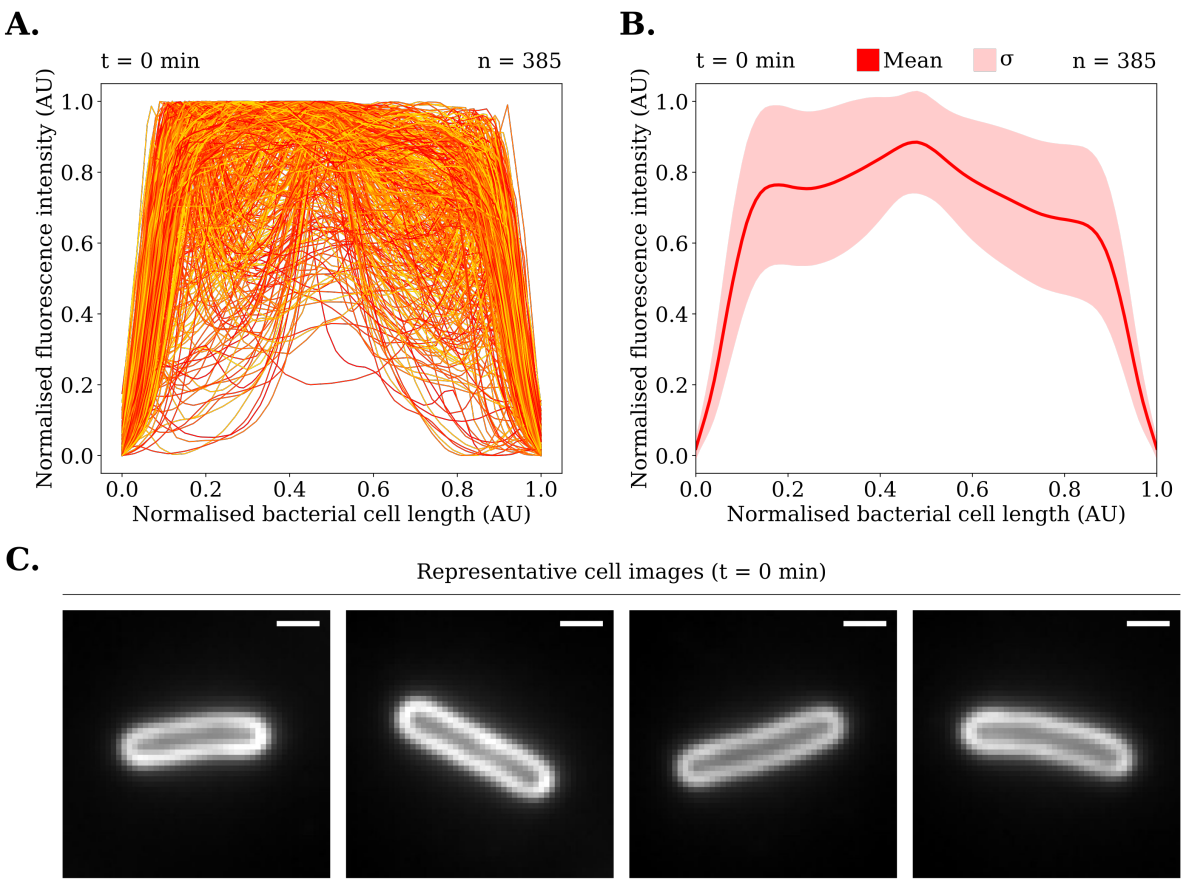

Figure 5.13: OmpF pulse chase labelling in *E. coli* BE3000 after 0 minutes of growth. **A.** Normalised fluorescence intensity profiles along the normalised long axis length of all cells imaged. **B.** Average normalised fluorescence intensity profile. Red: mean fluorescence intensity profile. Pink envelope: ± standard deviation. **C.** Representative cell images, all images were contrast adjusted to the same arbitrary value for visibility. All images were taken on an Oxford Nanoimager S. Scale bars represent a distance of 1 µm. For this timepoint a total of 385 cells were analysed.

When cells were allowed to grow for 30 minutes after labelling and then imaged a subtle change could be observed. Viewing the fluorescence intensity traces in bulk (Figure 5.14.A.) most cells had one marginally more intense pole than the other. This observation was borne out in the average fluorescence profile (Figure 5.14.B.) wherein the poles differed in normalised intensity by approximately 0.2 AU. Representative cell images also showed the subtle fluorescence intensity disparity between the cell poles (Figure 5.14.C.).

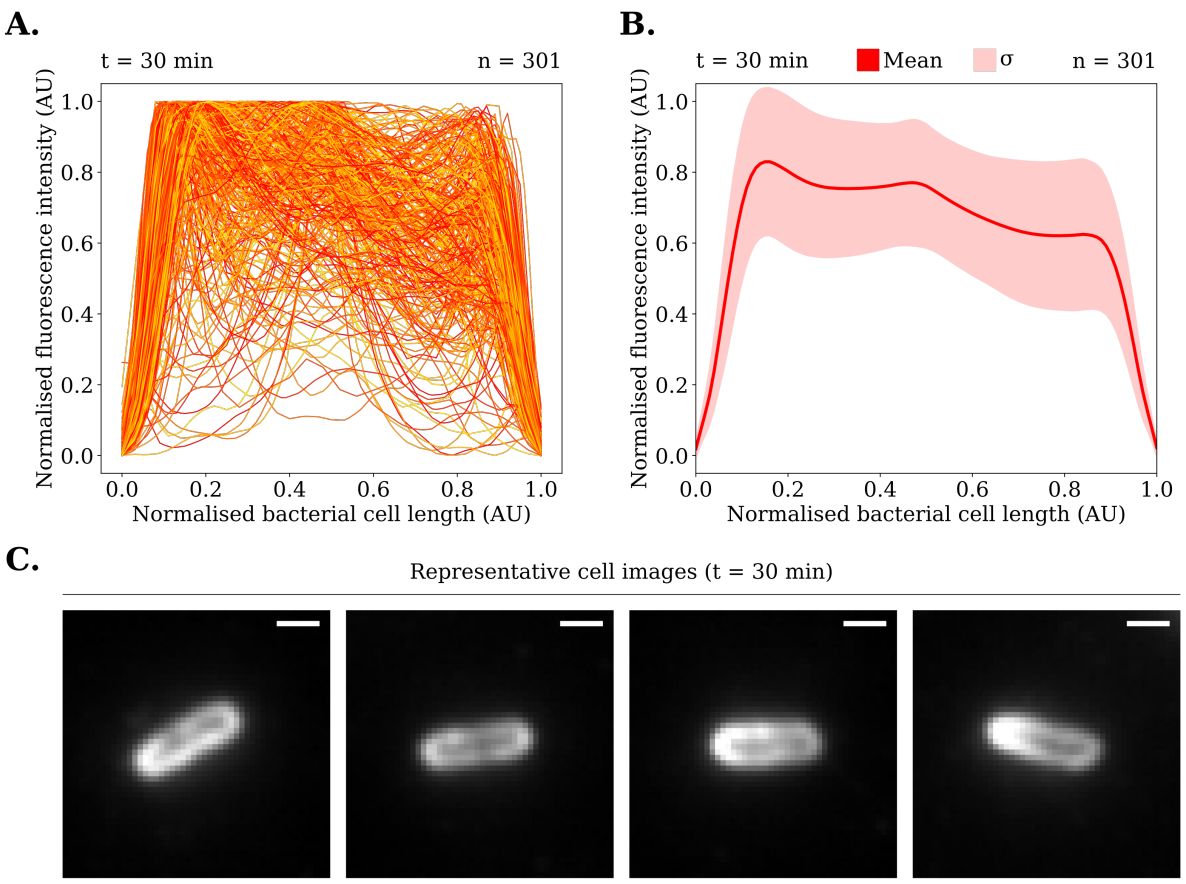

Figure 5.14: OmpF pulse chase labelling in *E. coli* BE3000 after 30 minutes of growth. **A.** Normalised fluorescence intensity profiles along the normalised long axis length of all cells imaged. **B.** Average normalised fluorescence intensity profile. Red: mean fluorescence intensity profile. Pink envelope: ± standard deviation. **C.** Representative cell images, all images were contrast adjusted to the same arbitrary value for visibility. All images were taken on an Oxford Nanoimager S. Scale bars represent a distance of 1 µm. For this timepoint a total of 301 cells were analysed.

After 60 minutes of growth the disparity between the relative intensities of the two poles increased, as can be observed in the individual fluorescence profile traces (Figure 5.15.A.) and the average fluorescence profiles (Figure 5.15.B.). The polar localisation of fluorescence signal can be seen clearly in the representative cell images (Figure 5.15.C.).

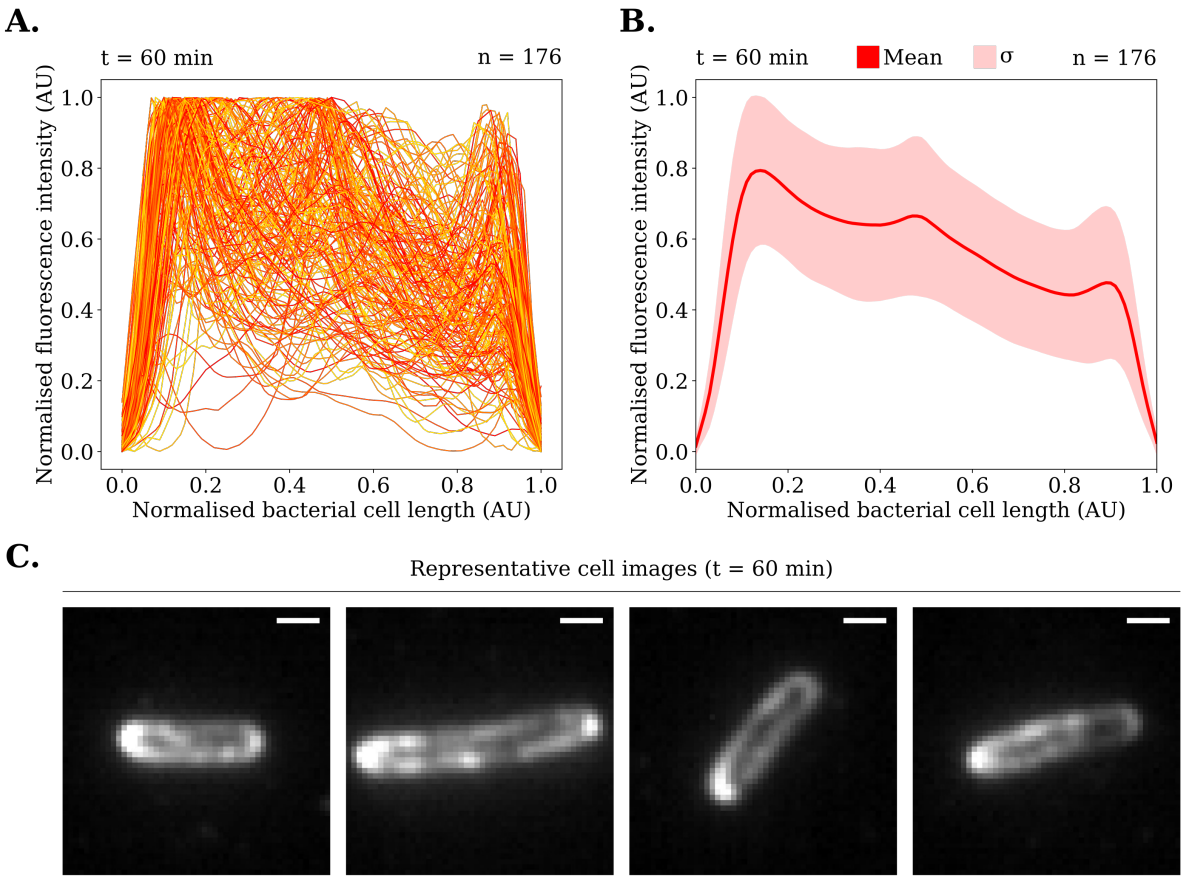

Figure 5.15: OmpF pulse chase labelling in *E. coli* BE3000 after 60 minutes of growth. **A.** Normalised fluorescence intensity profiles along the normalised long axis length of all cells imaged. **B.** Average normalised fluorescence intensity profile. Red: mean fluorescence intensity profile. Pink envelope: ± standard deviation. **C.** Representative cell images, all images were contrast adjusted to the same arbitrary value for visibility. All images were taken on an Oxford Nanoimager S. Scale bars represent a distance of 1 µm. For this timepoint a total of 176 cells were analysed.

At the final timepoint of 90 minutes the polar localisation of fluorescence signal reached its most significant point with fluorescence intensity profiles (Figure 5.16.A. and B.) and representative cell images (Figure 5.16.C.) displaying significant fluorescence intensity disparity between the two poles.

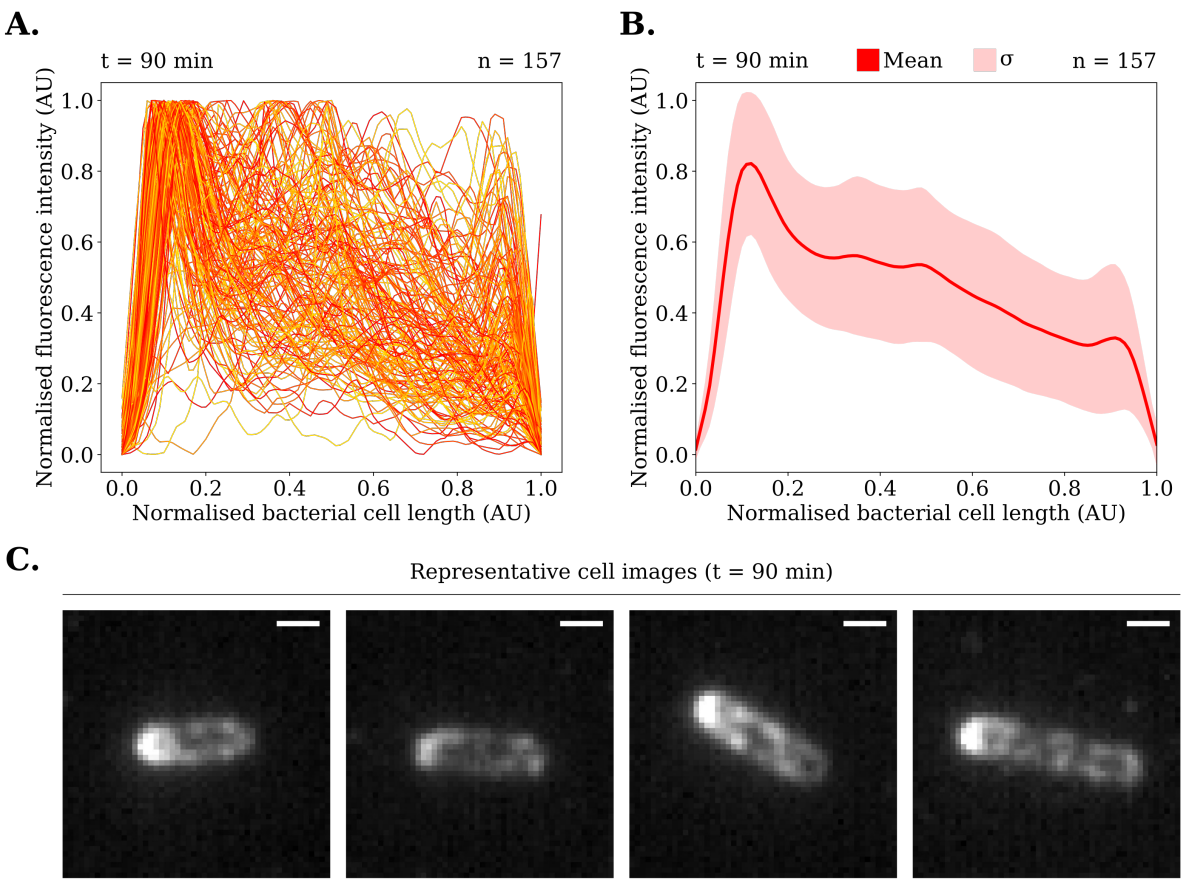

Figure 5.16: OmpF pulse chase labelling in *E. coli* BE3000 after 90 minutes of growth. **A.** Normalised fluorescence intensity profiles along the normalised long axis length of all cells imaged. **B.** Average normalised fluorescence intensity profile. Red: mean fluorescence intensity profile. Pink envelope: ± standard deviation. **C.** Representative cell images, all images were contrast adjusted to the same arbitrary value for visibility. All images were taken on an Oxford Nanoimager S. Scale bars represent a distance of 1 µm. For this timepoint a total of 157 cells were analysed.

From these pulse chase labelling experiments it can be inferred that over longer timescales on the order of an hour, OmpF accumulates at a single pole of the cell. Much like the monomeric OMP: BtuB, OmpF even though effectively immobile in the outer membrane can move on longer timescales. Diffusion cannot, therefore, account for polar localisation of OmpF. It is hence likely that the biogenesis of the outer membrane occurring preferentially at mid cell causes immobile OmpF to be pushed to both poles of the growing cell. Once the cell divides it will therefore form two daughter cells with old OmpF consigned to one pole in each of these daughter cells. This polar localisation is then retained at the poles as OmpF

cannot diffuse.

5.2.4 The Biogenesis of new OmpF can Display Subcellular Bias

To investigate whether OmpF biogenesis displayed subcellular bias, *E. coli* BZB1107 ($\Delta ompF$, $\Delta ompC$, $\Delta lamB$) was transformed with a pBAD-HismycB plasmid encoding OmpF (pNGH71) and grown to mid-log phase. Once at mid-log phase cells were induced with 1% arabinose for short bursts of 5, 7.5 or 10 minutes and then fixed immediately with 4% formaldehyde for 30 minutes. Labelling was conducted after fixation with 200 nM Colicin N^{1-185}mCherry for 1 hour. Epifluorescence images of OmpF distribution were captured at each induction time. From these images kymographs were generated to measure the change of fluorescence distribution with respect to cell length (Figure 5.17.A.) and the average fluorescence intensity of each cell at each induction time was determined and plotted (Figure 5.17.B.).

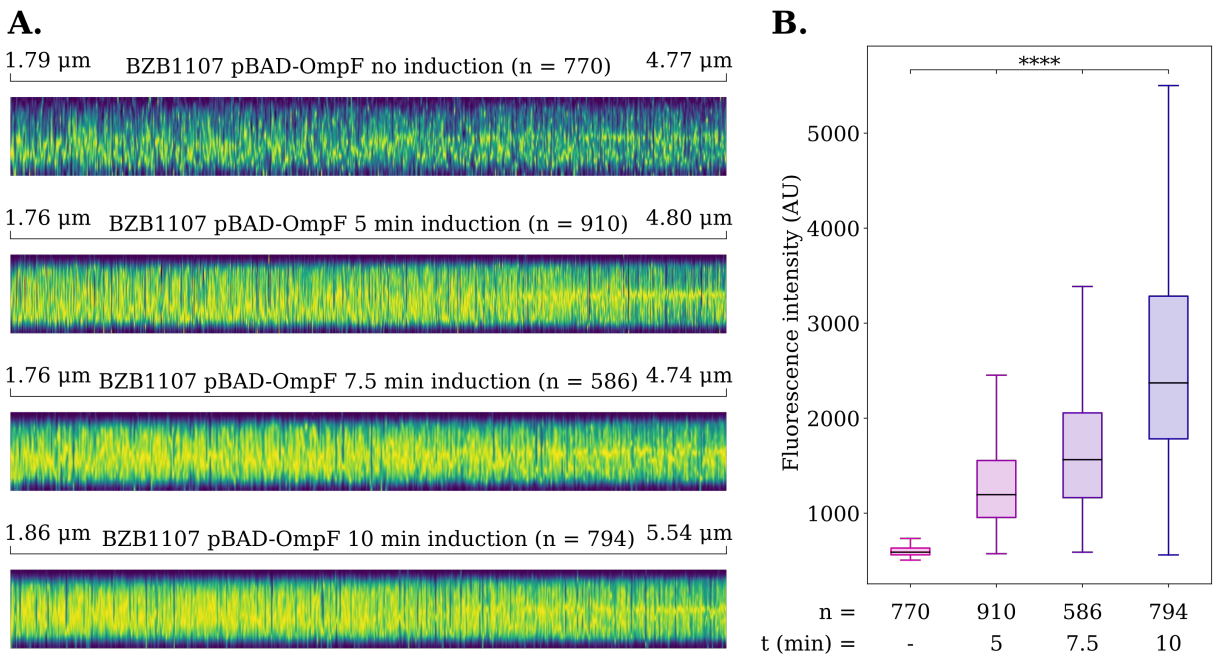

Figure 5.17: Pulsed OmpF expression kymographs and fluorescence quantification. A. Kymographs of OmpF distribution in uninduced (n = 770) and 5 minute (n = 910), 7.5 minute (n = 586) and 10 minute (n = 794) pulsed induction of OmpF. Each vertical line of pixels in the kymographs represent the normalised fluorescence intensity profile along the long axis of the cell. Cells are sorted by long axis length. Kymographs are scaled to the same dimensions. **B.** Box plots of average cell fluorescence for each induction condition. Median fluorescence intensity values: no induction = 590 AU, 5 minutes = 1195 AU, 7.5 minutes = 1563 AY, 10 minutes = 2371 AU. ns: no significant difference. * $p < 0.05$. ** $p < 0.005$. *** $p < 0.0005$. **** $p < 0.00005$. Statistical significance was determined using a two tailed Student's t-test assuming unequal variance.

When BZB1107 cells were not induced with arabinose a small residual level of leaky expression was observed, median fluorescence intensity values of 590 AU (Figure 5.17.B.) indicated that this expression was weak as the base level offset of the sensor used in the Oxford Nanoimager S is 414 A/D. When the kymograph was observed (Figure 5.17.A.) the distribution of fluorescence was noisy due to the low level of OmpF labelling. When OmpF expression was pulsed for short time periods, however, fluorescence intensity increased significantly (Figure 5.17.B.). Kymographs showed that with short pulses of OmpF expression there was a relative increase in OmpF biogenesis at mid cell as cell length increased. This bias for mid cell insertion was most apparent at the most contracted induction pulse time of 5 minutes (Figure 5.17.A.).

To investigate the subcellular bias of OmpF insertion in greater detail, average 1D and 2D fluorescence intensity profiles were extracted from the 5 minute induction pulse kymograph (Figure 5.18.)

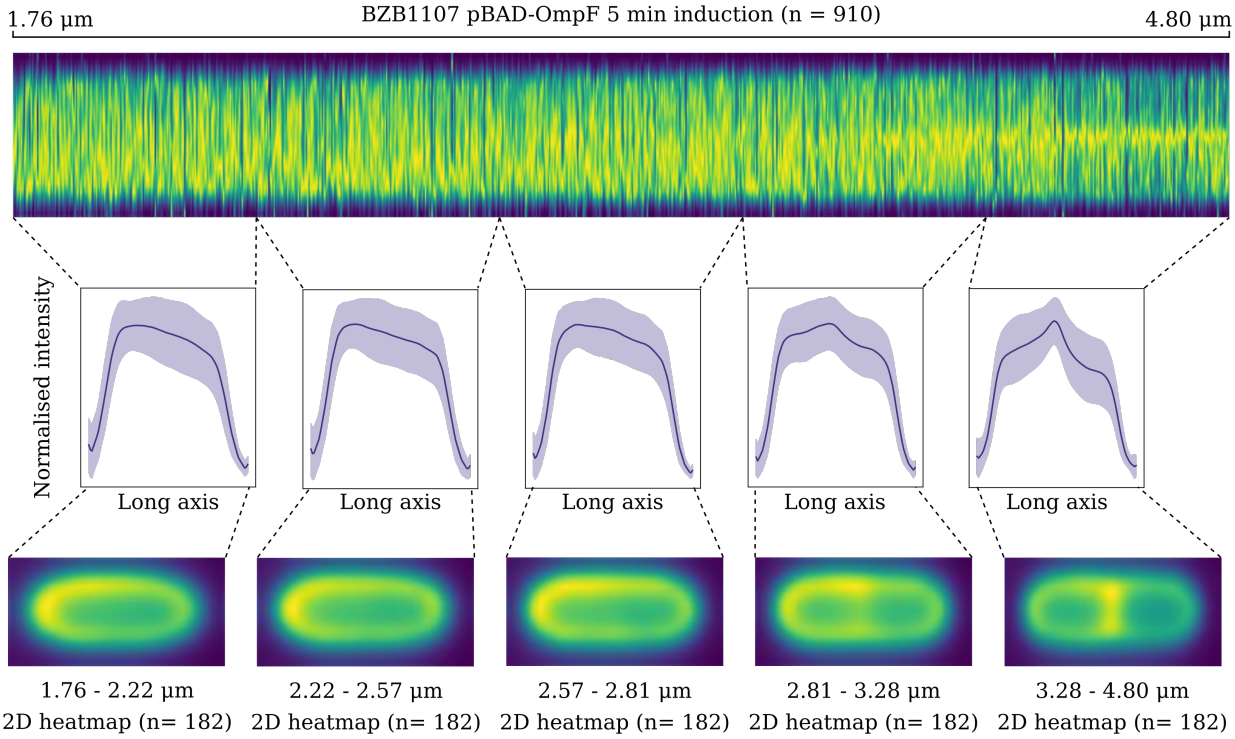

Figure 5.18: Kymograph of 5 minute pulsed OmpF expression in *E. coli* BZB1107. Top: Kymograph wherein each vertical line of pixels represents the fluorescence intensity profile along the long axis of a single cell. Cells are sorted by long axis length. 910 cells were used to construct the kymograph with lengths ranging from 1.76 to 4.80 µm. Centre: Average 1D long axis fluorescence intensity profiles extracted from 182 cell slices of the kymograph. Dark purple: mean intensity profile, light purple envelope: ± standard deviation. Bottom: Average 2D fluorescence intensity profiles from 182 cell kymograph slices, with length ranges denoted.

At shorter cell lengths OmpF biogenesis was relatively uniform along the cell, with one side of the cell displaying marginally greater fluorescence intensity than the other. However at longer cell lengths from 2.81 to 4.80 µm the appearance of mid cell OmpF biogenesis was observed and increased in intensity throughout this range.

The observation that as cells increased in length OmpF biogenesis was localised preferentially to mid-cell is consistent with observations from pulse chase labelling experiments

wherein "old" OmpF was pushed to the poles of the cell over successive generations. This subcellular bias of OMP insertion has interesting physiological implications.

Gunasinghe *et al.* conducted antibody labelling of BamA and BamC in permeabilised, fixed *E. coli*. Through the use of direct stochastic optical reconstruction microscopy (dSTORM) imaging it was shown that the BAM complex formed clusters in the outer membrane and, importantly, these clusters are distributed throughout the entire cell, including at the poles [194]. The observation of BAM clusters being distributed throughout the cell was confirmed through the imaging of antibody labelled BamA conducted by Mamou *et al.* using both diffraction limited widefield imaging and structured illumination microscopy [222]. Despite these observations it is clear that OmpF insertion is biased towards mid-cell. This implies that that the BAM complexes found at the poles of the cells are not inserting new OMPs in these regions. There are two potential explanations for this lack of polar OmpF insertion.

1. It has been observed for all OMPs, including OmpF, tracked over long time courses, that old OMPs accumulate at the cell poles [189, 193]. This accumulation could result in significant protein crowding at the poles of cells, this crowding could prevent the BAM complex from effectively inserting new OMPs due simply to a lack of space.

2. The BAM complex, containing the integral OMP: BamA, would be expected to migrate to the cell poles like all other OMPs. Hence polar BAM is likely older and has a greater likelihood of having accumulated damage. Hence it is possible that polar BAM is non-functional and as a result cannot insert new OMPs at the cell poles.

Furthermore, OmpF mid-cell biased biogenesis likely explains the non-uniform patterns of OmpF distribution observed in the OmpF labelling experiments detailed in Chapter 4. In that non-uniform patterns are simply a result of a bias of OmpF insertion at mid-cell causing enrichment of OmpF in those regions.

5.3 Conclusions

In *E. coli* BL21(DE3), OmpF displayed limited recovery approximately 2 minutes after photobleaching, by comparison the inner membrane protein TolA showed significant fluorescence recovery over the same time period. When protein crowding of the outer membrane of *E. coli* is reduced by knocking out the highly abundant OmpA, no significant effect on OmpF long range diffusion is observed. In both MG1655 and MG1655 $\Delta ompA$, no significant fluorescence recovery is observed. PALM based single particle tracking of OmpF and the development of an analysis pipeline enabled the tracking and analysis of thousands of OmpF proteins. This revealed that OmpF is effectively immobile in the outer membrane, irrespective of protein crowding by OmpA. OmpF displayed a median diffusion coefficient of 0.0018 [0.00176, 0.00193] $\mu m^2 s^{-1}$ (99.9% CI) and a median confinement radius of 72 [71.4, 73.7] nm (99.9% CI) in *E. coli* MG1655, however these statistics were likely captured at the resolution limit of the PALM-SPT technique. On longer timescales on the order of hours, pulse chase labelling experiments revealed that "old" OmpF is pushed to the poles of the cells during growth and pulsed expression of OmpF revealed that the force for this pushing is provided by biased biogenesis of new OmpF at mid-cell.

Chapter 6

Pal Organisation and Dynamics

6.1 Introduction

The outer membrane protein Pal, peptidoglycan associated lipoprotein, is distinct from OmpF, BtuB and FepA investigated in the preceding chapters. Unlike these proteins, Pal is not an integral OMP and is instead anchored to the inner leaflet of the outer membrane by N-terminal glycerylcysteine linked acyl chains [171]. As the outer membrane of *E. coli* is asymmetric, Pal finds itself in an environment distinct from that of the OMPs, with its lipid domain surrounded by phosphatidylethanolamine (75%), phosphatidylglycerol (20%) and cardiolipin [26]. Pal also differs in an additional, important aspect, that being its interactions with elements of the underlying cell envelope. Unlike OmpF, BtuB and FepA; Pal binds non-covalently to the *meso*-diaminopimelate residue of the cell wall peptide cross linker. [70, 79, 169].

These two aspects of Pal: localisation to the inner leaflet of the outer membrane and non-covalent binding to the peptidoglycan make it an appropriate candidate to investigate the effect that underlying cell envelope elements have on protein diffusion and the general contribution that membrane environment has on outer membrane protein dynamics.

Little is known about the mobility of proteins anchored to the inner leaflet of the outer

membrane. To date, the diffusion of no bacterial inner leaflet outer membrane protein has been measured.

In this chapter, I conduct PALM based single particle tracking on an *E. coli* strain expressing a Pal-PAmCherry fusion protein. By analysing the subcellular localisation of these tracks I show that Pal is distributed evenly throughout cells but upon the onset of division, accumulates at the septum of dividing cells, providing evidence for the mechanism by which Pal stabilises the outer membrane of *E. coli* during cell division.

By analysing the single particle trajectories of Pal molecules, I show that in non-dividing and dividing cells Pal is highly restricted in its diffusion. By repeating these PALM-SPT experiments on an *E. coli* strain expressing Pal-PAmCherry with the peptidoglycan binding domain removed, termed Lipoylated-PAmCherry, I show that Pal restricted diffusion is caused by peptidoglycan binding and establish that the inner leaflet permits proteins embedded within it to diffuse in a Brownian but slow manner.

6.2 Results and Discussion

6.2.1 Pal Distribution changes with the *E. coli* cell cycle

To assess the organisation of Pal in cells, PALM-SPT was conducted with RKCK16, a strain engineered by Renata Kaminska to express chromosomal Pal-PAmCherry, retaining the function of WT Pal [72]. Before quantitative analysis was conducted, superresolution reconstructions of Pal distributions were generated from the raw PALM-SPT data (Figure 6.1). This revealed an apparent enrichment of Pal at the septum of dividing cells.

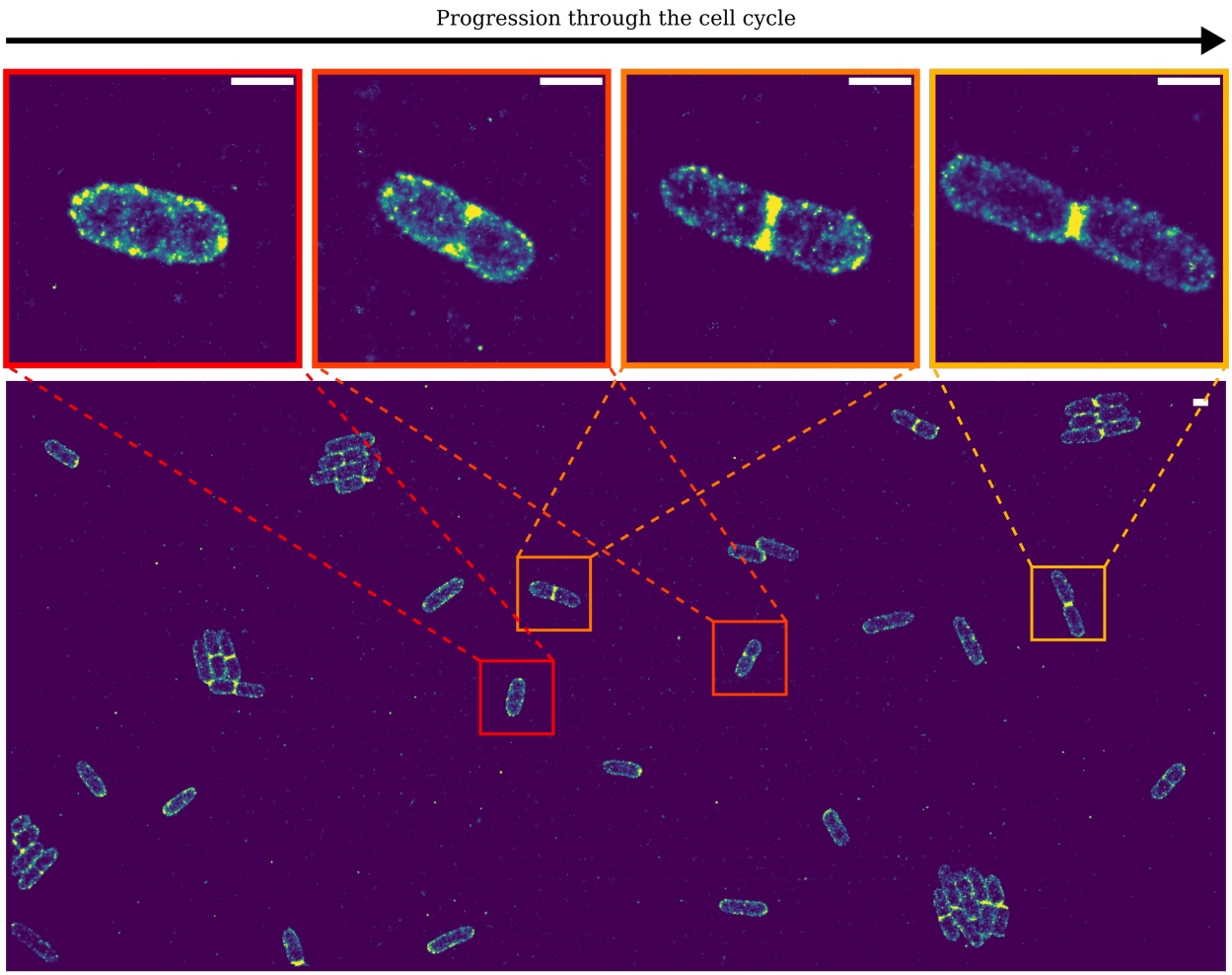

Figure 6.1: Superresolution reconstruction of Pal distribution in *E. coli*. PALM-SPT was conducted for 8638 frames at an exposure time of 50 ms. Laser lines and powers were used in an identical fashion as described for OmpF PALM-SPT. Gaussian fitting to localise particles was conducted using the ThunderSTORM ImageJ plugin. A normalised Gaussian representation at a magnification of 5 times relative to native sensor resolution was used to visualise the whole field of view of cells. For the magnified cells (top) a normalised Gaussian representation at a magnification of 20 times is used, cells were rotated for presentation at the same orientation. Scale bars represent a distance of 1 µm.

To quantitatively assess the distribution of Pal in dividing and non-dividing cells, PALM-SPT data was processed with the single particle tracking pipeline described in Chapter 5. Cells were categorised into dividing and non-dividing by the presence or absence of a septum in the superresolution reconstruction of the raw PALM-SPT data. For each Pal single particle track, the centroid coordinates were calculated and then normalised with respect to the cell.

Normalisation was conducted as follows:

1. For each field of view, a binary image of segmented cells was generated.

2. An ellipse was fitted to each segmented cell in the binary image to determine the long and short axis lengths of each cell.

3. Using the long and short axis lengths, the smallest bounding box that encapsulated the whole cell was determined.

4. The rotation of each bounding box was calculated and used to normalise the rotation of track centroids found within each cell. Rotation was conducted so that the cell's long axis was represented in the x dimension and short axis in the y.

5. The x and y dimensions of the rotated track centroids were then normalised so that the short axis spanned from 0 to 50 arbitrary units and the long axis from 0 to 100 arbitrary units.

Normalised track centroid data from multiple cells could then be compiled into a single normalised cell, before plotting as a heatmap of Pal distribution.

Track centroids from non-dividing cells were normalised and a heatmap of Pal distributions was generated (Figure 6.2). Pal was distributed with relative uniformity across the entirety of the cell. The normalised cell was subdivided into 5 regions: the 2 polar regions, the mid-cell region and 2 intermediate regions in between the mid-cell and each respective pole. The largest disparity of Pal distribution between regions was observed between the mid-cell (40 - 60 AU) and the right most pole (80 - 100 AU) at 3.4 percentage points (Figure 6.2).

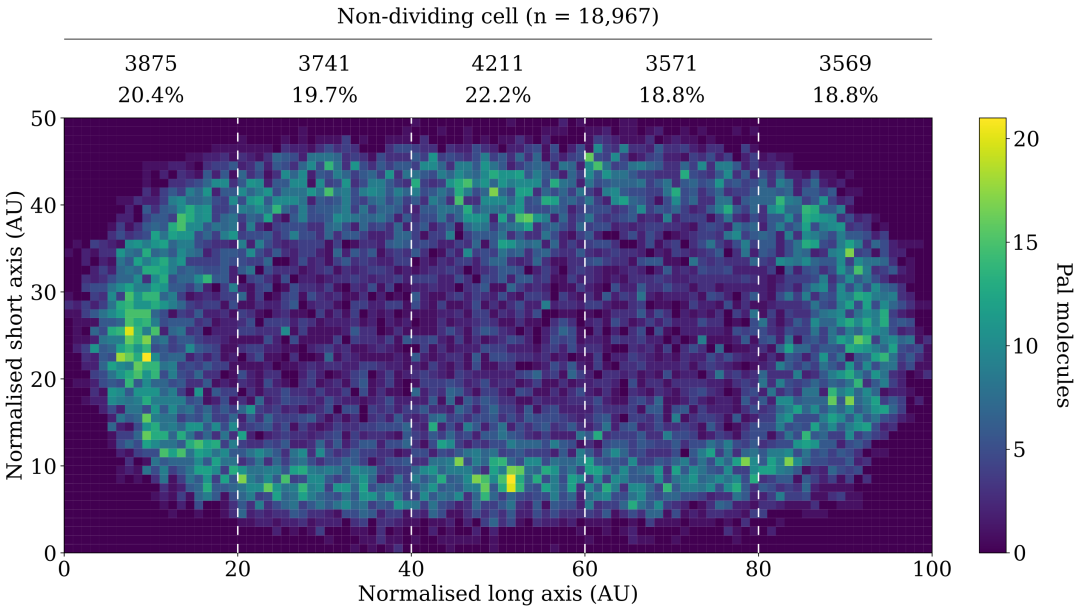

Figure 6.2: Distribution of Pal molecules in non-dividing *E. coli* cells. Single particle trajectory centroids were determined for each Pal molecule in PALM-SPT data. Track centroids were normalised with respect to the cell and the DBSCAN clustering algorithm was used to eliminate centroid outliers. A heatmap of Pal centroids was generated. The heatmap is subdivided into 5 regions: 2 polar regions, 2 intermediate regions and a mid-cell region. The number of particles within each region were measured.

The heatmap of Pal localisations for dividing cells differs significantly from that of non-dividing cells (Figure 6.3) Pal showed accumulation at mid cell in dividing cells. The largest disparity of Pal distribution in subcellular regions occurred between the septal/mid-cell (40 - 60 AU) region and the right most pole (80 - 100 AU) which differed by 21 percentage points. A 6 fold greater difference than observed in the equivalent regions in non-dividing cells.

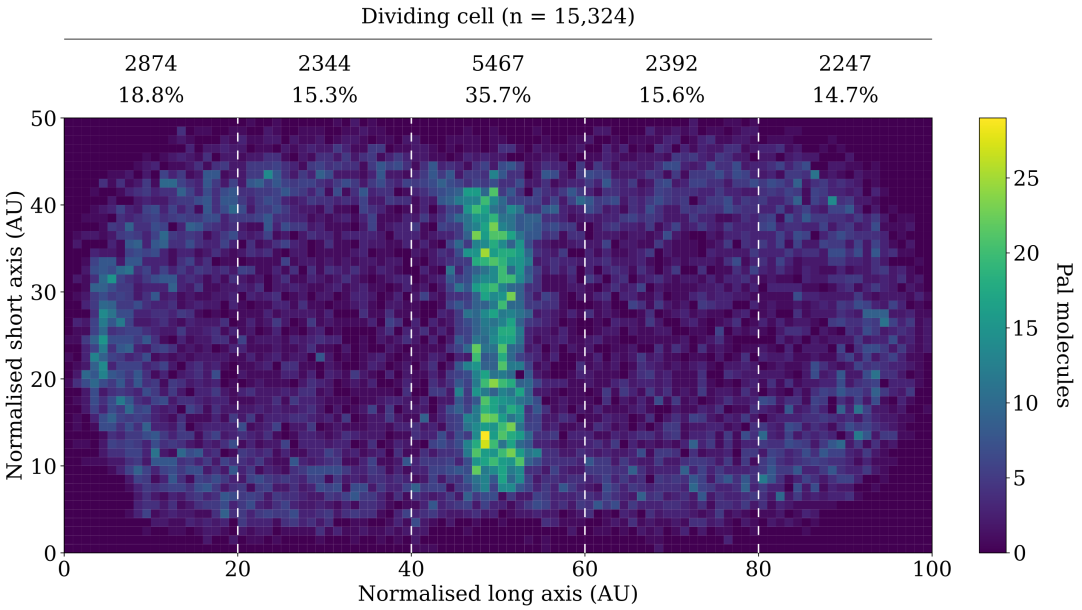

Figure 6.3: Distribution of Pal molecules in dividing *E. coli* cells. Single particle trajectory centroids were determined for each Pal molecule in PALM-SPT data. Track centroids were normalised with respect to the cell and the DBSCAN clustering algorithm was used to eliminate centroid outliers. A heatmap of Pal centroids was generated. The heatmap is subdivided into 5 regions: 2 polar regions, 2 intermediate regions and a mid-cell region. The number of particles within each region were measured.

By observing the subcellular locations of normalised Pal track centroids it is clear that Pal accumulates at the septum of dividing cells. This accumulation has physiological relevance for cell division in *E. coli*.

The location of Pal molecules shown in Figure 6.2 and Figure 6.3 were determined by conducting single particle tracking of Pal-PAmCherry molecules and for each track finding its centroid location and plotting this centroid location with respect to the cell. Track centroids were hence assumed to be equivalent to Pal-PAmCherry molecules. Importantly, gap-fitting was not conducted during the tracking of Pal-PAmCherry molecules, hence if a Pal-PAmCherry molecule were to briefly blink into an off state and begin fluorescing again it would be counted as two independent Pal-PAmCherry molecules. This would be a significant limitation if the absolute number of Pal-PAmCherry molecules needed to be counted, however, in the case of Pal-PAmCherry septal enrichment we were interested in the relative ratio of Pal-PAmCherry in the different regions of the cell. Hence, as blinking of

PAmCherry is stochastic, the probability of a blinking event would not be affected by the subcellular location of the Pal-PAmCherry molecule and therefore this blinking artefact is not likely to bias the results observed in Figure 6.2 and Figure 6.3.

Work conducted by Szczepaniak *et al.*, [72] to which data in this chapter contributed, showed by FRAP that TolA is required to recruit Pal molecules to mid-cell in a PMF dependent manner. Hence, the accumulation of Pal observed by PALM-SPT at mid-cell is not the result of biased biogenesis as observed in the case of OmpF, but instead is active recruitment of Pal molecules by the inner membrane Tol system. This enrichment of Pal at the septum is critical for proper septation of cells as Pal transduces the force of cell wall ingrowth to the outer membrane in order to aid in outer membrane invagination. The important role Pal plays in division is demonstrated in Pal knockout mutants which display multiple cell division defects including cell filamentation in low salt media and septal blebbing [223].

6.2.2 Pal Displays Highly Restricted Diffusion in the Outer Membrane

FRAP experiments of Pal-mCherry have shown that recovery after photobleaching occurs more readily in dividing cells compared to non-dividing cells over a time period of 10 minutes. To determine if this diffusion disparity is borne out on shorter timescales and at a finer lateral resolution, single particle tracks from non-dividing and dividing cells were analysed to extract diffusion coefficients and confinement radii.

Single particle tracks in non-dividing cells displayed slow diffusion (Figure 6.4) with a median diffusion coefficient of 0.004 [0.00376, 0.00428] $\mu m^2 s^{-1}$ (99.9% CI) from a total of 12,489 tracks. Normalised, representative tracks with diffusion coefficients in a narrow band around the median diffusion coefficient value showed constricted diffusion and appeared to lack Brownian motion (Figure 6.4. Inset).

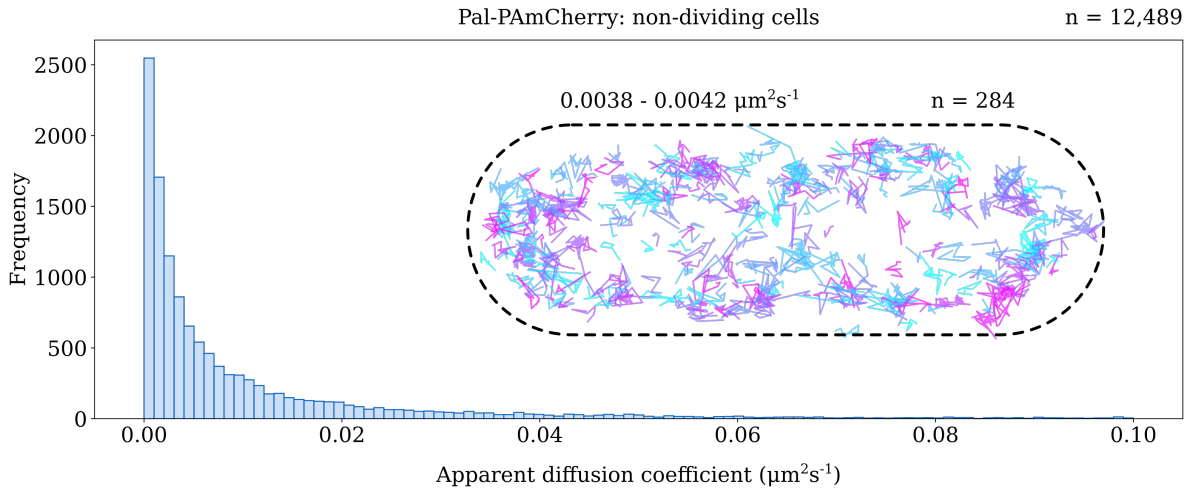

Figure 6.4: Pal diffusion coefficients and representative single particle tracks in non-dividing *E. coli* cells. Main: diffusion coefficient histogram of Pal single particle trajectories, the entire range of diffusion coefficients is not shown, only diffusion coefficients from 0 to 0.10 $\mu m^2 s^{-1}$ are displayed. From a total of 12,489 Pal trajectories a median diffusion coefficient of 0.0040 [0.00376, 0.00428] $\mu m^2 s^{-1}$ (99.9% CI) was calculated. The upper and lower bounds of the median diffusion coefficient were determined from bootstrapping, the data was resampled 100,000 times and the 0.05 and 99.95 percentiles of the resampled medians defined the 99.9% confidence interval. Inset: Pal representative tracks extracted from a narrow range around the median diffusion coefficient: 0.0038 - 0.0042 $\mu m^2 s^{-1}$. A total of 284 tracks are displayed. Tracks are normalised with respect to the cell they were collected from. Track colouring is for illustrative purposes only.

The confinement radii of Pal-PAmCherry tracks reflect the slow, constricted nature of diffusion (Figure 6.5.A. and Figure 6.5.B.) with a relatively constrained 92 [90.4, 94.7] nm (99.9% CI) median confinement radius.

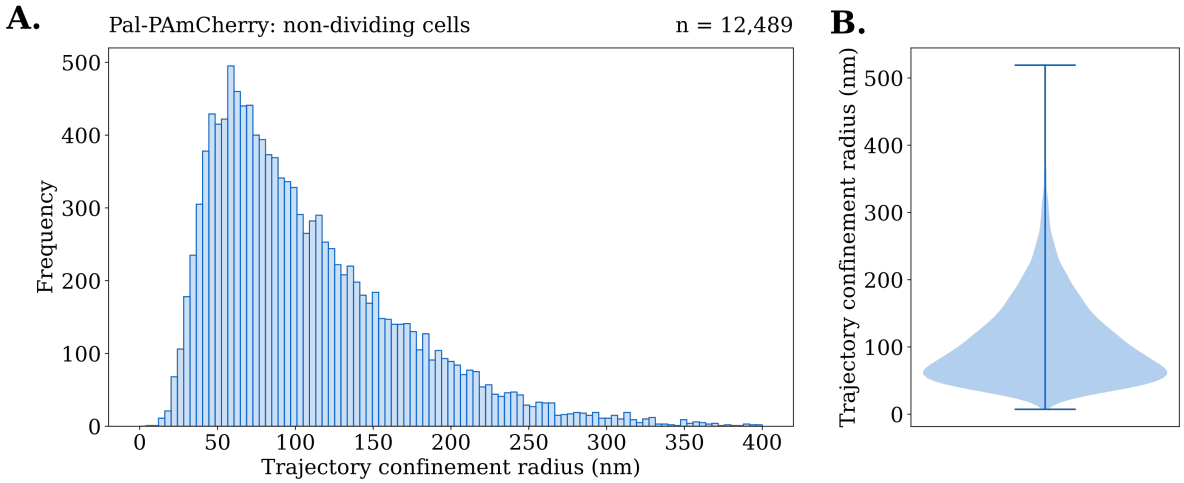

Figure 6.5: Pal confinement radii in non-dividing *E. coli* cells. A. Confinement radii histogram of Pal single particle trajectories, the entire range of confinement radii is not shown, only confinement radii from 0 to 400 nm are displayed. From a total of 12,489 Pal trajectories a median confinement radius of 92 [90.4, 94.7] nm (99.9% CI) was calculated. The upper and lower bounds of the median confinement radii were determined from bootstrapping, the data was resampled 100,000 times and the 0.05 and 99.95 percentiles of the resampled medians defined the 99.9% confidence interval. **B.** Violin plot of Pal confinement radii displaying the probability density for the entire range of confinement radii observed.

Pal single particle tracks in dividing cells displayed a similar diffusion coefficient distribution to those in non-dividing cells (Figure 6.6). From 10,305 single particle tracks a marginally higher diffusion coefficient of 0.0043 [0.00403, 0.00461] $\mu m^2 s^{-1}$ (99.9% CI) was calculated. Visually, Pal single particle tracks in dividing cells resembled those found in non-dividing cells, displaying little lateral motion (Figure 6.6. Inset).

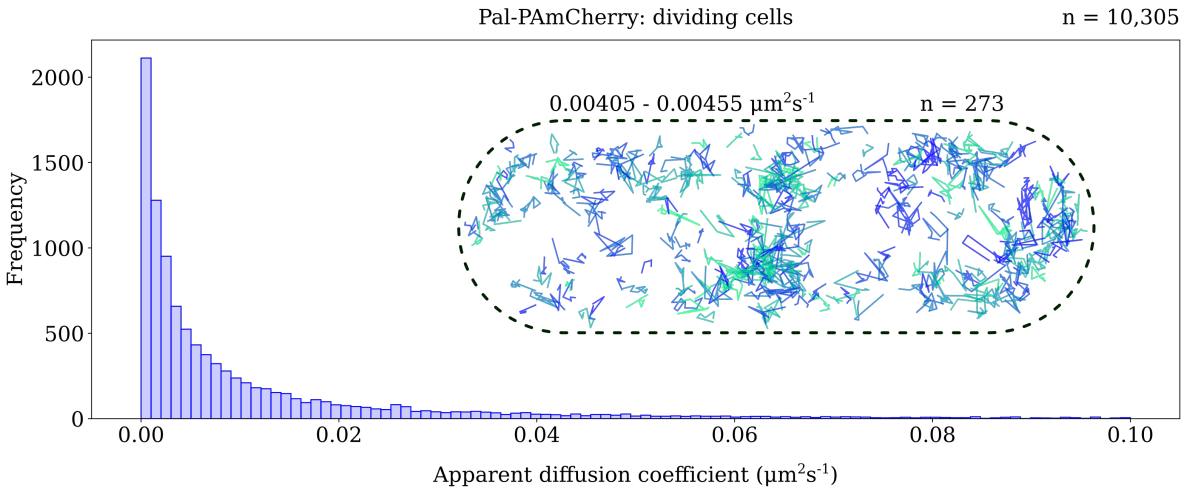

Figure 6.6: Pal diffusion coefficients and representative single particle tracks in dividing *E. coli* cells. Main: diffusion coefficient histogram of Pal single particle trajectories, the entire range of diffusion coefficients is not shown, only diffusion coefficients from 0 to 0.10 $\mu m^2 s^{-1}$ are displayed. From a total of 10,305 Pal trajectories a median diffusion coefficient of 0.0043 [0.00403, 0.00461] $\mu m^2 s^{-1}$ (99.9% CI) was calculated. The upper and lower bounds of the median diffusion coefficient were determined from bootstrapping, the data was resampled 100,000 times and the 0.05 and 99.95 percentiles of the resampled medians defined the 99.9% confidence interval. Inset: Pal representative tracks extracted from a narrow range around the median diffusion coefficient: 0.00405 - 0.00455 $\mu m^2 s^{-1}$. A total of 273 tracks are displayed. Tracks are normalised with respect to the cell they were collected from. Track colouring is for illustrative purposes only.

Consistent with diffusion coefficient data, Pal was highly constrained in the outer membrane (Figure 6.7.A. and Figure 6.7.B.) with an median confinement radius of 96 [93.4, 98.9] nm (99.9% CI), marginally greater than that observed for Pal in non-dividing cells at 92 [90.4, 94.7] nm (99.9% CI).

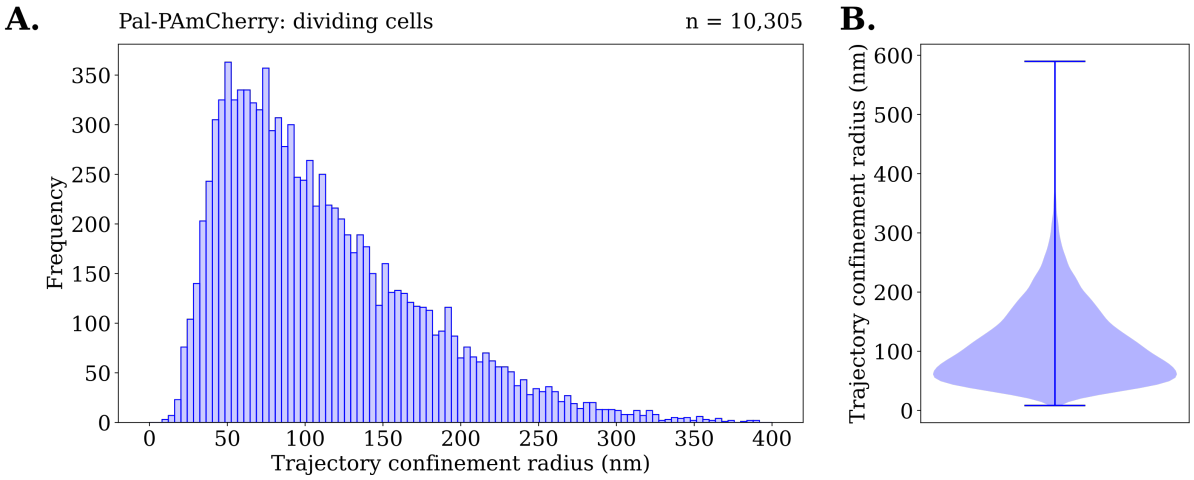

Figure 6.7: Pal confinement radii in dividing *E. coli* cells. A. Confinement radii histogram of Pal single particle trajectories, the entire range of confinement radii is not shown, only confinement radii from 0 to 400 nm are displayed. From a total of 10,305 Pal trajectories a median confinement radius of 96 [93.4, 98.9] nm was calculated. The upper and lower bounds of the median confinement radii were determined from bootstrapping, the data was resampled 100,000 times and the 0.05 and 99.95 percentiles of the resampled medians defined the 99.9% confidence interval. **B.** Violin plot of Pal confinement radii displaying the probability density for the entire range of confinement radii observed.

Direct comparisons of Pal diffusion coefficients (Figure 6.8.A.) and confinement radii (Figure 6.8.B.) reveal that the distribution of both is almost identical. Bootstrapping to determine confidence intervals shows that diffusion coefficients in non-dividing and dividing cells display no significant difference. However, the confinement of tracks in dividing cells were marginally but significantly larger in dividing cells than non-dividing cells at a CI of 95%.

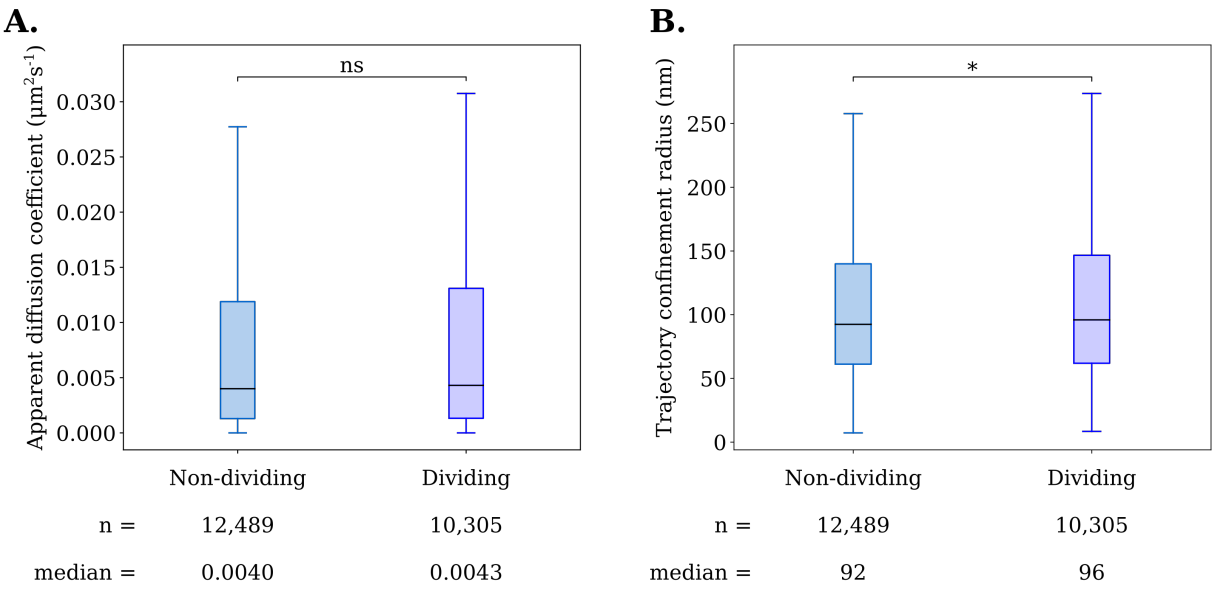

Figure 6.8: Comparison of diffusion coefficients and confinement radii for Pal in non-dividing and dividing cells. A. Box plots of Pal diffusion coefficients in non-dividing (light blue) and dividing cells (blue). **B.** Box plot of Pal confinement radii in non-dividing (light blue) and dividing cells (blue). Statistical significance was determined from bootstrapping, the data was resampled 100,000 times and the 95, 99 and 99.9% confidence intervals were determined. ns: no significant difference. * $p < 0.05$. ** $p < 0.01$. *** $p < 0.001$.

6.2.3 Pal Diffusion is Restricted by Peptidoglycan Binding

The diffusion of lipoylated inner leaflet outer membrane proteins have been rarely studied. The diffusion coefficients determined for Pal in this thesis and reported in [72] represent the first recorded for a lipoylated inner leaflet outer membrane protein in *E. coli*. As a result of this dearth of information there is no data available to suggest how such a class of protein would be expected to diffuse if unimpeded. Pal is unable to act as a benchmark in this case due to its interaction with the underlying cell wall.

Therefore, to investigate how an unimpeded lipoylated inner leaflet outer membrane protein diffuses, Renata Kaminska engineered an *E. coli* strain (RKCK19) expressing Pal-PAmCherry with the peptidoglycan binding domain removed, referred to as lipoylated-PAmCherry herein.

PALM-SPT was conducted on this strain and diffusion coefficients were determined from

a total of 30,640 individual lipoylated-PAmCherry trajectories (Figure 6.9.). The distribution of diffusion coefficients showed that lipoylated-PAmCherry diffused at greater rates than Pal, with a median diffusion coefficient of 0.0205 [0.0199, 0.0212] $\mu m^2 s^{-1}$ (99.9% CI). This was reflected visually in the representative tracks selected around the median. These tracks do not diffuse in the restricted manner observed for Pal and instead diffuse in a Brownian manner (Figure 6.9. Inset).

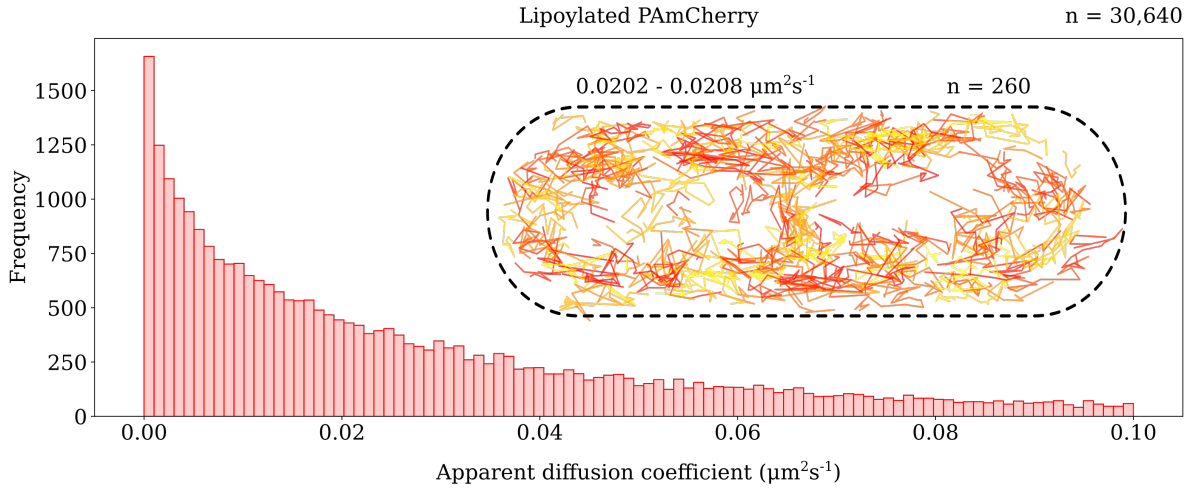

Figure 6.9: Lipoylated-PAmCherry diffusion coefficients and representative single particle tracks in *E. coli* cells. Main: diffusion coefficient histogram of Lipoylated-PAmCherry single particle trajectories, the entire range of diffusion coefficients is not shown, only diffusion coefficients from 0 to 0.10 $\mu m^2 s^{-1}$ are displayed. From a total of 30,640 Lipoylated-PAmCherry trajectories a median diffusion coefficient of 0.0205 [0.0199, 0.0212] $\mu m^2 s^{-1}$ (99.9% CI) was calculated. The upper and lower bounds of the median diffusion coefficient were determined from bootstrapping, the data was resampled 100,000 times and the 0.05 and 99.95 percentiles of the resampled medians defined the 99.9% confidence interval. Inset: Lipoylated-PAmCherry representative tracks extracted from a narrow range around the median diffusion coefficient: 0.0202 - 0.0208 $\mu m^2 s^{-1}$. A total of 260 tracks are displayed. Tracks are normalised with respect to the cell they were collected from. Track colouring is for illustrative purposes only.

The less restricted diffusion observer for lipoylated-PAmCherry is also reflected in the less constrained confinement radii observed: 148 [146.5, 149.7] nm (99.9% CI). The confinement radii histogram shows both a broader peak that is offset towards larger confinement radii compared to Pal (Figure 6.10.A. and Figure 6.10.B.).

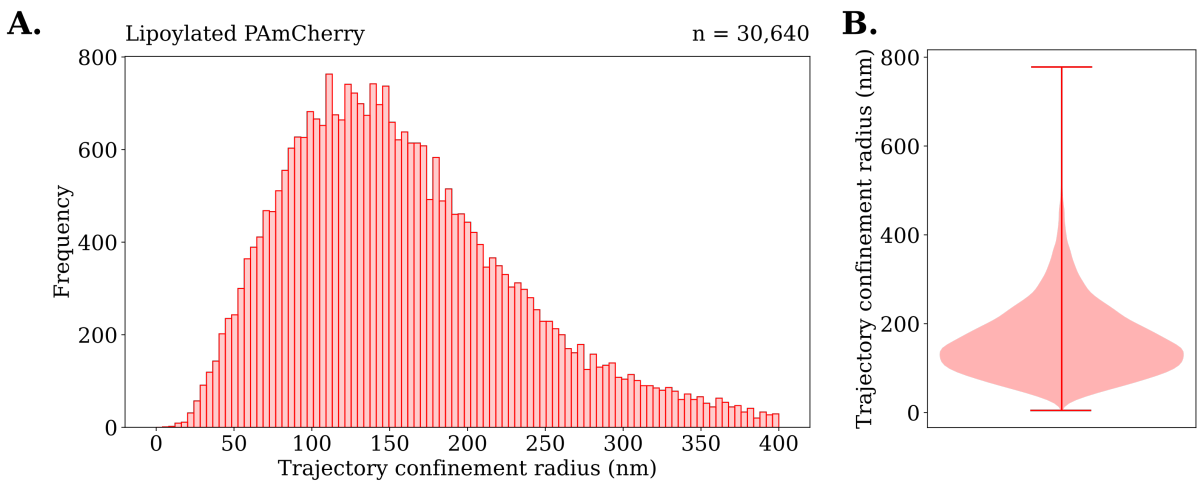

Figure 6.10: Lipoylated-PAmCherry confinement radii in *E. coli* cells. A. Confinement radii histogram of Lipoylated-PAmCherry single particle trajectories, the entire range of confinement radii is not shown, only confinement radii from 0 to 400 nm are displayed. From a total of 30,640 Lipoylated-PAmCherry trajectories a median confinement radius of 148 [146.5, 149.7] nm (99.9% CI) was calculated. The upper and lower bounds of the median confinement radii were determined from bootstrapping, the data was resampled 100,000 times and the 0.05 and 99.95 percentiles of the resampled medians defined the 99.9% confidence interval. **B.** Violin plot of Lipoylated-PAmCherry confinement radii displaying the probability density for the entire range of confinement radii observed.

Direct comparisons of Pal-PAmCherry (in non-dividing and dividing cells) and lipoylated-PAmCherry diffusion coefficients reveal that upon removal of the peptidoglycan binding domain, rate of diffusion increases significantly by a factor of almost 5, from 0.0042 [0.00394, 0.00434] $\mu m^2 s^{-1}$ (99.9% CI) to 0.0205 [0.0199, 0.0212] $\mu m^2 s^{-1}$ (99.9% CI) (Figure 6.11.A.). A significant increase in track confinement is also observed, an increase of 1.6 times, from 94 [92.4, 95.6] nm (99.9% CI) to 148 [146.5, 149.7] nm (99.9% CI) (Figure 6.11.B.).

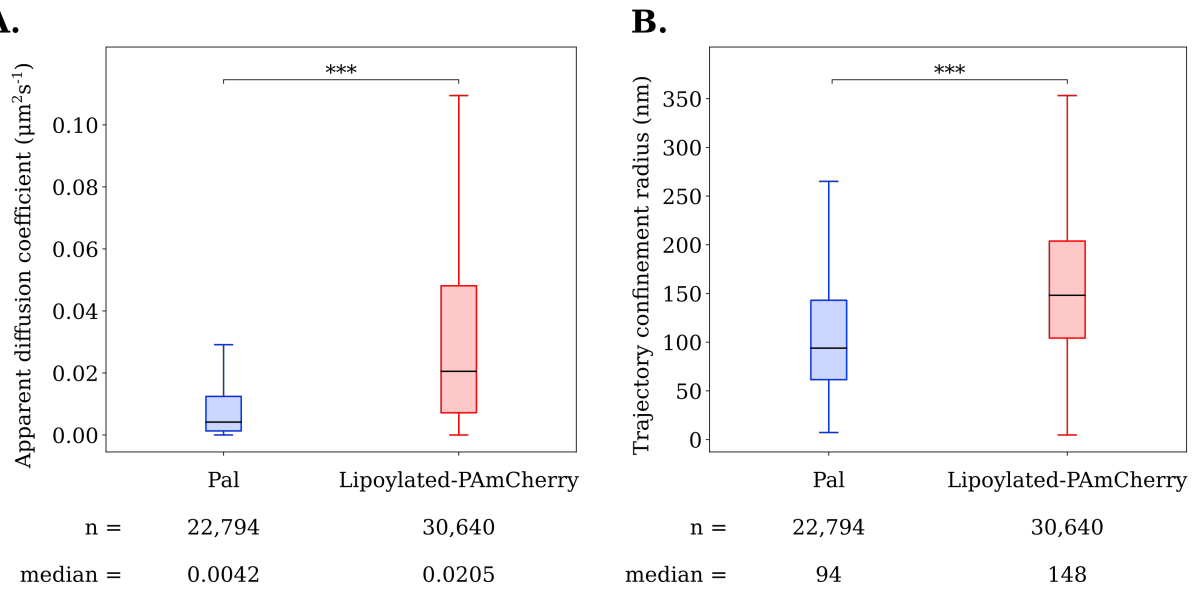

Figure 6.11: Comparison of diffusion coefficients and confinement radii for Pal-PAmCherry and lipoylated-PAmCherry. A. Box plots of Pal-PAmCherry (blue) and lipoylated-PAmCherry (red) diffusion coefficients. **B.** Box plots of Pal-PAmCherry (blue) and lipoylated-PAmCherry (red) confinement radii. Statistical significance was determined from bootstrapping, the data was resampled 100,000 times and the 95, 99 and 99.9% confidence intervals were determined. ns: no significant difference. * $p < 0.05$. ** $p < 0.01$. *** $p < 0.001$.

The significant increase in diffusion observed upon removal of the Pal peptidoglycan binding domain demonstrates that this non-covalent interaction is the cause of Pal's slow diffusion.

It is worth noting that the removal of the Pal peptidoglycan binding domain results in a phenotype wherein cells grow slower, have a more rounded morphology and can display a reduction in outer membrane integrity. It is hence possible that, specifically the reduction in outer membrane integrity, could cause faster diffusion of lipoylated proteins. A potential experiment that could determine the contribution of this phenotype to lipoylated-PAmCherry diffusion would be to repeat single particle tracking in the lipoylated-PAmCherry expressing strain in which WT Pal is reintroduced on an inducible plasmid to restore outer membrane integrity. The diffusion coefficients and confinement radii determined from this experiment would then indicate the contribution of outer membrane integrity on lipoylated-PAmCherry

diffusion.

In *E. coli*, benchmarks exist for diffusion of proteins in almost all physiologically relevant subcellular regions. FRAP investigations identified that cytoplasmic GFP diffused at a rapid rate of 9.0 $\mu m^2 s^{-1}$ [224]. Periplasmic GFP diffused at a marginally slower 2.6 $\mu m^2 s^{-1}$ [224], inner membrane freely diffusible TatA-GFP diffused at a rate of 0.13 $\mu m^2 s^{-1}$ [224]. Rates of diffusion are known for low copy number OMPs and high copy number OMPs, 0.013 and 0.0018 $\mu m^2 s^{-1}$, respectively (BtuB [189], OmpF (Chapter 5)). Conspicuously missing from these benchmarks of diffusion in subcellular regions, however, is the inner leaflet of the outer membrane. In this case, lipoylated-PAmCherry can act as the benchmark of inner leaflet outer membrane protein diffusion at 0.0205 $\mu m^2 s^{-1}$.

Despite the inner leaflet of the outer membrane and the inner membrane containing a similar composition of lipids: phosphatidylethanolamine (75%), phosphatidylglycerol (20%) and cardiolipin [26], the rate of free diffusion of proteins in these membrane differ by an order of magnitude. One explanation for this significant discrepancy could be the population of the outer membrane by OMPs. As OMPs are integral proteins, they span both leaflets of the outer membrane. Furthermore these OMPs, especially the most abundant among them such as OmpF (0.0018 $\mu m^2 s^{-1}$), are effectively immobile in this membrane (Chapter 5). Hence, any lipoylated protein tethered to the inner leaflet of the outer membrane by a lipid group must diffuse around a membrane densely populated by immobile proteins. It is therefore likely that such proteins would diffuse significantly slower than an inner membrane protein in which all elements that constitute that membrane—both proteins and lipids—are freely diffusible.

6.3 Conclusions

Through the use of PALM-SPT and a novel localisation normalisation program, the subcellular location of single molecules of Pal were determined. This found that Pal is distributed

throughout the cell with relative uniformity. Upon the onset of division, however, Pal accumulates at the septum of dividing cells. By analysing the diffusion coefficients and confinement radii of Pal-PAmCherry, Pal was shown to diffuse slowly and in a confined manner in both non-dividing and dividing cells. This confined diffusion was shown to be caused by non-covalent binding to the underlying cell wall by PALM-SPT of lipoylated-PAmCherry which diffused at a significantly faster rate. Diffusion of lipoylated-PAmCherry provides a benchmark for the diffusive properties one would expect to find of a lipoylated inner leaflet outer membrane protein.

Chapter 7

Discussion

7.1 General Discussion

7.1.1 Colicin N Uses OmpF as its Receptor and Translocator Making it an Appropriate Label Candidate.

The critical role OmpF plays in Colicin N binding and translocation was first revealed in cytotoxicity assays conducted in OmpF knockout strains. These strains were both insensitive to Colicin N and displayed little surface adsorption of radioactive Colicin N [185]. This was further reinforced when it was observed that antibodies directed against OmpF competed against Colicin N for OmpF binding [186]. The three domains of Colicin N (Figure 3.1) were first determined, with remarkable accuracy, by assessing the binding and cytotoxicity of various Colicin N fragments [225]. This showed that Colicin N contained an N-terminal domain required for translocation, a central OmpF binding domain and a C- terminal pore forming cytotoxic domain. When the crystal structure of Colicin N was determined, these three domains were apparent: a globular receptor binding domain, a predominantly alpha-helical pore forming domain and a translocation domain not present in the crystal structure (indicative of an intrinsically disordered structure, consistent with its function as a translocation domain which must thread through the outer membrane.) [202].

The crystal structure of Colicin N is notable in its compact structure. By contrast, Colicin Ia—also a pore forming colicin—has a structure remarkably distinct from Colicin N. Though containing a pore forming, receptor binding and translocation domain, Colicin Ia has a elongated structure 210 Å in length, in which the receptor binding domain and translocation domain are found on opposite sides of the molecule [226]. This difference in structure was logically consistent with the consensus reflected in the literature at the time; that BtuB was the receptor protein for Colicin Ia, and OmpF was the translocator protein, hence the long structure was required to ensure BtuB and OmpF could be engaged simultaneously by either end of the colicin; Colicin N however could be compact in its structure as its receptor and translocator were the same: OmpF [181].

This consensus, that Colicin N used OmpF as both its primary receptor protein and translocator protein, was overturned as the result of two investigations. The first found, through genome wide screens, that Colicin N sensitivity required expression of OmpF, the inner membrane Tol-Pal system components: TolA, TolQ and TolR and multiple genes related to LPS biogenesis [187]. Following this, it was shown through SPR and STD-NMR that the globular receptor binding domain of colicin N binds to the inner core of LPS [188]. These two studies led to suggestions in the literature that LPS represented the receptor for Colicin N, not OmpF [203, 227, 228].

The suggestion that OmpF was not the primary receptor of Colicin N had significant implications for the appropriateness of using Colicin N as the basis for a fluorescent label of OmpF. Work in this thesis contributed to a paper showing that Colicin N does, in fact, use OmpF as both its primary receptor and translocator in *E. coli* [199]. In this paper, mass spectrometry of a tryptic digest of OmpF and Colicin N revealed the presence of an OmpF binding site (OBS) on Colicin N which would necessarily bind within the lumen of an a single OmpF barrel. By the use of a modified Ouchterlony assay, Colicin N was shown to harbour an additional OmpF binding site. ITC showed that these binding sites existed as an N-terminal OBS consisting of residues 2-18 and the globular receptor binding domain,

residues 90 - 185. A key experiment that demonstrated Colicin N's exclusive binding to OmpF as its primary receptor was the labelling and fluorescence intensity quantification of various porin knockout strains (Figure 3.14). This showed that in the absence of OmpF expression no appreciable level of fluorescence labelling was observed despite the presence of LPS in these strains.

It should be noted, however, that although not in itself the primary receptor for Colicin N, LPS plays an important role in Colicin N toxicity in two ways.

1. Through ITC it was shown *in vitro* that the binding affinity of Colicin N to OmpF was increased two fold in the presence of LPS [199].

2. LPS and OmpF interact extensively in the outer membrane, this interaction is critical for the formation of stable OmpF trimers from metastable trimers [104]. Hence for OmpF to properly assemble into the outer membrane and therefore act as a receptor for Colicin N, LPS must be present. This provides an explanation for the requirement of LPS core biogenesis for Colicin N sensitivity.

The mechanism of Colicin N entry into target cells has therefore been shown to involve OmpF in both reception and translocation across the outer membrane. This makes Colicin N fluorescent fusion proteins appropriate labels for investigating OmpF organisation and dynamics. Understanding the mechanism of import of Colicin N has also allowed for appropriate control experiments to be conducted such as showing that TolA binding by the TABS within the translocation domain has no effect on apparent OmpF organisation (Chapter 4, section 2.3.).

7.1.2 The Organisation of OmpF and Pal are Both Linked to Cell Cycle but by Independent Mechanisms.

At copy numbers of up to 88,988 OmpF proteins per cell [44], the distribution of OmpF was expected to differ significantly from that of BtuB and FepA, expressed at levels an

order of magnitude lower. Comparing the image simulations of CSR distributions of BtuB and FepA to their experimental equivalent indicated that these proteins might be randomly distributed in the cell. Based on this, one could assume that OmpF would follow the same pattern and reflect its equivalent CSR simulation images. CSR simulation images predicted a uniform fluorescence signal all across the surface of the cell. This prediction was indeed often borne out in experimental images. However, a key observation made during high-throughput widefield imaging, revealed that although OmpF was often distributed "uniformly" it also formed 5 other categories of organisation. These 5 categories diverged significantly from the CSR simulation images. After confirming that these distributions were not simply the result of a labelling or imaging artefact, the following question could be raised: what is causing these non-uniform distributions?

Analysing the surface organisation of OMPs has been used in the past to investigate and understand the underlying mechanisms that give rise to such organisation [189, 191]. By imaging LamB using timelapse fluorescence microscopy the organisation of this protein into puncta was shown to be a result of outer membrane biogenesis by Ursell *et al.* [191]. Rassam *et al.*, showed that puncta of BtuB and the BAM complex component: BamC, colocalised in the outer membrane, showing that BtuB assembly into the OM by the BAM complex resulted in its distribution [189].

By displaying OmpF distributions as a kymograph, sorted by cell length, a likely cause of the non-uniform OmpF distributions could be deduced. Short cells typically recapitulated the unipolar OmpF distribution, as cells elongated fluorescence intensity increased at mid cell recapitulating both the mid-cell island and two island distributions and the longest cells recapitulated the septal OmpF distribution. Further PALM imaging supported the conclusion from this kymograph data that OmpF organisation was linked to the cell cycle.

By conducting short, pulsed expression of OmpF in the $\Delta ompF$, $\Delta ompC$, $\Delta lamB$ strain BZB1107, the biogenesis of OmpF was shown to display mid-cell bias in growing cells. This implied that the non-uniform distributions of OmpF are result of subcellular bias of OmpF

insertion into the outer membrane leading to areas of relative OmpF enrichment.

Pal distribution also displayed a link to the cell cycle. In non-dividing cells Pal was observed throughout the cell with relative uniformity. However, upon the onset of cell division Pal became enriched in the septum. Based on what was observed for OmpF it could be expected that Pal enrichment at the septum occurred by an analogous mechanism. *i.e.* the lipoprotein outer membrane biogenesis machinery: Lol, preferentially assembled Pal into the outer membrane at the division site. However, Pal accumulation at the septum requires functional TolA, TolQ, TolR and TolB [72, 229, 230], indicating that existing Pal is reorganised and recruited to the septum of dividing cells in a PMF dependent manner. At the septum Pal carries out one of its major functions: transducing the force of cell wall ingrowth to the outer membrane to aid in OM invagination [72].

7.1.3 The Dynamics of OmpF Shares Similarities With Low Copy Number OMPs but Differs in a Few Important Ways.

FRAP of OmpF labelled with Colicin N^{1-185}mCherry in BL21(DE3), MG1655 and MG1655 Δ*ompA* revealed that in all of these strains, OmpF displayed no significant long range diffusion. Analogous FRAP experiments of BtuB in *E. coli* JM83, revealed a similar lack of long range diffusion, with no significant fluorescence recovery observed 180 s post-bleach [189].

Despite OmpF and BtuB both lacking long range diffusion, differences in diffusion can be observed when investigated at finer resolutions. Two studies have investigated the diffusion of BtuB in the OM [189,231]. Single particle tracking of antibody labelled BtuB revealed a slow average apparent diffusion coefficient of 0.05 $\mu m^2 s^{-1}$ from a total of 101 tracks [231]. Single particle tracking of Colicin E9 labelled BtuB revealed a slower average apparent diffusion coefficient of 0.013 $\mu m^2 s^{-1}$ from 63 tracks [189]. OmpF, by contrast, displays a significantly slower average apparent diffusion coefficient of 0.0018 $\mu m^2 s^{-1}$ though it can be concluded that, in actuality, OmpF is likely to be essentially immobile in the outer membrane and that

this diffusion coefficient is a measure of experimental noise as fixed *E. coli* cells displayed an average OmpF diffusion coefficient of 0.0029 $\mu m^2 s^{-1}$.

LPS, being a major component of the outer leaflet of the outer membrane, is likely to have a significant effect on diffusion. LPS has been shown to diffuse slowly in the outer membrane [Sandip Kumar, unpublished observations.] and OmpF has been shown to interact extensively with LPS, harbouring LPS binding sites. Furthermore, investigations into outer membrane protein-protein interactions show that diffusion of BtuB is identical in the presence or absence of LPS [232]. Taken together, the difference in diffusion between OmpF and BtuB could be caused by interaction with slowly moving LPS. With OmpF interacting extensively with LPS, slowing its diffusion relative to BtuB which doesn't undergo such interactions.

In addition to this possible physiological difference, it is worth noting the effect of statistical strength on determining an accurate value for diffusion coefficients. By collecting and determining diffusion coefficients from individual tracks, one is effectively sampling from a distribution, the more tracks analysed results in this distribution being represented with greater accuracy. Determining average apparent diffusion coefficients for BtuB from 101 and 63 tracks [189, 231], results in the complete distribution of diffusion coefficients being sampled with relatively few tracks. This may result in average diffusion coefficients with limited accuracy and therefore makes direct comparisons against OmpF diffusion difficult. It is hence possible that BtuB could be as immobile in the outer membrane as OmpF and the measures for BtuB diffusion coefficients represent the limit of SPT resolution, much like the diffusion coefficients for OmpF diffusion in this thesis are likely to represent the resolution limit achievable with PALM-SPT.

When observed on longer timescales, in the order of hours, OmpF and other OMPs share similar dynamics. OmpF undergoes gradual movement towards "old" poles in growing cells. This polar localisation is clearly visible after only 30 minutes and becomes more pronounced through to 90 minutes of growth. Using a different method involving confocal timelapse imaging of BtuB, Rassam *et al.*, showed that BtuB undergoes this same polar localisation

on equivalent timescales [189]. Bergmiller *et al.*, showed that the transmembrane drug efflux pump TolC-AcrAB also localised to the poles of cells after multiple cell divisions and this polar localisation was dependent on the presence of the outer membrane TolC protein [193]. In the cases of BtuB and OmpF, a subcellular bias for insertion of new OMPs into the outer membrane was shown. This biased insertion represents the driving force for OMP polar localisation.

The observation that both low copy number OMPs (BtuB) and high copy number OMPs (OmpF), localise to the poles during growth supports the hypothesis proposed by Rassam *et al.*, that polar localisation represents the method by which *E. coli* achieves outer membrane protein turnover [189].

The outer membrane of *E. coli* is a relatively inaccessible subcellular region, this combined with the significant stability of folded β-barrel OMPs [233], means that once OMPs are inserted into the OM they cannot be removed. In the absence of metabolic turnover, polar localisation of OMPs provides the cell with a means to rapidly turnover the protein content of its outer membrane: a viable method by which fast dividing bacteria such as *E. coli* can react to changes in the environment.

7.1.4 The Two Leaflets of the OM Represent Vastly Different Environments That Affect Protein Mobility.

In the inner leaflet of the outer membrane, Pal diffused in a confined manner with a median diffusion coefficient of 0.0042 $\mu m^2 s^{-1}$. This rate of diffusion is significantly greater (99.9% CI) than OmpF in fixed cells at 0.0029 $\mu m^2 s^{-1}$ as this value represents the effective resolution limit of PALM-SPT. We can hence be confident that OmpF diffuses significantly slower than Pal, a remarkable difference considering that Pal is known to bind to the immobile cell wall.

Upon removal of the peptidoglycan binding domain of Pal-PAmCherry, yielding lipoylated-PAmCherry, the rate of diffusion increased almost 5 fold and tracks diffused in a visibly Brownian manner. The diffusion coefficient obtained for lipoylated-PAmCherry of 0.0205 $\mu m^2 s^{-1}$

represents a benchmark for unimpeded diffusion of lipoylated outer membrane proteins in *E. coli*.

The inner leaflet of the outer membrane has a composition similar to that of the inner membrane, phosphatidylethanolamine (75%), phosphatidylglycerol (20%) and cardiolipin [26]. Hence it would be logical to predict that diffusion of proteins would be similar in these two subcellular regions. However lipoylated-PAmCherry diffuses at a rate over 6 times slower than inner membrane TatA-GFP at 0.13 $\mu m^2 s^{-1}$. This indicates that although the inner leaflet of the outer membrane has a similar lipid composition to the inner membrane, it represents an environment that restricts the diffusion of proteins tethered to it. This observation is logically consistent with what is known about diffusion in the outer membrane. OMPs span both leaflets of the outer membrane, in this membrane OmpA, BtuB, Cir and LamB are known to diffuse extremely slowly and OmpF to be effectively immobile. Therefore lipoylated proteins must navigate an extremely crowded environment of immobile proteins, likely leading to slower diffusion compared to the relatively fluid inner membrane.

Taken together, it can be concluded that the outer leaflet of the outer membrane is an environment that permits very little lateral diffusion of OmpF, to such a degree that proteins that bind to the immobile cell wall display faster diffusion. The inner leaflet, by contrast, is an environment that permits much faster and freer diffusion of tethered inner membrane proteins. However, the presence of outer and inner leaflet spanning OMPs limits the rate of diffusion in this leaflet compared to the inner membrane.

Table 7.1: The diffusion of *E. coli* outer membrane proteins. Diffusion coefficients and confinement radii for *E. coli* outer membranes proteins from the literature. N number refers to the number of individual tracks used to determine diffusion coefficients and confinement radii. NR: not reported.

Protein	**D_{app} ($\mu m^2 s^{-1}$)**	**Confinement Radius (nm)**	**N**	**Reference**
LamB	0.15	15	1	[192]
LamB	0.059	NR	NR	[234]
BtuB	0.05	NR	101	[231]
BtuB	0.10	NR	70	[231]
BtuB	0.013	300	62	[189]
Cir	0.019	300	41	[189]
OmpF	0.006	50	172	[231]
Porins	$2x10^{-7}$	NR	NR	Benn
OmpF	0.0018	72	21,336	This Thesis
Pal	0.0042	94	22,794	This Thesis
Lipoylated PAmCherry	0.0205	148	30,640	This Thesis

Diffusion coefficients and confinement radii of OMPs in the literature vary greatly (Table 7.1). There are multiple potential causes for this variation including: the use of different experimental techniques, use of different microscopy systems and differences in the methods used for diffusion coefficient calculation. It is likely that the PALM-SPT and particular experimental set up used in this thesis has a resolution limit close to the value of OmpF diffusion in fixed MG1655 cells (0.0029 $\mu m^2 s^{-1}$) in which, theoretically, no diffusion is occurring. Therefore it can be concluded that OmpF diffusion in live cells (with a measured diffusion coefficient of 0.0018 $\mu m^2 s^{-1}$) is diffusing sufficiently slowly as to be unresolvable with our PALM-SPT technique. This is supported by AFM experiments in which Porins were tracked at high resolution for up to 20 minutes revealing an extremely slow diffusion coefficient of

$2x10^{-7}$ $\mu m^2 s^{-1}$, well below the PALM-SPT resolution limit presented here [235]. It may be possible that the diffusion coefficients quoted for LamB, BtuB, Cir and OmpF in references [189, 192, 231, 234] are also effectively immobile and these diffusion coefficients instead indicate the resolution limit of their respective systems. However, without the inclusion of an appropriate negative control for diffusion this cannot be conclusively determined.

Pal and lipoylated PAmCherry diffuse at rates significantly faster (99.9% CI) than the fixed OmpF negative control. Hence we can be more confident that the diffusion coefficients determined for these two proteins are likely to be an accurate description of their true diffusion.

7.1.5 Broader implications

The polar localisation of OmpF in growing cells supports the same observations made for BtuB and TolC [189,193]. When this is viewed in relation to research on BAM complex localisation [194, 222] which shows these OMP biogenesis complexes to be distributed throughout the cell, an important physiological phenomenon is implied. This implication is that BAM complex activity and hence OMP biogenesis varies along the length of the cell. With the greatest activity at mid-cell (supported by pulsed OmpF expression experiments) and effectively no activity at the poles of the cell. It is important to note that such a mechanism can only exist in a membrane that does not permit the lateral diffusion of the OMPs inserted within it. The OM of *E. coli*, shown by OmpF single particle tracking experiments in this thesis, is such a membrane.

The observation that the BAM complex itself, lacks activity at the poles of the cells has significant implications for Gram positive bacterial physiology. As has been shown, the OMPs that localise to the poles represent the oldest in the OM. Hence it follows that these proteins are more likely to have accumulated damage over time and in the case of BAM this accumulated damage may be what renders the complexes at the poles of the cells inactive. This could then provide a universal model for β-barrel outer membrane protein turnover

in Gram negative bacteria. Wherein, new, active proteins are assembled preferentially at mid cell and as the cell grows these active proteins move to the poles of the cell where they become inactive (instead of being degraded enzymatically which is not possible at the outer membrane).

Much, however, is still unknown about the functionality of proteins at the poles of the cell. It has been shown that TolC, unlike BamA, retains its activity at the poles of the cell. This had implications for drug resistance in clonal populations of *E. coli* in that the accumulation of TolC-AcrAB drug efflux pumps at the poles of cells caused "older" cells to display greater antibiotic resistance [193]. It is hence critical to understand the functionality of OMPs at the cell poles. Porins, such as OmpF represent a category of OMPs for which this understanding is crucial. It has been shown that OmpF represents the main route of entry of many antibiotics, including β-lactams, through the outer membrane [236]. As polar localisation can have a significant impact on antibiotic sensitivity, it is critical to assess the function of OmpF at the poles of the cell in order to understand how antibiotics can be used with greater efficiency and how outer membrane protein biogenesis can be exploited to sensitise Gram negative bacteria to antibiotics.

The localisation of Pal to the septum of cells provided a foundation for the mobilisation-and-capture model of outer membrane invagination during cell division (Figure 1.11). This model whereby Pal is enriched in the septum and aids invagination of the OM by transducing the force of peptidoglycan ingrowth to the OM [72], is likely to occur in all Gram negative bacteria that contain Tol-Pal system homologues.

The single particle tracking of lipoylated-PAmCherry presented in this thesis provides a benchmark for the free diffusion of an outer membrane lipoylated protein. This hence represents a value to which the diffusion of further lipoylated outer membrane proteins can be compared against. It also represents the likely dynamics of Pal bound to the soluble periplasmic protein TolB that competes with peptidoglycan for Pal binding, enabling Pal diffusion, critical for its accumulation at the septum.

7.1.6 Reproducibility

Table 7.2: Details of experimental replicates. Illustrative Figures and those for which replicates are not appropriate are excluded. Biological replicate: an experiment repeated with a different colony of bacteria. Technical replicate: an experiment repeated on a different day. In all cases where repeats were conducted they were done so on different days with a different colony of bacteria.

Figure	**n represents:**	**n**	**Biological replicates**	**Technical replicates**	**Notes**
3.12	number of cells	1232, 1006, 1092	1	1	
3.13	number of cells	313, 945, 2118, 409, 2085	1	1	
3.14	number of cells	375, 537, 513, 458, 387	2	2	
4.4	N/A	N/A	N/A	N/A	Representative images from one technical and biological repeat shown
4.5	N/A	N/A	N/A	N/A	Representative images from one technical and biological repeat shown
4.6	N/A	N/A	N/A	N/A	Representative images from one technical and biological repeat shown
4.7	N/A	N/A	N/A	N/A	Representative images from one technical and biological repeat shown

4.8	N/A	N/A	N/A	N/A	Representative images from one technical and biological repeat shown
4.9	N/A	N/A	N/A	N/A	Representative images from one technical and biological repeat shown
4.10	number of cells	878, 499	1	1	
4.11	number of cells	679, 83	1	1	
4.12	number of OMP islands	704, 890	1	1	
4.13	number of OMP islands	704, 890, simulations: 1000	1	1	
4.14	number of cells	38, 78, 42, 14, 82, 36	1	1	
4.17	number of cells	11, 18, 6, 6, 6, 4	1	1	
4.18	number of cells	19, 37, 82, 43, 39, 23	2	2	
4.19	number of cells	44, 40, 82, 24, 62, 17	2	2	

4.20	number of cells	11, 29, 97, 37, 17, 14	1	1	
4.21	number of cells	1850	1	1	
4.22	number of cells	3930	1	1	
4.28	number of cells	43	1	1	Together with Fig 4.29, represents 2 biological and technical repeats
4.29	number of cells	35	1	1	Together with Fig 4.28, represents 2 biological and technical repeats
4.31	number of cells	50	1	1	Simulation
5.1	number of cells	50, 45	3	3	
5.2	number of cells	50, 45	3	3	
5.3	number of cells	30, 30	2	2	
5.4	number of cells	30, 30	2	2	
5.6	number of tracks	21336	2	2	
5.7	number of confinement radii	21336	2	2	
5.8	number of tracks	8224	1	1	

5.9	number of confinement radii	8224	1	1	
5.10	number of tracks	5956	2	2	
5.11	number of confinement radii	5956	2	2	
5.13	number of cells	385	5	5	
5.14	number of cells	301	5	5	
5.15	number of cells	176	5	5	
5.16	number of cells	157	5	5	
5.17	number of cells	770, 910, 586, 794	1	1	
5.18	number of cells	910	1	1	
6.2	number of Pal molecules	18967	3	3	
6.3	number of Pal molecules	15324	3	3	
6.4	number of tracks	12489	3	3	

6.5	number of confinement radii	12489	3	3	
6.6	number of tracks	10305	3	3	
6.7	number of confinement radii	10305	3	3	
6.9	number of tracks	30640	3	3	
6.10	number of confinement radii	30640	3	3	

Diffusion coefficient and confinement radii data presented in this thesis display significant spread and in many cases the difference in the median values for these statistics differ by only a small degree. Hence, it is important to understand how experimental variability affects each experiment, as there are likely to be small differences in sample preparation (such as the optical density to which cells grow), and differences in microscope behaviour such as changes in drift and laser power from one experimental replicate to another. Therefore to better establish the statistical significance of these differences between technical and biological repeats, in future analysis I would determine the confidence intervals of each biological and experimental replicate. If no significant difference were observed between repeats then we could be confident that experimental variability is not significantly biasing results.

Reproducibility of the data presented in this thesis would also be improved by providing laser powers in power output per unit area. In future work I intend to provide all laser powers in mW/cm^2. I would calculate this by determining the area of illumination of each laser line used and divide the laser power output in mW by this area, likely obtained through laser calibration.

7.2 Future work

7.2.1 CSR simulation tool

The CSR simulation tool detailed in Chapter 4, provided useful control images and simulated PALM and TIRF-PALM datasets. Simulating widefield microscopy images allowed artefacts that result from imaging low-copy number surface proteins at below the diffraction limit to be revealed. The simulated PALM-TIRF datasets allowed the effect of membrane curvature on experimental PALM-TIRF data to be investigated, showing artefacting to be negligible.

The CSR simulation program, however, remains limited beyond such applications due to its relative simplicity. In its current state, simulations of CSR surface distributions can be made with the user defining: the dimensions of the cell, the number of molecules to be

distributed, and if TIRF data is required: the depth of evanescent wave penetration. For the simulation of diffraction limited images, the user can define further parameters: the pixel size and numerical aperture of the microscope to be simulated and the maximum emission wavelength of the fluorophore simulated.

The versatility of the CSR simulation tool could be improved with the addition of a number of features:

1. Sensor noise. To better approximate experimental images, sensor noise could be simulated. Allowing users to more accurately generate simulated images for their microscope simulations.

2. Background sample fluorescence. When labelling cells exogenously, such as with antibody labelling, background fluorescence can often be observed caused by unbound fluorescent labels in the imaging plane. Simulating this background fluorescence would allow users to generate control datasets to aid in sample preparation.

3. PALM imaging simulation. PALM datasets can currently be simulated as a point cloud projected onto a 2D plane. This PALM imaging feature, however, would allow the user to simulate diffraction limited images of individual frames of PALM datasets. This could be used to generate control datasets to test the localisation precision of various fitting modes.

4. Simulation of CSR distribution in dividing cells. Simulating dividing cells would generate useful control data showing the effect of septum formation on CSR surface distribution and how this distribution would be represented in diffraction limited imaging.

5. Mid-cell biased biogenesis OMP simulation. It is likely that OMPs display mid-cell bias in their insertion into the outer membrane. Therefore, a tool that could bias CSR distributions to mid cell could provide useful control data for OMP biogenesis experiments.

7.2.2 BtuB and FepA PALM

As demonstrated in Chapter 4, it is difficult to extract information such as clustering from low-copy number OMPs by using diffraction limited imaging. Therefore to determine if clustering is a feature shared by both low-copy number OMPs and high copy number OMPs such as OmpF, PALM amenable labels for FepA and BtuB could be developed. PALM-TIRF followed by spatial statistics analysis could unambiguously determine if BtuB and FepA islands are indeed enriched in their respective OMP islands.

7.2.3 OMP expression modulation

By changing the expression levels of different OMPs, questions regarding the universal nature of some observations can be answered. For example, the biogenesis of OmpF is biased to the mid-cell in elongating cells, likely causing the non-uniform distributions observed. If BtuB and FepA were overexpressed to the same level as OmpF in the cell, the subcellular bias of their insertion and resultant distributions could be checked. If sharing the same characteristics of OmpF, this would provide further evidence that mid-cell bias of OMP insertion is a universal feature of all OMPs and defines the organisation of all OMPs on the surface of the cell.

Further to this, one limitation of the pulsed OmpF expression experiments, is the leaky expression of OmpF in pBAD-OmpF transformed BZB1107 cells. This leaky expression occurs at a very low level, however, would likely preclude the pulsing of expression for shorter than 5 minutes as the fluorescence signal would approach that observed for leaky expression. Through the development of an OmpF knockout in *E. coli* MG1655 which contains the *araC* gene, very tight expression regulation of OmpF could be achieved [237] allowing for very short OmpF expression pulses to be investigated.

Chapter 8

Appendix

8.1 Colicin N Killing Assays

The killing assay performed on *E. coli* BE3000 was repeated with *E. coli* MG1655 (Figure 8.1) and *E. coli* BW25113 (Figure 8.2), due to their frequent use in microscopy experiments presented in this thesis.

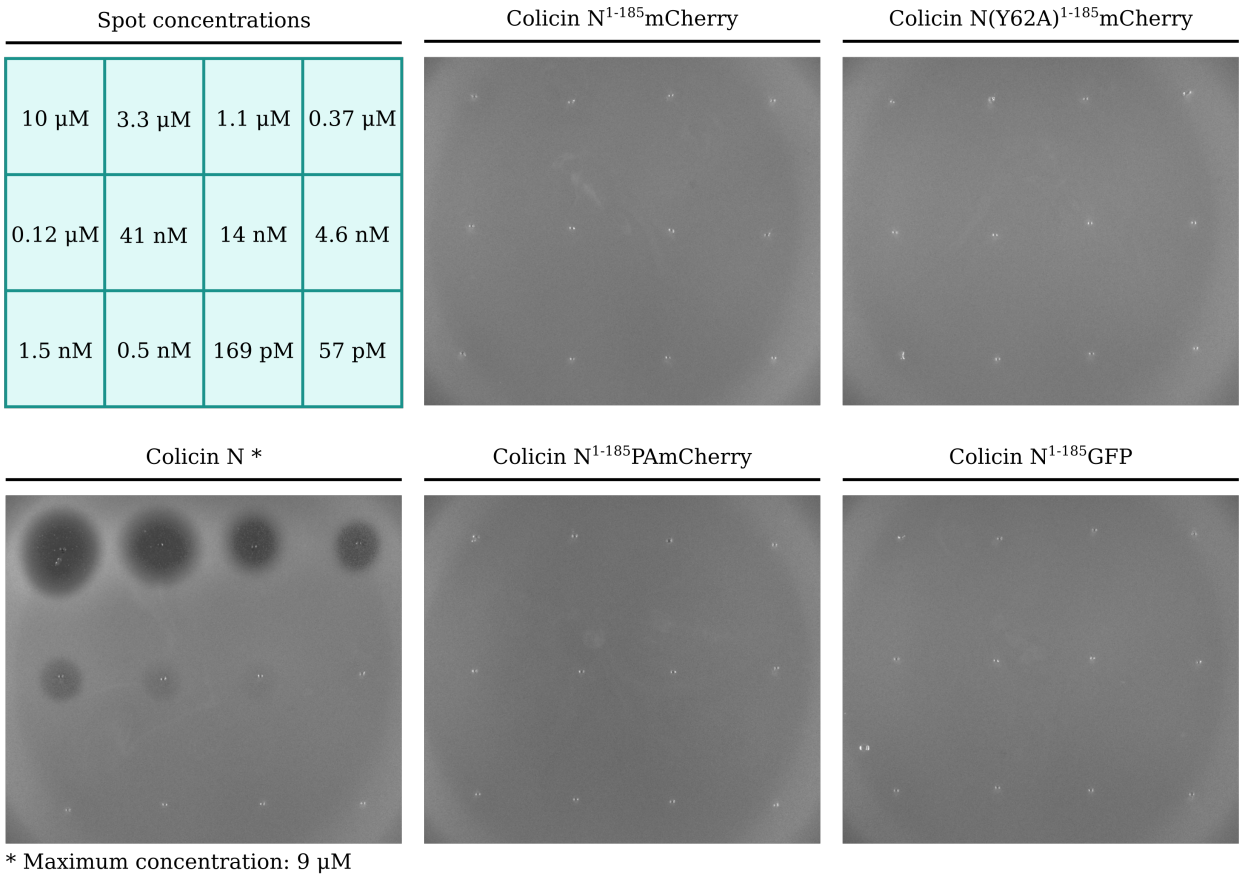

Figure 8.1: Colicin N fluorescent fusion protein spot killing assays in *E. coli* MG1655. For each protein, 2.5 µl aliquots of each serial dilution were spotted onto plates inoculated with *E. coli* MG1655. The highest concentration of wild type Colicin N used was 9 µM.

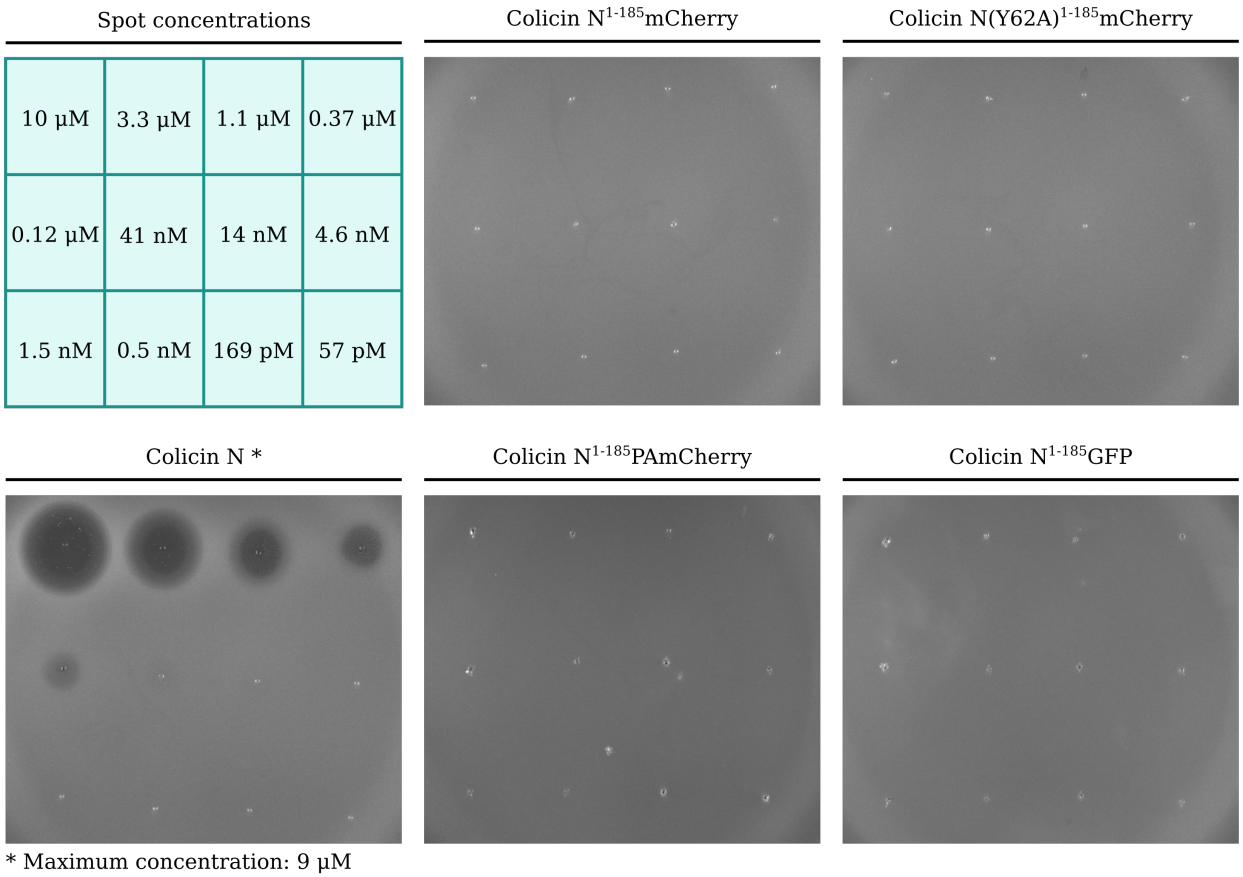

Figure 8.2: Colicin N fluorescent fusion protein spot killing assays in *E. coli* BW25113. For each protein, 2.5 µl aliquots of each serial dilution were spotted onto plates inoculated with *E. coli* BW25113. The highest concentration of wild type Colicin N used was 9 µM.

WT Colicin N displayed killing down to concentrations of 41 nM in *E. coli* MG1655 and 0.12 µM in *E. coli* BW25113. In both strains, no appreciable level of killing was observed at any concentration for any of the fluorescent fusion proteins.

8.2 Colicin N Fluorescent Fusion Protein Purifications

All Colicin N fluorescent fusion proteins were purified in the manner described in Chapters 2 and 3. Presented here are Ni affinity and size exclusion chromatography steps for each Colicin N fluorescent fusion protein used in this thesis.

8.2.1 Colicin N^{1-185}PAmCherry Purification

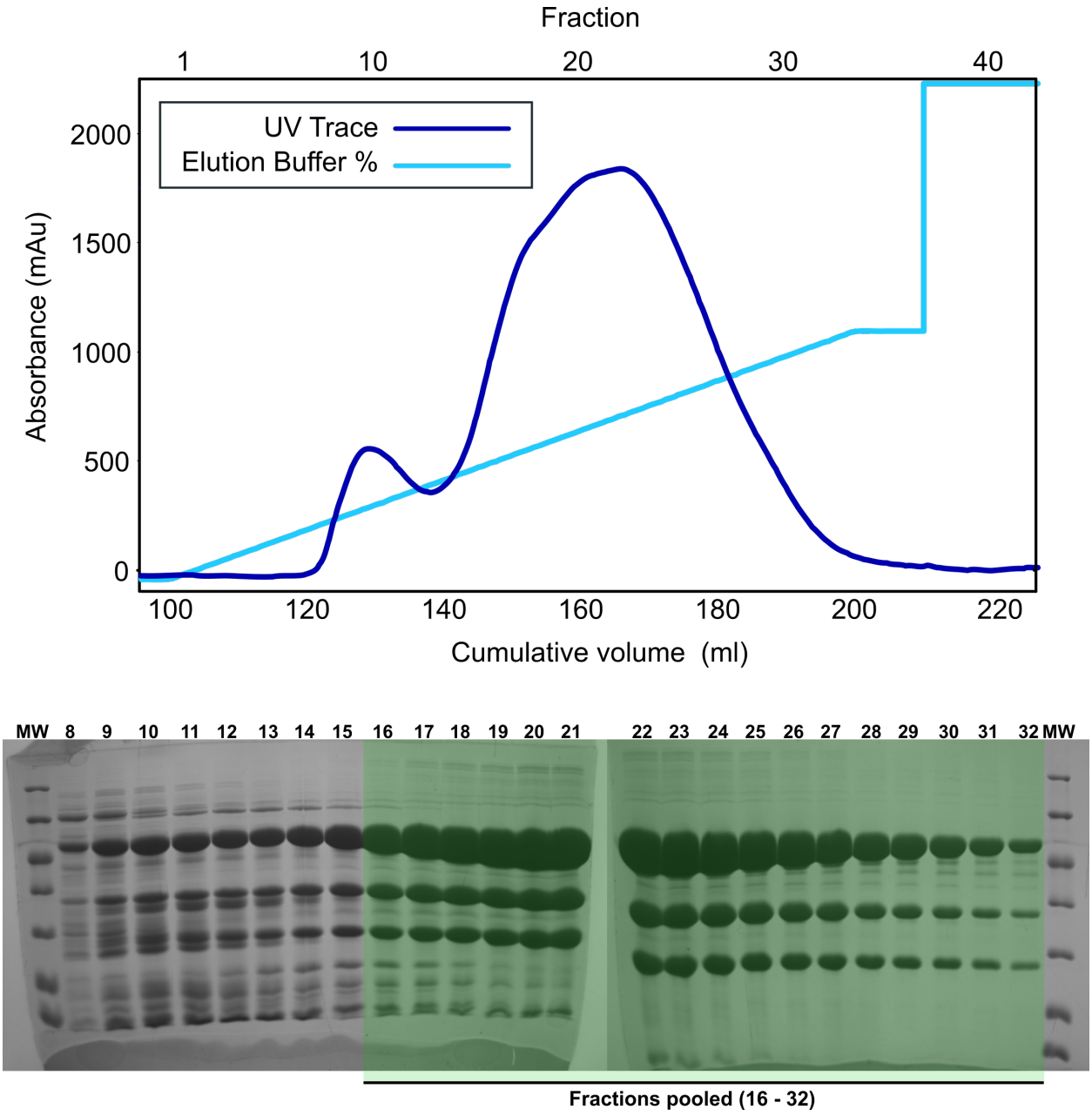

Figure 8.3: Colicin N^{1-185}PAmCherry purification: Ni affinity chromatography. Top: Ni affinity chromatogram of filtered cell extract. Elution of protein was monitored at an absorbance of 280 nm (blue). Eluent (750 mM imidazole, 500 mM NaCl, 20 mM Tris-HCl pH 7.5) concentration was increased at a gradient to 50% (light blue). Bottom: SDS-PAGE (12% polyacrylamide) analysis of Ni affinity chromatography fractions.

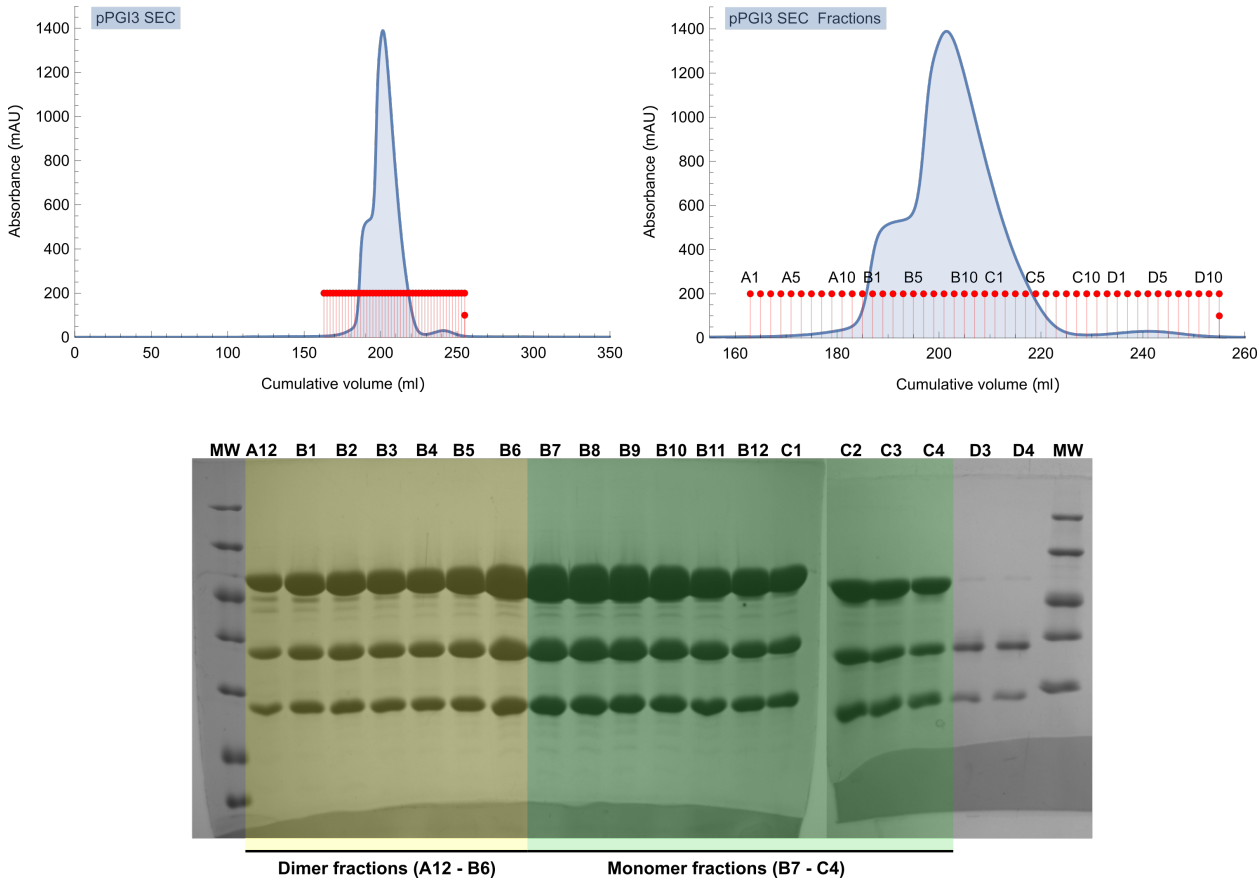

Figure 8.4: Colicin N^{1-185}PAmCherry purification: size exclusion chromatography. Top: Size exclusion chromatogram of pooled, dialysed Ni affinity chromatography fractions. Elution of protein was monitored at an absorbance of 280 nm (blue). A 25 mM Tris, 150 mM NaCl, pH 7.5 running buffer was used. Bottom: SDS-PAGE (12% polyacrylamide) analysis of size exclusion chromatography fractions.

The final yield of purified Colicin N^{1-185}PAmCherry was 33.92 mg per litre of culture.

8.2.2 Colicin N^{1-185}(Y62A)mCherry Purification

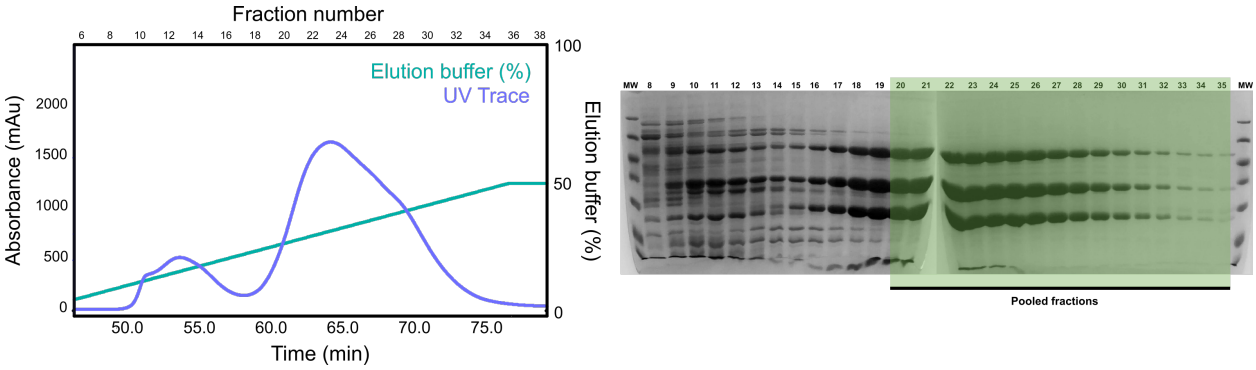

Figure 8.5: Colicin N^{1-185}(Y62A)mCherry purification: Ni affinity chromatography. Top: Ni affinity chromatogram of filtered cell extract. Elution of protein was monitored at an absorbance of 280 nm (blue). Eluent (750 mM imidazole, 500 mM NaCl, 20 mM Tris-HCl pH 7.5) concentration was increased at a gradient to 50% (turquoise). Bottom: SDS-PAGE (12% polyacrylamide) analysis of Ni affinity chromatography fractions.

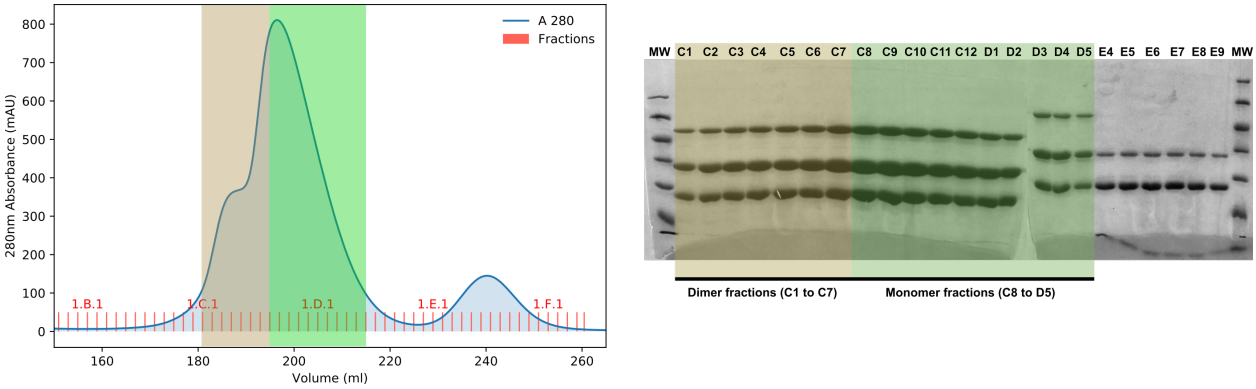

Figure 8.6: Colicin N^{1-185}(Y62A)mCherry purification: size exclusion chromatography. Top: Size exclusion chromatogram of pooled, dialysed Ni affinity chromatography fractions. Elution of protein was monitored at an absorbance of 280 nm (blue). A 25 mM Tris, 150 mM NaCl, pH 7.5 running buffer was used. Fractions analysed by SDS-PAGE are highlighted. Bottom: SDS-PAGE (12% polyacrylamide) analysis of size exclusion chromatography fractions.

The final yield of purified Colicin N^{1-185}(Y62A)mCherry was 25.02 mg per litre of culture.

8.2.3 Colicin N^{1-185}GFP Purification

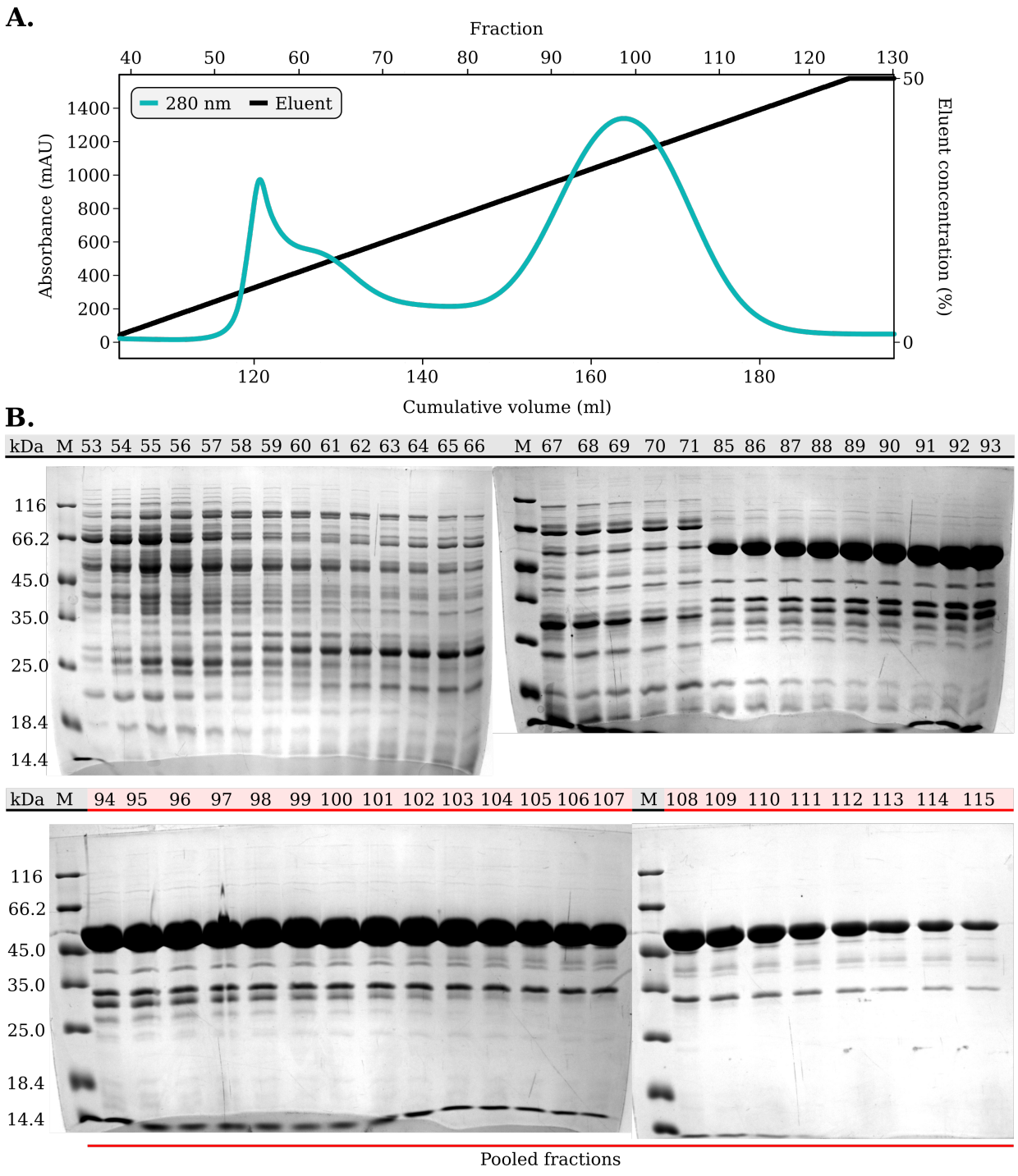

Figure 8.7: Colicin N^{1-185}GFP purification: Ni affinity chromatography. A. Ni affinity chromatogram of filtered cell extract. Elution of protein was monitored at an absorbance of 280 nm (blue). Eluent (750 mM imidazole, 500 mM NaCl, 20 mM Tris-HCl pH 7.5) concentration was increased at a gradient to 50% (black). **B.** SDS-PAGE (12% polyacrylamide) analysis of Ni affinity chromatography fractions.

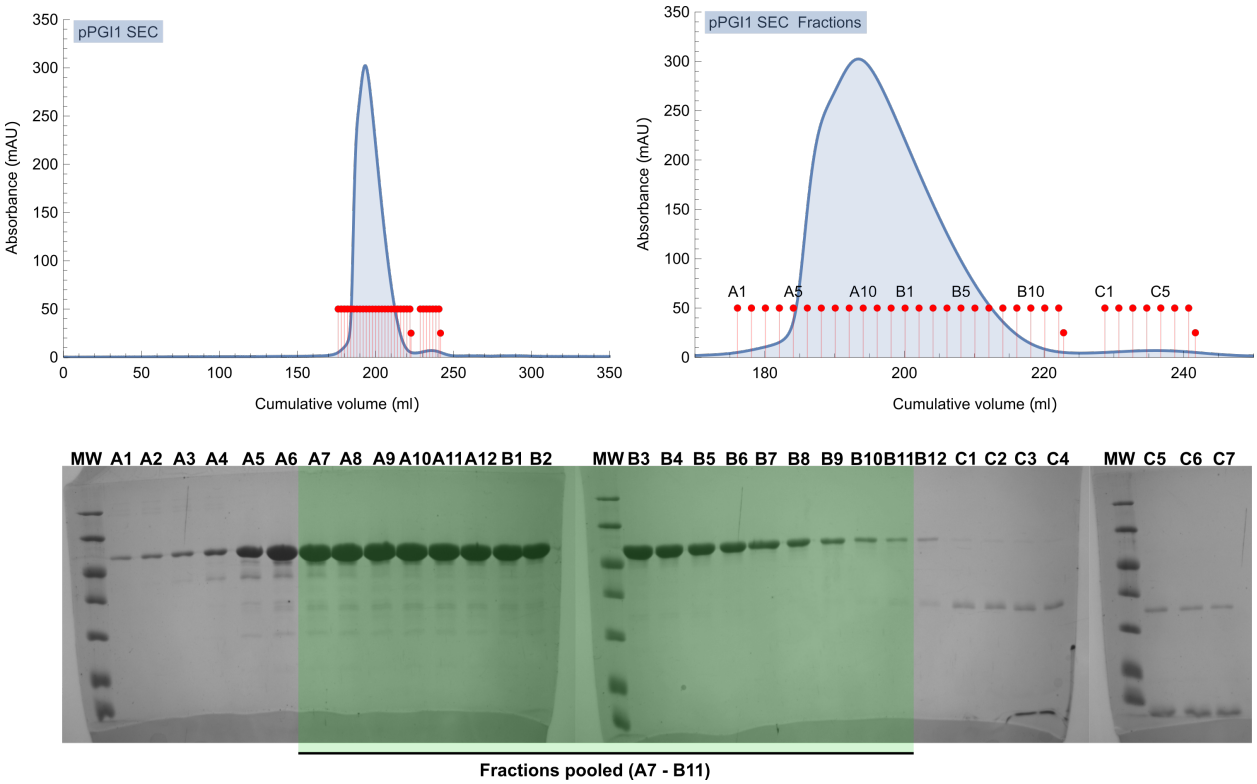

Figure 8.8: Colicin N^{1-185}GFP purification: size exclusion chromatography. Top: Size exclusion chromatogram of pooled, dialysed Ni affinity chromatography fractions. Elution of protein was monitored at an absorbance of 280 nm (blue). A 25 mM Tris, 150 mM NaCl, pH 7.5 running buffer was used. Bottom: SDS-PAGE (12% polyacrylamide) analysis of size exclusion chromatography fractions.

The final yield of purified Colicin N^{1-185}GFP was 4.52 mg per litre of culture.

8.3 OmpF uniform and non-uniform distributions

In Chapter 4, six categories of OmpF distribution were described, one of which was termed "Uniform" (Figure 4.14). When the kymograph of OmpF distribution in *E. coli* BE3000 was generated (Figure 4.22), it was clear that distribution was notably more uniform in this strain. The figure presented here (Figure 8.9.) shows OmpF distribution in *E. coli* BE3000 cells from the same sample of labelled cells on the same microscopy slide. In two different randomly selected regions of the slide, one region cells displayed overwhelming uniformity of OmpF distribution (Figure 8.9.A.), however, another region cells displayed overwhelmingly

non-uniform OmpF distributions (Figure 8.9.B.). Suggesting that the balance between cells displaying uniform OmpF distribution and strongly cell cycle linked OmpF distributions is random and not related to environmental factors such as nutrient availability.

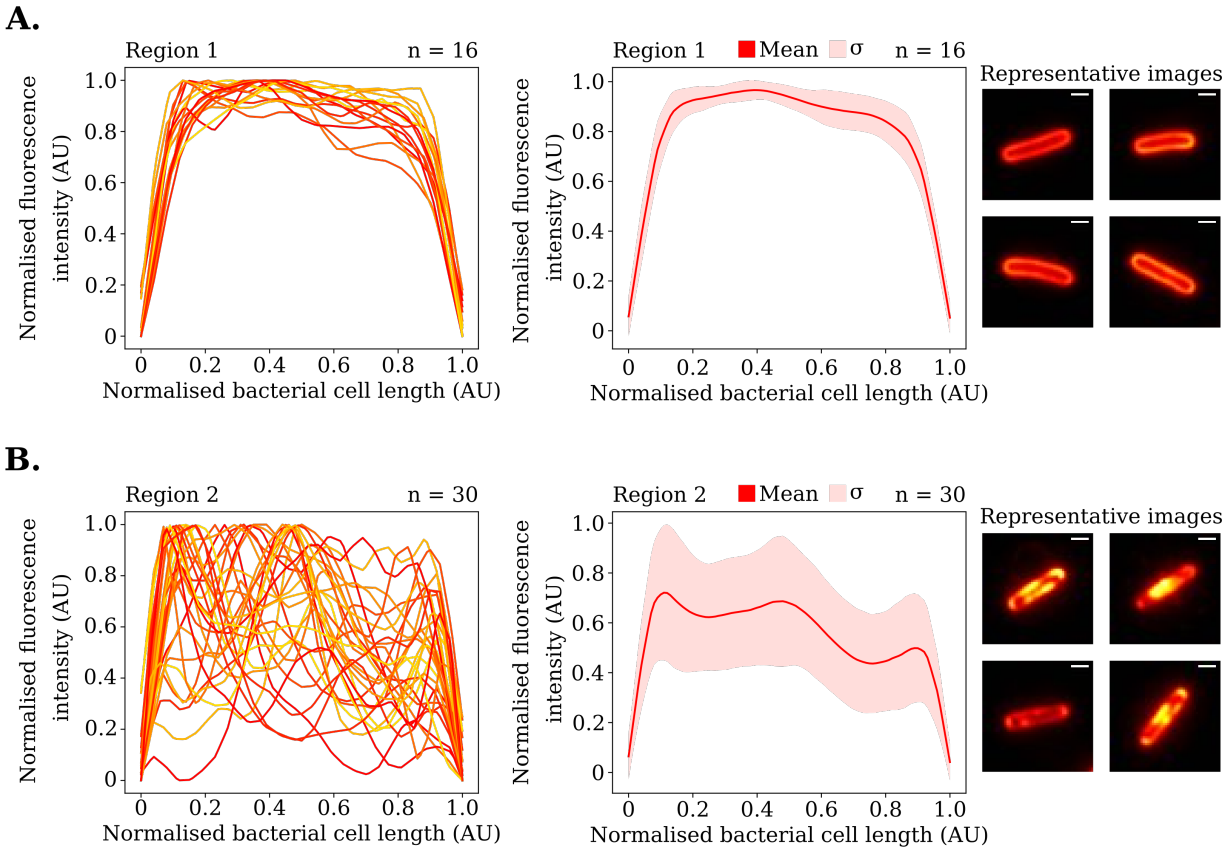

Figure 8.9: Uniform and Non-Uniform OmpF distribution in *E. coli* BE3000. A. Normalised fluorescence intensity profiles, average cell intensity profile and representative cell images of Colicin N^{1-185}mCherry labelled *E. coli* BE3000 from a randomly selected region on a loaded microscopy slide. **B.** Normalised fluorescence intensity profiles, average cell intensity profile and representative cell images of Colicin N^{1-185}mCherry labelled *E. coli* BE3000 from a distinct, randomly selected region on the same microscopy slide as in **A.**.

Bibliography

[1] "Frits Zernike, 1888-1966," *Biogr. Mems Fell. R. Soc*, vol. 13, pp. 392–402, nov 1967.

[2] M. A. Peshkoff, "Fine structure and mechanism of division of the nuclei of the bacterium Caryophanon latum," *Nature*, vol. 157, p. 137, feb 1946.

[3] H. Stempen, "Demonstration of the chromatinic bodies of Escherichia coli and Proteus vulgaris with the aid of the phase contrast microscope," *J. Bacteriol.*, vol. 60, pp. 81–87, jul 1950.

[4] J. Hillier, S. Mudd, and A. G. Smith, "Internal structure and nuclei in cells of Escherichia coli as shown by improved electron microscopic techniques," *J. Bacteriol.*, vol. 57, pp. 319–338, mar 1949.

[5] V. R. F. Matias, A. Al-Amoudi, J. Dubochet, and T. J. Beveridge, "Cryo-transmission electron microscopy of frozen-hydrated sections of Escherichia coli and Pseudomonas aeruginosa," *J. Bacteriol.*, vol. 185, pp. 6112–6118, oct 2003.

[6] R. F. Baker and D. C. Pease, "Sectioning of the bacterial cell for the electron microscope," *Nature*, vol. 163, p. 282, feb 1949.

[7] A. Birch-Andersen, O. Maaløe, and F. S. Sjostrand, "High-resolution electron micrographs of sections of E. coli," *Biochim. Biophys. Acta*, vol. 12, pp. 395–400, nov 1953.

[8] G. B. Chapman and A. J. Kroll, "Electron microscopy of ultrathin sections of Spirillum serpens," *J. Bacteriol.*, vol. 73, pp. 63–71, jan 1957.

[9] E. Kellenberger and A. Ryter, "Cell Wall and Cytoplasmic Membrane of Escherichia coli," *The Journal of Biophysical and Biochemical Cytology*, vol. 4, no. 3, pp. 323–326, 1958.

[10] G. B. Chapman, "Electron microscopy of ultrathin sections of bacteria iii," *Journal of Bacteriology*, vol. 78, no. 1, pp. 96–104, 1959.

[11] A. M. Glauert and M. J. Thornley, "The Topography of the Bacterial Cell Wall," *Annual Review of Microbiology*, vol. 23, no. 1, pp. 159–198, 1969.

[12] T. Miura and S. Mizushima, "Separation by density gradient centrifugation of two types of membranes from spheroplast membrane of Escherichia coli K12," *Biochim. Biophys. Acta*, vol. 150, pp. 159–161, jan 1968.

[13] C. A. Schnaitman, "Protein Composition of the Cell Wall and Cytoplasmic Membrane of Escherichia coli," *Journal of Bacteriology*, vol. 104, no. 2, pp. 890–901, 1970.

[14] M. J. Osborn, J. E. Gander, E. Parisi, and J. Carson, "Mechanism of assembly of the outer membrane of Salmonella typhimurium. Isolation and characterization of cytoplasmic and outer membrane," *J. Biol. Chem.*, vol. 247, pp. 3962–3972, jun 1972.

[15] Y. Kamio and H. Nikaido, "Outer membrane of Salmonella typhimurium: accessibility of phospholipid head groups to phospholipase c and cyanogen bromide activated dextran in the external medium," *Biochemistry*, vol. 15, pp. 2561–2570, jun 1976.

[16] C. Filip, G. Fletcher, J. L. Wulff, and C. F. Earhart, "Solubilization of the cytoplasmic membrane of Escherichia coli by the ionic detergent sodium-lauryl sarcosinate," *J. Bacteriol.*, vol. 115, pp. 717–722, sep 1973.

[17] D. A. White, W. J. Lennarz, and C. A. Schnaitman, "Distribution of Lipids in the Wall and Cytoplasmic Membrane Subfractions of the Cell Envelope of Escherichia coli," *Journal of Bacteriology*, vol. 109, no. 2, pp. 686–690, 1972.

[18] C. A. Schnaitman, "Solubilization of the Cytoplasmic Membrane of Escherichia coli by Triton X-100," *Journal of Bacteriology*, vol. 108, no. 1, pp. 545–552, 1971.

[19] I. Yamato, Y. Anraku, and K. Hirosawa, "Cytoplasmic membrane vesicles of Escherichia coli. A simple method for preparing the cytoplasmic and outer membranes," *J. Biochem.*, vol. 77, pp. 705–718, apr 1975.

[20] A. W. Sedar and R. M. Burde, "Localization of the succinic dehydrogenase system in Escherichia coli using combined techniques of cytochemistry and electron microscopy," *J. Cell Biol.*, vol. 24, pp. 285–295, feb 1965.

[21] I. C. West and P. Mitchell, "The proton-translocating ATPase of Escherichia coli," *FEBS Lett.*, vol. 40, pp. 1–4, mar 1974.

[22] Y. Akiyama and K. Ito, "Topology analysis of the SecY protein, an integral membrane protein involved in protein export in Escherichia coli," *EMBO J.*, vol. 6, pp. 3465–3470, nov 1987.

[23] P. J. Schatz, P. D. Riggs, A. Jacq, M. J. Fath, and J. Beckwith, "The secE gene encodes an integral membrane protein required for protein export in Escherichia coli," *Genes Dev.*, vol. 3, pp. 1035–1044, jul 1989.

[24] E. H. Manting, C. van Der Does, H. Remigy, A. Engel, and A. J. Driessen, "SecYEG assembles into a tetramer to form the active protein translocation channel," *EMBO J.*, vol. 19, pp. 852–861, mar 2000.

[25] B. C. Berks, F. Sargent, E. De Leeuw, A. P. Hinsley, N. R. Stanley, R. L. Jack, G. Buchanan, and T. Palmer, "A novel protein transport system involved in the biogenesis of bacterial electron transfer chains," *Biochim. Biophys. Acta*, vol. 1459, pp. 325–330, aug 2000.

[26] C. Sohlenkamp and O. Geiger, "Bacterial membrane lipids: diversity in structures and pathways," *FEMS Microbiology Reviews*, vol. 40, pp. 133–159, jan 2016.

[27] N. Ruiz, D. Kahne, and T. J. Silhavy, "Advances in understanding bacterial outer-membrane biogenesis," *Nat. Rev. Microbiol.*, vol. 4, pp. 57–66, jan 2006.

[28] E. J. Lugtenberg and R. Peters, "Distribution of lipids in cytoplasmic and outer membranes of Escherichia coli K12," *Biochim. Biophys. Acta*, vol. 441, pp. 38–47, jul 1976.

[29] J. Smit, Y. Kamio, and H. Nikaido, "Outer membrane of Salmonella typhimurium: chemical analysis and freeze-fracture studies with lipopolysaccharide mutants," *J. Bacteriol.*, vol. 124, pp. 942–958, nov 1975.

[30] C. R. H. Raetz and C. Whitfield, "Lipopolysaccharide Endotoxins," *Annual Review of Biochemistry*, vol. 71, no. 1, pp. 635–700, 2002.

[31] H. G. Boman and D. A. Monner, "Characterization of lipopolysaccharides from Escherichia coli K-12 mutants," *J. Bacteriol.*, vol. 121, pp. 455–464, feb 1975.

[32] A. Ebbensgaard, H. Mordhorst, F. M. Aarestrup, and E. B. Hansen, "The Role of Outer Membrane Proteins and Lipopolysaccharides for the Sensitivity of Escherichia coli to Antimicrobial Peptides," *Frontiers in Microbiology*, vol. 9, 2018.

[33] V. Urdaneta and J. Casadesús, "Interactions between Bacteria and Bile Salts in the Gastrointestinal and Hepatobiliary Tracts," *Front. Med.*, vol. 4, p. 163, oct 2017.

[34] K. L. May and M. Grabowicz, "The bacterial outer membrane is an evolving antibiotic barrier," *Proc. Natl. Acad. Sci. U. S. A.*, vol. 115, pp. 8852–8854, sep 2018.

[35] S. Tamaki, T. Sato, and M. Matsuhashi, "Role of lipopolysaccharides in antibiotic resistance and bacteriophage adsorption of Escherichia coli K-12," *J. Bacteriol.*, vol. 105, pp. 968–975, mar 1971.

[36] C. Sharp, C. Boinett, A. Cain, N. G. Housden, S. Kumar, K. Turner, J. Parkhill, and C. Kleanthous, "O-Antigen-Dependent Colicin Insensitivity of Uropathogenic Escherichia coli," *J. Bacteriol.*, vol. 201, feb 2019.

[37] T. C. Meredith, P. Aggarwal, U. Mamat, B. Lindner, and R. W. Woodard, "Redefining the requisite lipopolysaccharide structure in Escherichia coli," *ACS Chem. Biol.*, vol. 1, pp. 33–42, feb 2006.

[38] X. Wang and P. J. Quinn, "Lipopolysaccharide: Biosynthetic pathway and structure modification," *Prog. Lipid Res.*, vol. 49, pp. 97–107, apr 2010.

[39] G. Klein, B. Lindner, W. Brabetz, H. Brade, and S. Raina, "Escherichia coli K-12 Suppressor-free Mutants Lacking Early Glycosyltransferases and Late Acyltransferases: minimal lipopolysaccharide structure and induction of envelope stress response," *J. Biol. Chem.*, vol. 284, pp. 15369–15389, jun 2009.

[40] Y. Hong and P. R. Reeves, "Diversity of o-antigen repeat unit structures can account for the substantial sequence variation of wzx translocases," *J. Bacteriol.*, vol. 196, pp. 1713–1722, may 2014.

[41] P. Zhang, S. Snyder, P. Feng, P. Azadi, S. Zhang, S. Bulgheresi, K. E. Sanderson, J. He, J. Klena, and T. Chen, "Role of N-acetylglucosamine within core lipopolysaccharide of several species of gram-negative bacteria in targeting the DC-SIGN (CD209)," *J. Immunol.*, vol. 177, pp. 4002–4011, sep 2006.

[42] V. Braun and K. Rehn, "Chemical Characterization, Spatial Distribution and Function of a Lipoprotein (Murein-Lipoprotein) of the E. coli Cell Wall. The Specific Effect of Trypsin on the Membrane Structure," *European Journal of Biochemistry*, vol. 10, no. 3, pp. 426–438, 1969.

[43] B. Lugtenberg, J. Meijers, R. Peters, P. van der Hoek, and L. van Alphen, "Electrophoretic resolution of the "major outer membrane protein" of Escherichia coli K12 into four bands," *FEBS Lett.*, vol. 58, pp. 254–258, oct 1975.

[44] G.-W. Li, D. Burkhardt, C. Gross, and J. S. Weissman, "Quantifying absolute protein synthesis rates reveals principles underlying allocation of cellular resources," *Cell*, vol. 157, pp. 624–635, apr 2014.

[45] K. Nakamura, D. N. Ostrovsky, T. Miyazawa, and S. Mizushima, "Infrared spectra of outer and cytoplasmic membranes of Escherichia coli," *Biochimica et Biophysica Acta (BBA) - Biomembranes*, vol. 332, no. 3, pp. 329–335, 1974.

[46] J. P. Rosenbusch, "Characterization of the Major Envelope Protein from Escherichia coli," *Journal of Biological Chemistry*, vol. 249, no. 24, pp. 8010–8029, 1974.

[47] J. M. DiRienzo, K. Nakamura, and M. Inouye, "The Outer Membrane Proteins of Gram-Negative Bacteria: Biosynthesis, Assembly and Functions," *Annual Review of Biochemistry*, vol. 47, pp. 481–532, 1978.

[48] K. Inokuchi, N. Mutoh, S. I. Matsuyama, and S. Mizushima, "Primary structure of the ompF gene that codes for a major outer membrane protein of Escherichia coli K-12," *Nucleic Acids Research*, vol. 10, no. 21, pp. 6957–6968, 1982.

[49] T. Mizuno, M. Y. Chou, and M. Inouye, "A comparative study on the genes for three porins of the Escherichia coli outer membrane. DNA sequence of the osmoregulated ompC gene," *J. Biol. Chem.*, vol. 258, pp. 6932–6940, jun 1983.

[50] N. Overbeeke, H. Bergmans, F. van Mansfeld, and B. Lugtenberg, "Complete nucleotide sequence of phoE, the structural gene for the phosphate limitation inducible outer membrane pore protein of Escherichia coli K12," *J. Mol. Biol.*, vol. 163, pp. 513–532, feb 1983.

[51] J. Grodberg and J. J. Dunn, "ompT encodes the Escherichia coli outer membrane protease that cleaves T7 RNA polymerase during purification," *J. Bacteriol.*, vol. 170, pp. 1245–1253, mar 1988.

[52] H. Homma, T. Kobayashi, N. Chiba, K. Karasawa, H. Mizushima, I. Kudo, K. Inoue, H. Ikeda, M. Sekiguchi, and S. Nojima, "The DNA sequence encoding pldA gene, the structural gene for detergent-resistant phospholipase A of E. coli," *J. Biochem.*, vol. 96, pp. 1655–1664, dec 1984.

[53] K. Heller and R. J. Kadner, "Nucleotide sequence of the gene for the vitamin B12 receptor protein in the outer membrane of Escherichia coli," *J. Bacteriol.*, vol. 161, pp. 904–908, mar 1985.

[54] E. Gilson, H. Nikaido, and M. Hofnung, "Sequence of the malK gene in E.coli K12," *Nucleic Acids Research*, vol. 10, no. 22, pp. 7449–7458, 1982.

[55] R. Voulhoux, M. P. Bos, J. Geurtsen, M. Mols, and J. Tommassen, "Role of a highly conserved bacterial protein in outer membrane protein assembly," *Science*, vol. 299, pp. 262–265, jan 2003.

[56] J. F. Stegmeier and C. Andersen, "Characterization of pores formed by YaeT (Omp85) from Escherichia coli," *J. Biochem.*, vol. 140, pp. 275–283, aug 2006.

[57] S.-S. Chng, N. Ruiz, G. Chimalakonda, T. J. Silhavy, and D. Kahne, "Characterization of the two-protein complex in Escherichia coli responsible for lipopolysaccharide assembly at the outer membrane," *Proc. Natl. Acad. Sci. U. S. A.*, vol. 107, pp. 5363–5368, mar 2010.

[58] R. M. Garavito and J. P. Rosenbusch, "Three-dimensional crystals of an integral membrane protein: an initial x-ray analysis," *J. Cell Biol.*, vol. 86, pp. 327–329, jul 1980.

[59] R. M. Garavito, J. Jenkins, J. N. Jansonius, R. Karlsson, and J. P. Rosenbusch, "X-ray diffraction analysis of matrix porin, an integral membrane protein from Escherichia coli outer membranes," *Journal of Molecular Biology*, vol. 164, no. 2, pp. 313–327, 1983.

[60] M. S. Weiss, T. Wacker, J. Weckesser, W. Welte, and G. E. Schulz, "The three-dimensional structure of porin from Rhodobacter capsulatus at 3 A resolution," *FEBS Lett.*, vol. 267, pp. 268–272, jul 1990.

[61] R. A. Pauptit, T. Schirmer, J. N. Jansonius, J. P. Rosenbusch, M. W. Parker, A. D. Tucker, D. Tsernoglou, M. S. Weiss, and G. E. Schultz, "A common channel-forming motif in evolutionarily distant porins," *J. Struct. Biol.*, vol. 107, pp. 136–145, oct 1991.

[62] S. Cowan, T. Schirmer, G. Rummel, R. Steiert, R. Ghosh, R. Paupit, J. Jansonius, and J. Rosenbusch, "Crystal structures explain functional properties of two E. coli porins," *Nature*, vol. 358, pp. 727–733, 1992.

[63] R. Henderson and P. N. T. Unwin, "Three-dimensional model of purple membrane obtained by electron microscopy," *Nature*, vol. 257, no. 5521, pp. 28–32, 1975.

[64] T. J. Silhavy, D. Kahne, and S. Walker, "The bacterial cell envelope," *Cold Spring Harb. Perspect. Biol.*, vol. 2, p. a000414, may 2010.

[65] H. Tokuda and S.-I. Matsuyama, "Sorting of lipoproteins to the outer membrane in E. coli," *Biochimica et Biophysica Acta (BBA) - Molecular Cell Research*, vol. 1693, no. 1, pp. 5–13, 2004.

[66] X. Vila-Farrés, R. Parra-Millán, V. Sánchez-Encinales, M. Varese, R. Ayerbe-Algaba, N. Bayó, S. Guardiola, M. E. Pachón-Ibáñez, M. Kotev, J. García, M. Teixidó, J. Vila, J. Pachón, E. Giralt, and Y. Smani, "Combating virulence of Gram-negative bacilli by OmpA inhibition," *Scientific Reports 2017 7:1*, vol. 7, pp. 1–11, oct 2017.

[67] X. He, Q. Wang, L. Peng, Y. Qu, S. Puthiyakunnon, X. Liu, C. Hui, S. Boddu, H. Cao, and S. Huang, "Role of uropathogenic Escherichia coli outer membrane protein T in pathogenesis of urinary tract infection," *Pathogens and disease*, vol. 73, apr 2015.

[68] A. Abir T and C. Jean-François, "Lpp, the Braun lipoprotein, turns 50 - major achievements and remaining issues," *FEMS Microbiology Letters*, vol. 365, no. 18, 2018.

[69] V. Braun, "Covalent lipoprotein from the outer membrane of Escherichia coli," *Biochimica et Biophysica Acta (BBA) - Reviews on Biomembranes*, vol. 415, no. 3, pp. 335–377, 1975.

[70] T. Mizuno, "A novel peptidoglycan-associated lipoprotein found in the cell envelope of Pseudomonas aeruginosa and Escherichia coli," *J. Biochem.*, vol. 86, pp. 991–1000, oct 1979.

[71] E. Cascales, A. Bernadac, M. Gavioli, J.-C. Lazzaroni, and R. Lloubes, "Pal Lipoprotein of Escherichia coli Plays a Major Role in Outer Membrane Integrity," *Journal of Bacteriology*, vol. 184, no. 3, pp. 754–759, 2002.

[72] J. Szczepaniak, P. Holmes, K. Rajasekar, R. Kaminska, F. Samsudin, P. G. Inns, P. Rassam, S. Khalid, S. M. Murray, C. Redfield, and C. Kleanthous, "The lipoprotein Pal stabilises the bacterial outer membrane during constriction by a mobilisation-and-capture mechanism," *Nat. Commun.*, vol. 11, p. 1305, mar 2020.

[73] J. C. Malinverni, J. Werner, S. Kim, J. G. Sklar, D. Kahne, R. Misra, and T. J. Silhavy, "YfiO stabilizes the YaeT complex and is essential for outer membrane protein assembly in Escherichia coli," *Molecular Microbiology*, vol. 61, no. 1, pp. 151–164, 2006.

[74] S.-I. Matsuyama, N. Yokota, and H. Tokuda, "A novel outer membrane lipoprotein, LolB (HemM), involved in the LolA (p20)-dependent localization of lipoproteins to the outer membrane of Escherichia coli," *The EMBO Journal*, vol. 16, no. 23, pp. 6947–6955, 1997.

[75] T. Wu, A. C. McCandlish, L. S. Gronenberg, S.-S. Chng, T. J. Silhavy, and D. Kahne, "Identification of a protein complex that assembles lipopolysaccharide in the outer membrane of Escherichia coli," *Proc. Natl. Acad. Sci. U. S. A.*, vol. 103, pp. 11754–11759, aug 2006.

[76] W. Vollmer, D. Blanot, and M. A. D. Pedro, "Peptidoglycan structure and architecture," *FEMS Microbiol. Rev.*, vol. 32, pp. 149–167, 2008.

[77] H. Labischinski, E. W. Goodell, A. Goodell, and M. L. Hochberg, "Direct proof of a "more-than-single-layered" peptidoglycan architecture of Escherichia coli W7: a neutron small-angle scattering study.," *Journal of Bacteriology*, vol. 173, no. 2, p. 751, 1991.

[78] R. D. Turner, A. F. Hurd, A. Cadby, J. K. Hobbs, and S. J. Foster, "Cell wall elongation mode in Gram-negative bacteria is determined by peptidoglycan architecture," *Nature Communications 2013 4:1*, vol. 4, pp. 1–8, feb 2013.

[79] L. M. Parsons, F. Lin, and J. Orban, "Peptidoglycan Recognition by Pal, an Outer Membrane Lipoprotein," *Biochemistry*, vol. 45, no. 7, pp. 2122–2128, 2006.

[80] J. S. Park, W. C. Lee, K. J. Yeo, K. Ryu, M. Kumarasiri, D. Hesek, M. Lee, S. Mobashery, J. H. Song, S. I. Kim, J. C. Lee, C. Cheong, Y. H. Jeon, and H. Kim, "Mechanism of anchoring of OmpA protein to the cell wall peptidoglycan of the Gram-negative bacterial outer membrane," *The FASEB Journal*, vol. 26, no. 1, pp. 219–228, 2012.

[81] V. Braun and V. Bosch, "Repetitive sequences in the murein-lipoprotein of the cell wall of Escherichia coli," *Proc. Natl. Acad. Sci. U. S. A.*, vol. 69, pp. 970–974, apr 1972.

[82] T. Nakae and H. Nikaido, "Outer membrane as a diffusion barrier in Salmonella typhimurium. Penetration of oligo- and polysaccharides into isolated outer mem-

brane vesicles and cells with degraded peptidoglycan layer," *J. Biol. Chem.*, vol. 250, pp. 7359–7365, sep 1975.

[83] J. W. Payne and C. Gilvarg, "Size restriction on peptide utilization in Escherichia coli," *J. Biol. Chem.*, vol. 243, pp. 6291–6299, dec 1968.

[84] H. Nikaido, S. A. Song, L. Shaltiel, and M. Nurminen, "Outer membrane of Salmonella XIV. Reduced transmembrane diffusion rates in porin-deficient mutants," *Biochem. Biophys. Res. Commun.*, vol. 76, pp. 324–330, may 1976.

[85] T. Nakae, "Identification of the outer membrane protein of E.coli that produces transmembrane channels in reconstituted vesicle membranes," *Biochemical and Biophysical Research Communications*, vol. 71, no. 3, pp. 877–884, 1976.

[86] P. Bavoil, H. Nikaido, and K. von Meyenburg, "Pleiotropic transport mutants of Escherichia coli lack porin, a major outer membrane protein," *Molecular and General Genetics MGG*, vol. 158, no. 1, pp. 23–33, 1977.

[87] J. F. Lutkenhaus, "Role of a major outer membrane protein in Escherichia coli," *Journal of Bacteriology*, vol. 131, no. 2, pp. 631–637, 1977.

[88] T. Nakae, J. Ishii, and M. Tokunaga, "Subunit structure of functional porin oligomers that form permeability channels in the other membrane of Escherichia coli," *J. Biol. Chem.*, vol. 254, pp. 1457–1461, mar 1979.

[89] F. Yu, I. Shigeyuki, and S. Mizushima, "A major outer membrane protein (O-8) of Escherichia coli K-12 exists as a trimer in sodium dodecyl sulfate solution," *FEBS Letters*, vol. 100, no. 1, pp. 71–74, 1979.

[90] W. Van Alphen, "Pores in the outer membrane of Escherichia coli K12. Involvement of proteins b and c in the permeation of cephaloridine and ampicillin," *FEMS Microbiology Letters*, vol. 3, no. 2, pp. 103–106, 1978.

[91] N. Overbeeke and B. Lugtenberg, "Expression of outer membrane protein e of Escherichia coli K12 by phosphate limitation," *FEBS Letters*, vol. 112, no. 2, pp. 229–232, 1980.

[92] L. A. Pratt, W. Hsing, K. E. Gibson, and T. J. Silhavy, "From acids to osmZ: multiple factors influence synthesis of the OmpF and OmpC porins in Escherichia coli," *Mol. Microbiol.*, vol. 20, pp. 911–917, jun 1996.

[93] M. N. Hall and T. J. Silhavy, "Genetic analysis of the ompB locus in Escherichia coli K-12," *J. Mol. Biol.*, vol. 151, pp. 1–15, sep 1981.

[94] K. Makino, H. Shinagawa, M. Amemura, T. Kawamoto, M. Yamada, and A. Nakata, "Signal transduction in the phosphate regulon of Escherichia coli involves phosphotransfer between PhoR and PhoB proteins," *J. Mol. Biol.*, vol. 210, pp. 551–559, dec 1989.

[95] K. B. Gehring and H. Nikaido, "Existence and purification of porin heterotrimers of Escherichia coli K12 OmpC, OmpF, and PhoE proteins," *J. Biol. Chem.*, vol. 264, pp. 2810–2815, feb 1989.

[96] S. Ichihara and S. Mizushima, "Arrangement of Proteins O-8 and O-9 in Outer Membrane of Escherichia coli K-12. Existence of Homotrimers and Heterotrimers," *European Journal of Biochemistry*, vol. 100, no. 2, pp. 321–328, 1979.

[97] S. W. Cowan, R. Garavito, J. Jansonius, J. Jenkins, R. Karlsson, N. Konig, E. Pai, R. Pauptit, P. Rizkallah, and J. Rosenbusch, "The structure of OmpF porin in a tetragonal crystal form," *Structure*, vol. 15, no. 3(10), pp. 1041–50, 1995.

[98] A. Baslé, G. Rummel, P. Storici, J. P. Rosenbusch, and T. Schirmer, "Crystal Structure of Osmoporin OmpC from E. coli at 2.0 Å," *Journal of Molecular Biology*, vol. 362, no. 5, pp. 933–942, 2006.

[99] G. Ried, I. Hindennach, and U. Henning, "Role of lipopolysaccharide in assembly of Escherichia coli outer membrane proteins OmpA, OmpC, and OmpF," *J. Bacteriol.*, vol. 172, pp. 6048–6053, oct 1990.

[100] D. L. Diedrich, M. A. Stein, and C. A. Schnaitman, "Associations of Escherichia coli K-12 OmpF trimers with rough and smooth lipopolysaccharides," *J. Bacteriol.*, vol. 172, pp. 5307–5311, sep 1990.

[101] K. Sen and H. Nikaido, "Lipopolysaccharide Structure Required for Invitro Trimerization of Escherichia-Coli OmpF Porin," *J Bacteriol*, vol. 173, no. 2, pp. 926–928, 1991.

[102] D. Fourel, S. Mizushima, and J. M. Pagès, "Dynamics of the exposure of epitopes on OmpF, an outer membrane protein of Escherichia coli," *Eur. J. Biochem.*, vol. 206, pp. 109–114, may 1992.

[103] J. Reid, H. Fung, K. Gehring, P. E. Klebba, and H. Nikaido, "Targeting of porin to the outer membrane of Escherichia coli. Rate of trimer assembly and identification of a dimer intermediate," *J. Biol. Chem.*, vol. 263, pp. 7753–7759, jun 1988.

[104] M. W. Laird, A. W. Kloser, and R. Misra, "Assembly of LamB and OmpF in deep rough lipopolysaccharide mutants of Escherichia coli K-12," *J. Bacteriol.*, vol. 176, pp. 2259–2264, apr 1994.

[105] W. Arunmanee, M. Pathania, A. S. Solovyova, A. P. Le Brun, H. Ridley, A. Baslé, B. van den Berg, and J. H. Lakey, "Gram-negative trimeric porins have specific LPS binding sites that are essential for porin biogenesis," *Proc. Natl. Acad. Sci. U. S. A.*, vol. 113, pp. E5034—-43, aug 2016.

[106] S. Stumpe, R. Schmid, D. L. Stephens, G. Georgiou, and E. P. Bakker, "Identification of OmpT as the protease that hydrolyzes the antimicrobial peptide protamine before

it enters growing cells of Escherichia coli," *J. Bacteriol.*, vol. 180, pp. 4002–4006, aug 1998.

[107] L. Vandeputte-Rutten, R. A. Kramer, J. Kroon, N. Dekker, M. R. Egmond, and P. Gros, "Crystal structure of the outer membrane protease OmpT from Escherichia coli suggests a novel catalytic site," *EMBO J.*, vol. 20, pp. 5033–5039, sep 2001.

[108] C. J. Scandella and A. Kornberg, "Membrane-bound phospholipase A1 purified from Escherichia coli," *Biochemistry*, vol. 10, no. 24, pp. 4447–4456, 1971.

[109] P. de Geus, I. van Die, H. Bergmans, J. Tommassen, and G. de Haas, "Molecular cloning of pldA, the structural gene for outer membrane phospholipase of E. coli K12," *Molecular and General Genetics MGG*, vol. 190, no. 1, pp. 150–155, 1983.

[110] N. Dekker, "Outer-membrane phospholipase A: known structure, unknown biological function," *Mol. Microbiol.*, vol. 35, pp. 711–717, feb 2000.

[111] J. E. Cronan Jr and D. L. Wulff, "A role for phospholipid hydrolysis in the lysis of Escherichia coli infected with bacteriophage T4," *Virology*, vol. 38, pp. 241–246, jun 1969.

[112] K. L. Hardaway and C. S. Buller, "Effect of ethylenediaminetetraacetate on phospholipids and outer membrane function in Escherichia coli," *J. Bacteriol.*, vol. 137, pp. 62–68, jan 1979.

[113] M. P. Bos, B. Tefsen, P. Voet, V. Weynants, J. P. M. van Putten, and J. Tommassen, "Function of neisserial outer membrane phospholipase a in autolysis and assessment of its vaccine potential," *Infect. Immun.*, vol. 73, pp. 2222–2231, apr 2005.

[114] A. P. Pugsley and M. Schwartz, "Colicin E2 release: lysis, leakage or secretion? Possible role of a phospholipase," *The EMBO Journal*, vol. 3, no. 10, pp. 2393–2397, 1984.

[115] J. Luirink, C. van der Sande, J. Tommassen, E. Veltkamp, F. K. De Graaf, and B. Oudega, "Effects of divalent cations and of phospholipase A activity on excretion of cloacin DF13 and lysis of host cells," *J. Gen. Microbiol.*, vol. 132, pp. 825–834, mar 1986.

[116] N. Dekker, J. Tommassen, and H. M. Verheij, "Bacteriocin release protein triggers dimerization of outer membrane phospholipase A in vivo," *J. Bacteriol.*, vol. 181, pp. 3281–3283, may 1999.

[117] R. Voulhoux and J. Tommassen, "Omp85, an evolutionarily conserved bacterial protein involved in outer membrane protein assembly," *Research in Microbiology*, vol. 155, no. 3, pp. 129–135, 2004.

[118] J. Werner and R. Misra, "YaeT (Omp85) affects the assembly of lipid-dependent and lipid-independent outer membrane proteins of Escherichia coli," *Mol. Microbiol.*, vol. 57, pp. 1450–1459, sep 2005.

[119] L. Sánchez-Pulido, D. Devos, S. Genevrois, M. Vicente, and A. Valencia, "POTRA: a conserved domain in the FtsQ family and a class of β-barrel outer membrane proteins," *Trends in Biochemical Sciences*, vol. 28, no. 10, pp. 523–526, 2003.

[120] S. Kim, J. C. Malinverni, P. Sliz, T. J. Silhavy, S. C. Harrison, and D. Kahne, "Structure and function of an essential component of the outer membrane protein assembly machine," *Science*, vol. 317, pp. 961–964, aug 2007.

[121] N. Noinaj, A. J. Kuszak, J. C. Gumbart, P. Lukacik, H. Chang, N. C. Easley, T. Lithgow, and S. K. Buchanan, "Structural insight into the biogenesis of β-barrel membrane proteins," *Nature*, vol. 501, pp. 385–390, sep 2013.

[122] N. Noinaj, A. J. Kuszak, C. Balusek, J. C. Gumbart, and S. K. Buchanan, "Lateral opening and exit pore formation are required for BamA function," *Structure*, vol. 22, pp. 1055–1062, jul 2014.

[123] R. Albrecht, M. Schütz, P. Oberhettinger, M. Faulstich, I. Bermejo, T. Rudel, K. Diederichs, and K. Zeth, "Structure of BamA, an essential factor in outer membrane protein biogenesis," *Acta Crystallographica Section D Biological Crystallography*, vol. 70, no. 6, pp. 1779–1789, 2014.

[124] A. I. C. Höhr, C. Lindau, C. Wirth, J. Qiu, D. A. Stroud, S. Kutik, B. Guiard, C. Hunte, T. Becker, N. Pfanner, and N. Wiedemann, "Membrane protein insertion through a mitochondrial β-barrel gate," *Science*, vol. 359, pp. 6373–6834, 2018.

[125] C. L. Hagan, S. Kim, and D. Kahne, "Reconstitution of outer membrane protein assembly from purified components," *Science*, vol. 328, pp. 890–892, may 2010.

[126] J. G. Sklar, T. Wu, L. S. Gronenberg, J. C. Malinverni, D. Kahne, and T. J. Silhavy, "Lipoprotein SmpA is a component of the YaeT complex that assembles outer membrane proteins in Escherichia coli," *Proc. Natl. Acad. Sci. U. S. A.*, vol. 104, pp. 6400–6405, apr 2007.

[127] J. Bakelar, S. K. Buchanan, and N. Noinaj, "The structure of the β-barrel assembly machinery complex," *Science*, vol. 351, no. 6269, pp. 180–186, 2016.

[128] M. G. Iadanza, A. J. Higgins, B. Schiffrin, A. N. Calabrese, D. J. Brockwell, A. E. Ashcroft, S. E. Radford, and N. A. Ranson, "Lateral opening in the intact β-barrel assembly machinery captured by cryo-EM," *Nature Communications*, vol. 7, pp. 1–12, sep 2016.

[129] D. Tomasek, S. Rawson, J. Lee, J. Wzorek, S. Harrison, Z. Li, and D. Kahne, "Structure of a nascent membrane protein as it folds on the BAM complex," *Nature*, vol. 583, pp. 473–478, jul 2020.

[130] L. Xiao, L. Han, B. Li, M. Zhang, H. Zhou, Q. Luo, X. Zhang, and Y. Huang, "Structures of the β-barrel assembly machine recognizing outer membrane protein substrates," *The FASEB Journal*, vol. 35, p. e21207, jan 2020.

[131] A. J. M. Driessen and N. Nouwen, "Protein Translocation Across the Bacterial Cytoplasmic Membrane," *Annual Review of Biochemistry*, vol. 77, no. 1, pp. 643–667, 2008.

[132] N. W. Rigel and T. J. Silhavy, "Making a beta-barrel: assembly of outer membrane proteins in Gram-negative bacteria," *Curr. Opin. Microbiol.*, vol. 15, pp. 189–193, apr 2012.

[133] N. Noinaj, J. C. Gumbart, and S. K. Buchanan, "The β-barrel assembly machinery in motion," *Nature Reviews Microbiology*, vol. 15, no. 4, pp. 197–204, 2017.

[134] M. Braun and T. J. Silhavy, "Imp/OstA is required for cell envelope biogenesis in Escherichia coli," *Mol. Microbiol.*, vol. 45, pp. 1289–1302, sep 2002.

[135] Z. Zhou, K. A. White, A. Polissi, C. Georgopoulos, and C. R. Raetz, "Function of Escherichia coli MsbA, an essential ABC family transporter, in lipid A and phospholipid biosynthesis," *J. Biol. Chem.*, vol. 273, pp. 12466–12475, may 1998.

[136] P. Sperandeo, R. Cescutti, R. Villa, C. Di Benedetto, D. Candia, G. Dehò, and A. Polissi, "Characterization of lptA and lptB, two essential genes implicated in lipopolysaccharide transport to the outer membrane of Escherichia coli," *J. Bacteriol.*, vol. 189, pp. 244–253, jan 2007.

[137] P. Sperandeo, F. K. Lau, A. Carpentieri, C. De Castro, A. Molinaro, G. Dehò, T. J. Silhavy, and A. Polissi, "Functional analysis of the protein machinery required for transport of lipopolysaccharide to the outer membrane of Escherichia coli," *J. Bacteriol.*, vol. 190, pp. 4460–4469, jul 2008.

[138] N. Ruiz, L. S. Gronenberg, D. Kahne, and T. J. Silhavy, "Identification of two inner-membrane proteins required for the transport of lipopolysaccharide to the outer membrane of Escherichia coli," *Proc. Natl. Acad. Sci. U. S. A.*, vol. 105, pp. 5537–5542, apr 2008.

[139] S. Okuda, D. J. Sherman, T. J. Silhavy, N. Ruiz, and D. Kahne, "Lipopolysaccharide transport and assembly at the outer membrane: the PEZ model," *Nat. Rev. Microbiol.*, vol. 14, pp. 337–345, jun 2016.

[140] T. W. Owens, R. J. Taylor, K. S. Pahil, B. R. Bertani, N. Ruiz, A. C. Kruse, and D. Kahne, "Structural basis of unidirectional export of lipopolysaccharide to the cell surface," *Nature*, vol. 567, pp. 550–553, mar 2019.

[141] Y. Li, B. J. Orlando, and M. Liao, "Structural basis of lipopolysaccharide extraction by the LptB2FGC complex," *Nature*, vol. 567, no. 7749, pp. 486–490, 2019.

[142] F. Lauber, J. C. Deme, S. M. Lea, and B. C. Berks, "Type 9 secretion system structures reveal a new protein transport mechanism," *Nature 2018 564:7734*, vol. 564, pp. 77–82, nov 2018.

[143] H. Dong, Q. Xiang, Y. Gu, Z. Wang, N. G. Paterson, P. J. Stansfeld, C. He, Y. Zhang, W. Wang, and C. Dong, "Structural basis for outer membrane lipopolysaccharide insertion," *Nature*, vol. 511, pp. 52–56, jul 2014.

[144] S. Qiao, Q. Luo, Y. Zhao, X. C. Zhang, and Y. Huang, "Structural basis for lipopolysaccharide insertion in the bacterial outer membrane," *Nature*, vol. 511, pp. 108–111, jul 2014.

[145] I. Hindennach and U. Henning, "The Major Proteins of the Escherichia coli Outer Cell Envelope Membrane. Preparative Isolation of All Major Membrane Proteins," *European Journal of Biochemistry*, vol. 59, no. 1, pp. 207–213, 1975.

[146] U. Henning, H. D. Royer, R. M. Teather, I. Hindennach, and C. P. Hollenberg, "Cloning of the structural gene (ompA) for an integral outer membrane protein of Escherichia coli K-12," *Proc. Natl. Acad. Sci. U. S. A.*, vol. 76, pp. 4360–4364, sep 1979.

[147] E. Beck and E. Bremer, "Nucleotide sequence of the gene ompA coding the outer membrane protein II* of Escherichia coli K-12," *Nucleic Acids Research*, vol. 8, no. 13, pp. 3011–3028, 1980.

[148] R. Chen, W. Schmidmayr, C. Krämer, U. Chen-Schmeisser, and U. Henning, "Primary structure of major outer membrane protein II (ompA protein) of Escherichia coli K-12," *Proc. Natl. Acad. Sci. U. S. A.*, vol. 77, pp. 4592–4596, aug 1980.

[149] I. Sonntag, H. Schwarz, Y. Hirota, and U. Henning, "Cell envelope and shape of Escherichia coli: multiple mutants missing the outer membrane lipoprotein and other major outer membrane proteins," *J. Bacteriol.*, vol. 136, pp. 280–285, oct 1978.

[150] D. B. Datta, B. Arden, and U. Henning, "Major proteins of the Escherichia coli outer cell envelope membrane as bacteriophage receptors," *J. Bacteriol.*, vol. 131, pp. 821–829, sep 1977.

[151] L. Van Alphen, L. Havekes, and B. Lugtenberg, "Major outer membrane protein d of Escherichia coli K12. Purification and in vitro activity of bacteriophages k3 and f-pilus mediated conjugation," *FEBS Lett.*, vol. 75, pp. 285–290, mar 1977.

[152] K. Hantke, "Compilation of Escherichia coli K-12 outer membrane phage receptors - their function and some historical remarks," *FEMS Microbiology Letters*, vol. 367, no. 2, 2020.

[153] T. Chai and J. Foulds, "Demonstration of a missing outer membrane protein in tolG mutants of Escherichia coli," *Journal of Molecular Biology*, vol. 85, no. 3, pp. 465–474, 1974.

[154] J. K. Davies, P. Reeves, D. JK, and R. P, "Genetics of resistance to colicins in Escherichia coli K-12: cross-resistance among colicins of group A," *Journal of Bacteriology*, vol. 123, pp. 102–117, jul 1975.

[155] E. Sugawara and H. Nikaido, "Pore-forming activity of OmpA protein of Escherichia coli," *J. Biol. Chem.*, vol. 267, pp. 2507–2511, feb 1992.

[156] E. Sugawara and H. Nikaido, "OmpA protein of Escherichia coli outer membrane occurs in open and closed channel forms," *J. Biol. Chem.*, vol. 269, pp. 17981–17987, jul 1994.

[157] M. M. Gromiha, M. Michael Gromiha, and P. K. Ponnuswamy, "Prediction of transmembrane β-strands from hydrophobic characteristics of proteins," *International Journal of Peptide and Protein Research*, vol. 42, no. 5, pp. 420–431, 2009.

[158] A. Pautsch and G. E. Schulz, "Structure of the outer membrane protein A transmembrane domain," *Nature Structural Biology*, vol. 5, no. 11, pp. 1013–1017, 1998.

[159] A. Arora, F. Abildgaard, J. H. Bushweller, and L. K. Tamm, "Structure of outer membrane protein A transmembrane domain by NMR spectroscopy," *Nat. Struct. Biol.*, vol. 8, pp. 334–338, apr 2001.

[160] R. Koebnik, "Proposal for a peptidoglycan-associating alpha-helical motif in the C-terminal regions of some bacterial cell-surface proteins," *Molecular Microbiology*, vol. 16, no. 6, pp. 1269–1270, 1995.

[161] F. Samsudin, M. L. Ortiz-Suarez, T. J. Piggot, P. J. Bond, and S. Khalid, "OmpA: A Flexible Clamp for Bacterial Cell Wall Attachment," *Structure*, vol. 24, pp. 2227–2235, dec 2016.

[162] N. Lee, E. Cheng, and M. Inouye, "Optical properties of an outer membrane lipoprotein from Escherichia coli," *Biochim. Biophys. Acta*, vol. 465, pp. 650–656, mar 1977.

[163] K. Hantke and V. Braun, "Covalent binding of lipid to protein. Diglyceride and amide-linked fatty acid at the N-terminal end of the murein-lipoprotein of the Escherichia coli outer membrane," *Eur. J. Biochem.*, vol. 34, pp. 284–296, apr 1973.

[164] M. Inouye, J. Shaw, and C. Shen, "The assembly of a structural lipoprotein in the envelope of Escherichia coli," *J. Biol. Chem.*, vol. 247, pp. 8154–8159, dec 1972.

[165] D. S. Choi, H. Yamada, T. Mizuno, and S. Mizushima, "Trimeric structure and localization of the major lipoprotein in the cell surface of Escherichia coli," *J. Biol. Chem.*, vol. 261, pp. 8953–8957, jul 1986.

[166] W. Shu, J. Liu, H. Ji, and M. Lu, "Core structure of the outer membrane lipoprotein from Escherichia coli at 1.9 angstrom resolution," *Journal of Molecular Biology*, vol. 299, no. 4, pp. 1101–12, 2000.

[167] A. T. Asmar, J. L. Ferreira, E. J. Cohen, S.-H. Cho, M. Beeby, K. T. Hughes, and J.-F. Collet, "Communication across the bacterial cell envelope depends on the size of the periplasm," *PLoS Biol.*, vol. 15, p. e2004303, dec 2017.

[168] E. J. Cohen, J. L. Ferreira, M. S. Ladinsky, M. Beeby, and K. T. Hughes, "Nanoscale-length control of the flagellar driveshaft requires hitting the tethered outer membrane," *Science*, vol. 356, pp. 197–200, apr 2017.

[169] N. Hazumi, H. Yamada, and S. Mizushima, "Two new peptidoglycan-associated proteins in the outer membrane of Escherichia coli K-12," *FEMS Microbiology Letters*, vol. 4, no. 5, pp. 275–277, 1978.

[170] J.-C. Lazzaroni and R. Portalier, "The excC gene of Escherichia coli K-12 required for cell envelope integrity encodes the peptidoglycan-associated lipoprotein (PAL)," *Molecular Microbiology*, vol. 6, no. 6, pp. 735–742, 1992.

[171] R. Chen and U. Henning, "Nucleotide sequence of the gene for the peptidoglycan-associated lipoprotein of Escherichia coli K12," *Eur. J. Biochem.*, vol. 163, pp. 73–77, feb 1987.

[172] A. Bernadac, M. Gavioli, J.-C. Lazzaroni, S. Raina, and R. Lloubes, "Escherichia coli tol-pal Mutants Form Outer Membrane Vesicles," *Journal of Bacteriology*, vol. 180, no. 18, pp. 4872–4878, 1998.

[173] R. E. Webster, "The tol gene products and the import of macromolecules into Escherichia coli," *Molecular Microbiology*, vol. 5, no. 5, pp. 1005–1011, 1991.

[174] E. Bouveret, R. Derouiche, A. Rigal, R. Lloubès, C. Lazdunski, and H. Bénédetti, "Peptidoglycan-associated lipoprotein-TolB interaction. A possible key to explaining the formation of contact sites between the inner and outer membranes of Escherichia coli," *J. Biol. Chem.*, vol. 270, pp. 11071–11077, may 1995.

[175] T. Clavel, P. Germon, A. Vianney, R. Portalier, and J. C. Lazzaroni, "TolB protein of Escherichia coli K-12 interacts with the outer membrane peptidoglycan-associated proteins Pal, Lpp and OmpA," *Molecular Microbiology*, vol. 29, no. 1, pp. 359–367, 1998.

[176] E. Cascales, M. Gavioli, J. N. Sturgis, and R. Lloubes, "Proton motive force drives the interaction of the inner membrane TolA and outer membrane Pal proteins in Escherichia coli," *Molecular Microbiology*, vol. 38, no. 4, pp. 904–915, 2000.

[177] E. Cascales, R. Lloubès, and J. N. Sturgis, "The TolQ-TolR proteins energize TolA and share homologies with the flagellar motor proteins MotA-MotB," *Molecular Microbiology*, vol. 42, no. 3, pp. 795–807, 2008.

[178] R. Sender, S. Fuchs, and R. Milo, "Revised Estimates for the Number of Human and Bacteria Cells in the Body," *PLoS Biol.*, vol. 14, p. e1002533, aug 2016.

[179] L. Journet and E. Cascales, "The Type VI Secretion System in Escherichia coli and Related Species," *EcoSal Plus*, vol. 7, may 2016.

[180] S. Aoki, R. Pamma, A. Hernday, J. Bickham, B. Braaten, and D. Low, "Contact-Dependent Inhibition of Growth in Escherichia coli," *Science*, vol. 309, no. 5738, pp. 1245–1248, 2005.

[181] E. Cascales, S. K. Buchanan, D. Duché, C. Kleanthous, R. Lloubès, K. Postle, M. Riley, S. Slatin, and D. Cavard, "Colicin biology," *Microbiol. Mol. Biol. Rev.*, vol. 71, pp. 158–229, mar 2007.

[182] J. Davies and P. Reeves, "Genetics of resistance to colicins in Escherichia coli K-12: cross-resistance among colicins of group B," *Journal of bacteriology*, vol. 123, pp. 102–117, jul 1975.

[183] S. Schein, B. Kagan, and A. Finkelstein, "Colicin K acts by forming voltage-dependent channels in phospholipid bilayer membranes," *Nature*, vol. 276, no. 5684, pp. 159–163, 1978.

[184] M. El Ghachi, A. Bouhss, H. Barreteau, T. Touze, G. Auger, D. Blanot, and D. Mengin-Lecreulx, "Colicin M exerts its bacteriolytic effect via enzymatic degradation of undecaprenyl phosphate-linked peptidoglycan precursors," *The Journal of biological chemistry*, vol. 281, pp. 22761–22772, aug 2006.

[185] J. Tommassen, A. P. Pugsley, J. Korteland, J. Verbakel, and B. Lugtenberg, "Gene encoding a hybrid OmpF-PhoE pore protein in the outer membrane of Escherichia coli K12," *Molecular and General Genetics*, vol. 197, pp. 503–508, nov 1984.

[186] J. Bourdineaud, H. Fierobe, C. Lazdunski, and J. Pages, "Involvement of OmpF during reception and translocation steps of colicin N entry," *Molecular microbiology*, vol. 4, no. 10, pp. 1737–1743, 1990.

[187] O. Sharma, K. Datsenko, S. Ess, M. Zhalnina, B. Wanner, and W. Cramer, "Genome-wide screens: novel mechanisms in colicin import and cytotoxicity," *Molecular microbiology*, vol. 73, pp. 571–585, aug 2009.

[188] C. L. Johnson, H. Ridley, R. Marchetti, A. Silipo, D. C. Griffin, L. Crawford, B. Bonev, A. Molinaro, and J. H. Lakey, "The antibacterial toxin colicin N binds to the inner core of lipopolysaccharide and close to its translocator protein," *Molecular Microbiology*, vol. 92, pp. 440–452, mar 2014.

[189] P. Rassam, N. A. Copeland, O. Birkholz, C. Tóth, M. Chavent, A. L. Duncan, S. J. Cross, N. G. Housden, R. Kaminska, U. Seger, D. M. Quinn, T. J. Garrod, M. S. P. Sansom, J. Piehler, C. G. Baumann, and C. Kleanthous, "Supramolecular assemblies underpin turnover of outer membrane proteins in bacteria," *Nature*, vol. 523, pp. 333–336, jun 2015.

[190] K. A. Gibbs, D. D. Isaac, J. Xu, R. W. Hendrix, T. J. Silhavy, and J. A. Theriot, "Complex spatial distribution and dynamics of an abundant Escherichia coli outer membrane protein, LamB," *Molecular microbiology*, vol. 53, pp. 1771–1783, sep 2004.

[191] T. S. Ursell, E. H. Trepagnier, K. C. Huang, and J. A. Theriot, "Analysis of Surface Protein Expression Reveals the Growth Pattern of the Gram-Negative Outer Membrane," *PLOS Computational Biology*, vol. 8, p. e1002680, sep 2012.

[192] L. Oddershede, J. K. Dreyer, S. Grego, S. Brown, and K. Berg-Sørensen, "The Motion of a Single Molecule, the λ-Receptor, in the Bacterial Outer Membrane," *Biophysical Journal*, vol. 83, pp. 3152–3161, dec 2002.

[193] T. Bergmiller, A. M. C. Andersson, K. Tomasek, E. Balleza, D. J. Kiviet, R. Hauschild, G. Tkačik, and C. C. C. Guet, "Biased partitioning of the multidrug efflux pump AcrAB-TolC underlies long-lived phenotypic heterogeneity," *Science*, vol. 356, pp. 311–315, apr 2017.

[194] S. D. Gunasinghe, T. Shiota, C. J. Stubenrauch, K. D. Elgass, R. A. Strugnell, S. D. Gunasinghe, T. Shiota, C. J. Stubenrauch, K. E. Schulze, and C. T. Webb, "The WD40 Protein BamB Mediates Coupling of BAM Complexes into Assembly Precincts in the

Bacterial Article The WD40 Protein BamB Mediates Coupling of BAM Complexes into Assembly Precincts in the Bacterial Outer Membrane," *CellReports*, vol. 23, no. 9, pp. 2782–2794, 2018.

[195] K. A. Datsenko and B. L. Wanner, "One-step inactivation of chromosomal genes in Escherichia coli K-12 using PCR products," *Proceedings of the National Academy of Sciences*, vol. 97, pp. 6640–6645, jun 2000.

[196] M. S. Guyer, R. R. Reed, J. A. Steitz, and K. B. Low, "Identification of a Sex-factor-affinity Site in E. coli as $\gamma\delta$," *Cold Spring Harbor Symposia on Quantitative Biology*, vol. 45, pp. 135–140, jan 1981.

[197] R. Michael Garavito and J. P. Rosenbusch, "Isolation and crystallization of bacterial porin," *Methods in Enzymology*, vol. 125, pp. 309–328, jan 1986.

[198] R. Ghosh, M. Steiert, A. Hardmeyer, Y.-F. Wang, and J. P. Rosenbusch, "Overexpression of Outer Membrane Porins in E. coli Using pBluescript-Derived Vectors," *Gene Expression*, vol. 7, no. 3, p. 149, 1998.

[199] K. Jansen, P. Inns, N. Housden, J. Hopper, R. Kaminska, S. Lee, C. Robinson, H. Bayley, and C. Kleanthous, "Bifurcated binding of the OmpF receptor underpins import of the bacteriocin colicin N into Escherichia coli," *The Journal of biological chemistry*, vol. 295, pp. 9147–9156, jul 2020.

[200] E. Raggett, G. Bainbridge, L. Evans, L. Cooper, and J. Lakey, "Discovery of critical Tol A-binding residues in the bactericidal toxin colicin N: a biophysical approach," *Molecular Microbiology*, vol. 28, no. 6, pp. 1335–1343, 1998.

[201] H. Wilmsen, A. Pugsley, and F. Pattus, "Colicin N forms voltage and pH dependent channels in planar lipid bilayer membranes," *European biophysics journal : EBJ*, vol. 18, pp. 149–158, apr 1990.

[202] I. R. Vetter, M. W. Parker, A. D. Tucker, J. H. Lakey, F. Pattus, and D. Tsernoglou, "Crystal structure of a colicin N fragment suggests a model for toxicity," *Structure*, vol. 6, pp. 863–874, jul 1998.

[203] Y. C. Kim, A. W. Tarr, and C. N. Penfold, "Colicin import into E. coli cells: A model system for insights into the import mechanisms of bacteriocins," *Biochimica et Biophysica Acta (BBA) - Molecular Cell Research*, vol. 1843, pp. 1717–1731, aug 2014.

[204] P. White, A. Joshi, P. Rassam, N. G. Housden, R. Kaminska, J. D. Goult, C. Redfield, L. C. McCaughey, D. Walker, S. Mohammed, and C. Kleanthous, "Exploitation of an iron transporter for bacterial protein antibiotic import," *Proceedings of the National Academy of Sciences*, vol. 114, pp. 12051–12056, nov 2017.

[205] L. A. Gross, G. S. Baird, R. C. Hoffman, K. K. Baldridge, and R. Y. Tsien, "The structure of the chromophore within DsRed, a red fluorescent protein from coral," *Proceedings of the National Academy of Sciences*, vol. 97, pp. 11990–11995, oct 2000.

[206] X. Shu, S. Nathan C, Y. Corinne A, T. Roger Y, and R. S James, "Novel Chromophores and Buried Charges Control Color in mFruits," *Biochemistry*, vol. 45, pp. 9639–9647, aug 2006.

[207] M. Ormo, A. Cubitt, K. Kallio, L. Gross, R. Tsien, and S. Remington, "Crystal structure of the Aequorea victoria green fluorescent protein," *Science (New York, N.Y.)*, vol. 273, pp. 1392–1395, sep 1996.

[208] C. Johnson, H. Ridley, R. Pengelly, M. Salleh, and J. Lakey, "The unstructured domain of colicin N kills Escherichia coli," *Molecular microbiology*, vol. 89, pp. 84–95, jul 2013.

[209] P. Rassam, K. R. Long, R. Kaminska, D. J. Williams, G. Papadakos, C. G. Baumann, and C. Kleanthous, "Intermembrane crosstalk drives inner-membrane protein organization in Escherichia coli," *Nature Communications*, vol. 9, no. 1, pp. 1–8, 2018.

[210] L. J. A. Evans, A. Cooper, and J. H. Lakey, "Direct Measurement of the Association of a Protein with a Family of Membrane Receptors," *Journal of Molecular Biology*, vol. 255, pp. 559–563, feb 1996.

[211] F. Schabert, C. Henn, A. Engel, S. FA, H. C, and E. A, "Native Escherichia coli OmpF porin surfaces probed by atomic force microscopy," *Science*, vol. 268, no. 5207, pp. 92–94, 1995.

[212] N. A. Amro, L. P. Kotra, K. Wadu-Mesthrige, A. Bulychev, S. Mobashery, and G.-y. Liu, "High-Resolution Atomic Force Microscopy Studies of the Escherichia coli Outer Membrane: Structural Basis for Permeability," *Langmuir*, vol. 16, pp. 2789–2796, mar 2000.

[213] P. Higgs, R. Larsen, and K. Postle, "Quantification of known components of the Escherichia coli TonB energy transduction system: TonB, ExbB, ExbD and FepA," *Molecular microbiology*, vol. 44, no. 1, pp. 271–281, 2002.

[214] K. S. Grussmayer, K. Yserentant, and D.-P. Herten, "Photons in - numbers out : perspectives in quantitative fluorescence microscopy for in situ protein counting," *Methods and Applications in Fluorescence*, vol. 7, no. 1, p. 012003, 2019.

[215] M. A. Kiskowski, J. F. Hancock, and A. K. Kenworthy, "On the Use of Ripley's K-Function and Its Derivatives to Analyze Domain Size," *Biophysical Journal*, vol. 97, pp. 1095–1103, aug 2009.

[216] S. Wang, J. R. Moffitt, G. T. Dempsey, X. S. Xie, and X. Zhuang, "Characterization and development of photoactivatable fluorescent proteins for single-molecule-based superresolution imaging," *Proceedings of the National Academy of Sciences of the United States of America*, vol. 111, pp. 8452–8457, jun 2014.

[217] P. Annibale, S. Vanni, M. Scarselli, U. Rothlisberger, and A. Radenovic, "Identification of clustering artifacts in photoactivated localization microscopy," *Nature Methods 2011 8:7*, vol. 8, pp. 527–528, jun 2011.

[218] L. Patel, D. Williamson, D. M. Owen, and E. A. Cohen, "Blinking statistics and molecular counting in direct stochastic reconstruction microscopy (dSTORM)," *Bioinformatics*, vol. 37, pp. 2730–2737, sep 2021.

[219] M. A. de Pedro, C. G. Grünfelder, and H. Schwarz, "Restricted Mobility of Cell Surface Proteins in the Polar Regions of Escherichia coli," *Journal of Bacteriology*, vol. 186, p. 2594, may 2004.

[220] A. Ghosh and K. Young, "Helical disposition of proteins and lipopolysaccharide in the outer membrane of Escherichia coli," *Journal of bacteriology*, vol. 187, pp. 1913–1922, mar 2005.

[221] G. S. Verhoeven, M. Dogterom, and T. den Blaauwen, "Absence of long-range diffusion of OmpA in E. coli is not caused by its peptidoglycan binding domain," *BMC Microbiology*, vol. 13, pp. 1–9, mar 2013.

[222] G. Mamou, P. G. Inns, D. Sun, R. Kaminska, N. G. Housden, R. Cohen-Khait, H. Miller, K. M. Storek, S. T. Rutherford, J. Payandeh, and C. Kleanthous, "Spatiotemporal organization of BamA governs the pattern of outer membrane protein distribution in growing Escherichia coli cells," *bioRxiv*, p. 2021.01.27.428258, jan 2021.

[223] J. Szczepaniak, C. Press, and C. Kleanthous, "The multifarious roles of Tol-Pal in Gram-negative bacteria," *FEMS Microbiol. Rev.*, may 2020.

[224] C. W. Mullineaux, A. Nenninger, N. Ray, and C. Robinson, "Diffusion of green fluorescent protein in three cell environments in Escherichia coli," *Journal of Bacteriology*, vol. 188, pp. 3442–3448, may 2006.

[225] R. el Kouhen, H. Fierobe, S. Scianimanico, M. Steiert, F. Pattus, and J. Pages, "Characterization of the receptor and translocator domains of colicin N," *European journal of biochemistry*, vol. 214, no. 3, pp. 635–639, 1993.

[226] M. Wiener, D. Freymann, P. Ghosh, and R. Stroud, "Crystal structure of colicin Ia," *Nature*, vol. 385, pp. 461–464, jan 1997.

[227] K. Jakes, "Daring to be different: colicin N finds another way," *Molecular microbiology*, vol. 92, no. 3, pp. 435–439, 2014.

[228] H. Ridley and J. H. Lakey, "Antibacterial toxin colicin N and phage protein G3p compete with TolB for a binding site on TolA," *Microbiology*, vol. 161, p. 503, mar 2015.

[229] M. A. Gerding, Y. Ogata, N. D. Pecora, H. Niki, and P. A. J. De Boer, "The trans-envelope Tol-Pal complex is part of the cell division machinery and required for proper outer-membrane invagination during cell constriction in E. coli," *Molecular Microbiology*, vol. 63, no. 4, pp. 1008–1025, 2007.

[230] M. Petiti, B. Serrano, L. Faure, R. Lloubes, T. Mignot, and D. Duche, "Tol Energy-Driven Localization of Pal and Anchoring to the Peptidoglycan Promote Outer-Membrane Constriction," *Journal of molecular biology*, vol. 431, pp. 3275–3288, aug 2019.

[231] J. Spector, S. Zakharov, Y. Lill, O. Sharma, W. A. Cramer, and K. Ritchie, "Mobility of BtuB and OmpF in the Escherichia coli outer membrane: Implications for dynamic formation of a translocon complex," *Biophysical Journal*, vol. 99, no. 12, pp. 3880–3886, 2010.

[232] M. Chavent, A. L. Duncan, P. Rassam, O. Birkholz, J. Hélie, T. Reddy, D. Beliaev, B. Hambly, J. Piehler, C. Kleanthous, and M. S. P. Sansom, "How nanoscale protein in-

teractions determine the mesoscale dynamic organisation of bacterial outer membrane proteins," *Nature Communications 2018 9:1*, vol. 9, pp. 1–12, jul 2018.

[233] C. P. Moon, N. R. Zaccai, P. J. Fleming, D. Gessmann, and K. G. Fleming, "Membrane protein thermodynamic stability may serve as the energy sink for sorting in the periplasm," *Proceedings of the National Academy of Sciences*, vol. 110, pp. 4285–4290, mar 2013.

[234] E. Rothenberg, L. Sepulveda, S. Skinner, L. Zeng, P. Selvin, and I. Golding, "Single-virus tracking reveals a spatial receptor-dependent search mechanism," *Biophysical journal*, vol. 100, no. 12, pp. 2875–2882, 2011.

[235] G. Benn, I. V. Mikheyeva, P. G. Inns, J. C. Forster, N. Ojkic, C. Bortolini, M. G. Ryadnov, C. Kleanthous, T. J. Silhavy, and B. W. Hoogenboom, "Phase separation in the outer membrane of Escherichia coli," *Proceedings of the National Academy of Sciences of the United States of America*, vol. 118, nov 2021.

[236] U. Choi and C. R. Lee, "Distinct Roles of Outer Membrane Porins in Antibiotic Resistance and Membrane Integrity in Escherichia coli," *Frontiers in Microbiology*, vol. 10, no. APR, p. 953, 2019.

[237] L. M. Guzman, D. Belin, M. J. Carson, and J. Beckwith, "Tight regulation, modulation, and high-level expression by vectors containing the arabinose P(BAD) promoter," *Journal of Bacteriology*, vol. 177, no. 14, pp. 4121–4130, 1995.